FABRICATION OF NOVEL CORE-SHELL NANOSTRUCTURES FOR PHOTONICS APPLICATIONS

A DISSERTATION SUBMITTED TO
MATERIALS SCIENCE AND NANOTECHNOLOGY PROGRAM
OF THE GRADUATE SCHOOL OF ENGINEERING AND SCIENCE
OF BILKENT UNIVERSITY
IN PARTIAL FULFILLMENT OF THE REQUIREMENTS
FOR THE DEGREE OF
DOCTOR OF PHILOSOPHY

By
Tural Khudiyev
July, 2013

I certify that I have read this thesis and that in my opinion it is fully adequate, in scope and in quality, as a thesis of the degree of Doctor of Philosophy.

…….

Assoc. Prof. Dr. Mehmet Bayındır (Advisor)

I certify that I have read this thesis and that in my opinion it is fully adequate, in scope and in quality, as a thesis of the degree of Doctor of Philosophy.

…….

Prof. Dr. Salim Çıracı

I certify that I have read this thesis and that in my opinion it is fully adequate, in scope and in quality, as a thesis of the degree of Doctor of Philosophy.

…….

Prof. Dr. Adnan Akay

I certify that I have read this thesis and that in my opinion it is fully adequate, in scope and in quality, as a thesis of the degree of Doctor of Philosophy.

…….

Prof. Dr. Adil Denizli

I certify that I have read this thesis and that in my opinion it is fully adequate, in scope and in quality, as a thesis of the degree of Doctor of Philosophy.

…….

Assoc. Prof. Dr. Hamza Kurt

Approved for the Institute of Engineering and Science:

…….

Prof. Dr. Levent Onural

Director of the Graduate School

ABSTRACT

FABRICATION OF NOVEL CORE-SHELL NANOSTRUCTURES FOR PHOTONICS APPLICATIONS

Tural Khudiyev
Ph.D. in Materials Science and Nanotechnology
Supervisor: Assoc. Prof. Dr. Mehmet Bayındır
July, 2013

Developments in nanoscale fabrication and characterization techniques have led to fundamental changes in the scientific understanding of many fields, and novel nanostructures have been utilized to investigate the conceptual underpinnings behind a diverse array of natural phenomena. However, nanofabrication methods are frequently hindered by issues such as misalignment, small batch sizes, high production costs and constraints in material choice or nanostructure diversity, which decrease their potential utility and prevent their widespread application in nanoscale optics and photonics.

In this work, a new top-down nanofabrication method is described, which is called Iterative Size Reduction (ISR), where step-by-step reduction is utilized to decrease structure dimensions from macro- to nanosizes and produce indefinitely long one-dimensional core-shell nanostructures with properties highly suitable for use in optical applications. Plateau-Rayleigh instabilities are then utilized to thermally degrade ISR-produced nanowire arrays into complex core-shell schemes, which are produced successively in a hitherto-undescribed transitory region between core-shell nanowires and core-shell nanospheres.

A diverse array of optical phenomena have been observed on fabricated novel core-shell nano-platforms, which are utilized in the design of novel nanostructures for emerging photonics applications. Briefly, (a) the resonant Mie scattering behavior is characterized on glass-polymer nanostructures and these nanostructures are designed

for large-area structural coloration, (b) a novel non-resonant Mie scattering regime responsible for the scattering characteristics exhibited by all-polymer core-shell nanowires is described, (c) a nanoscale analogue to the thin film interference phenomenon is demonstrated that occurs on the core-shell boundary of ISR-produced micro- and nanostructures, (d) an unusual photonic crystal structure observed in the neck feathers of mallard drakes is investigated and imitated, (e) a series of all-polymer core-shell nanowires to function as novel light-trapping platforms and sensors are engineered and (f) the generation of supercontinuum light in well-ordered arrays of As_2Se_3 nanowires is reported.

Keywords: Top-down nanofabrication technique, fiber drawing, thermal instability, Mie scattering, core-shell nanostructures, nanoshell interference, photonic crystal, supercontinuum generation, light trapping, optical sensor

ÖZET

FOTONİK UYGULAMALAR İÇİN YENİ ÇEKİRDEK-KABUK NANOYAPILARININ ÜRETİLMESİ

Tural Khudiyev
Malzeme Bilimi ve Nanoteknoloji, Doktora
Tez Yöneticisi: Doç. Dr. Mehmet Bayındır
Temmuz, 2013

Nano-üretim ve karakterizasyon tekniklerindeki ilerlemeler bilimin, birden fazla alanında sürdürülen araştırmaları hızlandırmış ve bu alanlardaki konuların daha iyi anlaşılmalarını sağlamıştır. Üretilen yeni nanoyapılar, bu araştırmalarda kolaylıklar sağlamış ve yeni olayların gözlemlenmesine yardımcı olmuştur. Bu nanoyapılar, nano-üretim tekniklerinden kaynaklanan hizalanma, üretim miktarı, yüksek üretim maliyetleri, kısıtlı malzeme seçeneği ve çeşitliliği gibi sorunlardan dolayı, olası uygulanabilirliklerini ve kolaylıklarını kaybetmektedirler. Özellikle nano-optik ve fotonik uygulamalarında, bu nedenlerden kaynaklanan sorunlar öne çıkmaktadır.

Bu tez çalışmasında, yeni bir nano-üretim tekniği olarak 'Tekrarlamalı Fiber Çekme (TFÇ)' yöntemi tanımlanmıştır. Bu tekniği kullanarak, yapıların ölçüsü aşamalı şekilde makroboyutlardan nanoboyutlara indirilebilinir ve bu şekilde istenilen uzunlukta bir boyutlu çekirdek-kabuk nanoyapılar elde edilebilinir. Daha sonra 'Plateau-Rayleigh' kararsızlığını kullanarak TFÇ yöntemiyle elde edilen nanoteller, üretimi zor, farklı, çekirdek-kabuk yapılarına dönüştürebilinir ve bu şekilde nanotel-nanoküre arasında olan, daha önce farkedilmemiş bir geçiş bölgesinin olduğu gözlemlenebilinir.

Üretilen çekirdek-kabuk nano-platformları kullanarak değişik optik olaylar gözlemlenmiş ve bunlar yeni fotonik uygulamaları için tasarlanmıştır. Kısaca, (a) cam-polimer nanoyapılarında rezonant Mie saçılması incelenmiş ve geniş-alan renklenmesi için düzenlenmiştir, (b) üretilen tümü-polimer nanotellerin Mie saçılmasında rezonant

olmayan bir bölgeye denk geldiğini ve bu bölgenin yeni özelliklere sahip olduğu gözlemlenmiştir, (c) ince-film girişimi olayının çekirdek-kabuk mikro- ve nanoyapılarındaki karşılığı olan nanokabuk girişimi incelenmiştir, (d) yaban ördeği tüyünde gözlemlenen alışılmadık bir fotonik kristal yapısı incelenmiş ve TFÇ yöntemi kullanılarak taklit edilmiştir, (e) tümü-polimer çekirdek-kabuk nanoyapılarının ışığı toplama potansiyelini incelenmiş ve emilimi ciddi bir şekilde arttırdığı gözlemlenmiştir, (f) As_2Se_3 dan oluşan nanotel dizileri verimli geniş-bantlı ışık üretiminde kullanılmıştır.

Anahtar kelimeler: Yukarıdan-aşağıya nanoüretim tekniği, fiber çekme, termal kararsızlık, Mie saçılması, çekirdek-kabuk nanoyapılar, nanokabuk girişimi, fotonik kristal, geniş-bantlı ışık üretme, ışık hapsetme, sensör

Acknowledgement

Foremost, I would like to express my sincere gratitude to my advisor Assoc. Prof. Mehmet Bayindir due to his continued support, motivation, immense knowledge and sharing personal and academic experiences in order to overcome encountered problems. He has guided me through the progress of my Ph.D study and provided me opportunity to participate in interesting reseach topics. It was great pleasure to study directly with him and I will never forget overnight studies which inspired original ideas and new insights. I have learned a lot from him which I believe will be useful for my future academic studies.

Besides my advisor, I would like to thank to Prof. Dr. Salim Çıracı and Prof. Dr. Adnan Akay for their encouragement and insightful comments during the progress of my Ph.D study. I would like to thank Prof. Dr. Salim Çıracı also due to establishing world-class nanocenter, UNAM, care and attention on my studies, and support my participation in prestigous nanotechnology workshop.

I acknowledge TÜBİTAK for funding with 2215 - Graduate Scholarship Programme for International Students and TÜBİTAK ULAKBİM for providing access to use high-speed computers.

My sincere thanks also goes to my groupmate Tamer Dogan for his determined cooperative hard work and fruitful discussions, which led to successful results.

I owe special thank to Alper D. Özkan for his fruitful discussions, critical reading of the thesis and sharing his useful academic writing knowledge.

I thank my fellow groupmates in Bayindir Group: Tugrul Cinkara, Huseyin Duman, Erol Özgür, Ozan Aktaş, Adem Yıldırım, Mehmet Kanık, Bihter Dağlar, Muhammet H. Dolaş, Muhammet Çelebi, Yunus Çetin, Pınar Beyazkılıç, Ersin Huseyinoğlu, Pelin Tören, Fahri Öztürk for the working together, and for all the fun we have had in my Ph.D years.

I would like to thank staff and scientists in our group; Ms. Neşe Özgür, Eng. Murat Dere, Eng. Dilara Öksüz, Eng. Emel Gürbüz and researchers Dr. İbrahim Yılmaz, Dr. Osama Tobail, Dr. Mostafa M. El-Ashry and Dr. Gökçen Birlik Demirel. I owe special thank to Dr. Osama Tobail due to critical reading of my thesis. I am also grateful to TEM specialist Eng. Mustafa Güler for his help in using electron microscopes.

I would like to thank my parents for their continued support, trust, love, and encouragement in all phases of my life. Above all, I would like to thank my wife and unborn daughter Maryam who are my main motivation and I dedicate this thesis to them.

Contents

List of Figures

List of Tables

Chapter 1

Introduction

Light-matter interactions are an integral part of our life. They play a crucial role in many biological systems (such as photosynthesis, vitamin D synthesis and circadian rhytms), are responsible for mediating many natural phenomena (such as rainbow, glory and airglow) and form the basis of processes such as lasing, diffraction, interference, absorption, refraction and reflection, which are harnessed for human convenience in such devices as eyeglasses, phones, sensors and LEDs. While light-matter interactions in the macroscale are well-characterized, developments in nanotechnology have spurred the discovery of a vast number of new light-matter interactions that can only be observed under smaller scales (while electromagnetic effects are scalable across a wide size range, nanoscale structures must be utilized for these effects to occur in the visible region of light). In addition, nanostructures may also display a variety of unique effects by virtue of their size alone, as quantum effects become significant at the size scales involved. As such, nanoscale materials have received much attention in the recent decade for the

reproduction of a variety of optical phenomena in the visible range, for both academic research and practical applications.

In optics, the minimum size at which a structure is capable of effecting the concentration of light is known as the diffraction limit [1]. In other words, light can only propagate through structures above a certain size limit, which is equal to half of the propagating wavelength. However, metal nanostructures are capable of breaking this size limit by the confining the photons into deep-subwavelength structures [2] via the cluster oscillation of free electrons. The investigation of this phenomenon is the study area of plasmonics and constitutes an important part of nanophotonics. Dielectric materials are generally considered preferable to metals in optical applications due to their higher biocompatibility, low optical losses, broad material options, cost-effectiveness and flexibility. While the diffraction-limit problem renders it difficult to utilize nanostructures with dielectric compositions for optical purposes, absorption by and scattering from small particles which result with leaky-mode resonances can bypass such issues. Such interactions fall in the domain of the Lorenz-Mie theory [3]. In addition, the diffraction limit can also be bypassed by using dielectric materials in nanostructure arrays, which behave as an effective medium [4] and can be characterized by effective medium models, or fabricating them as periodic structures to display the photonic crystal effect [5]. Likewise, light can be guided inside a high refractive index dielectric structure at selective wavelengths, which is different from the fiber guiding mechanism [6]. The multiple scattering phenomenon, an effect similar to but distinct from photonic crystals and individual particle scattering, [7] can also be utilized for the optical functionalization of dielectrics.

Advances in nanofabrication techniques have resulted in the discovery of a vast variety of novel optical effects, each associated with a unique set of application areas. Nanomaterials displaying such unique optical phenomena can be utilized in the development of novel designs and devices for such diverse purposes as the engineering of nanoscale structures for the enhancement of light absorption

efficiency or the fabrication of large-scale nanostructure arrays exhibiting structural coloration. Among nanoscale materials, nanowires and nanospheres are arguably the most studied configurations and comprise outstanding media for the investigation of light-matter interactions, having been utilized in numerous occassions for the practical utilization of nanoscale optical phenomena [8,9].

Nature also plays a key role in the progress of optical nanoscience. Photonic structures in biological systems are generally in the nanoscale, and may display a diverse array of optical features. Photonic crystals observed in peacock feathers [10] and the anti-reflective surfaces [11] displayed by the eyes of nocturnal insects are two well-known examples of nanoscale optical phenomena in biological systems. These structures can be mimicked by using advanced fabrication techniques [12].

Consequently, advances in nano-optics rely on both the investigation of biological structures and conventional materials engineering strategies. This combination is expected to play a key role in the solution of many global problems, and can be alleviate pressing energy, food, environment, communication and health issues experienced by the modern world.

Numerous fabrication techniques exist for the production of nanostructures with zero-dimensional (0D), one-dimensional (1D) and/or two-dimensional (2D) features. Thin film nanostructures [13] can be fabricated via physical techniques, such as laser ablation and electron beam evaporation, or chemical techniques, such as chemical vapor deposition and sol-gel processing methods. Many top-down [14,15,16] and bottom-up [17,18,19] techniques are also known for the fabrication of 0D and 1D nanostructures. Top-down fabrication methods for such purposes include lithographic, AAO template and electrospinning methods, while many chemical techniques constitute examples of bottom-up approaches for nanostructure fabrication. Existing methods, however, are constrained by several limitations, which include:

Alignment: Nanostructures produced by current fabrication methods are generally randomly oriented and require post-synthesis processing. A number of techniques [20,21] have been developed to overcome this problem. However, these specialized methods are often expensive and cannot be applied for large-scale production of aligned nanomaterials.

Material constraints: Fabrication techniques are often inapplicable to all but a select number of materials [22,23], and fabrication steps frequently require all material components involved to display a specific physical property to function. Such material properties include elasticity (electrospinning), selectivitiy (lithography), chemical compatibility and/or high-temperature stability (chemical techniques).

Length and mass production: Many nanofabrication methods can produce nanostructures in lengths of up to several millimeters [24]. However, the mass production of 1D nanostructures remains a challenge and current fabrication methods are generally incapable of scaling up their production output.

Uniformity and smoothness: Nanofabrication techniques frequently produce structures with rough or non-uniform surfaces problem [25,26]. This is especially undesirable in light-matter interactions, where surface irregularities may cause unwanted spectral shifts or optical aberrations.

Fabrication speed and cost: Nanoscale structures are must be fabricated rapidly and without incurring extravagant costs in order to fully integrate themselves in our daily lives. However, some fabrication methods may require longer processing times, and many others are only useful for the production of prototypes [27,28,29] due to their prohibitively expensive costs.

Nanostructure diversity: As each nanostructure arrangement is associated with a number of unique phenonena, the production of novel nanostructure configurations is one of the driving factors in nanotechnology [30]. Many novel electrical, optical, mechanical and thermal properties can only be observed in nanoscale materials

displaying specific shapes and arrangements. However, many nanofabrication techniques are applicable for only a select number of nanostructures, and cannot be utilized for the production of complex nanostructure configurations.

In this thesis, I focus on the investigation of new fabrication techniques capable of fulfilling the rigid requirements expected of nanomaterials suitable for utilization in emerging optical applications. To this end, we developed a cost-effective, rapid and high-throughput top-to-down approach, which we call Iterative Size Reduction (ISR), capable of producing arbitrarily long, uniform, globally aligned nanostructures [31]. I demonstrate this method to be successful in the fabrication of hard-to-produce glass/polymer and all-polymer core-shell nanowires. I also show that all-polymer photonic crystal structure and monolayer nanowires can be produced by modifying this approach.

Then I demonstrate a combined iterative size reduction-thermal manipulation method by which a large diversity of indefinitely long, globally parallel, complex nanostructure arrays with high surface uniformity and low optical variation can be fabricated from PES-embedded core-shell As_2Se_3-PVDF nanowires [32]. Nanosprings, nanoshell-embedded discrete nanorods and nanospheres, and nanochains are produced in succession by a hitherto-undescribed, Plateau-Rayleigh instability-mediated deformation, eventually culminating in the fragmentation of the nanostructure array and the formation of core-shell nanospheres. Structure sizes, profiles, instability wavelengths and optical properties can be modified by minor alterations in process temperature and duration. As such, a great diversity of nano-configurations with highly desirable features (*i.e.*, smoothness, length, uniformity, and alignment) can be obtained by using this combined thermal nanofabrication technique.

I observe and report a variety of optical phenomena that take place in fabricated novel core-shell nanostructures, which I engineer for several important applications. Resonant Mie scattering is a well-known optical phenomenon and results from the

interaction of light with small, high–refractive index particles, and I produce and characterize a diverse set of core-shell nanoschemes for structural coloring based on this phenomenon [33]. I also observe that low-refractive index materials in a specific size range are capable of displaying a non-resonant form of Mie scattering [34], report for the first time that thin film interference occurs on the core-shell interface of micron-scale glass-polymer spheres [33], utilize all-polymer core-shell nanowires to mimic the unusual photonic crystal structures observed in the head feathers of *Anas platyrhynchos* drakes [35], demonstrate the sensing capabilities associated with NRM scattering and the nanoshell interference phenomenon, show that all-polymer core-shell nanowire coatings are capable of enhancing light absorption in solar cells via NRM scattering and the textured effect [36], and combine the inherent nonlinearity of chalcogenide glasses with our ability to produce nonlinear arrays of nanowires to generate broad-spectrum supercontinua with high power throughputs [37].

This thesis is organized as follows: In Chapter 2, I describe the details of a novel fabrication technique, Iterative Size Reduction (ISR), for the synthesis of 1D core-shell nanostructures, and detail the materials utilized throughout the fabrication process. The fabrication mechanisms of glass-polymer and all-polymer core-shell nanowires, photonic crystal and monolayer structures are elaborated in this chapter. In Chapter 3, I demonstrate that ISR-produced glass-polymer nanowires are modified into a diverse array of core-shell nanostructures via Plateau-Rayleigh instability-mediated deformation following heat treatment, and characterize the temperature region in which these nanoparticles are produced from core-shell nanowires. In Chapter 4, I detail the analytical and numerical techniques that I utilized in order to predict the behavior of light in fabricated core-shell nanostructures. In addition, this chapter features detailed analytical solutions for the characterization of scattering from core-shell nanostructures. In Chapter 5, I explain the theoretical background of the Resonant Mie scattering phenomenon and how it can be engineered for

observation of structural coloration in the diverse core-shell nanoschemes. In Chapter 6, I characterize a novel, non-resonant form of Mie scattering in low-refractive index materials and discuss the potential of this phenomenon in photonics applications. In Chapter 7, I prove that an analogue of the thin-film interference phenomenon, which is called nanoshell interference, occurs on the core-shell interface of glass-polymer spheres. In Chapter 8, I investigate and imitate the unusual photonic crystal structures observed in *Anas platyrhynchos* neck feathers. In Chapter 9, I provide the theoretical and experimental demonstration of light absorption enhancement by all-polymer core-shell nanowires, and discuss sensor applications of NRM scattering and nanoshell interference phenomena. In Chapter 10, I present a proof-of-concept scheme for the generation of supercontinua using nanowires of highly nonlinear chalcogenide glasses, and utilize dispersion engineering procedures to design a nanowire array displaying high-performance spectral broadening. In Chapter 11, I summarize the topics investigated throughout the course of this thesis.

Chapter 2

Iterative Size Reduction Technique for Production of Nanostructures

2.1 Iterative Size Reduction Technique

The method described in this chapter, Iterative Size Reduction (ISR), is a recently developed top-down nanofabrication technique [31] involving the repeated reduction of macroscopic structure sizes by a series of successive drawing steps. This technique is inspired by the Taylor wire drawing process [38], which we successfully improve and utilize as a nanotechnology toolkit for the production of 1D nanostructures. Due to the physical properties of used materials, fabrication of nanostructures can be performed at relatively low temperatures (approx. 300 °C maximum). Nanostructures are formed entirely by physical interactions, mediated primarily by viscosity and surface tension.

Figure 2.1: Photographs of macroscopic preforms. Preforms are macro prototype of fabricated micro- or nanostructures. The design of preform may change depending on the purpose of fabrication and geometry of nanostructures.

As such, this method does not rely on the chemical properties of material components, and can be utilized for a wide range of materials.

The nanostructure produced by this approach are closely match the initial macroscopic preform in profile thanks to mutually compatible viscoelastic properties of the material set used, which also prevents the structures from collapsing and results in the creation of uniform nanostructures.

Amorphous materials are advantageous for thermal nanofabrication method, including ISR, due to their continuous glass transition temperatures. As such, the present top-down methodology can be utilized to draw chalcogenide based glasses with a variety of polymeric materials.

The ISR procedure involves a macroscopic preform, prepared prior to fabrication, being reduced to smaller scales using a novel fabrication system designed for thermal drawing. The fabrication process may utilize several iterative steps in order to obtain the required sizes. At the end of each step, structures are characterized by electron microscopy prior to their use in subsequent steps.

Preforms (Figure 2.1) are macroscopic structures that form nanostructures following multiple elongation and size reduction steps. They are composed of two or more functional layers. Conventional preforms consist of a glassy material filling contained by an outer polymer shell. Here, the glass serves as a functional component and can be selected according to the electrical, optical, mechanical and/or thermal properties required of the micro- or nanoscale material. The outer polymer sheath provides flexibility and makes the handling of fabricated structures feasible. These preforms also can be produced by (a) wrapping the core and shell layers around a glass rod, which is subsequently removed prior to fabrication ("tube" synthesis), or (b) wrapping two polymer layers (the sheath and shell regions) and a glass or polymer-based filling material (the core region) successively around each other ("core-shell" synthesis). Depending on the purpose of fabrication, the sheath region can be removed by etchant treatment and free-standing bare nanowires, core-shell nanowires and nanotubes can be obtained. In-fiber cases nanostructures produced by this method are also very useful in number of applications. Further alterations in starting configuration (*i.e.* multilayered structures or structures with square, triangular cross-sections) can also be utilized for nanostructure synthesis. Following their production, macroscopic structures are held in the furnace for the consolidation process to occur. Consolidation is performed under vacuum to conserve structural

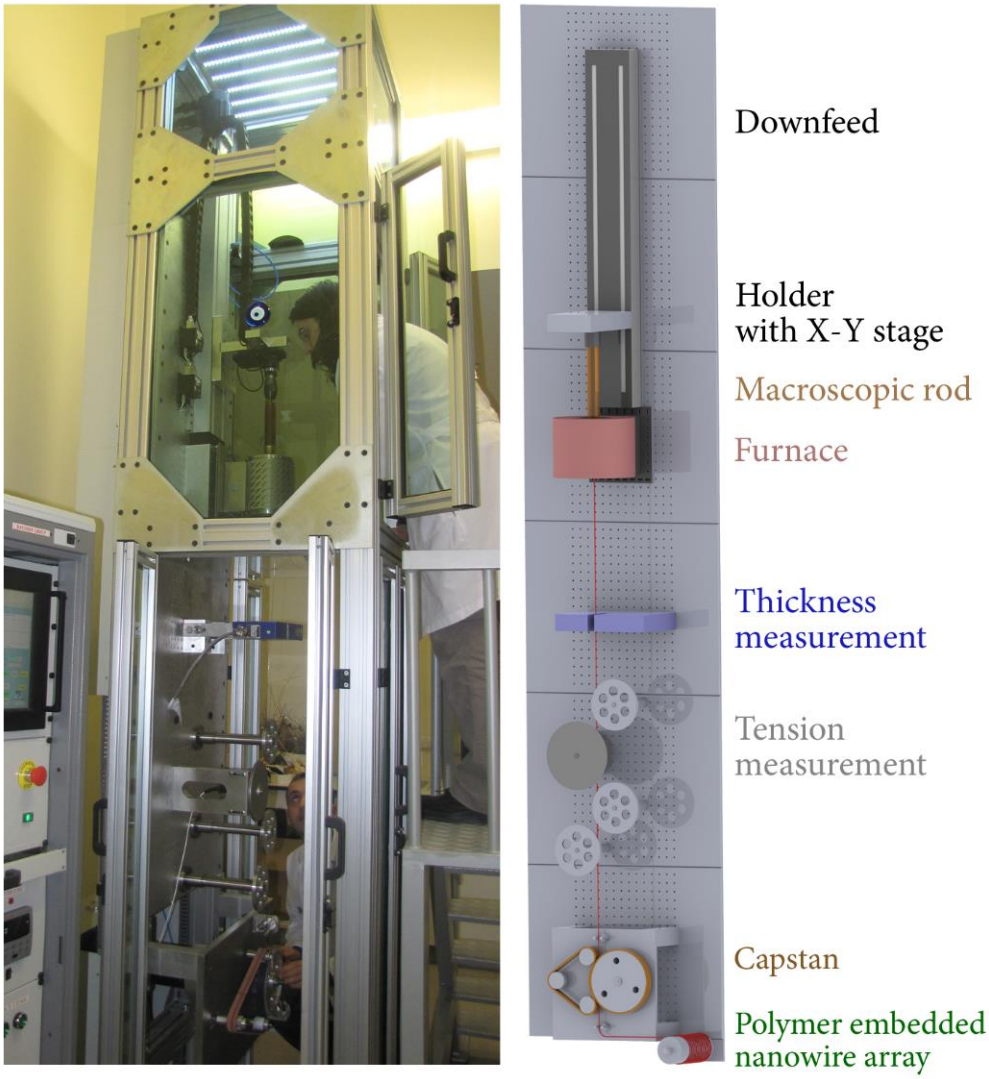

Figure 2.2: Home-built fiber tower system designed in order to reduce sizes of macroscopic preforms. The 2.5 m tower consists of thermally isolated double zone furnace, feeding, capstan, thickness, and tension meter units. Furnace temperatures may exceeds 300 °C which is sufficient for the fabrication process due to the low glass transition temperatures of the materials utilized. A mass is hanged from the top of the perforated preform in order to apply mechanical stress and facilitate the drawing of preform when a certain material viscosity is reached. For uniform heat treatment, the position of preform is arranged by using the x-y stage. Down-feed and capstan speeds are arranged prior to fiber drawing. Sizes of inner structures are controlled by altering the outer diameter of the fiber. Tension is used as a feedback for the settings of down-feed, capstan and furnace units. Polymer fiber thickness is measured with a laser micrometer, and fiber tension by a transverse tensiometer.

homogeneity and prevent defect formation, and sufficient time is provided for the polymer layers to fuse into a distinctive sheath region.

Consolidated preforms measuring several centimeters in diameter are then thermally drawn in a custom-built fiber tower system. The fiber tower consist of several important structural components, which are detailed in Figure 2.2. Preform positions are fixed with a holder and, if necessary, can be changed by a x-y stage for uniform heat treatment. Preforms are generally inserted 8 cm into the top of the furnace prior to heat treatment. This distance corresponds to the position of the hot zone of our furnace, which has an effective length of 2.5 cm. Amorphous preforms are conventionally drawn in a material-specific temperature region in which viscous forces are balanced with an applied mechanical stress. This stress originated from a load hanged to the bottom of the preform. When the mechanical stress (weight of mass) exceeds the viscous forces present (which decrease due to applied heat) the perforated portion of the preform stretches slightly and is cut off. The tapered section of the preform is wrapped around reels as described in Figure 2.2. Following the fixation of the tapered section, the capstan rotated in clockwise direction and a down-feed speed value is supplied. Here temperature, down-feed and capstan speed are engineered to obtain the structure sizes required without deforming the initial structure profile or breaking the fiber. Structure sizes are controlled by monitoring total fiber diameter using a laser micrometer. The tension on the fiber continuously measured in order to prevent fiber rupture.

Microstructures obtained after step I cut and prepared for the second step of fabrication (Figure 2.3). Composite fibers with outer diameters of several hundred microns are embedded in a polymer sheath (a hollow preform prepared in order to hold first step microfibers) in hexagonal arrays of several hundred microfibers and redrawn to produce indefinitely long nanowire arrays. The process can be repeated for subsequent steps if smaller sizes are required. Reduction factors between 25 to 500 can be obtained in each drawing step.

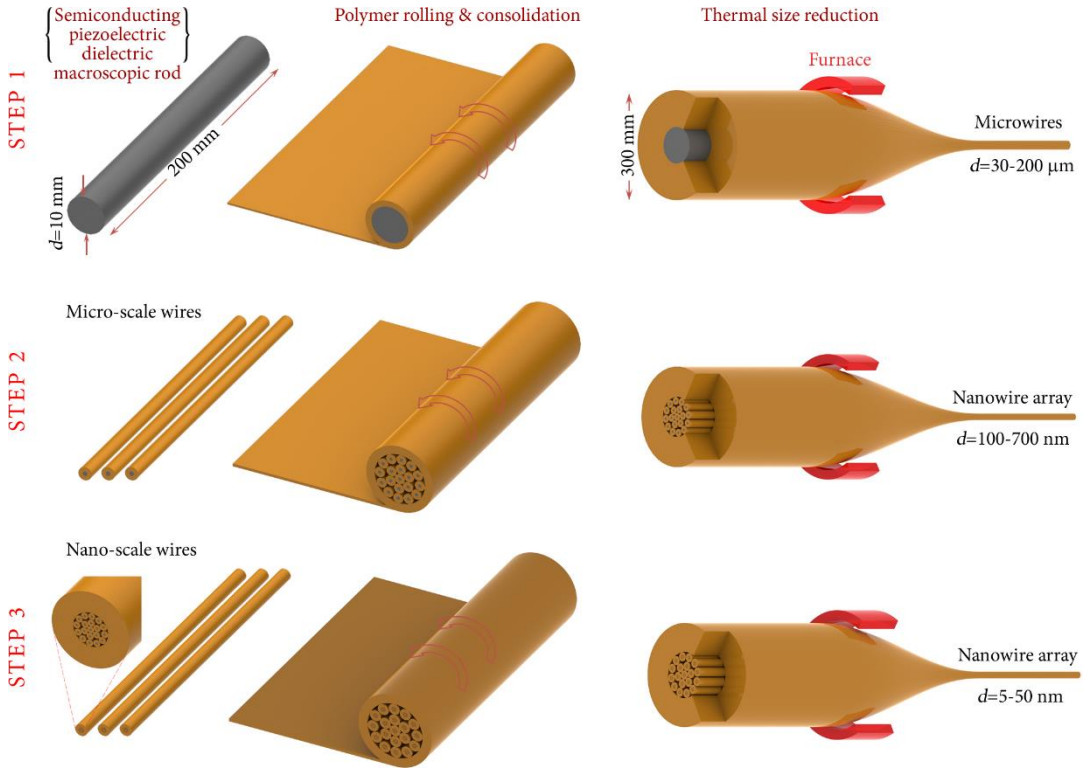

Figure 2.3: Low temperature, multimaterial fiber drawing method used for the iterative size reduction of a macroscopic layered rod down to nanoscale. Microstructures obtained after the first thermal drawing step are cut in cm-scale strips, arranged in hexagonal arrays of several hundred microwires and embedded in dielectric polymer sheath prior to a second drawing step. Same procedure repeated for third or higher steps if smaller sizes required. Kilometer-long, ordered nanowires which can be fabricated in a broad nanowire diameter range are obtained after the second or higher steps.

Very high reduction factors, however, render the handling and subsequent drawing process difficult, and very small reduction factors hinder efficient fabrication efforts.

Ordered and globally aligned in–fiber nanostructures can be obtained at the end of designed multi-step fabrication process. These fibers display ideal characteristics for their direct use in a diverse array of applications without using post-synthesis assembly techniques that drive up fabrication costs.

This step-by-step drawing technique allows the production of indefinitely long nanostructures with aspect ratios as high as 10^{12}. This fabrication method also allows the large-scale production of these nanostructures, which are well-suited for flexible surface applications due to their outer polymer layer. ISR-fabricated nanostructures are highly uniform and possess smooth surfaces due to the thermal origin of fabrication. In addition, this technique is very cheap and rapid compared to other nanofabrication techniques.

2.2 Chalcogenide Glasses and Polymeric Materials

Materials I use in the production of nanostructures are amorphous and suitable for described thermal drawing process due to their thermoplastic properties. Chalcogenide glasses have low softening points and continuous glass transition temperatures, which render it possible to co-draw these materials with high-temperature engineering polymeric materials.

Chalcogenide glasses can be synthesized from individual elemental components using high-temperature furnaces. I prefer to use arsenic selenide (As_2Se_3) glass, in the fabrication of glass-polymer core-shell nanowires. To this end, As_2Se_3 rods, 4 mm in diameter and 8 cm in length, are prepared by melting commercially bought glasses (Amorphous Materials) in a vacuum-sealed quartz tube followed by water quenching.

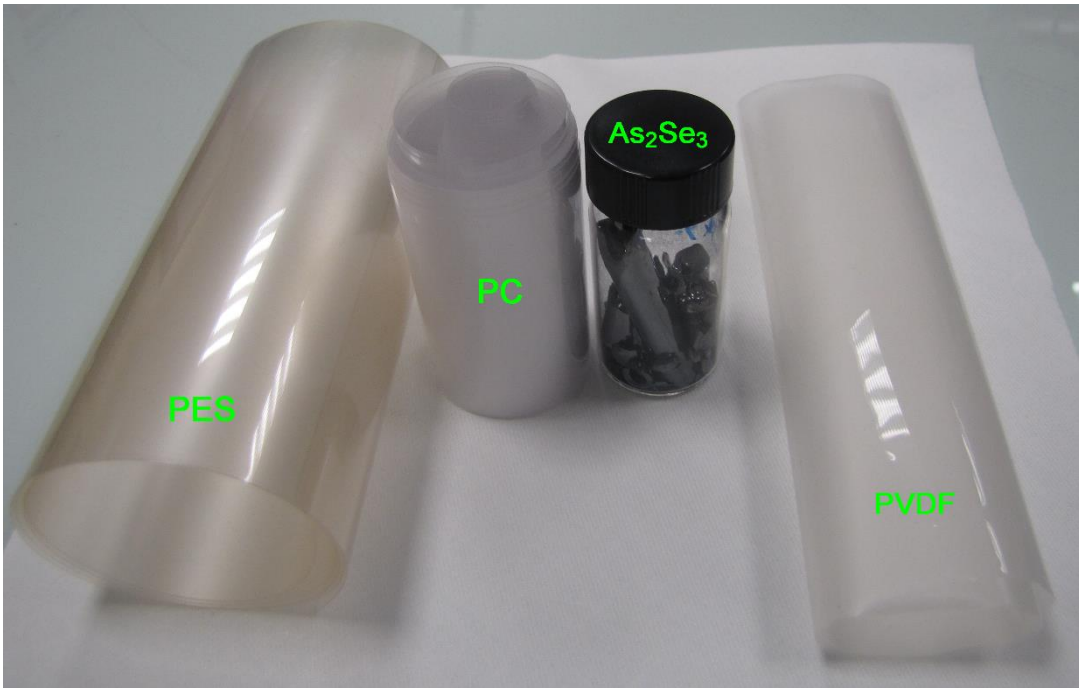

Figure 2.4: Bulk materials that are used in the fabrication of nanostructures. The black color of As_2Se_3 suggests a very high absorption capacity in visible wavelengths, while polymers generally do not absorb in the visible spectrum. PES and PVDF polymers bear a slight but nonetheless visually distinguishable absorption capacity, in contrast to the highly transparent PC material.

The weighted materials are then placed in a quartz tube under nitrogen atmosphere in a glove box (H_2O, O_2 below 0.1 ppm), which is kept at 420 °C for a 2 hour under vacuum to remove surface oxides, sealed in a glass ampoule (10^{-6} Torr), rocked for 18 h at 600 °C and quenched in iced water prior to use. As_2Se_3 rods display a bright black color (Figure 2.4).

Polymeric materials are commercially provided by Ajedium Inc. I frequently use polyvinylidene fluoride (PVDF), polycarbonate (PC) and polyethersulfone (PES) polymers in the fabrication of nanostructures. Commercially bought PVDF and PC polymer films used in our fabrication efforts have film thicknesses of 65 μm and 50 μm, respectively, while PES films are available in 25 μm and 100 μm thicknesses.

Due to lack of absorption in the visible region, all polymers are observed to be almost fully transparent. PES and PVDF polymers absorb slightly in the visible region, which accounts for their fawn colors and in contrast PC polymers are highly transparent and possess whitish colors (Figure 2.4). All polymer and glass rod components were cleaned with methanol and kept in vacuum oven at 140 °C at least one day before their use in fabrication in order to prevent swelling.

Glass transition temperature of arsenic selenide is measured to be around 190 °C by differential scanning calorimetry, while PC and PES have glass transition temperatures of 180 °C and 190 °C, respectively, and PVDF is observed to transition at 170 °C. These parameters are considered during the selection of material sets. Our focus is on the fabrication of core-shell structures, which necessitate the use of at least three thermally compatible materials. Arsenic selenide rods, which are used as core-materials, can only be embedded inside PES due to the latter's stability at higher temperatures. PVDF and PC can be used as shell materials due to their lower transition and melting temperatures; which are slightly lower than the than glass transition temperature of As_2Se_3 glass. In addition, PC/PVDF and PES/PVDF can be drawn together for nanostructure fabrication as long as PVDF is utilized in the inner sections. It should also be noted that PC and PES are easily etched by dichloromethane (DCM), which is utilized in the acquisition of free-standing micro- and nanostructures. In contrast, PVDF and As_2Se_3 rods are highly resistant to this solvent. As such, I preferred PVDF polymer as a shell layer in all fabrication designs.

The optical features of fabrication components should also be considered in order to facilitate the simulation of their optical features and to obtain an effective agreement between theoretical and experimental investigations.

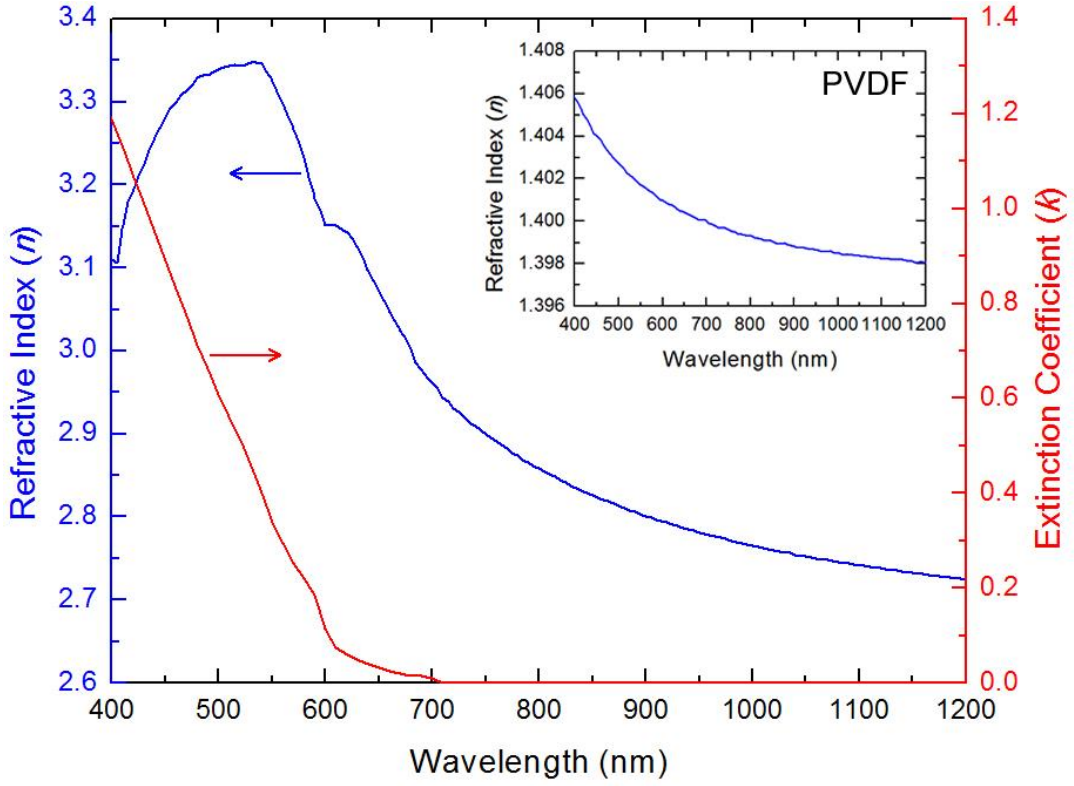

Figure 2.5: Optical properties of chalcogenide glass, As_2Se_3, and piezoelectric polymer PVDF. Optical constants of arsenic selenide (As_2Se_3) and PVDF polymer were measured by spectroscopic ellipsometry. As_2Se_3 is a high-refractive index material, which enables the confinement of light for Mie resonances in very small dimensions. Thin film interference is also facilitated by As_2Se_3, regarding the high index difference between the core and the shell. PVDF, on the other hand is a convenient material for core-shell nanostructure applications, because it has a low refractive index and virtually no absorption in visible wavelengths.

I choose As_2Se_3 as the filling (or core) material in the fabrication of glass-polymer core-shell nanostructures. Prior to experimentation, the optical constants of bulk arsenic selenide material were measured. A V-Vase ellipsometer is used in the determination of the (n,k) parameters of As_2Se_3, which is found to possess an average refractive index of 3.25 (3.40-3.00) and high absorption throughout the visible spectrum (Figure 2.5). Measured data is fitted to the Lorentz model.

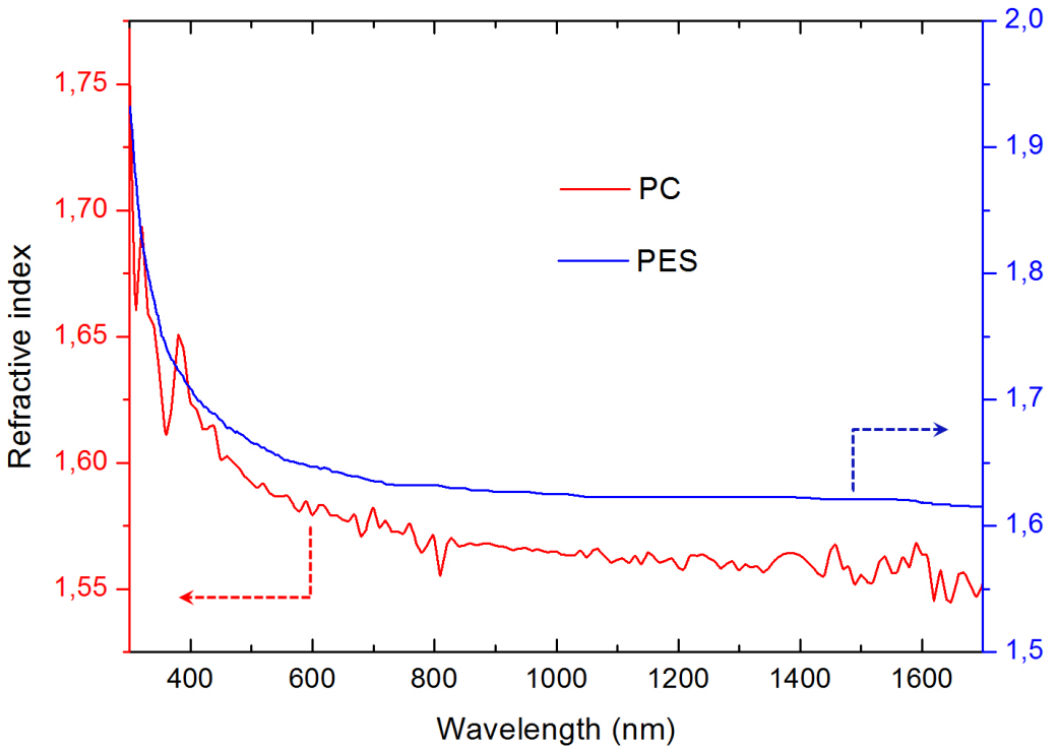

Figure 2.6: Optical properties of polymeric fabrication components, PES and PC, investigated by ellipsometry. PC, which is used as a core polymer in all-polymer core-shell nanowire fabrication, possesses an average refractive index of 1.58, while PES displays a higher average optical index of 1.65. Neither polymer displays significant absorption in the visible spectrum.

As_2Se_3 is an optically suitable material, especially in the observation of resonant Mie scattering based effects, due to its high refractive indices. It also possesses one of the known highest optical nonlinearity indices among nonlinear materials. This renders it highly advantageous for nonlinear photonics applications. Moreover, the high absorption capacity of As_2Se_3 in the visible spectrum can be utilized for applications where absorption enhancement is required.

I use PVDF polymer as a shell layer due to its resistivity into DCM. It also has exceptional optical features that I utilize during the implementation of theoretically predicted results. Its low refractive index and lack of absorption makes it especially

suitable for nanoshell interference observations. It also has useful surface properties that can be used for increasing hydrophobicity, especially in solar cell applications. Optical constants of the PVDF polymer is also determined by a V-VASE ellipsometer. Its refractive index does not change significantly, and has an average value around 1.41 (Figure 2.5).

In the fabrication of all-polymer structures (*i.e.* all-polymer nanowire, photonic crystal structure and monolayer nanowires) I utilize PC as a core layer due to its lower refractive index and high transparency (Figure 2.6). The outer polymer is chosen as PC, which serves as a sacrificial layer and can be easily removed if free standing nanostructures are required.

PES is used as a holding layer during the multistep fabrication of glass-polymer nanostructures, and is also used as a component of all-polymer core-shell nanowires. Free standing nanostructures can be obtained by etching this layer. Ellipsometric data demonstrate that this polymer bears an average refractive index of 1.65 and displays little to no absorption in the visible spectrum (Figure 2.6). Optical properties of in-fiber As_2Se_3 nanostructures are not significantly affected by PES sheath due to the high refractive index contrast between these two materials.

2.3 Fabrication of Glass-Polymer Core-Shell Nanowires

Glass-polymer core-shell nanowires are very useful nano-schemes in various nanophotonics applications [104,39]. However, the production of these nanostructures is generally problematic, and even successful fabrication efforts are limited by small batch sizes, constraints in material choice and non-uniformity issues.

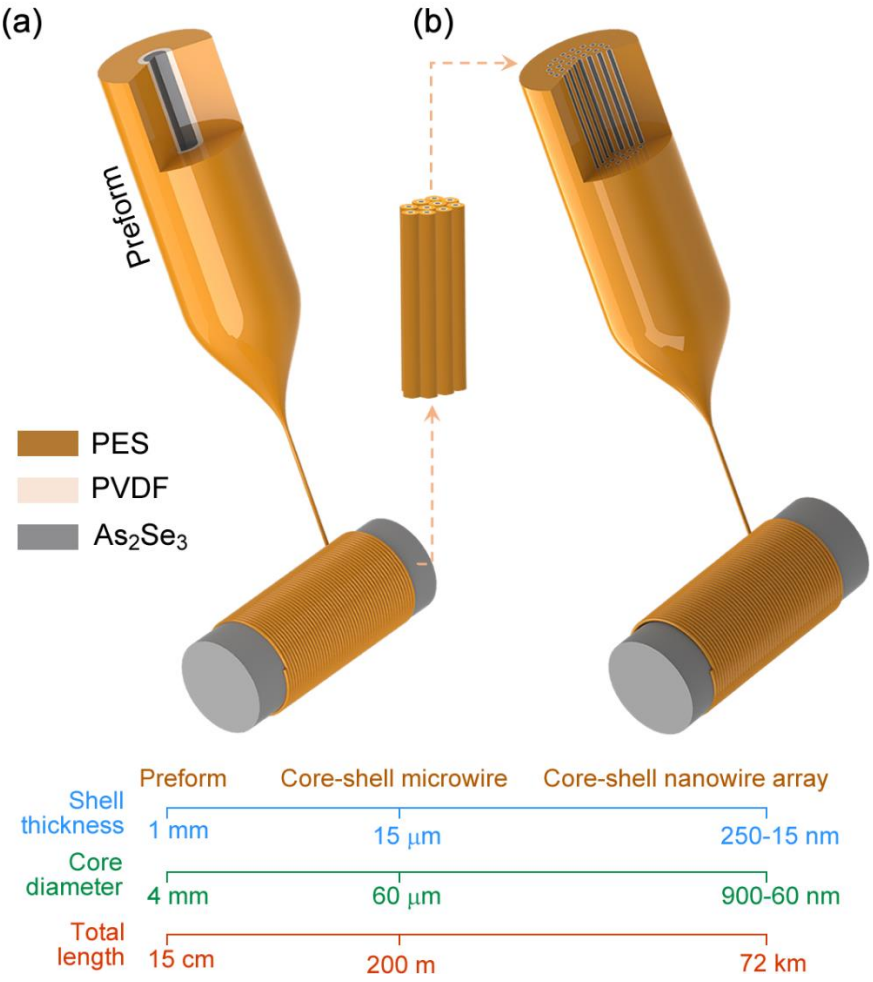

Figure 2.7: Fabrication of glass-polymer core-shell nanowires. Low temperature, multimaterial fiber drawing method is used for the iterative size reduction of a macroscopic layered rod down to core-shell nanowires. Microstructures obtained after the first thermal drawing step are cut in 10 cm strips, arranged in hexagonal arrays of 360 microwires and embedded in dielectric PES prior to a second drawing step. Kilometer-long, ordered As_2Se_3/PVDF core-shell nanowires are obtained after the second step and can be fabricated in a broad nanowire diameter range (50 nm-1000nm).

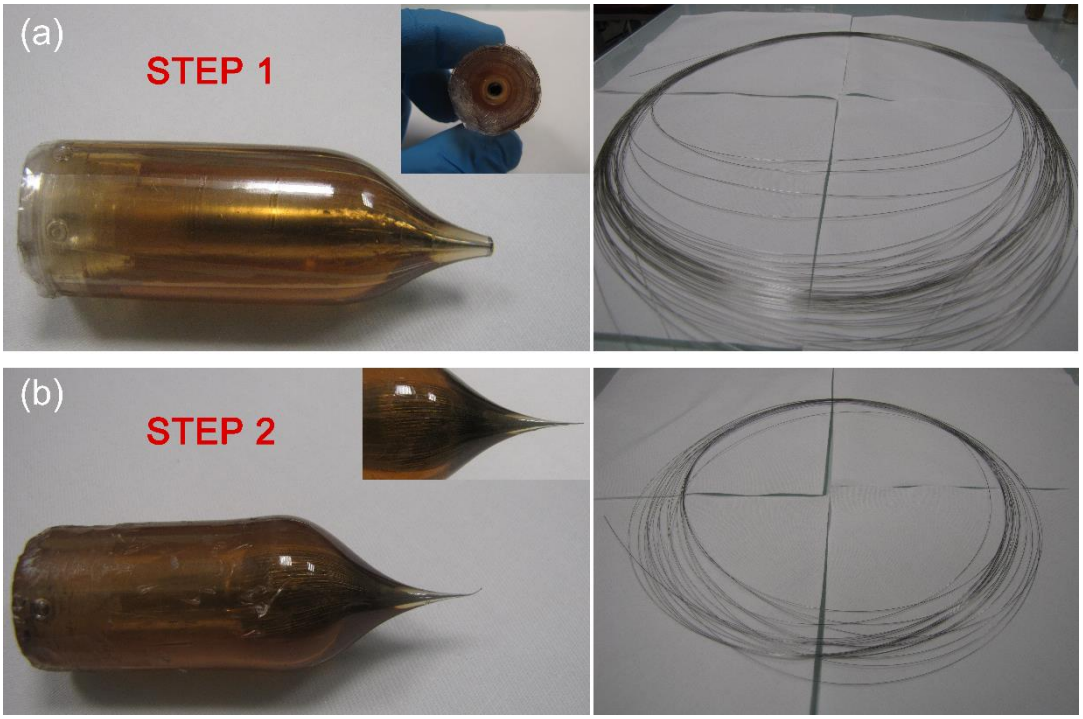

Figure 2.8: Preforms that were used in the fabrication of glass-polymer core-shell nanowires. (a) Step I and (b) step II preforms contain single and 360 fibers respectively. Fabrication of arbitrarily long micro- and nanostructures were accomplished after two iterative steps.

I use ISR for the successful production indefinitely-long, uniform core-shell nanowire arrays in a broad diameter range, which can be altered by effecting minor changes on the reduction factor during fabrication. In order to obtain glass-polymer core-shell nanowires, macroscopic preforms are prepared from a macroscopic As_2Se_3 glass rod with diameter of 4 mm and length of 15 cm, wrapped in a PVDF polymer sheet of 1 mm thickness, and consolidated in a PES jacket, with total preform diameter of 25 mm.

For consolidation, the macroscopic preform is initially kept in a T= 140 °C for t= 2 h, and the temperature is subsequently increased at a rate of 2 °C/min to 250 °C. Preforms are then retained at this maximum temperature for t= 20 min.

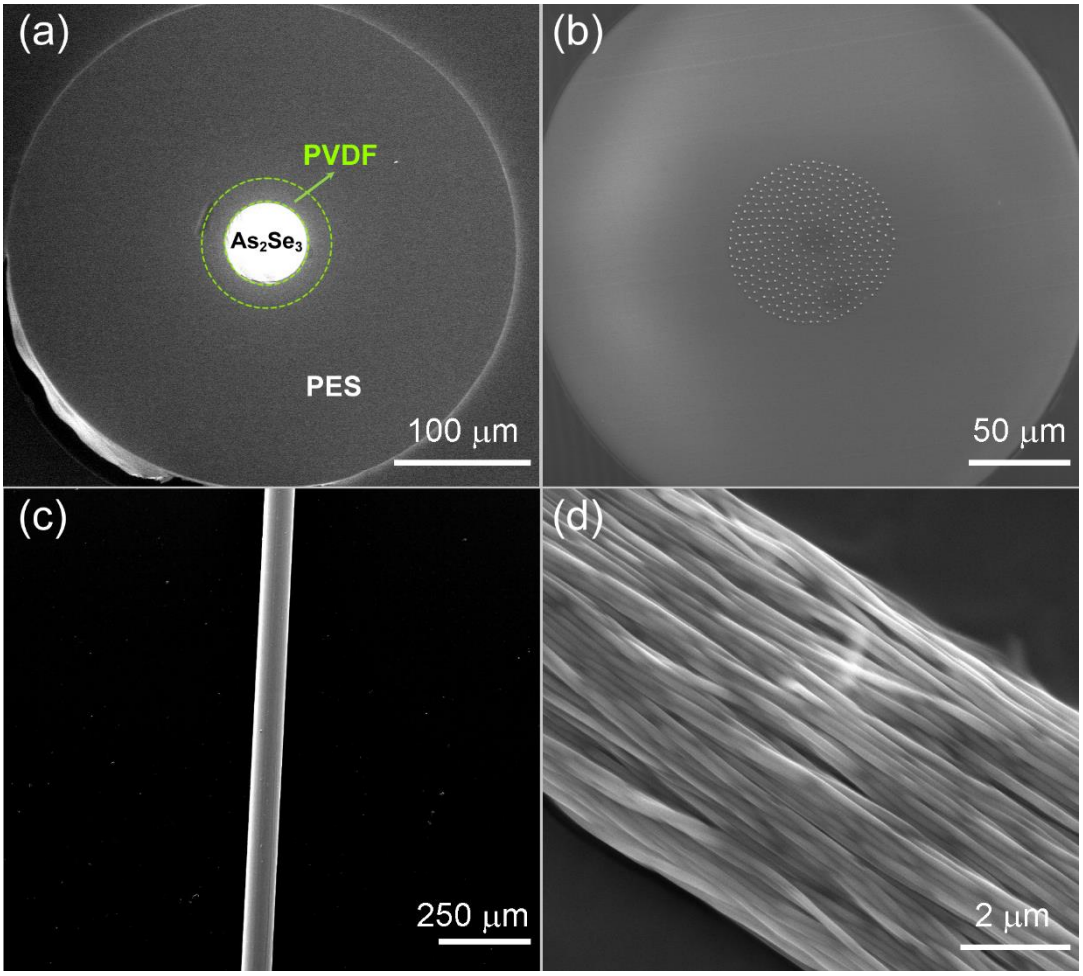

Figure 2.9: SEM images of step I and step II fibers. Cross-sectional images of (a) step I and (b) step II fibers are obtained by a low temperature, multimaterial fiber drawing method. Free-standing nanostructures obtained by etching the PES sheath by DCM prior to SEM imaging. Longitudinal images of (c) step I and (d) step II micro- and nanostructures are also provided.

Thermal drawing of the resulting preform is carried out by controlling tension, temperature, feed-in, and drawing speed in a custom-built fiber tower optimized for nanowire production. Temperatures fluctuate between 270 °C and 290 °C, but are mainly kept stable at 270 °C, during the drawing process. After the first drawing step, 60 μm As_2Se_3 microwires with a 15 μm PVDF shell embedded in a PES fiber of 400 μm total thickness are obtained (Figure 2.7a).

Following the first step of synthesis, 360 pieces of 15 cm long step I fibers are cut, embedded in a PES jacket, and consolidated in a second drawing step. After the second thermal drawing (Figure 2.7b), core shell nanowires in the diameter range of 50 nm - 1000 nm are obtained. Precise diameters can be set by altering the reduction factor. By repeating this procedure for a third time, the production of core-shell nanowires with diameters up to 14 nm are achieved.

Arbitrarily long and any desired sizes of micro- and nanostructures can be following two iterative drawing steps. This capacity is demonstrated by producing 100 m of microwires with an outer diameter of 400 μm via step I production (Figure 2.8a), and representative 20 m PES-embedded core-shell nanowires with a core diameter of ~700 nm using two thermal drawing steps (Figure 2.8b).

Characterizations of nanostructures are performed by Scanning Electron (SEM) and Tunneling Electron Microscopies (TEM)**.** DCM (Carlo Erba) is utilized to etch the PES sheath covering the core-shell nanostructure arrays and expose the structures for imaging. Briefly, PES-embedded nanostructure arrays are placed on a glass substrate, and the PES layer is etched by DCM drop-cast directly onto the surface. The exposed nanostructures are rinsed gently with DCM to remove residual polymer. PVDF shells of core-shell nanostructures are highly resistant to DCM etching, and are not damaged during the nanostructure extraction process. SEM imaging reveals

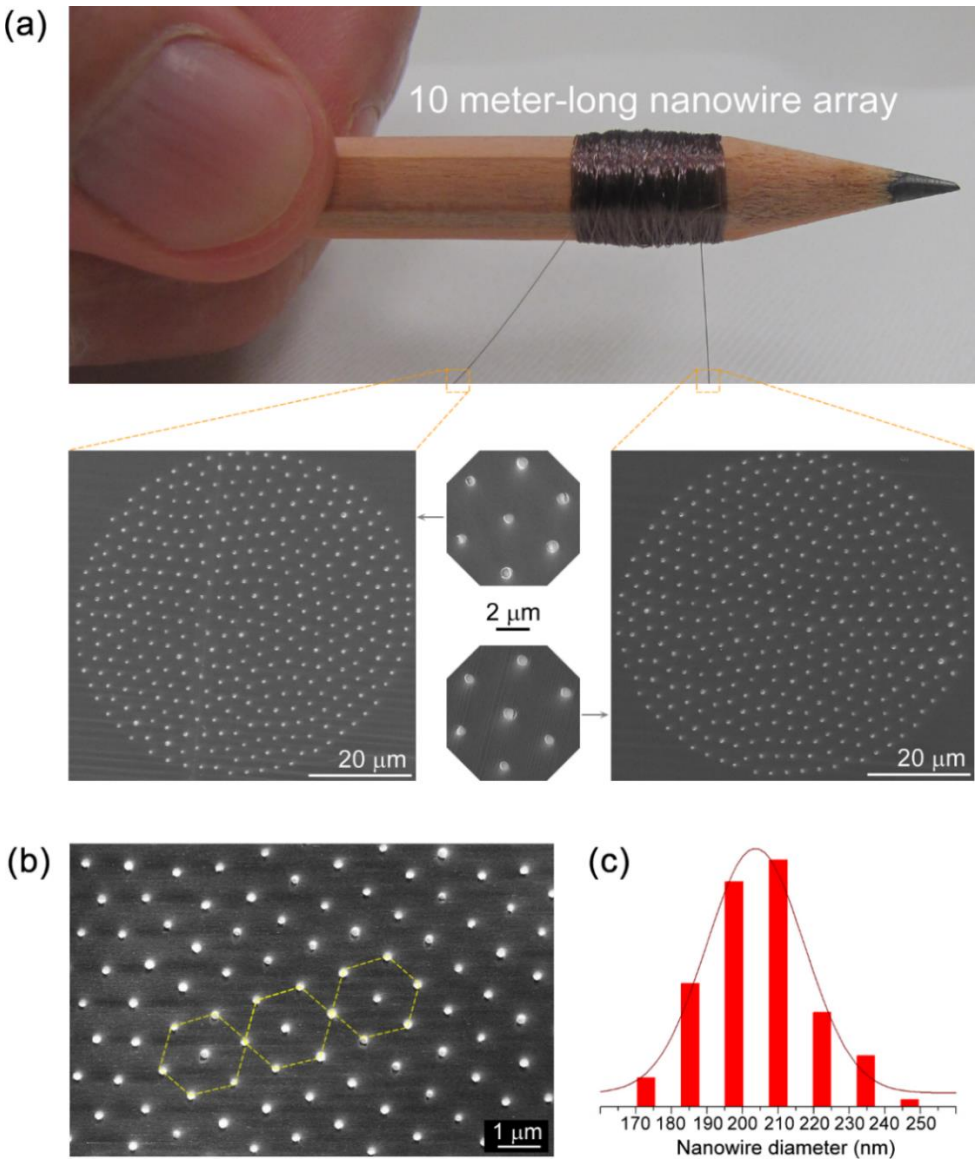

Figure 2.10: (a) A polymer-embedded nanowire array rolled around a pencil truly spans the macroscopic and nanoscale worlds. Cross-sectional SEM micrographs from both sides of a 10-m-long polymer fiber containing hundreds of As_2Se_3–PVDF core–shell nanowires prove that nanowire arrays are axially uniform to less than 1% for macroscopic distances. (b) High-precision hexagonal packing of core–shell nanowires in the polymer matrix. (c) Radial size distribution of the nanowires, shown as a histogram, is uniform with a standard deviation of 6.5%.

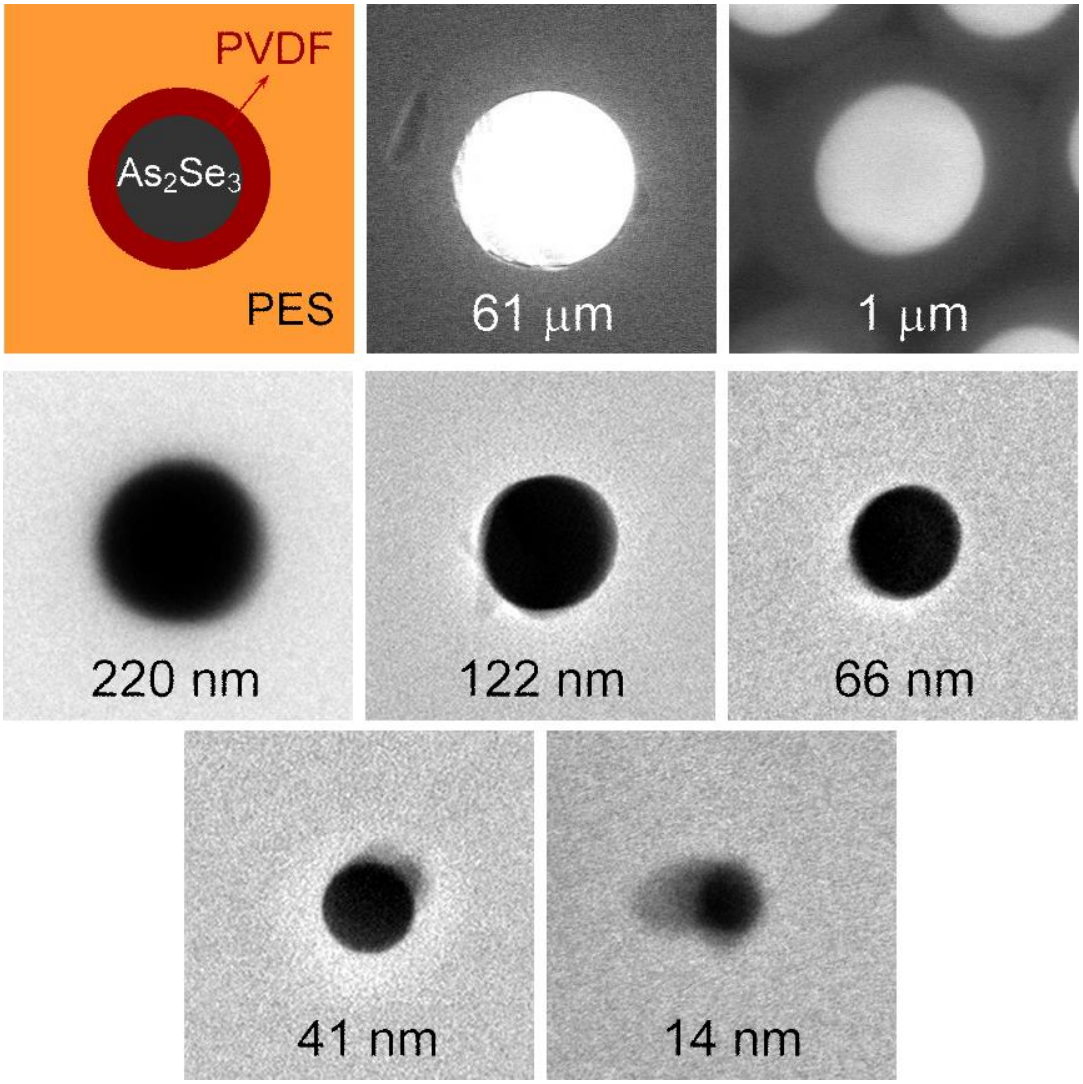

Figure 2.11: Kilometer-long nanowires can be produced with any diameter within the 100 μm-10 nm range while preserving ordered geometry. As_2Se_3–PVDF core–shell nanowires scale regularly from 200 μm to 14 nm.

that fiber uniformity is preserved in both step I and step II structures (Figure 2.9c,d). Particularly in step II (Figure 2.9b) the fabricated core-shell nanostructures also possess long-range hexagonal alignment and high cross-sectional uniformity, which further increases their utility in optical applications. Core-shell ratios of nanostructures remain approximately identical at the end of each drawing step (Figure 2.9a).

Large-area arrays can be obtained for nanowires, and uniform production of an each size can be accomplished by the optimization of process parameters. PES-embedded nanowires do not compromise the structural integrity of the nanofiber, and indefinitely long arrays can be produced (Figure 2.10a).

Cross-sectional SEM images of arbitrarily long in-fiber nanowires demonstrate that fabricated nanostructures display in-phase alignment in globally parallel hexagonal nanostructure arrays and preserve their uniformity both axially and radially (Figure 2.10a,b). Radial size distribution of the nanowires, shown as a histogram (Figure 2.10c), is uniform with a standard deviation of 6.5%, and axial uniformity is less than 1% for macroscopic distances.

Described fabrication technique is also scalable across different core-shell structure sizes. A broad range of sizes can be fabricated from macroscale structures while preserving core-shell ratio and integrity throughout the fiber. In Figure 2.11, it is demonstrated that structure diameters can be range from 200 μm to 14 nm using three subsequent fabrication steps. Step I, step II and step III fibers are cut with an ultramicrotome prior to imaging. Samples are embedded inside resin to increase cutting accuracy. Images of higher structure diameters are obtained via SEM, while TEM is used in order to obtain cross-sectional images of nanowires with diameters as small as 14 nm.

2.4 Fabrication of All-Polymer Core-Shell Nanowires

In photonics, polymer nanowires are considered exceptional due to their low refractive indices and wide range of material choices. However, while methods used for the fabrication of polymer nanostructures, including ion etching [40], laser irradiation [41], template wetting process [42], electrospinning [43], solution chemistry [44] and nanolithography [45] may be powerful and versatile, a wide range of issues are nonetheless associated with current production efforts. For device applications one-dimensional polymer nanostructures are required to be sufficiently long, uniform and well-ordered, which is difficult to achieve by conventional fabrication techniques. In this section, I describe the production of all-polymer core-shell nanowires by the use of thermal drawing technique. One-dimensional polymer nanostructures are obtained with well-controlled and consistent sizes, morphologies and extremely high (up to 10^{12}) aspect ratios by using this top-down nanofabrication approach.

Polymer preforms are prepared by wrapping a 4 mm Teflon-coated glass tube with 6 mm thickness of PC film, with the latter acting as the core region. Teflon makes the physical extraction of the glass tube possible even after the consolidation process. PVDF, which serves as shell layer, is then wrapped around the PC layer to a thickness of 4 mm. PC was again utilized as a sheath, and wrapped around the core-shell structure to an overall diameter of 36 mm. The complete preform, which measured 20 cm in length, was kept in a consolidator for the fusion of wrapped layers under a vacuum of 10^{-3} Torr. For consolidation, macroscopic preform is kept at T= 140 °C for t= 2 h, temperatures were subsequently increased at a rate of 2 °C/min to 186 °C, and the preform was held at this temperature for t= 40 min. The consolidated preform is thermally drawn in our fiber tower system at T=260 °C (Figure 2.12a). Microstructures with 160 μm core diameters and extended lengths are obtained after first step fabrication (Figure 2.13a).

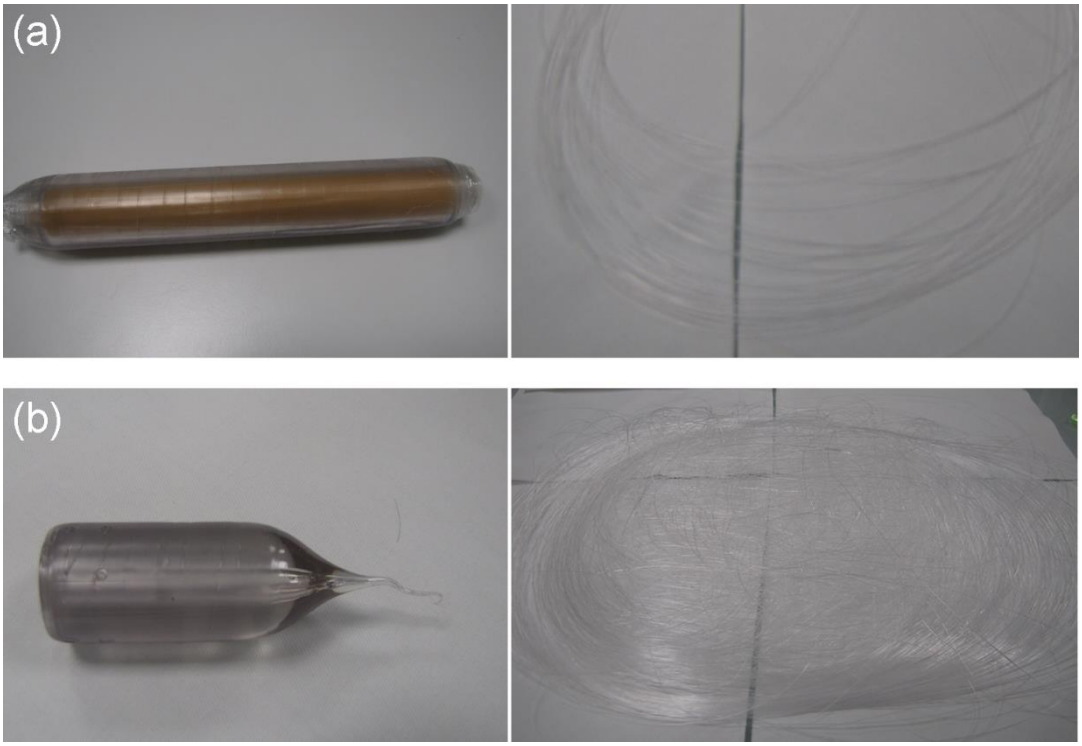

Figure 2.12: Macroscopic preforms of (a) step I and (b) step II used in the fabrication of all-polymer core-shell nanowires. At the end of second fabrication step, I achieve the production of kilometer long fibers composed of ~500 all-polymer nanowires arranged in a nanostructure array.

Around 500 of these microfibers are cut in 20 cm length, placed in hollow PC preform (Figure 2.12b) and subjected to a second drawing step to produce core-shell nanowires with core diameters up to 200 nm (Figure 2.13b). The overall reduction factor at the end of the two drawing steps is 10^5. SEM images of the outputs of the first and second fabrication steps are shown in demonstrated in Figure 2.13c-f, with both cross-sectional and longitudinal views. Core-shell ratios of polymer nanowires do not significantly change by following thermal drawing.

Fabricated 1D polymer nanowires are self-aligned, uniform and suitable for in-fiber applications.

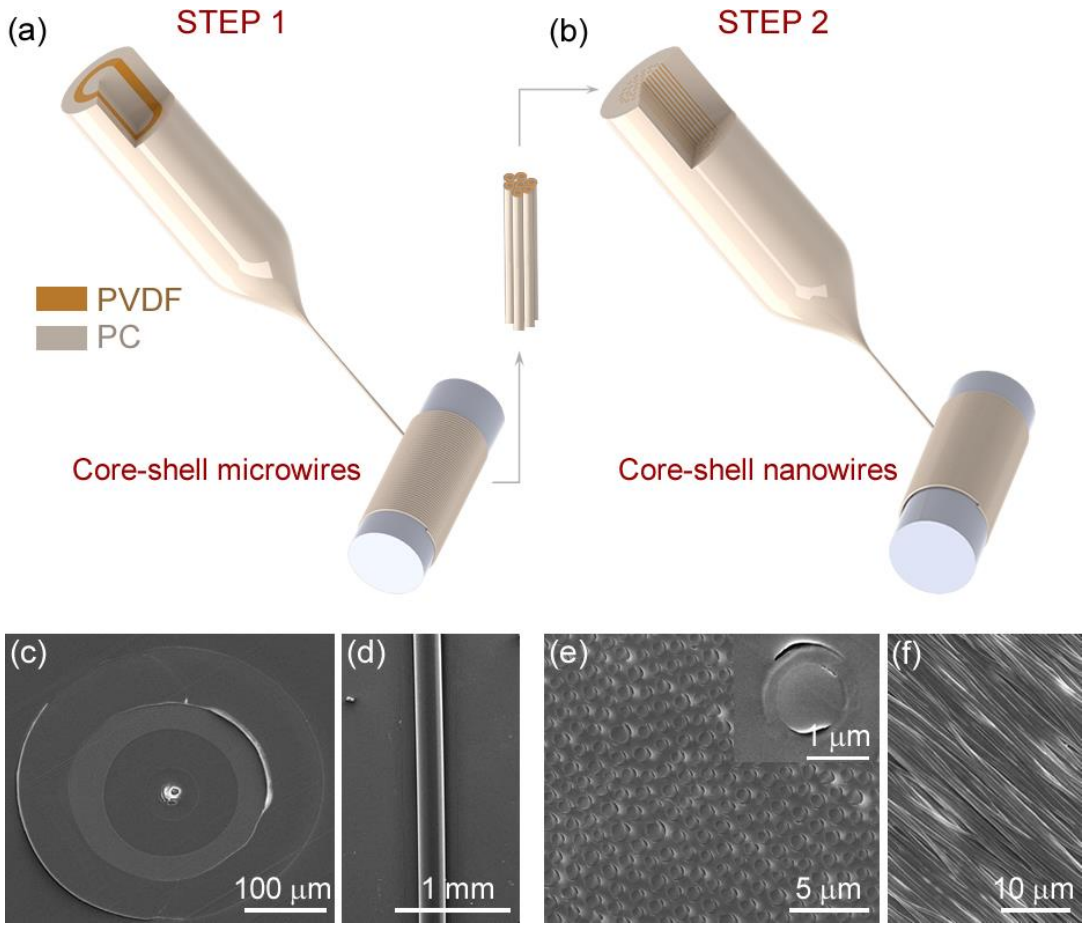

Figure 2.13: Iterative size reduction method used to fabricate all polymer core-shell nanostructures. (a) At the end of first step, core-shell structures with the ~200 μm overall diameters are obtained. (b) A second drawing step is performed using step I microwires to produce core-shell nanostructures displaying a broad size range of 200-2000 nm. Cross-secitonal and longitudinal SEM images of (c,d) step I and (e,f) step II fibers display that ISR can be utilized for the production of well-ordered nanowire arrays in macroscale lengths.

They can also be utilized for flexible surface applications due to their size scale and polymer composition. One-dimensional nanostructures with metal, semiconductor or even some polymer compositions have raised environmental and health concerns due to their toxicities. All-polymer, PVDF/PC, core-shell nanowires, however, bypass these issues, as their material components are environmentally friendly and FDA-approved for use in humans. As such, these nanostructures are highly promising for use in biological applications.

High-density of nanowire arrays [46] can also be accessible by the use of a post-processing step involving the etching of the PC sheaths of step II and III fibers to facilitate the assembly of core-shell polymer nanowires into ultra-high density arrays.

2.5 Fabrication of All-Polymer Photonic Crystal Structure

Photonic crystals are periodic structures commonly used in the manipulation the light interactions, as they are responsible for the creation of bands and band-gaps similar to electron-induced band diagrams observed in semiconductors. Intentional defects can also be included in photonic crystal designs in order to trap or guide photons. While photonic crystals can be designed in 1D, 2D and 3D arrangements, here I concentrate on the production of 2D photonic crystals.

It is demonstrated that described fabrication scheme can be utilized for the production of photonic crystals by initating an unusual 2D photonic crystal structure observed in the head feathers of *Anas platyrhynchos* drakes. This structure consists of high refractive index rod embedded in a shell structure with a lower refractive index. This arrangement is different from commonly used 2D photonic crystal designs, which utilize either an array of rods interspersed with air-filled gaps, or a series of holes in a material matrix.

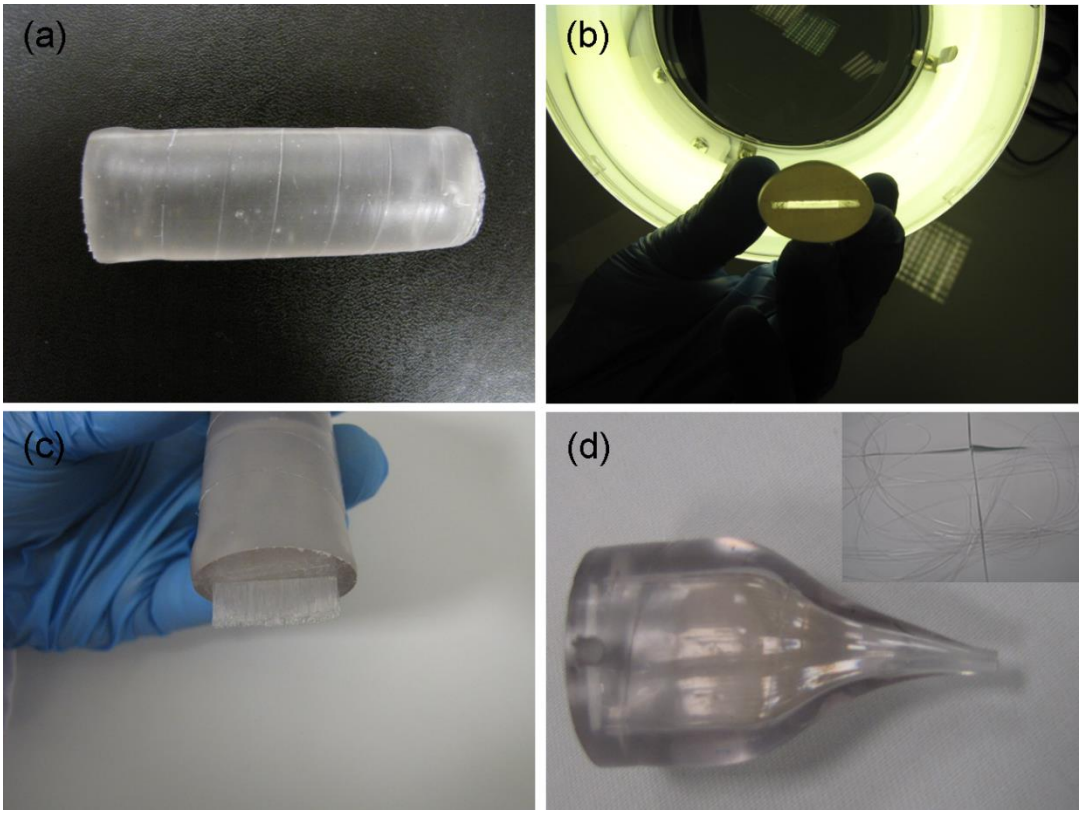

Figure 2.14: Preform preparation of step I fiber is similar to step I of all-polymer core-shell nanowires. However, step II design exhibit significant differences such as, rectangular cross-section design and extraction of outer sheath of step I fibers prior to insertion into step II preform. Around 8 row and 80 column of step I fiber can be inserted into rectangular hole.

The first step of photonic crystal fabrication is identical to the first step of all-polymer core-shell nanowire fabrication. An alternative way of step I fabrication for all-polymer core-shell structures is rely on using polymer rod instead of rolling polymer film on glass tube. To this end, pre-obtained hollow bare PC preform with 30 mm diameter is used in order to fabricate PC rod. Hollow structure is cut into four equal piece and quarter is used for the rod fabrication. PC piece tailored into

cylindrical rod with the diameter of 10 mm using turning machine. Later this polymer rod is used in preform preparation as a filling or core zone.

PVDF polymer is directly rolled on this rod till the diameter of 12 mm reached. As an outer layer PC with 4 mm thickness is used. It is kept in consolidator in 10 min at T= 185 for further fusing of added layers. First step fabrication performed in T=224 °C in fiber tower system. Fibers with 400 μm outside diameter is obtained as a result of fabrication. Unlike previous fabrications here I strip outer PC layer easily by taking advantage of non-adhesive layer of PVDF and outer PC film (Figure 2.15a, b). This is important because it is aimed to obtain PVDF embedded PC rods and render them as a photonic crystals. To this end, around 500 of them with 4 cm length cut and inserted into unusual designed preform.

This preform possesses rectangular cross-section which is harnessed to mimic configuration exists in the mallard feather. This provides maximization of aspect ratio which is critical in coloration of livings. Preform with rectangular hole is prepared by rolling PC films around bare glass substrate with the dimensions of 20 mm-1.5 mm-7 cm. Outer diameters after the rolling is 35 mm in width and 15 mm in thickness.

Resulting structure later kept in furnace for consolidation process. Here heating time is extended in order to obtain preform that is inner size takes the shape of quartz glass substrate. Hence after removal of this glass by using % 48 HF perfect rectangular hole is obtained. Cross-sectional and longitudinal images of macroscopic preform used in step II fabrication is demonstrated in Figure 2.14a and 2.14b respectively.

Photograph images of preforms are also taken prior to (Figure 2.14c) and after (Figure 2.14d) the second step drawing of 500 step I nanowires arranged inside a PC sheath. Final preform is used in second step thermal drawing for the temperature of 230 °C and other proper settings (i.e. capstan and down-feed speed) in the home-made fiber tower system.

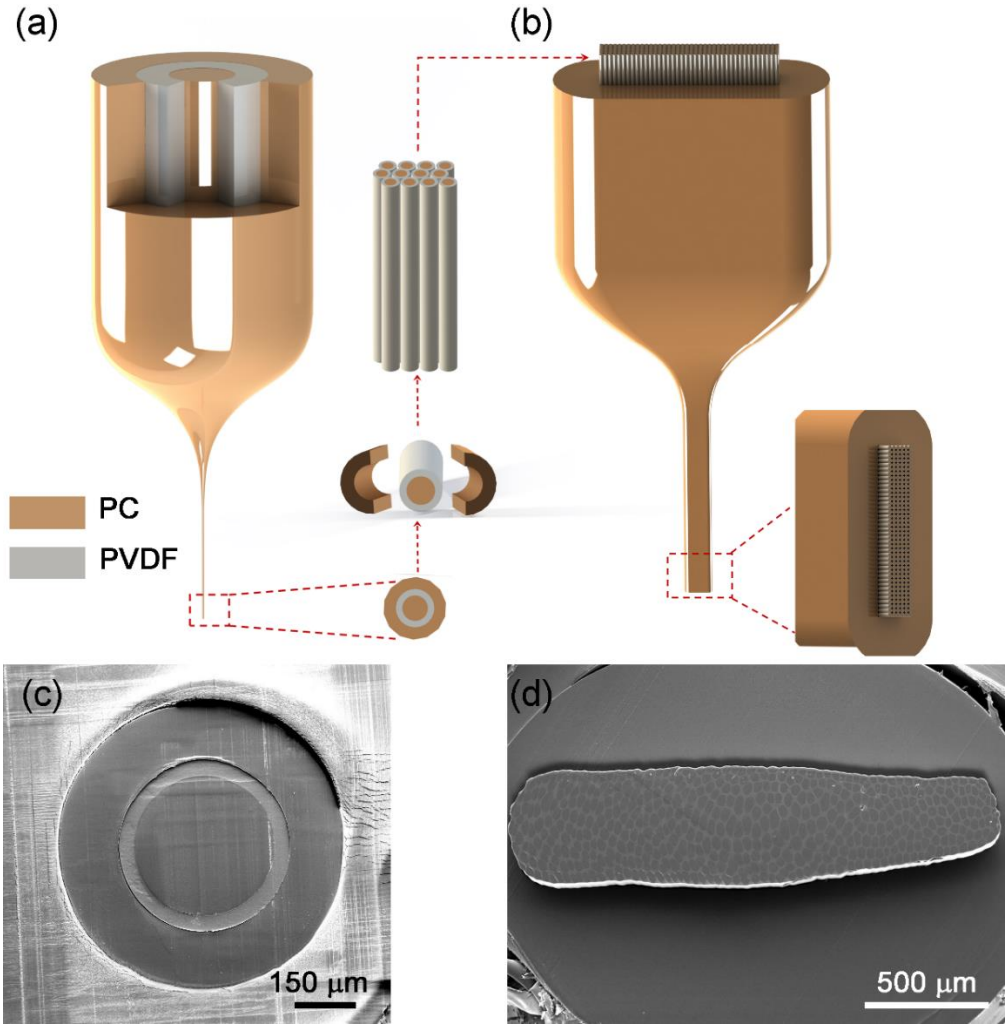

Figure 2.15: Schematics for fabrication of all-polymer photonic crystal structure. First step can be obtained either by rolling polymer films around quartz tube or starting from rod. Second step fabrication slightly different from previous ones. Here rectangular cross-section used in order to increase aspect ratio. Prior to second step fabrication outer layer of step I fibers removed. At the end of step II PVDF embedded PC microwires are fabricated which possess lattice constant of several microns. Using step III by repeating step I and step II procedures lattice constant reduced down to 100-300 nm as required.

Fabrication is designed to result fibers with outer size of 1.5 mm to facilitate further size reduction of structure in subsequent step. Third step preform is similar to scheme used in step II but contains single step II structure. By performing step III fabrication nanoscale lattice constants are reached.

Cross-sectional SEM images of step I and step II fibers reveals potential of used size reduction technique. Step I fiber (Figure 2.15c) possesses superior cross-sectional regularity which also preserves it throughout the fiber. In step II fibers (Figure 2.15d) array of nanowires which preserves initial structure profile can be observed from their cross-sections. Cross-sectional SEM images of step III fibers is demonstrated in Chapter 8.

2.6 Fabrication of Monolayer Nanowires

Single layer free-standing nanostructures bear a significant practical importance in optical applications. Much effort has been expanded in order to obtain monolayer nanostructures from pre-obtained random structures by using post-synthesis assembly techniques [20] such as magnetic and electric induced methods. However, all such methods are expensive and their implementation is difficult for large-scale and high-throughput applications. There exist self-assembly methods which can be used for this purpose even they are suffer from uncontrolled fabrication and alignment issues.

In this section, two different approaches are proposed in order to fabricate highly parallel nanowires. It is demonstrated that it is possible to fabricate highly uniform almost monolayer parallel arrays of core-shell nano-platforms either using shell embedded nanowire scheme fabrication (Figure 2.17a,b) or simply etching step II nanowires in order to obtain self-aligned nanowire arrays.

2.6.1 First Approach

Fabrication methodology of monolayer nanowires is similar to photonic crystal structure fabrication approach. First step is obtained by repeating procedures described in step I fabrication of all-polymer photonic crystal fabrication. It is also demonstrated that it is possible to fabricate single layer structures starting from rolling process instead of using PC rod. In fabrication of step II fibers, the monolayer 100 microfibers with 240 μm outer diameter are inserted inside of prepared preform with narrow rectangular entrance that prevent overlapping of inserted structures (Figure 2.16c). Preparation of preform is same with step II of photonic crystal fabrication. Only difference is dimensions of glass substrate used in order to form inner profile. Here glass substrate which possesses dimensions of 24 mm-0.8 mm-7 cm is used. Then glass substrate is removed by using % 48 HF as required. Prior to insertion of prepared step I microstructures I removed outer PC by repeating procedures described in photonic crystal fabrication. Macroscopic preform used in second step fabrication is demonstrated in Figure 2.16a,b. It possesses very high aspect ratio of 30:1 which is designed in order to maximize surface area of final nanostructure array. Size of step II fibers are reduced 20-fold (Figure 2.16d). Highly-ordered fiber embedded monolayer microstructures obtained as a result of this fabrication step. Fiber drawing temperature is adequately high to melt PVDF shell. Therefore at the end of second fabrication step shell layer soften and create an embedding matrix for PC wires. Thickness of PVDF layer on PC wires is very small and does not prevent applicability of fabricated structures in optical applications. Surface of PVDF shell also possesses to nanoroughnesses (Figure 2.17 c,d).

Step III is performed in order to reduce sizes further and reach desired diameter range of 500-700 nm nanowires embedded in a PVDF nanoshell. These structures are aimed to use in absorption enhancement applications.

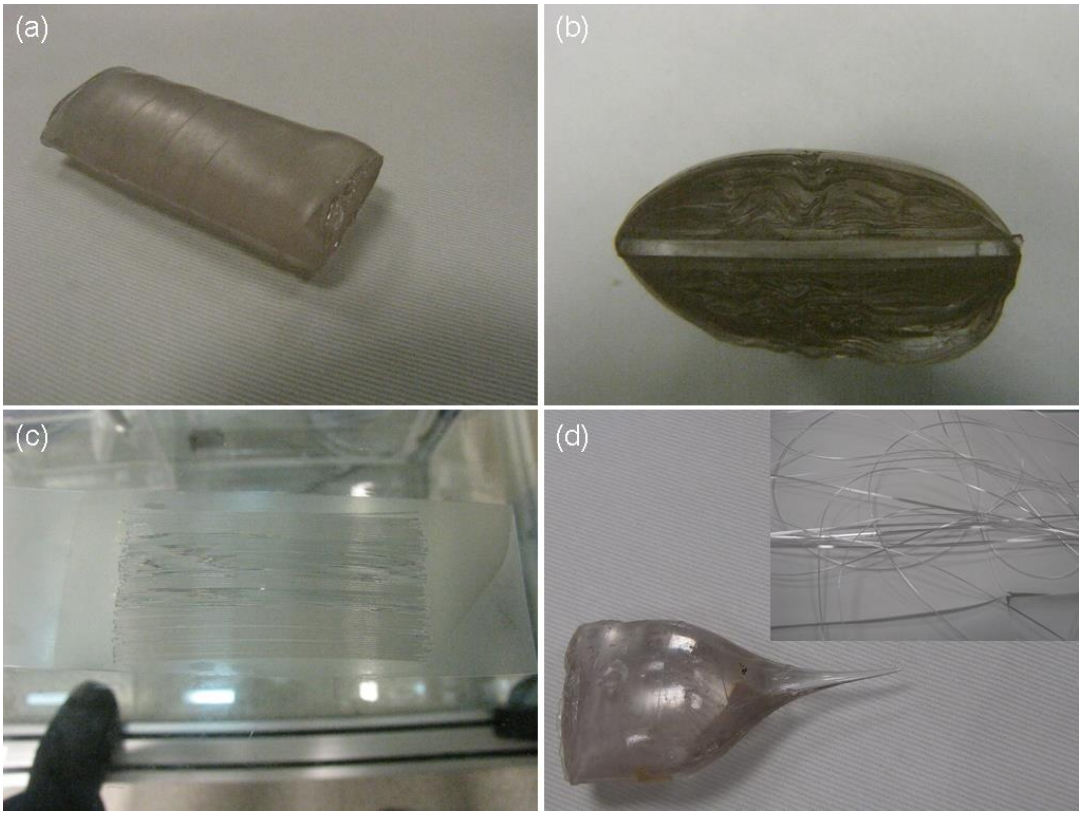

Figure 2.16: Cross-section of step II preform of monolayer structures has very high aspect ratio (30:1) which is utilized in order to maximize number of adjacent nanowires and permit for only single layer of structures to insert.

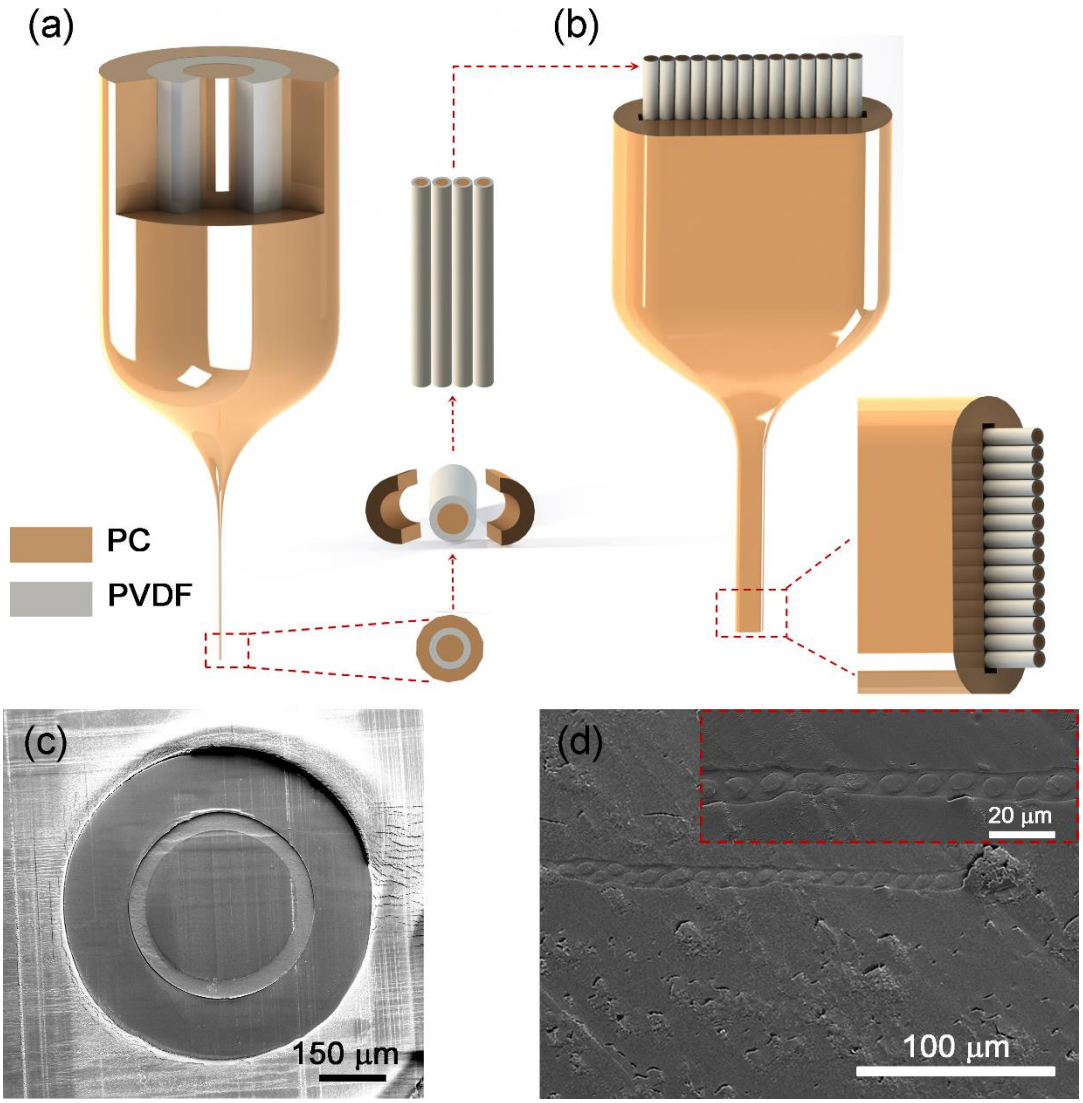

Figure 2.17: Schematics for fabrication of all-polymer monolayer structures. First step can be obtained either by rolling polymer films around quartz tube or starting from rod. Second step fabrication relies on insertion of uniform 100 microfibers with 240 micron outer diameter into preform with rectangular cross-section. Prior to second step fabrication holding polymer of step I fibers removed to permit fabrication of PVDF embedded PC microwires. By using step III, diameters of embedded structures are reduced up to 500 nm.

2.6.2 Second Approach

Conventional step II or higher step fibers can also be used (hexagonal array of nanowires inside cylindrical fiber) in order to obtain almost single layer structures. Cross-sectional images of step II fibers reveals that nanowires are hexagonally located inside the fiber (Figure 2.9b). As I etched outer polymer of fiber, nanowire array self-aligned into assembly of highly parallel and almost single layer structures.

Separation between nanostructures significantly prevents overlapping cases. Non-adhesive feature of PVDF polymer is another advantageous factor in formation of single layer structures. I particularly used glass-polymer core-shell nanowires for this purpose. Step II fibers are fixed from two edge prior to etching. Then by dropping DCM outside polymer was precisely removed. This DCM-etched nanowires readily assemble into monolayers on glass surfaces (Figure 2.18), suggesting that without the post-processing step monolayer nanowires can be obtained.

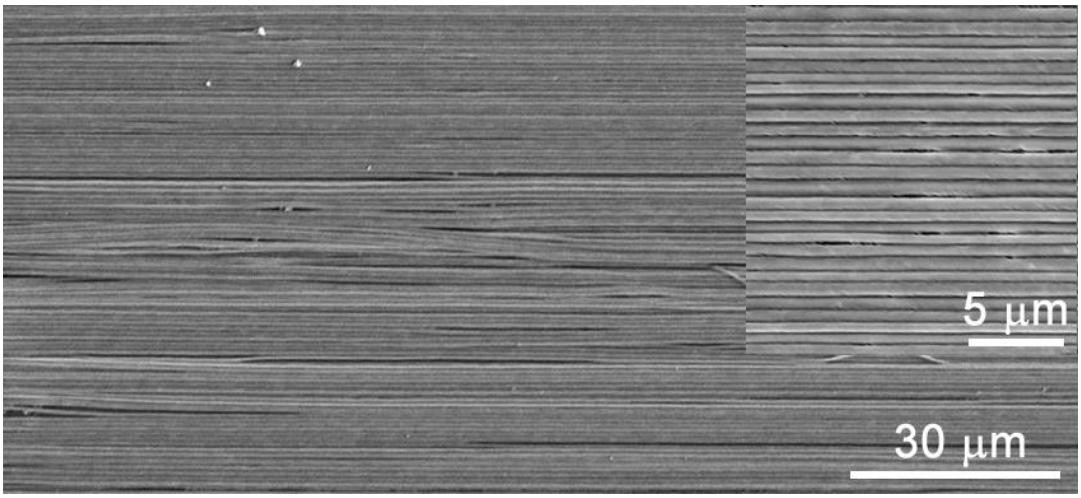

Figure 2.18: Step II fibers contain globally aligned 360 nanowires inside it. Highly ordered single-layer core-shell nanowire array is obtained after removing outer PES polymer of fiber.

By using this feature we can cover large-area surfaces just by etching out holding polymer. Particularly in Figure 2.18 it was demonstrated several hundred micron lengths nanowires cover the glass substrate surface without the overlapping errors. Overlapping cases can be overcome by applying stress from two non-etched edges of step II fibers. This works especially in all-polymer core-shell nanowires due to higher elasticity of polymer materials.

Chapter 3

Production of Complex Nanostructures

3.1 Thermal Instability Technique

The dynamics of spherical structure formation in heat-treated polymer-glass core-shell structures have previously been investigated in detail and demonstrated to be mediated by Plateau-Rayleigh instabilities[47], which depend strongly on the surface tension and viscoelastic properties of the core and shell regions. However, while the mechanisms underlying nanosphere production from polymer-glass nanowires have been investigated in detail, no evidence was so far provided on whether the effect in question could extend to other core-shell materials, and the production of more complex nanostructures have yet to be demonstrated by this process. Here I describe a combined iterative size reduction-thermal manipulation method by which a large diversity of indefinitely long, globally parallel, complex nanostructure arrays with high surface uniformity and low optical variation can be fabricated from PES-embedded core-shell As_2Se_3-PVDF nanowires, and provide evidence that Plateau-Rayleigh instabilities are responsible for the successive transition between different

nanostructure configurations. Nanosprings, nanoshell-embedded discrete nanorods and nanospheres, and nanochains are produced in succession by a hitherto-undescribed, Plateau-Rayleigh instability-mediated deformation, eventually culminating in the fragmentation of the nanostructure array and the formation of core-shell nanospheres. Structure sizes, profiles, instability wavelengths and optical properties can be modified by minor alterations in process temperature and duration. Optical applications of core-shell nanostructures are also demonstrated by theoretical calculations and Mie scattering experiments on large area nanoarrays designed for structural coloration (Chapter 5). Precise, low-cost, high-throughput thermal engineering of in-fiber hierarchical nanoparticle structures is promising for a wide range of applications, which are detailed throughout the length of this chapter.

The effect of Plateau-Rayleigh instabilities on the nanowire-nanosphere conversion was initially demonstrated on a polymer-glass core-shell matrix [36]. While glass-polymer (as opposed to polymer-glass) nanowires are utilized in my fabrication scheme, similarities in fragmentation conditions suggest that the transitory spectrum observed in my demonstrations is also caused by Plateau-Rayleigh instabilities. This spectrum exists in a critical temperature range at which the "soft" core can easily deform and is constrained by the "harder" polymer shell, and it is likely that the surface tension stress between the core and shell regions is the driving force behind the formation of the distinctive structures observed. This stress is caused by differences in the rates at which the viscosities of the core and shell regions decrease with increasing process temperatures, and deformations start to occur when the surface tension in the core-shell interface exceeds a certain limit. Higher temperatures are capable of altering the structures of both regions inside the PES matrix, leading to the production of nanochains and core-shell nanospheres. However, further theoretical insight is required to fully elucidate the governing dynamics of the intermediate nanostructures obtained via the fabrication method described in this chapter.

I had previously described a nanofabrication method, ISR, where step-by-step reduction is utilized to decrease structure dimensions from macro- to nanosizes and produce 1D core-shell nanostructures highly suitable for use in optical applications (Chapter 2) [48]. While ISR is conventionally limited to the production of nanowires, this constraint has recently been overcome by utilizing Plateau-Rayleigh instabilities to thermally degrade ISR-produced nanowire arrays. However, while the fabrication of spherical structures [49] was demonstrated using ISR and thermal degradation, more complex architectures have yet to be created using this combination.

In this chapter, I report the presence of a transitory region where a diverse array of nanostructures is produced from glass-polymer core-shell nanowires during the progress of a combined ISR-thermal instability technique. Nanosprings, nanowire-embedded discrete nanorods and nanospheres, and nanochains can be fabricated in succession by halting the thermal degradation process prior to core-shell nanosphere formation (Figure 3.1). While the production of similar dielectric structures has been accomplished by pyrolysis of polymeric precursors [50], thermal annealing of catalyst decorated glass powders [51], template-directed approaches [52], self-assembly methods [53,54,55,56], and electrospinning [57], the present method avoids previous issues involving limited control over separation distance, uniformity, alignment and/or length, and is capable of producing a diverse array of core-shell nanoarchitectures in a single fabrication scheme by relying on minor alterations in process temperature to switch between nanostructure configurations.

The fabricated structures are highly uniform, closely match the initial nanowire in profile and can be produced from nanowires of arbitrary lengths and thicknesses; final particle sizes can also be controlled by altering the nanowire's initial dimensions or physically restraining it during the thermal contraction process. In addition, the process is easy to perform, rapid, cost effective and applicable on a wide spectrum of materials, requires relatively low temperatures (approx. 300 °C

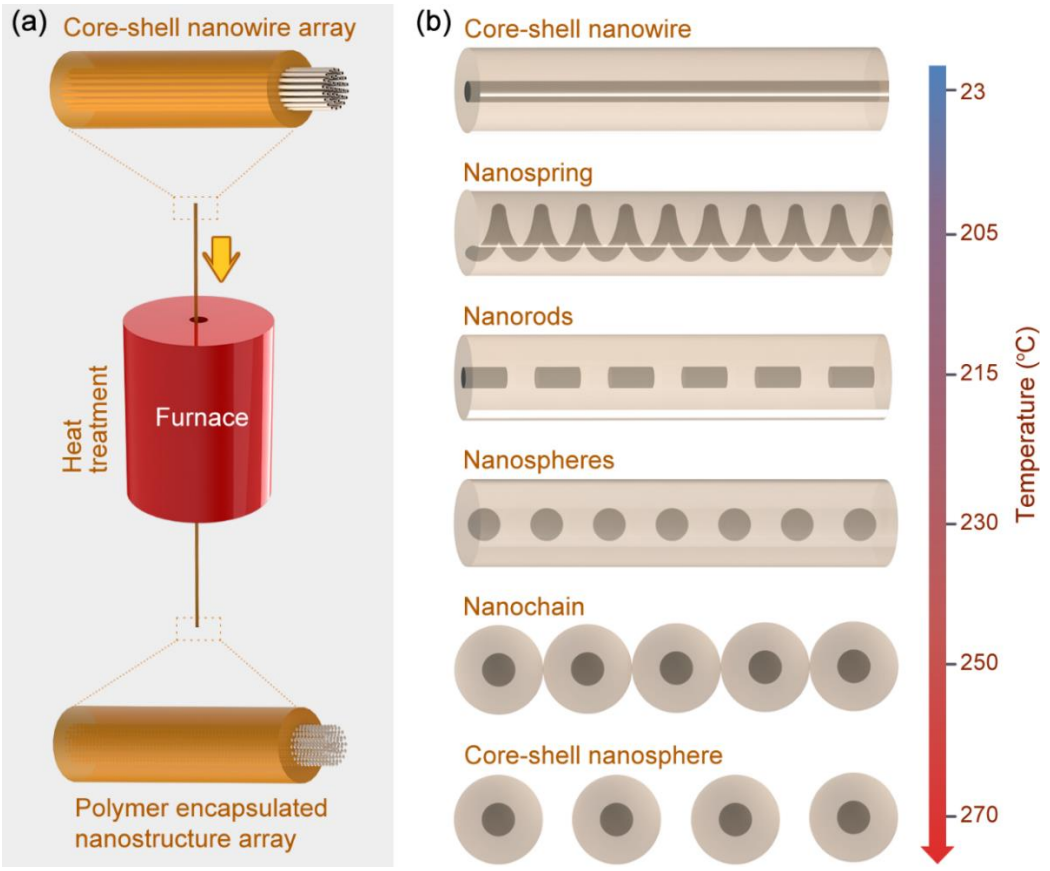

Figure 3.1: Novel nanoschemes produced by structural changes in a nanowire array subjected to heat treatment. Thermal compatibility of chalcogenide glass, PES and PVDF polymers permit the production of different combinations of nanostructures. Gradual increases in temperature result in structural alterations in the nanowire, up to and including the fragmentation of the core region. The structural transition can be halted at any point to obtain the desired nanomaterial configuration. Versatile nanostructures can be obtained by using a suitable combination of temperature, initial nanowire diameter and process duration. The transformation and breakup process is based on the material's physical parameters, such as viscosity and surface tension.

maximum), allows precise control of nanostructure geometry, does not rely on chemical properties and can be upscaled as required.

Fabrication of hierarchical nanostructures can be accomplished by subjecting previously fabricated core-shell nanowires to heat treatment. Any conventional furnace can be used for heating, though a uniform heat distribution is required to reduce potential fluctuations in nanostructure dimensions. In addition, the heating apparatus should be capable of reaching temperatures exceeding the glass transition temperatures of the nanowire components (300-350 °C in my experiments). Prior to heat treatment, PES-embedded core-shell nanowire arrays can be wrapped around a glass tube or placed as is on a glass substrate, with or without edge restriction.

Edge restriction fixes the macroscopic structure and prevents the thermal contraction of the fiber during heat treatment, resulting in fabricated structures bearing diameters similar to that of the original nanowire. Larger nanostructure diameters can be obtained by restricting wire ends in “slack” lines to partially allow thermal contraction, or by using free-standing fibers. Heated fibers deform into nanosprings, shell-embedded discrete rods, shell-embedded spheres, nanochains and core-shell nanospheres with increasing temperatures. Several measurements were performed to investigate the effects of heating time and nanowire thickness on final nanostructure dimensions, as well as to optimize the production of specific nanostructure arrays for fixed heating times and nanowire thicknesses.

3.2 Fabrication of Nanosprings

Core-shell nanowires are heat-modified to obtain a great diversity of hierarchical nanostructures, mediated by the mutually compatible viscoelastic properties of the As_2Se_3 glass core, PVDF polymer shell and PES matrix sheath. Heat treatment induces the transition of the core-shell nanowire into nanosprings at temperatures just above the glass transition temperature of arsenic selenide. Controlled synthesis of nanosprings is achieved by altering the nanowire diameter (d), process temperature (T) and/or process duration (t) within the transitory range, which typically occurs in the ~200-210 °C region for t = 2 min and d = 90 nm and is increased for lower exposure times (*e.g.* 220-230 °C, t = ~10 sec and d = 90 nm) and higher nanowire diameters (*e.g.* ~220-230 °C, t = 2 min and d = 200 nm). SEM images (Figure 3.2b,d) reveal that large-area uniform core-shell nanosprings can be fabricated from core-shell nanowires (Figure 3.2a,c) following the optimization of process temperature and duration.

Core-shell nanosprings with specific pitch sizes, periodicities and spring diameters can be engineered by changing process conditions and initial nanowire dimensions. As the production of uniform and smooth nanosprings with versatile optical, mechanical and electrical properties is critical for the characterization of light-material interactions, the thermal drawing method described in the present work is potentially able to answer a large host of problems inherent in nanoscale optics. In particular, in-fiber nanosprings may be utilized to great effect in photonic topological insulators [58] and photonic metamaterials [59], while free-standing nanospring arrays may find applications in enhanced catalytic converters [60], SERS substrates [61], artificial olfaction [62], energy storage [63], and the manipulation of viscoelasticity [64] and thermal conductivity [65] in polymers.

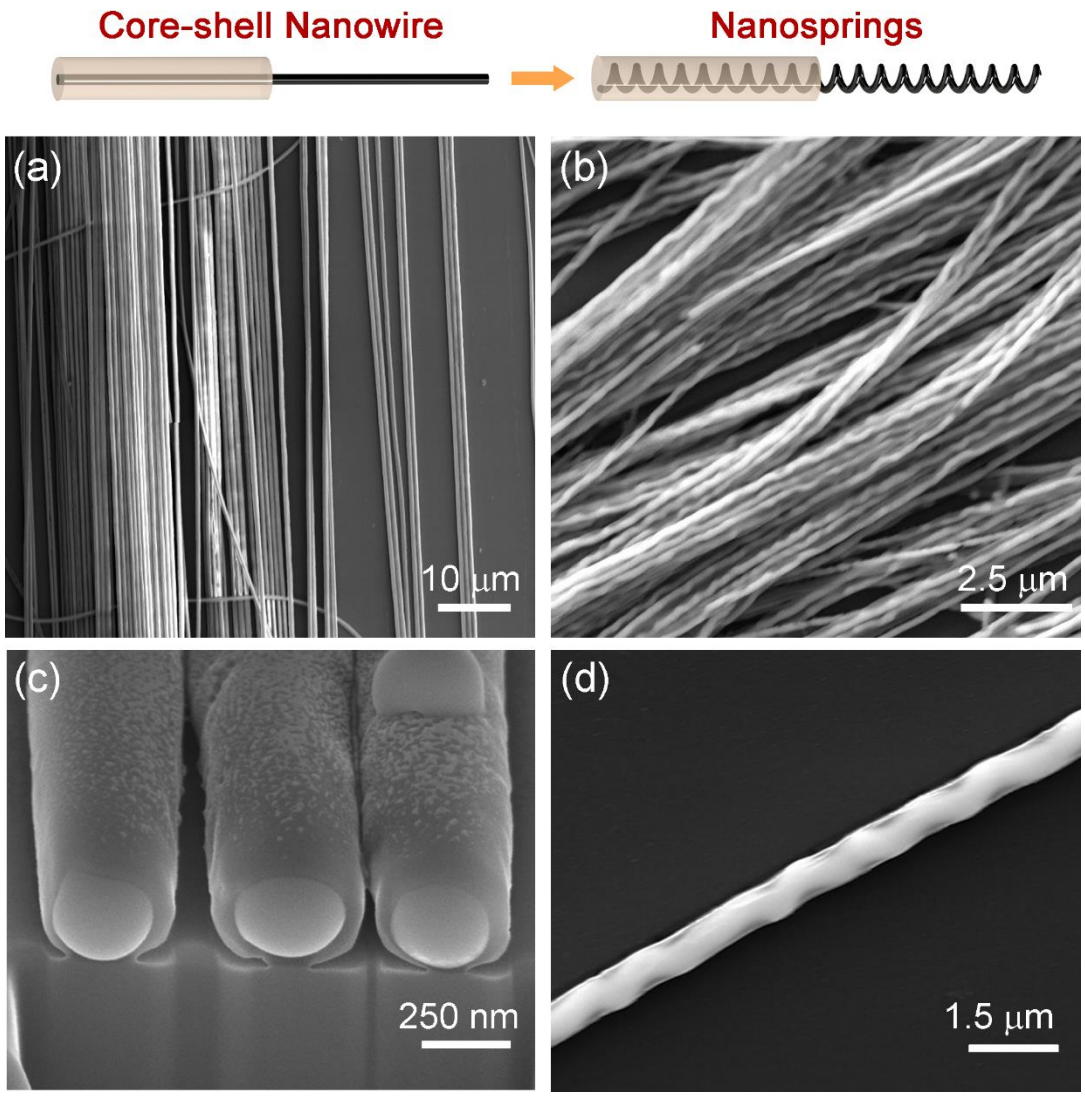

Figure 3.2: Fabrication of core-shell nanosprings can be accomplished by applying heat on a nanowire array. Gradual increases in temperature result in structural alterations in the nanowire, including the deformation of the core region and the consequent production of helical nanostructures. Pitch sizes and periods can be manipulated by altering temperature, initial nanowire diameter and process duration.

3.3 Fabrication of Nanoshell Embedded Rods

Temperatures above the core-shell nanospring-associated region trigger the production of shell-embedded discrete rods. By now, the core of the core-shell nanowire has fragmented into well-separated rods inside the polymer nanoshell, as the surface tension in the core-shell interface overcomes the viscosity of the core region and triggers the development of core instabilities until the nanowire core breaks into a series of discrete rods. This configuration can be obtained in the temperature range of ~210-220 °C for t = 2 min and d = 90 nm, though the temperature required decreases with longer process durations and smaller nanowire diameters. SEM images of this scheme demonstrate that large-area and uniform (Figure 3.3) production of shell embedded discrete rods can be accomplished by the present fabrication method, and the structures in question retain the thickness and profile of the initial nanowire array. As the PVDF shell and As_2Se_3 core are thermally compatible, the breaking process occurs without deforming the shell region.

In-fiber fabrication of discrete rods readily eliminates alignment issues associated with other fabrication methods, which is crucial for plasmonics applications (especially in metallic structures). Nanorod lengths and separation distances can be engineered for specific applications by optimizing initial nanowire diameter, temperature and process duration. In-fiber production of discrete nanorod arrays within a PVDF shell and PES matrix could provide many opportunities in nanoscale optics, including potential applications as dielectric antennae [66], high brightness LEDs [67], gas sensors [68] and hybrid nanowire-polymer solar cells [69].

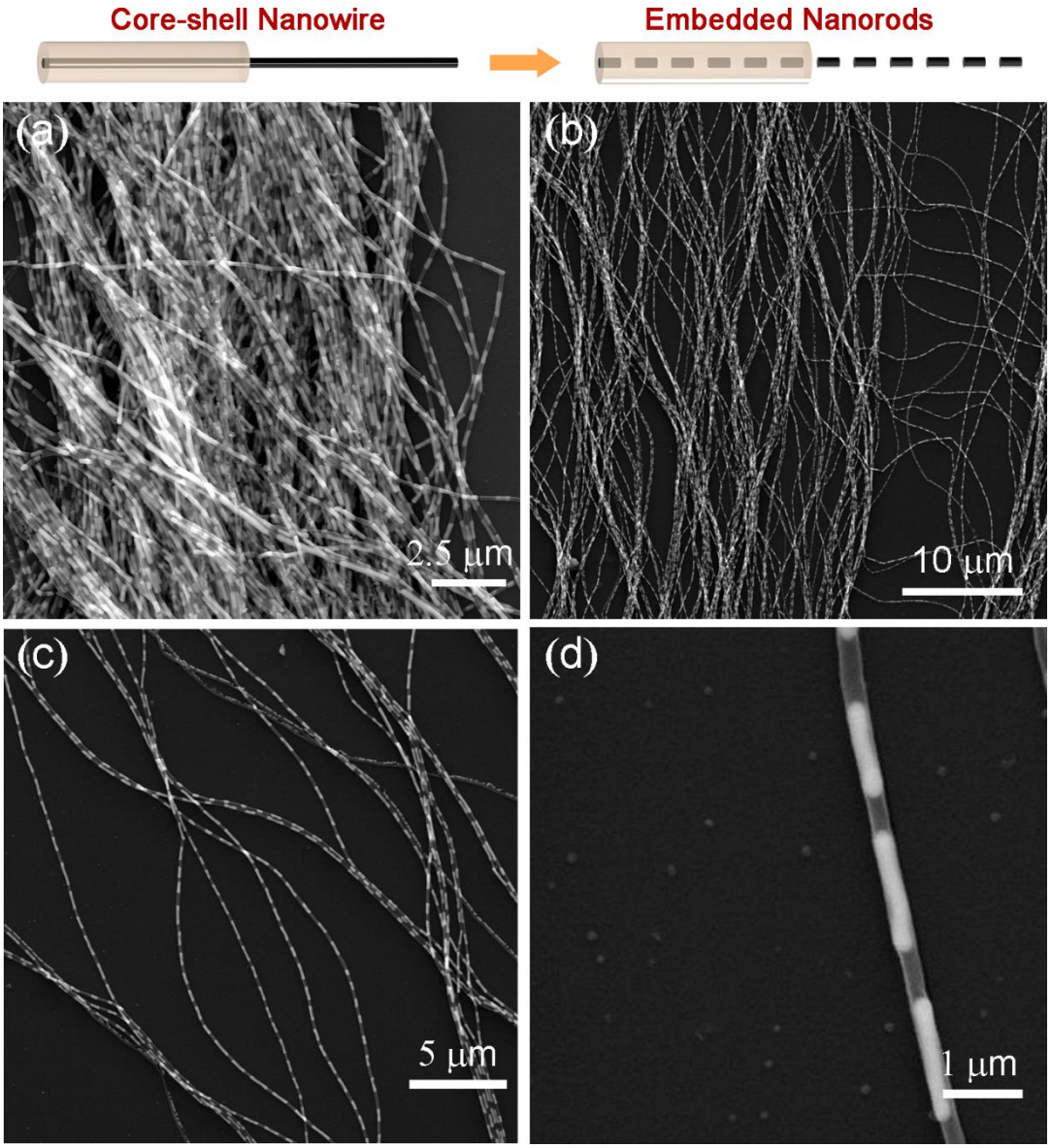

Figure 3.3: Fabrication of shell-embedded nanorods. Further heating of core-shell nanowires (e.g. to 215 °C for t = 2 min and d = 90 nm) results in the fragmentation of the arsenic selenide core into discrete rods inside the PVDF nanoshell.

3.4 Fabrication of Nanoshell Embedded Spheres

Nanorod lengths decrease with higher temperatures, and core fragmentation eventually culminates in the production of shell-embedded nanospheres. As with shell-embedded rods, this configuration is characterized by a series of nanostructures occurring at regular intervals within the polymer shell, which are produced in the temperature range of ~225-240 °C for t = 2 min and d = 90 nm. As with discrete nanorods, initial nanowire diameters, process duration and the temperature can be altered for the fabrication of nanosphere arrays of varying sizes embedded inside the shell region. Again, thermal instability-mediated deformations only act upon the core region and the shell remains unaltered throughout the nanosphere formation process, though higher surface tensions are required to overcome the inertial viscous forces and facilitate the conversion of nanorods into nanospheres. At the temperature ranges necessary for shell-embedded nanosphere formation, the PES region still remains solid and is not subject to deformation. However, it is necessary to utilize a thick layer of PES in order to keep the region surrounding the core highly viscous, as core deformation may otherwise damage the shell and sheath regions during nanostructure formation.

Large-area images of this configuration are given in Figure 3.4, and demonstrate that the present method is suitable for the fabrication of nanosized arrays of shell-embedded spheres within a PES fiber. Figure 3.4d in particular displays shell embedded spheres with diameters around 250 nm. In addition, SEM micrographs suggest that nanosphere arrays display a uniform distribution and preserve the profile of the initial nanowire. However, an increase in nanostructure diameters is also observed during nanowire-nanosphere conversion, possibly due to the concentration of core mass into a series of well-separated nanospheres. It is also notable that the As_2Se_3 core can fragment into discrete rods and eventually form spherical structures without damaging or deforming the outer nanoshell.

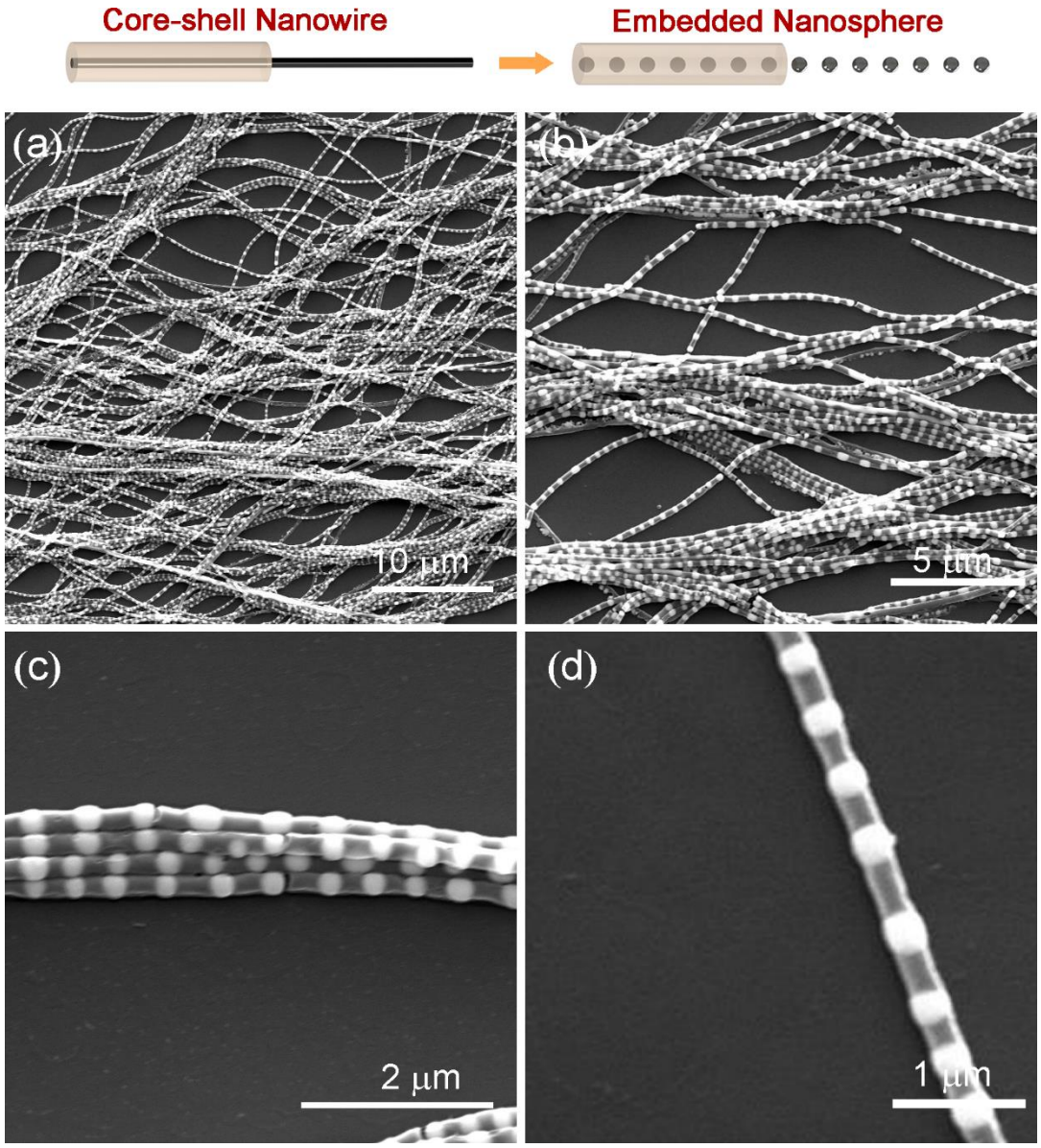

Figure 3.4: Fabrication of shell embedded spheres. Temperature above the heat treatment in higher temperatures particularly in 215 °C cause to breaking of core arsenic selenide into periodically separated spheres inside the PVDF nanoshell.

Shell-embedded spheres are difficult to produce by conventional means, and are of significant practical importance in photonics applications. Sphere diameters and separation distances can be engineered for the production of dielectric antennae [70]. They can be also utilized in CCW applications, where they display promising coupling features. This point has been theoretically investigated, and is detailed in Chapter 5.

3.5 Fabrication of Nanochains

Following the production of shell-embedded nanospheres, further heat treatment results in the structural deformation of the shell region, producing a series of nanochains. This configuration can be described as a series of As_2Se_3 nanospheres linked by PVDF bridges. Here, both the shell and the core of the core-shell nanowire are deformed into chain-like (Figure 3.5) structures. This configuration can be obtained in the temperature range of ~245-260 °C for a process duration of 2 min and a core-shell nanowire diameter of 90 nm.

Despite the deformation of both core and shell regions, the PES polymer sheath remains intact following the application of heat and preserves its integrity to a reasonable degree, though thicker sheath thicknesses may be necessary for procedures requiring higher temperatures. SEM images of this configuration demonstrate that large-area and uniform nanochain arrays can be obtained with proper fabrication settings. Sizes of the chain links are in the nanoscale, and around 200 nm for all images in Figure 3.5a-c. FIB sections for nanoscale chains are difficult to obtain, as the chain links are damaged easily even under the lowest current setting possible. As such, I instead provide a cross-sectional image of two microchain links connected by the PVDF outer shell.

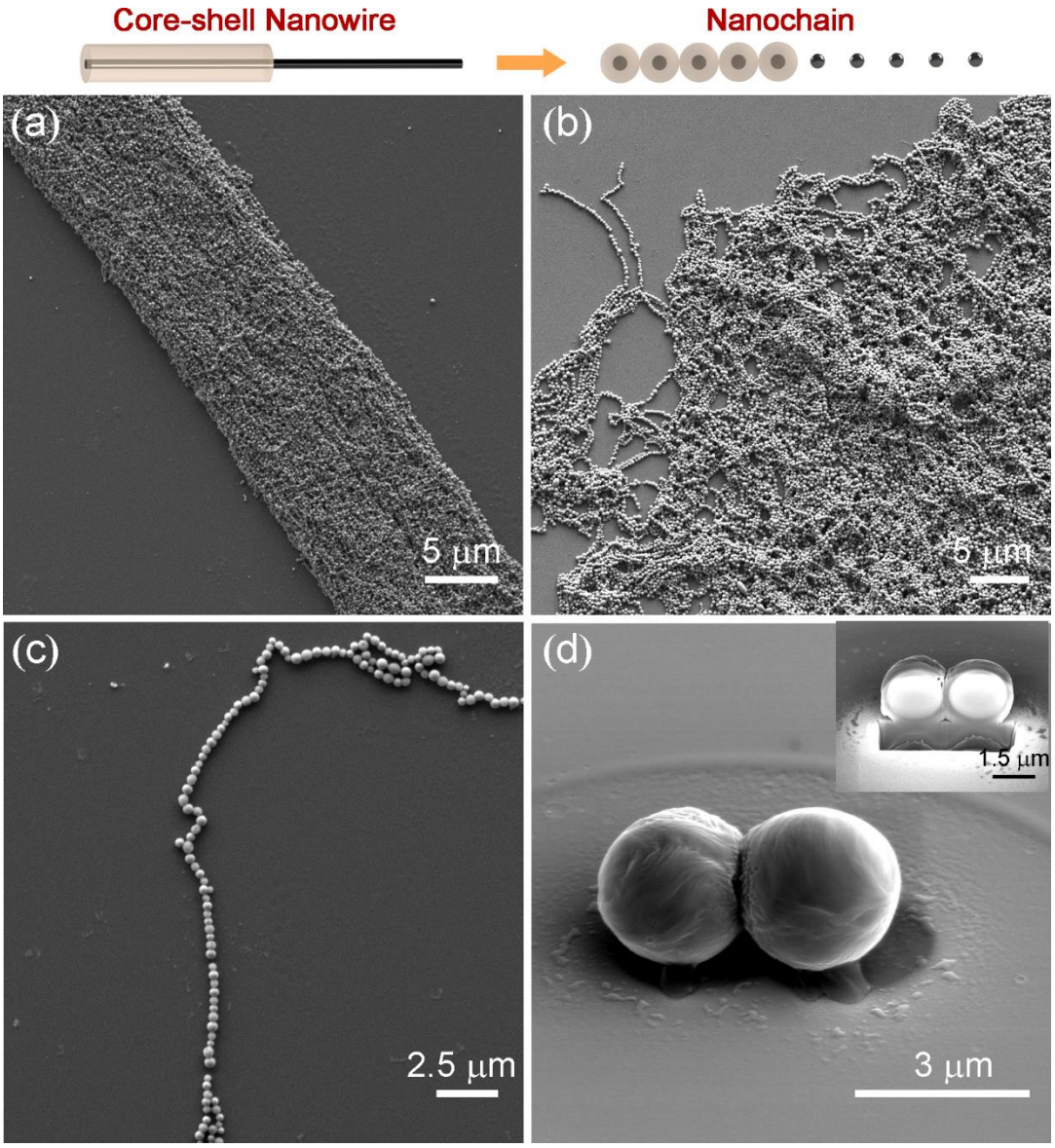

Figure 3.5: Fabrication of nanochains, accomplished in this case by raising process temperature to 250 °C. Higher temperatures causes the PVDF bridges to separate, resulting in a series of PVDF-arsenic selenide nanospheres within the PES sheath.

Nanochains are relatively novel structures and can be tailored to fit the needs of a wide range of applications, including solar thermal absorbers [71], luminescent platforms [72] and single electron transistors [73].

3.6 Fabrication of Core-Shell Nanosphere

The final product of heat treatment is a series of nanospheres. Here, the core and shell regions are both fragmented, resulting in core-shell nanospheres connected only by the PES sheath (Figure 3.6). Both shell and core region affected by thermal instability. Surface tension is adequately high from viscous force hence result with the breaking of both region of the core-shell nanowire.

This configuration can be obtained in the temperature range of ~265-280 °C for t = 2 min and d = 90 nm. SEM images of this configuration demonstrate that uniform, large-area nanosphere arrays can be obtained following the optimization of fabrication settings. FIB was also utilized to obtain cross-section images of a single core-shell sphere (Figure 24d). Core-shell nanospheres can be used for a range of applications, including photonic crystal barcodes [74] and the development of novel sensors [75].

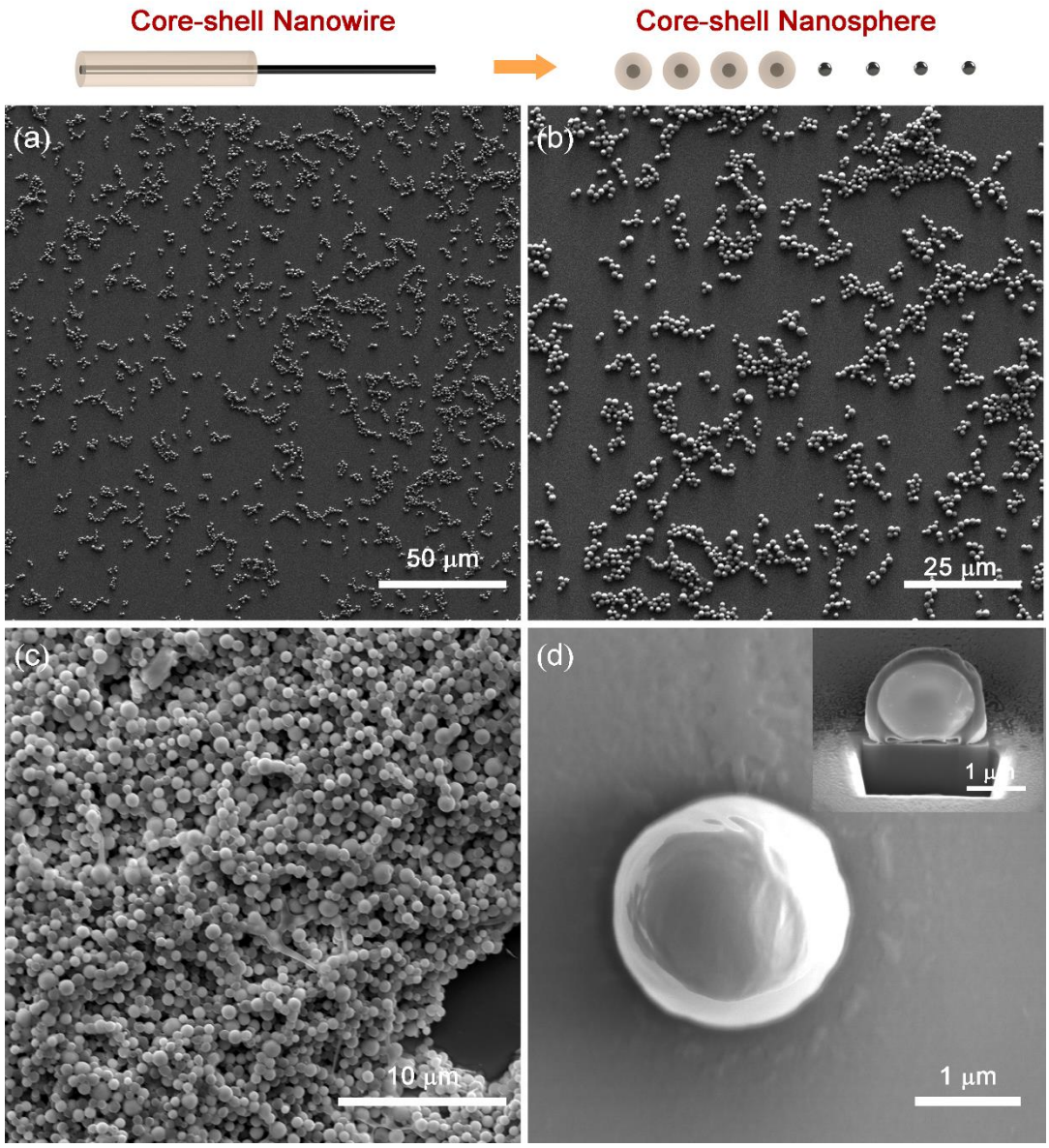

Figure 3.6: Complete deformation of core-shell nanowires into core-shell nanosphere occurs at temperatures above 270 °C. Core-shell nanospheres are supported by the PES sheath, which is unaffected by applied heat.

3.7 Features of the Fabrication Method

The combination ISR-thermal instability technique described in Chapters 2 and 3 provides excellent fabrication facilities, many of which are inherited from the features of the ISR method. It is especially notable that the thermal alteration of PES-embedded nanowires does not compromise the structural integrity of the nanofiber, and indefinitely long arrays can be produced for any of the schemes described. I demonstrate this effect by fabricating a 2 meter-long array of spherical structures (Figure 3.7a) inside a PES sheath, while preserving the distribution of bundle components within the local area in which the nanostructures are embedded.

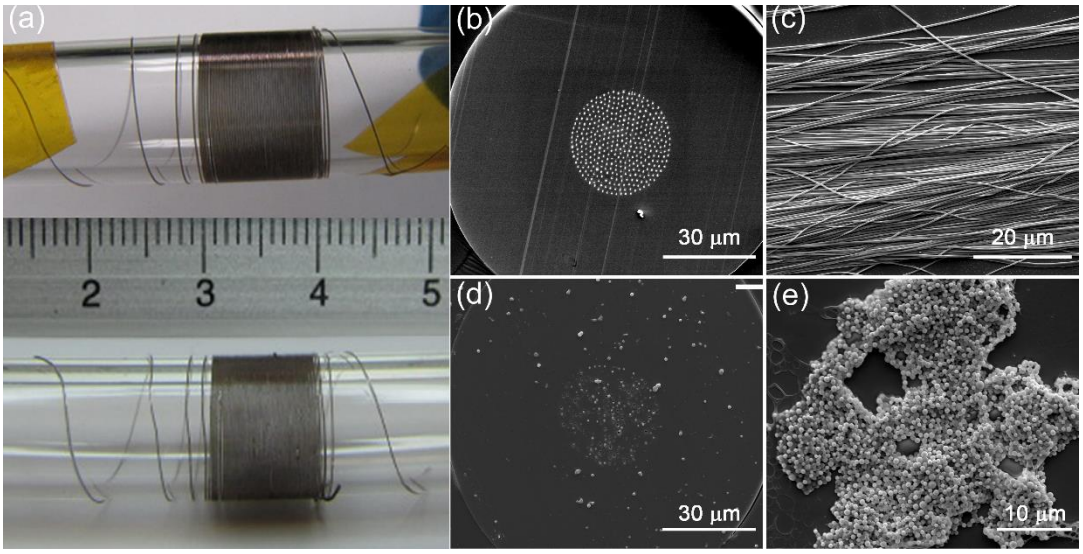

Figure 3.7: Indefinitely long nanostructures. (a) A 2 m nanowire array converted into spherical nanostructures, demonstrating that fiber integrity is not significantly altered by heat treatment, and that nanostructure arrays can be produced in macro-scale lengths by the present method. (b) Cross-sectional and (c) longitudinal images of nanowires (d=450 nm). Produced spherical nanostructures with (d) out of phase, aligned, cross-sectional and (e) longitudinal image.

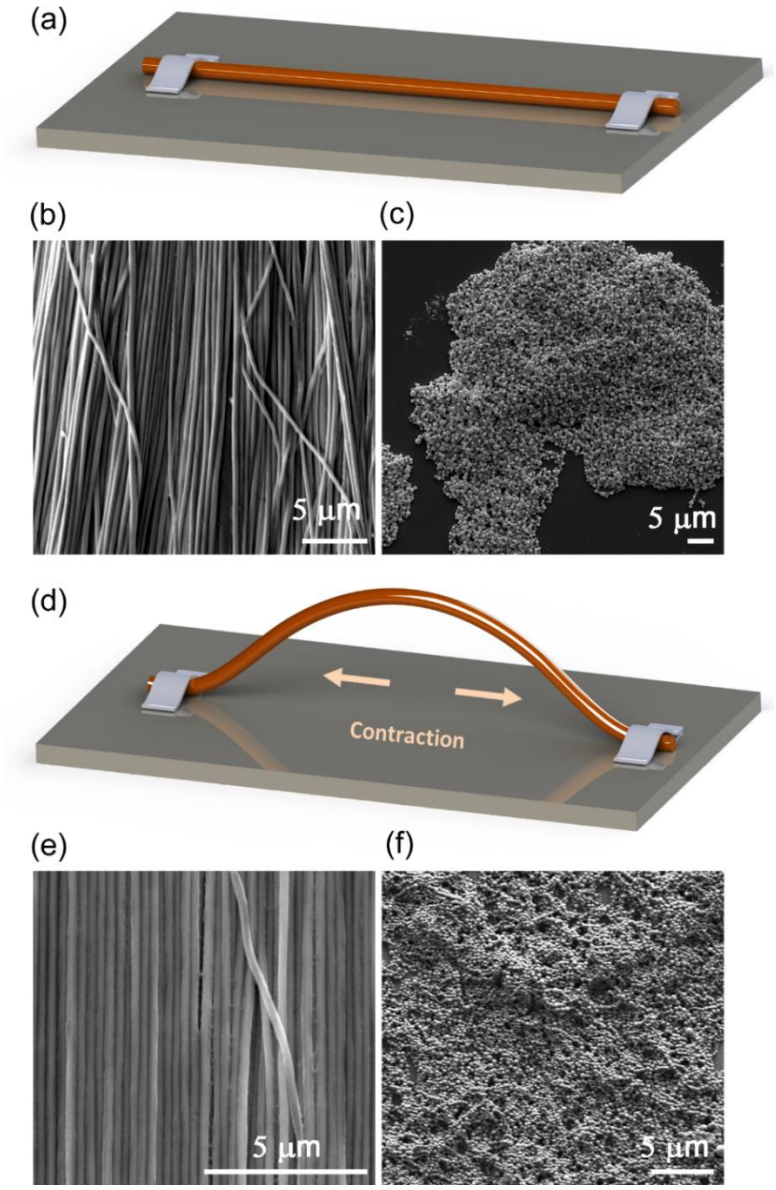

Figure 3.8: “Taut” and “slack” fabrication. (a-c) “Taut” fibers produce nanochains with average diameters (500) similar to that of the initial nanowire (450 nm). (d-f) “Slack” fibers, in contrast, produce much higher diameters due to the thermal contraction of the fiber; originated from mass conservation. The SEM micrograph displays nanochains with an average diameter of 400 nm, obtained from 200 nm core-shell nanowires.

While heat-modified nanostructures largely retain the profiles of the initial nanowire, the out-of-phase alignment of parallel nanostructure arrays prevents the observation of all nanostructures on a single cross section (Figure 3.7d).

Precise size control of spherical nanostructures is also demonstrated in step II nanowires by physically restraining the initial wire during nanochain formation. "Taut" (i.e. restrained with no room for contraction) nanowires produce spheres with diameters consistent with the initial structure, while "slack" microfibers contract during the process and form nanochains with larger diameters (Figure 3.8a-f). In order to demonstrate this point, I fabricated nanochains using two nanowires with identical (450 nm) diameters, applying edge restriction to one ("taut" fabrication) and leaving the other unrestricted ("slack" fabrication). The nanochains produced had diameters of 450 and 200 nm, respectively.

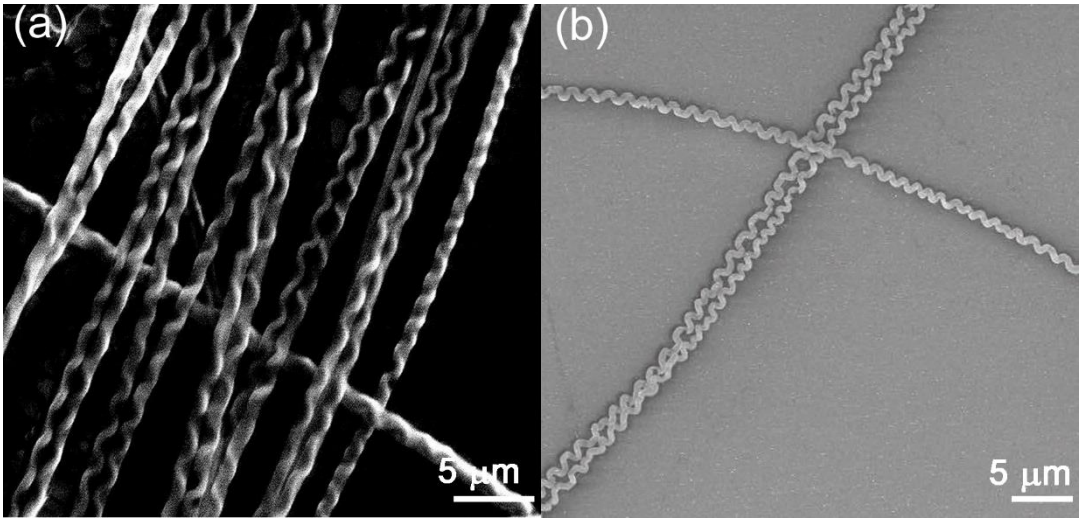

Figure 3.9: Core-only nanoschemes. In addition to (a) core-shell nanoschemes, (b) core-only structures can be obtained by removing the PVDF shell layer. I demonstrate this process by plasma etching an array of core-shell nanosprings, but etchant solvents or drawing core-only fibers may be utilized to the same effect.

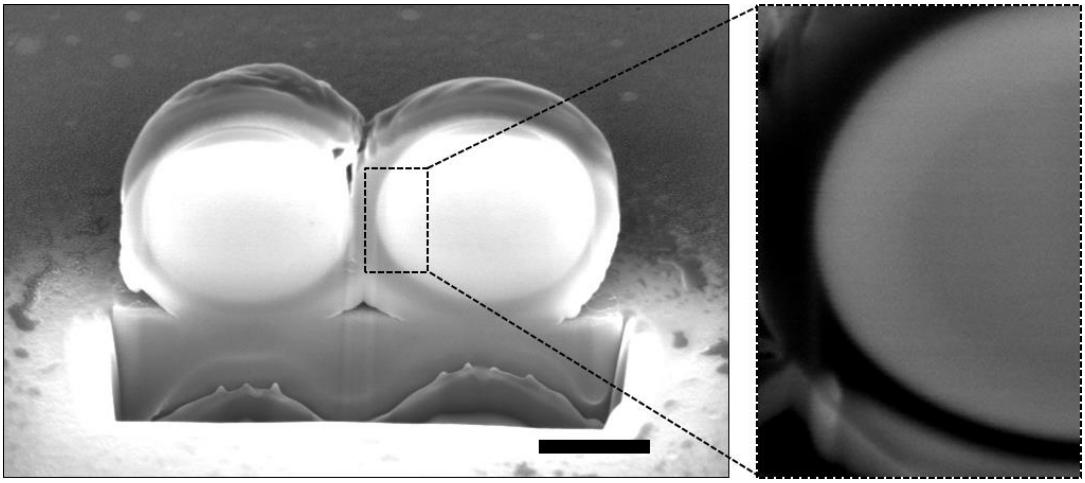

Figure 3.10: Smoothness of microscale structures. Two linked microsphere exhibit smooth surfaces and no apparent irregularities, even under high magnification. Scale bar, 500 nm.

In addition to core-shell configurations, core-only nanostructures can be produced by removing the shell region by plasma etching or exposure to PVDF-etching solvents. Bare nanosprings obtained by plasma etching are shown in Figure 3.9, and it is notable that such structures could be produced without deforming the core layer. Similarly, N,N-Dimethylacetamide (DMA) and DCM can be used as solvents to remove the PVDF polymer sheath. However, as PVDF is relatively resistant to DCM, the nanowires should be etched for a longer time periods (several dozen minutes for nanoscale shell sizes). Using this technique, any structure fabricated using the present method can be obtained in bare (sheathless) form, to be used in a variety of applications.

The fabrication method is scalable across a wide size range and can be used for the production of nano- and microscale structures by altering initial nanowire profile and dimensions. Micron-scale spheres obtained by heat treatment of Step II nanowires are shown in Figure 3.10 and confirm that it is also possible to obtain microspheres using the present method (*e.g.* for microresonator applications).

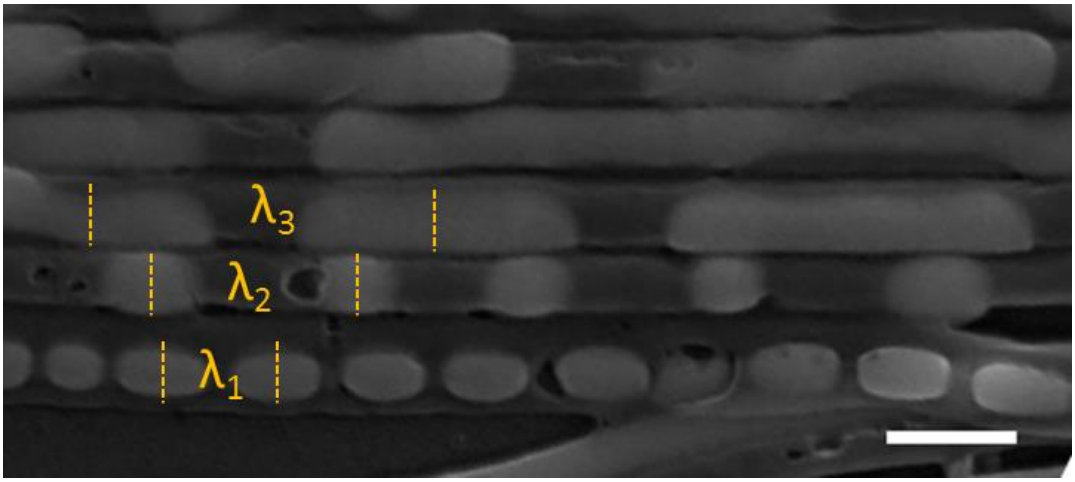

Figure 3.11: Adjustable instability wavelengths. Different processing times and temperature result in changes in instability wavelengths. Discrete rods displaying varying wavelengths (λ_1=140 nm, λ_2=240 nm, λ_3=580 nm,) were produced following the exposure of a nanowire array to a temperature gradient. Scale bar, 200 nm.

Thermal treatment also results in the production of highly smooth nanostructures, which are particularly crucial in optical applications. The high regularity inherent to the present fabrication method can be observed in the two microchain links shown in the magnified SEM micrograph in Figure 3.10.

Structure wavelengths and inter-structural distances are also correlated with process temperature and timing, with higher values being associated with lower wavelengths and distances. By applying a non-uniform heat gradient, I observed the production of a nanorod array displaying a spectrum of inter-spacial distances and lengths. Nanorods with instability wavelengths of λ_1=140 nm, λ_2=240 nm and λ_3=580 nm are displayed in Figure 3.11.

Chapter 4

Numerical and Analytical Techniques

4.1 FDTD Method

The finite-difference time-domain (FDTD) method is a mathematical technique that can be utilized for finding numerical solutions to Maxwell's equations [76]. This state of art method has several advantages over similar techniques, which are generally based on approximations and are only applicable to specific cases (i.e. Beam Propagation Method [77], DDA approximation [78], Lorenz-Mie Theory [79]). FDTD, however, can be applied to any complex geometry and is capable of simulating realistic conditions. Beside time and space solutions, it can also be utilized for frequency solutions by taking Fourier transforms of solutions obtained in the time domain.

FDTD simulations are performed using commercial finite-difference time-domain software [80] (Lumerical Solutions Inc.). The software utilized, Lumerical FDTD Solutions, provides conformal meshing for the simulations of electromagnetic problems and supports parallel computing in longer simulations. Minimum mesh

sizes utilized in simulations are limited by the capabilities of workstations used to run the simulation in question. However, conventional PCs are sufficient for the acquisition of accurate solutions to many electromagnetic problems. I used 2 workstations that possess 8 core processors in total, each with a speed of 3 Ghz and a RAM of 16 Mb. In order to minimize simulation time for very long simulations, I also used the facilities of TUBITAK Ulakbim, which are equipped with high performance computers and can significantly shorten simulation times by utilizing a parallel computing network of over 50 processors.

4.1.1 FDTD and Maxwell's Equations

The basic formalism behind the FDTD technique relies on fully vectorial solutions of Maxwell's curl equations in non-magnetic materials:

$$\frac{\partial \vec{D}}{\partial t} = \nabla \times \vec{H}$$

$$\vec{D}(\omega) = \varepsilon_0 \varepsilon_r(\omega) \vec{E}(\omega)$$

$$\frac{\partial \vec{H}}{\partial t} = -\frac{1}{\mu_0} \nabla \times \vec{E}$$

Here *E*, *H* and *D* correspond to electric, magnetic and displacement fields, respectively. $\varepsilon_r(\omega)$ is the complex relative dielectric constant, and its square root is the refractive index of the material in question. As the above equations are differential equations, a large variety of mathematical transformations can be utilized for their solution. Here, I preferred to use the FDTD method.

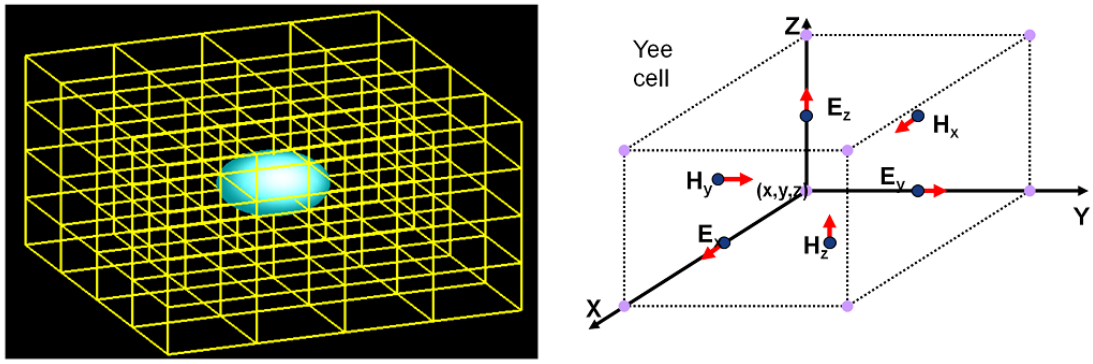

Figure 4.1: A simulation cell divided into a mesh network. Yee cells are the elemental volumes comprising the mesh structure.

Yee cells, discrete mesh elements that divide the material volume and the simulation region into discrete parts, have been utilized for simulation (Figure 4.1). Maxwell's equations are also solved in discrete time steps, which are each equal to the spatial mesh size divided by the speed of light.

4.1.2 FDTD Solutions

Conventional simulations require the input of simulation parameters for material structure, simulation domain, light source and data acquisition settings. Detailed information for each setting can be found in Ref. 80, but here I only provide the optimized settings utilized throughout my simulations.

Structures used in simulations have been defined as cylindrical or spherical core-shell structures. In cases of structural overlap, mesh orders were set so as to prioritize the lower order during simulation. Almost all calculations utilized for comparisons between simulated and measured data have been performed using real ellipsometric parameters given in Figure 2.5-2.6. For the rest of the calculations, I used constant

optical parameters to investigate the underlying phenomena and optical characteristics of the nanostructures of interest.

Simulation area settings define the boundary within which the calculations are performed. Either 2D or 3D simulation domains can be utilized for simulation. However, the properties of the simulated dimension should be applicable to the phenomenon to be investigated. To minimize simulation times, I assume a nanowire with infinite length, which reduces 3D simulations into their 2D FDTD equivalents. However, 2D simulations cannot be used for core-shell spheres, and 3D simulations were utilized for these nanostructures. Simulation time is initially set to 1000 fs and changed depending on the purpose of the simulation. Simulations are automatically stopped when the auto-shutoff criteria condition is reached. I used conventional PML boundary conditions in many simulations, which assumes that any light incident on a boundary is absorbed completely. In periodic systems, such as photonic crystal structures used for bio-mimicking (Chapter 8) and nanowire arrays coated on solar cells for the enhancement of light absorption (Chapter 9), I used a periodic boundary condition. In cases where circular symmetry is present (e.g. core-shell nanowires and nanospheres) I choose symmetric and anti-symmetric boundary conditions (the former is parallel to the electric field direction, and latter is parallel to the magnetic field). Auto-nonuniform meshing was generally used for simulations, and a fine mesh was defined around the monitored regions in order to increase simulation accuracy. FDTD Solutions simulation software also provides a conformal mesh option, which allows the simulation of curved regions and was utilized for all simulations.

A broad range of source options exist for the excitation of simulated structures. Each source is generally utilized for a specific purpose. A Total Field Scattered Field (TFSF) source is used for illumination in many scattering calculations, as this source type yields a scattered field separate from the incident field and is therefore well-suited for scattering analysis. For the characterization of nanoshell interference, a

plane-wave source is utilized. Nonlinear optics simulations require a more detailed set of source parameters, and pulse duration and bandwidth parameters (which are used to generate femtosecond pulses) need to be set prior to these simulations.

Monitors are used for collecting the data output. Frequency-domain power monitors are used for the observation of reflection, transmission, absorption and scattering data. Data points corresponding to specific wavelengths or frequencies can be set in order to increase the spectral resolution of the output. I preferred equal wavelength spacing in my simulations.

Frequency-domain profile monitors were used for the acquisition of spectral data, and near field profiles are obtained with the use of a frequency domain field and profile monitor. The resolutions of intensity and field profiles can be increased by decreasing spatial mesh sizes, and mesh sizes of 1-5 nm are utilized in my simulations to increase the quality of the near field profile data. Scripts were utilized to run series of simulations or to automatically save the resulting simulation data.

4.2 Analytical Solutions of Light Scattering from Core-Shell Nanostructures: Lorenz-Mie Formalism

Scattering from regular shapes (i.e. spheres and cylinders) can be modelled analytically using Lorenz-Mie formalism. As I frequently investigate scattering effects from core-shell nanostructures, their analytical solutions can be utilized to yield further support to my experimental and numerical results. Here, I solve the scattering equations for core-shell nanowires by using Lorenz-Mie formalism and provide the details of the solution procedures. Detailed solutions for scattering from coated spheres have previously been elucidated in the literature, and here I also provide analytical solutions for coated spheres.

4.2.1 Analytical Solutions for Core-shell Nanowires

I start from the scalar wave equation, which can be derived from Maxwell's equations.

$$\nabla^2\Psi + k^2\Psi = 0 ;$$

The wave equation in cylindrical coordinates can be expressed as follows;

$$\frac{1}{r}\frac{\partial}{\partial \mathrm{r}}\left(r\frac{\partial\Psi}{\partial r}\right) + \frac{1}{r^2}\frac{\partial^2\Psi}{\partial\Phi^2} + \frac{\partial^2\Psi}{\partial z^2} + k^2\Psi = 0 ;$$

The solutions are in the form of $\Psi_n(r,\Phi,z) = Z_n(\rho)e^{in\Phi}e^{ihz}$ (*n*= 0, ±1, …). Here $\rho = r\sqrt{k^2 - h^2}$, and Z_n can be obtained as the solution to the following Bessel equation;

$$\rho\frac{\mathrm{d}}{\mathrm{d}\rho}\left(\rho\frac{\partial Z_n}{\partial\rho}\right) + (\rho^2 - n^2)Z_n = 0 ;$$

Solutions of the above equations are linearly independent first and second kind Bessel functions. The vector cylindrical harmonics generated by the wave equation are;

$$M_n = \nabla \times (\hat{z}\Psi_n), \quad N_n = \frac{\nabla\times(M_n)}{k},$$

After inserting the parameters detailed in above equations, I obtain generating functions of the following form;

$$M_n = \sqrt{k^2 - h^2}(in\frac{Z_n(\rho)}{\rho}\hat{r} - Z_n'(\rho)\hat{\varphi})e^{i(n\varphi+hz)} \ ;$$

$$N_n = \frac{\sqrt{k^2-h^2}}{k}(ihZ_n'(\rho)\hat{r} - hn\frac{Z_n(\rho)}{\rho}\hat{\varphi} + \sqrt{k^2 - h^2}Z_n(\rho)\hat{z})e^{i(n\varphi+hz)} \ ;$$

These solutions assume a plane-wave light source incident on an infinite core-shell nanowire. However, it is useful to consider the TE and TM polarizations of the incident light and solve their equations separately to further characterize the scattering effect. For these solutions, I assume that light falls at a perpendicular angle onto the nanowire surface.

Derivation of equations for TM polarization:

Incident and scattered fields, as well as fields encompassed by the core and shell regions, can be expanded into wave harmonic equations by expressing their generating functions in their corresponding regions, and finding the scattering coefficient b_{n1};

$$h = -kcos\gamma \ ;$$

$$\Psi_n^i = J_n(krsin\gamma)e^{in\varphi}e^{-ikzcos\gamma} \ ;$$

$$\Psi_n^s = H_n^{(1)}(krsin\gamma)e^{in\varphi}e^{-ikzcos\gamma} \ ;$$

$$\Psi_n^1 = J_n(kr\sqrt{m_1^2 - cos^2\gamma})e^{in\varphi}e^{-ikzcos\gamma} \ ;$$

$$\Psi_n^2 = (cJ_n(kr\sqrt{m_2^2 - cos^2\gamma} + dY_n(kr\sqrt{m_2^2 - cos^2\gamma})e^{in\varphi}e^{-ikzcos\gamma} \ ;$$

Magnetic and electric fields for scattering, incidence, shell and core region fields can be expressed as generating functions, which are given in the Table 4.1.

$$E_{\mathrm{i}} = \sum_{n=-\infty}^{\infty} E_n {N_n}^{(i)} ;$$

$$H_{\mathrm{i}} = \frac{-ik}{\omega\mu} \sum_{n=-\infty}^{\infty} E_n {M_n}^{(i)} ;$$

$$E_1 = \sum_{n=-\infty}^{\infty} E_n \left(c_n {M_n}^{(1)} + d_n {N_n}^{(1)} \right) ;$$

$$H_1 = \frac{-ik_1}{\omega\mu_1} \sum_{n=-\infty}^{\infty} E_n \left(c_n {N_n}^{(1)} + d_n {M_n}^{(1)} \right) ;$$

$$E_2 = \sum_{n=-\infty}^{\infty} E_n \left(g_n {M_n}^{(2j)} + f_n {N_n}^{(2j)} + v_n {M_n}^{(2y)} + w_n {N_n}^{(2y)} \right) ;$$

$$H_2 = \frac{-ik_2}{\omega\mu_2} \sum_{n=-\infty}^{\infty} E_n \left(f_n {M_n}^{(2j)} + \mathrm{g} {N_n}^{(2j)} + w_n {M_n}^{(2y)} + v_n {N_n}^{(2y)} \right);$$

$$E_{\mathrm{s}} = -\sum_{n=-\infty}^{\infty} E_n \left(b_{n1} {N_n}^{(3)} + i a_{n1} {M_n}^{(3)} \right);$$

$$H_{\mathrm{s}} = \frac{ik}{\omega\mu} \sum_{n=-\infty}^{\infty} E_n \left(b_{n1} {M_n}^{(3)} + i a_{n1} {N_n}^{(3)} \right) ;$$

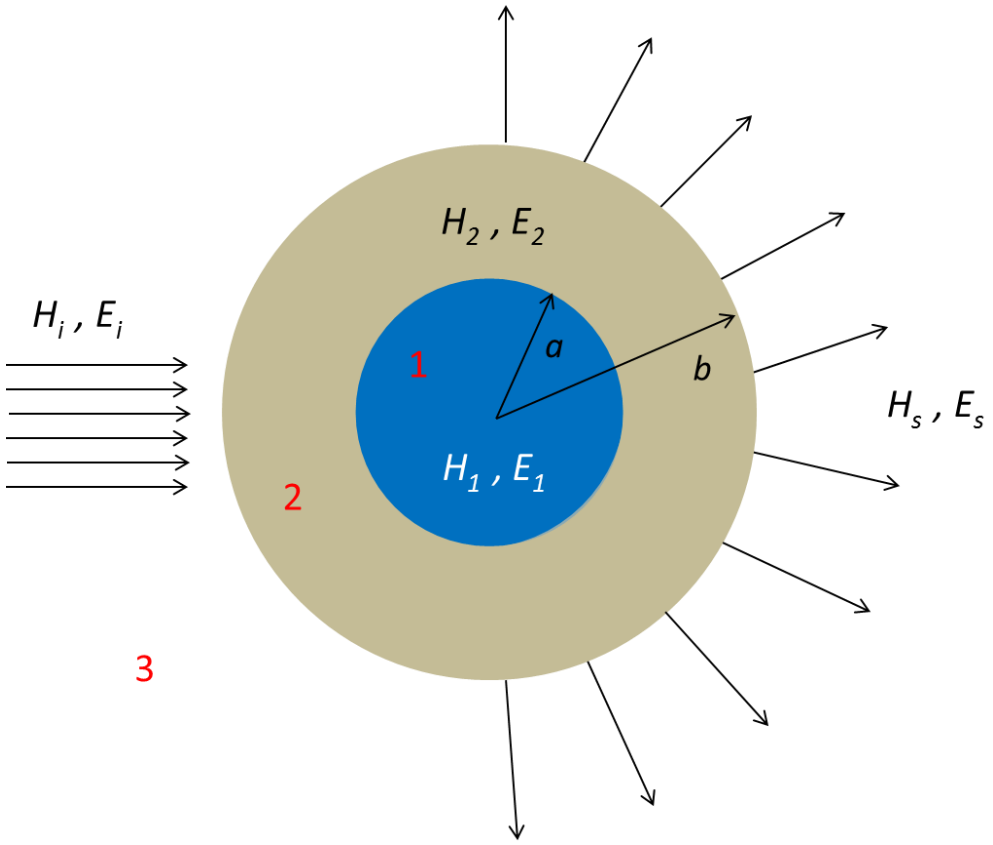

Figure 4.2: Schematic of the analytical solutions for scattering from a core-shell nanowire. The core medium possesses a higher refractive index than the shell region in my core-shell nanowires. The same equations could be used for nanotubes (or bare nanowires) by assuming a core (or shell) with the refractive index of air. Subscripts *i* and *s* indicate incident and scattered fields, respectively.

Derivation of equations for TE polarization:

Equations for the modelling of TE polarization were derived as described for TM polarization. Here I find the scattering coefficient a_{n1}. Wave harmonic expansions of core-associated, shell-associated, scattering and incident fields have been derived by defining the generating functions inside these regions.

$$E_{\mathrm{i}} = -i\sum_{n=-\infty}^{\infty} E_n {M_n}^{(i)} ;$$

$$H_{\mathrm{i}} = \frac{-k}{\omega\mu}\sum_{n=-\infty}^{\infty} E_n {N_n}^{(i)} ;$$

$$E_1 = -i\sum_{n=-\infty}^{\infty} E_n\left(c_n {M_n}^{(1)} + d_n {N_n}^{(1)}\right) ;$$

$$H_1 = \frac{-k_1}{\omega\mu_1}\sum_{n=-\infty}^{\infty} E_n\left(c_n {N_n}^{(1)} + d_n {M_n}^{(1)}\right) ;$$

$$E_2 = -i\sum_{n=-\infty}^{\infty} E_n\left(g_n {M_n}^{(2j)} + f_n {N_n}^{(2j)} + v_n {M_n}^{(2y)} + w_n {N_n}^{(2y)}\right) ;$$

$$H_2 = \frac{-k_2}{\omega\mu_2}\sum_{n=-\infty}^{\infty} E_n\left(f_n {M_n}^{(2j)} + \mathrm{g}{N_n}^{(2j)} + w_n {M_n}^{(2y)} + v_n {N_n}^{(2y)}\right) ;$$

$$E_{\mathrm{s}} = \sum_{n=-\infty}^{\infty} E_n\left(b_{n2} {N_n}^{(3)} + i a_{n2} {M_n}^{(3)}\right) ;$$

$$H_{\mathrm{s}} = \frac{k}{\omega\mu}\sum_{n=-\infty}^{\infty} E_n\left(i b_{n2} {M_n}^{(3)} + a_{n2} {N_n}^{(3)}\right) ;$$

M wavevector	N wavevector
M_n^i $= ksin\gamma(in\frac{J_n(krsin\gamma)}{krsin\gamma}\hat{r}$ $- J_n'(krsin\gamma)\hat{\varphi})e^{i(n\varphi-kzcos\gamma)}$	$N_n^i = sin\gamma(-ikcos\gamma J_n'(krsin\gamma)\hat{r} + kncos\gamma\frac{J_n(krsin\gamma)}{krsin\gamma}\hat{\varphi}$ $+ ksin\gamma J_n(krsin\gamma)\hat{z})e^{i(n\varphi-kzcos\gamma)}$
M_n^3 $= ksin\gamma(in\frac{H_n^{(1)}(krsin\gamma)}{krsin\gamma}\hat{r}$ $- H_n'^{(1)}(krsin\gamma)\hat{\varphi})e^{i(n\varphi-kzcos\gamma)}$	$N_n^3 = sin\gamma\left(-ikcos\gamma H_n'^{(1)}(krsin\gamma)\,\hat{r}\right.$ $+ kncos\gamma\frac{H_n^{(1)}(krsin\gamma)}{krsin\gamma}\hat{\varphi}$ $\left.+ ksin\gamma H_n^{(1)}(krsin\gamma)\hat{z}\right)e^{i(n\varphi-kzcos\gamma)}$
M_n^1 $= k_1sin\gamma(in\frac{J_n(kr\sqrt{m_1^2-cos^2\gamma})}{k_1rsin\gamma}\hat{r}$ $- J_n'(kr\sqrt{m_1^2-cos^2\gamma})\hat{\varphi})e^{i(n\varphi-kzcos\gamma)}$	N_n^1 $= sin\gamma\left(-ikcos\gamma J_n'(kr\sqrt{m_1^2-cos^2\gamma})\,\hat{r}\right.$ $+ k_1ncos\gamma\frac{J_n(kr\sqrt{m_1^2-cos^2\gamma})}{k_1rsin\gamma}\hat{\varphi}$ $\left.+ k_1sin\gamma J_n(kr\sqrt{m_1^2-cos^2\gamma})\hat{z}\right)e^{i(n\varphi-kzcos\gamma)}$
M_n^{2j} $= k_2sin\gamma(in\frac{J_n(kr\sqrt{m_2^2-cos^2\gamma})}{k_2rsin\gamma}\hat{r}$ $- J_n'(kr\sqrt{m_2^2-cos^2\gamma})\hat{\varphi})e^{i(n\varphi-kzcos\gamma)}$	N_n^{2j} $= sin\gamma\left(-ik_2cos\gamma J_n'(kr\sqrt{m_2^2-cos^2\gamma})\,\hat{r}\right.$ $+ k_2ncos\gamma\frac{J_n(kr\sqrt{m_2^2-cos^2\gamma})}{k_2rsin\gamma}\hat{\varphi}$ $\left.+ k_2sin\gamma J_n(kr\sqrt{m_2^2-cos^2\gamma})\hat{z}\right)e^{i(n\varphi-kzcos\gamma)}$
M_n^{2y} $= k_2sin\gamma(in\frac{Y_n(kr\sqrt{m_2^2-cos^2\gamma})}{k_2rsin\gamma}\hat{r}$ $- Y_n'(kr\sqrt{m_2^2-cos^2\gamma})\hat{\varphi})e^{i(n\varphi-kzcos\gamma)}$	N_n^{2y} $= sin\gamma\left(-ik_2cos\gamma Y_n'(kr\sqrt{m_2^2-cos^2\gamma})\,\hat{r}\right.$ $+ k_2ncos\gamma\frac{Y_n(kr\sqrt{m_2^2-cos^2\gamma})}{k_2rsin\gamma}\hat{\varphi}$ $\left.+ k_2sin\gamma Y_n(kr\sqrt{m_2^2-cos^2\gamma})\hat{z}\right)e^{i(n\varphi-kzcos\gamma)}$

Table 4.1. Generating functions of all three regions within the core-shell nanowire.

Boundary conditions:

Boundary conditions were set by taking into account the continuity of magnetic and electric fields throughout the core-shell and shell-air interfaces, and are expressed as follows;

$$(E_2 - E_1) \times \hat{r} = 0 \qquad (H_2 - H_1) \times \hat{r} = 0 \qquad @ \quad r = a$$
$$(E_s + E_i - E_2) \times \hat{r} = 0 \qquad (H_s + H_i - H_2) \times \hat{r} = 0 \qquad @ \quad r = b$$

By inserting the generating functions of electric and magnetic fields into the equation and utilizing the above-described boundary conditions, a single coefficient, b_n for TM polarization and a_n for TE polarization can be derived by converting the equalities into linear equations. The solved equations are given as follows;

$$b_n = \frac{J_n'(y)C - J_n(y)D}{H_n'^1(y)C - H_n^1(y)D} \quad \text{(For TM polarization);}$$

$$J = m_2 J_n(xm_2) - \frac{m_2^2}{m_1} J_n(xm_1) \frac{J_n'(xm_2)}{J_n'(xm_1)} ;$$

$$Y = \frac{m_2^2}{m_1} J_n(xm_1) \frac{Y_n'(xm_2)}{J_n'(xm_1)} - m_2 Y_n(xm_2);$$

$$C = m_2 J_n(ym_2) + m_2 \frac{J}{Y} Y_n(ym_2) ; \qquad D = m_2^2 J_n'(ym_2) + m_2^2 \frac{J}{Y} Y_n'(ym_2) ;$$

$$a_n = \frac{J_n'(y)D - J_n(y)C}{H_n'^1(y)D - H_n^1(y)C} \quad \text{(For TE polarization);}$$

$$J = m_1 J_n(xm_1) J_n'(xm_2) - m_2 J_n(xm_2) J_n'(xm_1) ;$$

$$Y = m_2 Y_n(xm_2) J_n'(xm_1) - m_1 J_n(xm_1) Y_n'(xm_2) ;$$

$$D = m_2^2 Y_n(ym_2) + m_2^2 \frac{Y}{J} J_n(ym_2)\ ; \qquad \mathrm{C}= m_2 Y_n'(ym_2) + m_2 \frac{Y}{J} J_n'(ym_2)\ ;$$

Scattering efficiency for unpolarized light can be written as follows;

$$Q_{sca}(x) = \frac{1}{x}\sum_{n=-\infty}^{n=\infty}(|a_n|^2 + |b_n|^2);$$

Here, $Q_{sca}(x) = \frac{C_{sca}}{2a}$, where C_{sca} is scattering cross-section and *a* is radius of cylinder.

4.2.2 Analytical Solutions for Core-shell Nanospheres

Lorenz-Mie formalism can also be utilized for the investigation of light scattering by core-shell nanospheres. Detailed solutions for core-shell nanospheres are well-known and are readily available in many texts on light scattering [81]. As such, the present work only lists the final solutions for light scattering from coated spheres.

$$a_n = \frac{\Psi_n(y)[\Psi_n'(m_2y) - A_n\chi_n'(m_2y)] - m_2\Psi_n'(y)[\Psi_n(m_2y) - A_n\chi_n(m_2y)]}{\xi_n(y)[\Psi_n'(m_2y) - A_n\chi_n'(m_2y)] - m_2\xi_n'(y)[\Psi_n(m_2y) - A_n\chi_n(m_2y)]}$$

$$b_n = \frac{m_2\Psi_n(y)[\Psi_n'(m_2y) - B_n\chi_n'(m_2y)] - \Psi_n'(y)[\Psi_n(m_2y) - B_n\chi_n(m_2y)]}{m_2\xi_n(y)[\Psi_n'(m_2y) - B_n\chi_n'(m_2y)] - \xi_n'(y)[\Psi_n(m_2y) - B_n\chi_n(m_2y)]}$$

$$A_n = \frac{m_2\Psi_n(m_2x)\Psi_n'(m_1x) - m_1\Psi_n'(m_2x)\Psi_n(m_1x)}{m_2\chi_n(m_2x)\Psi_n'(m_1x) - m_1\chi_n'(m_2x)\Psi_n(m_1x)}$$

$$B_n = \frac{m_2\Psi_n(m_1x)\Psi_n'(m_2x) - m_1\Psi_n(m_2x)\Psi_n'(m_1x)}{m_2\chi_n'(m_2x)\Psi_n(m_1x) - m_1\chi_n(m_2x)\Psi_n'(m_1x)}$$

Here, Ψ, χ and ξ are Riccati-Bessel functions. Scattering efficiency for unpolarized light can be expressed as follows;

$$Q_{sca}(x) = \frac{1}{x}\sum_{n=-\infty}^{n=\infty}(|a_n|^2 + |b_n|^2)$$

Here, $Q_{sca}(x) = \frac{C_{sca}}{\pi a^2}$, where C_{sca} is scattering cross-section and *a* is radius of sphere.

4.3 MODE Solutions

Mode Solutions is a commercial software developed by Lumerical Soft. Inc. for the finding solution of waveguide modes. This software is particularly useful in waveguide-type structures, and is utilized in this work to simulate the extent of dispersion between the waveguide and the material. Monitor, simulation, source, structure settings are similar to FDTD Solutions. Detailed information about MODE Solutions can be found in the Ref. 82.

Chapter 5

Resonant Mie Scattering

5.1 Mie Scattering

Light scattering from material surfaces is a well-known phenomenon in optics, though it is generally diffusive and uncontrollable in rough surfaces. However, controlled scattering can be very useful in a large number of applications. There are several types of scattering effects, including Rayleigh scattering, Mie scattering and inelastic scatterings such as Brillouin and Raman effects [3,83]. Many of them also take place in nature [84] (*e.g.* the blue color of the mid-noon sky, which is a result of Rayleigh scattering).

Among the scattering effects, Mie scattering is perhaps the most widely investigated phenomenon, and it is known for its far-reaching potential applications in nanoscale photonics [85,86,87,88]. In Mie scattering, light is scattered from small particles with enhanced scattering cross-sections and in resonant wavelength points. Sizes of scattered particles are comparable to the wavelength of the incident light in

the Mie scattering domain. Therefore, particles are required to be in the nano-scale in order to exhibit resonances in the visible spectrum of light (and thus to exhibit Mie scattering-mediated coloration in the visible region). Light cannot normally propagate through subwavelength structures. However, Mie scattering allows light to focus on even deep-subwavelength structures, provided that a correct combination of material parameters are present (refractive index and size parameters are key factors in material selection). Unlike micro-resonant systems, light in Mie scattering exhibits leaky mode resonances inside the scattering structure [89]. As such, light scattering can excite resonant modes inside the structure, which allows the efficient and continuous scattering of light from structures exhibiting Mie resonance modes. Light scattering from regular geometries can be analytically expressed by using the Lorenz-Mie formalism [90,91]. Analytical equations describing light scattering from core-shell nanowires and core-shell nanospheres are given in Chapter 4. In addititon to modelling, the absorption of a given material also can be maximized or minimized in desired wavelengths of light by altering particle sizes, and this phenomenon is facilitated by resonant Mie absorption. Hence, both absorption and scattering are significant when structure sizes are sufficiently small, though near-field effects are responsible for determining the extent of Mie absorption and far-field effects dominate the strength of the Mie scattering phenomenon.

5.2 Theoretical Investigation of Resonant Mie Scattering

Mie scattering in its resonant form can be observed in high-index nanomaterials and deep-subwavelength nanostructures. Many regular geometrical shapes have been designed to observe small particle scattering. Most of the structures studied are cylindrical [92,93,94] or spherical [95,96,97]. Here, I theoretically investigated resonant Mie scattering from core-shell nanowires and nanospheres.

5.2.1 Scattering from Core-shell Nanowires

Using FDTD simulations, scattering efficiencies of core-shell nanowires are investigated in the visible and NIR spectrum (300-1500 nm) for varying nanowire diameters (20-300 nm). Simulations are performed for both TM and TE polarizations using a constant refractive index of 3.25 for the As_2Se_3 core and 1.42 for the PVDF shell (Figure 5.1a,b).

For nanowire diameters below 300 nm, the PVDF shell thickness is insufficient to support thin film interference in the visible range, and Mie scattering from the core is the dominant form of scattering (this is the case for fabricated glass-polymer core-shell nanowires). The core diameter determines the structure and the number of whispering gallery type modes resonating inside the nanowire (Figure 5.2). The resonance conditions for Mie scattering in fabricated nanowires are identified as TM_{10}, TM_{11}, and TM_{21}. A single resonant mode is observed for dimensions smaller than 50 nm, and additional modes appear for larger nanostructures. For materials exhibiting Mie scattering, the absorption of light results in the omission of higher order modes and a decreased scattering efficiency. In stark contrast to TM polarization, no supporting mode is present inside structures below 50 nm in diameter for the TE polarization of visible wavelengths. However, a number of TE modes appear above this size, in addition to the above-mentioned modes resulting from TM polarization. In core-shell nanowires, resonant modes of TM polarization generally display a higher scattering efficiency compared to those of TE polarization.

The resonance-based origin of the scattering phenomenon is identified by near field mode profiles calculated for TM polarizations (Figure 5.2). It can be observed from these field profiles that light resonates inside the structure prior to scattering. Its modes are similar to whispering gallery type resonances [98,99]. Unlike the first mode, the second and third modes exhibit narrow resonances.

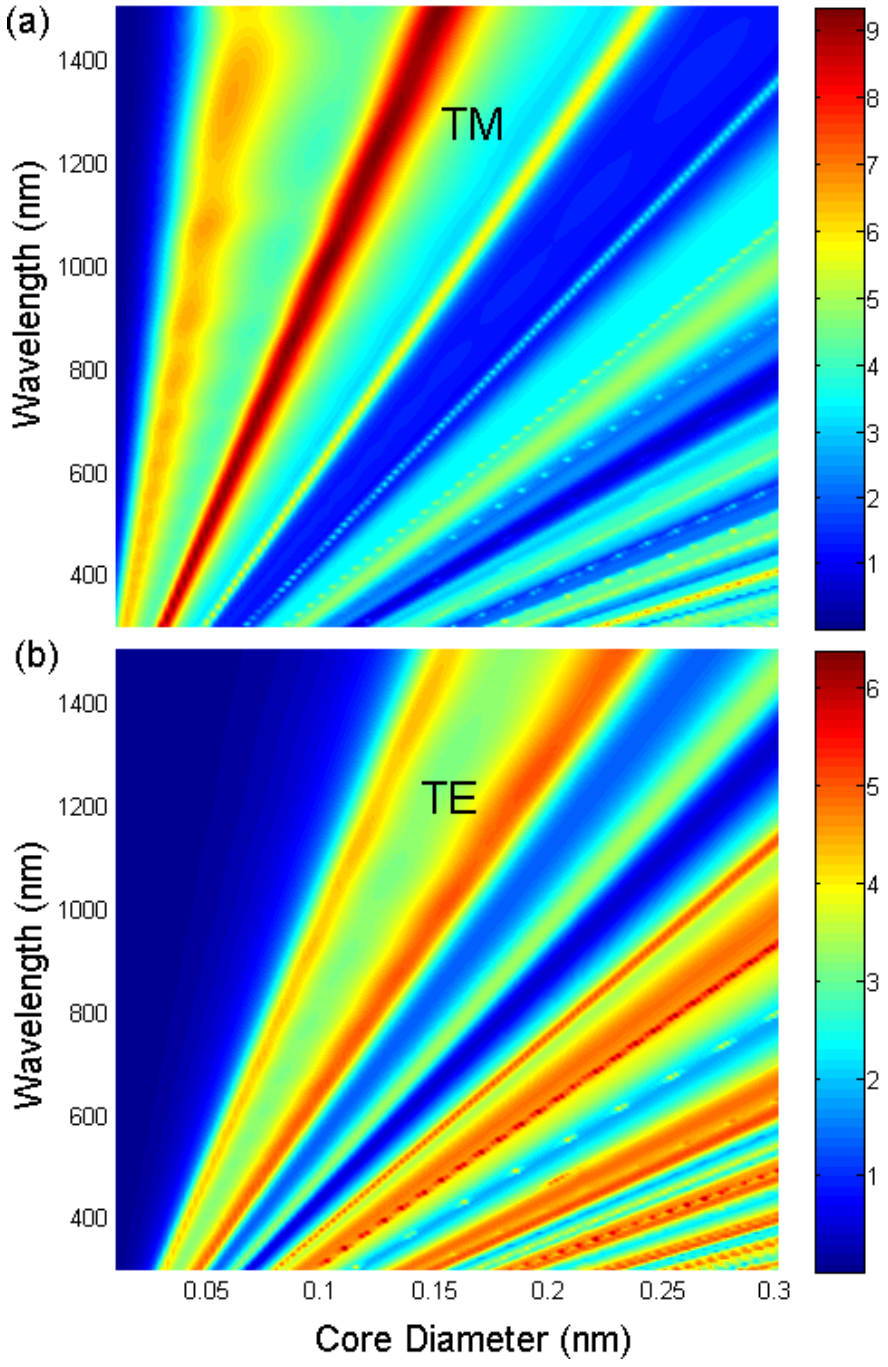

Figure 5.1: Map of resonant Mie scattering in core-shell nanowires. FDTD simulations are performed for (a) TE and (b) TM polarizations. Different resonant modes supported for both polarizations.

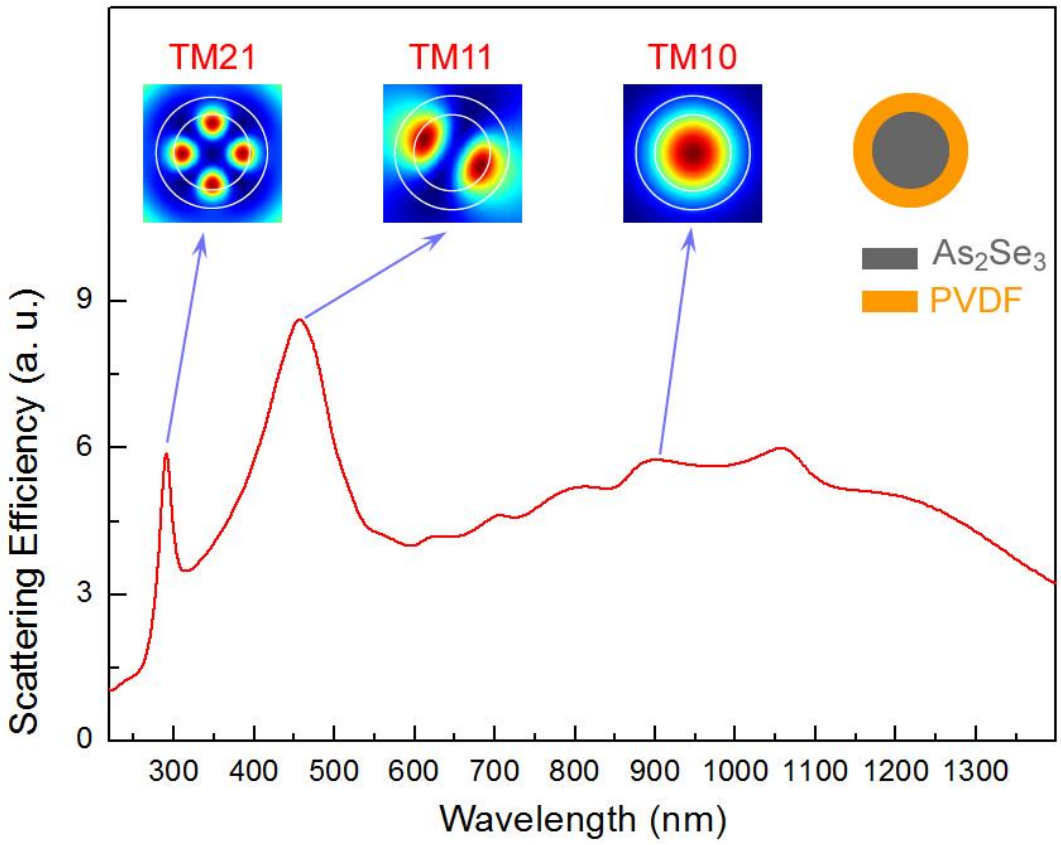

Figure 5.2: Mie scattering from cylindrical core/shell nanowires. Scattering from a 100 nm core and 25 nm shell structure was analyzed by FDTD simulations to demonstrate the modes supported by the nanostructure geometry. The fundamental mode (TM_{10}) and higher order modes (TM_{11} and TM_{21}) were present within the calculated geometry

We can roughly predict the resonant scattering wavelength from the equation $m\lambda/n_{eff} = \pi d$, where m = 1, 2, ..., λ is the free space wavelength of incident light, n_{eff} is the effective refractive index, and d is the diameter of the nanowire. For instance, a nanowire with a diameter of 175 nm would exhibit a scattering peak at 695 nm, as shown in Figure 5.2.

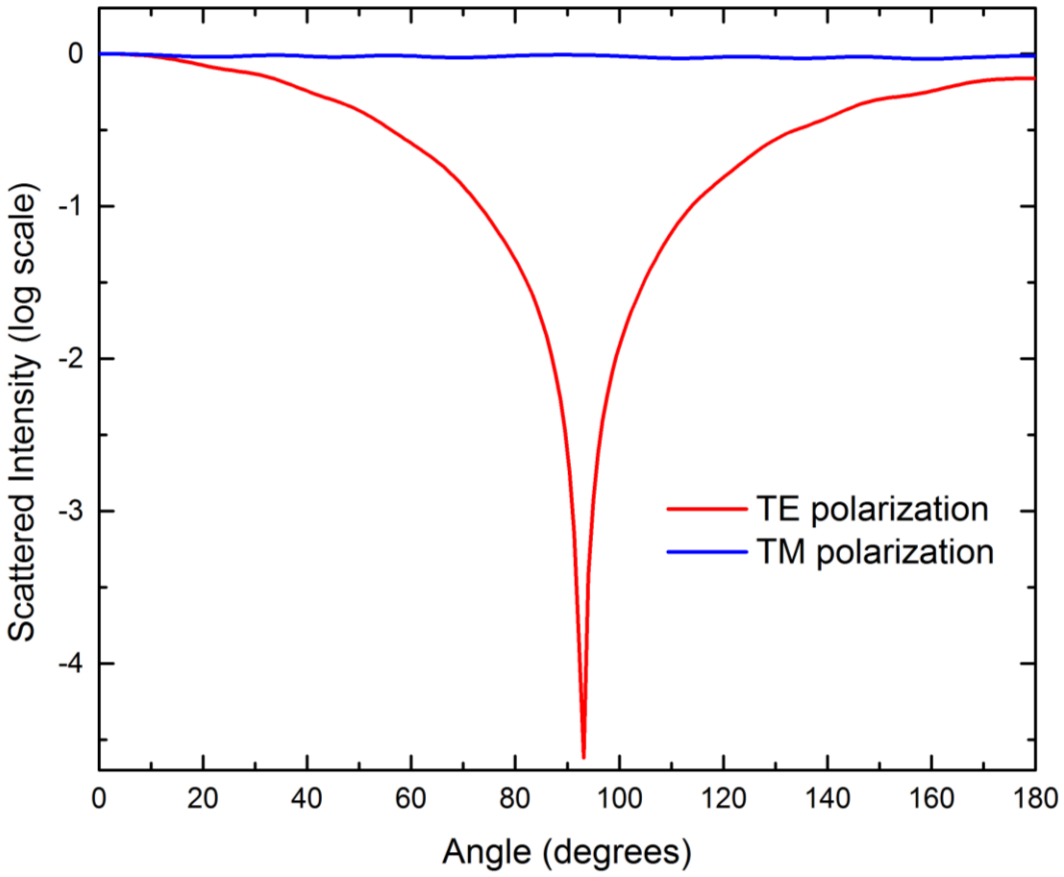

Figure 5.3: Far-field profile of scattered light for resonant Mie scattering. For TM polarized light, the nanostructure isotropically scatters light. In TE polarization, light is mostly scattered in the back and forward directions.

By using the above-described formula, we obtain a n_{eff} of 2.65 (for m = 2), which is close to the refractive index of As_2Se_3 core (2.95) at this wavelength (see Figure 2.5). A lower n_{eff} value is expected, because the TM_{11} mode is not exclusively confined to the high-index core region. The scattering efficiency and resonance wavelength can be directly calculated from Lorenz-Mie theory for unpolarized incident light. For unpolarized light, scattering efficiency can be expressed as;

$$Q_{sca}(x) = \frac{1}{x}\sum_{n=-\infty}^{n=\infty}(|a_n|^2 + |b_n|^2)$$

where $x = kd$ and the scattering coefficients a_n and b_n are obtained by solving Maxwell's equations with boundary conditions at interfaces. In Chapter 4, I describe the derivations of coefficients a_n and b_n for both TE and TM polarizations.

Far-field plots reflect the behaviour of the scattered light at a long distance from the scattering particle, which is useful for experimental measurements (which frequently satisfy this condition). Far-field plots for resonant Mie scattering show that light is isotropically scattered in the first mode of TM polarization, with its resonance concentrated on the core of the structure. In TE polarization, light scattering is in the forward and backward directions, which corresponds to the second order of resonance (Figure 5.3).

5.2.2 Scattering from Core-shell Nanospheres

The Mie scattering properties of spherical structures are studied extensively in the literature [100,101], and are of substantial importance in many areas in optics. In this work, I detail the investigation and characterization of Mie scattering from a high refractive index core coated with a PVDF shell. As with core-shell nanowires, I have run a set of simulations and plotted maps of resonant Mie scattering from coated spheres to characterize the resonant modes of these nanostructures. Unlike nanowires, Mie scattering from core-shell nanospheres is independent of polarization as expected from spherical symmetry (Figure 5.4a). It must be stressed that no supporting mode exists for Mie scattering in the visible range for PVDF-coated spheres below 70 nm in diameter. Near field profiles of the first three modes clearly

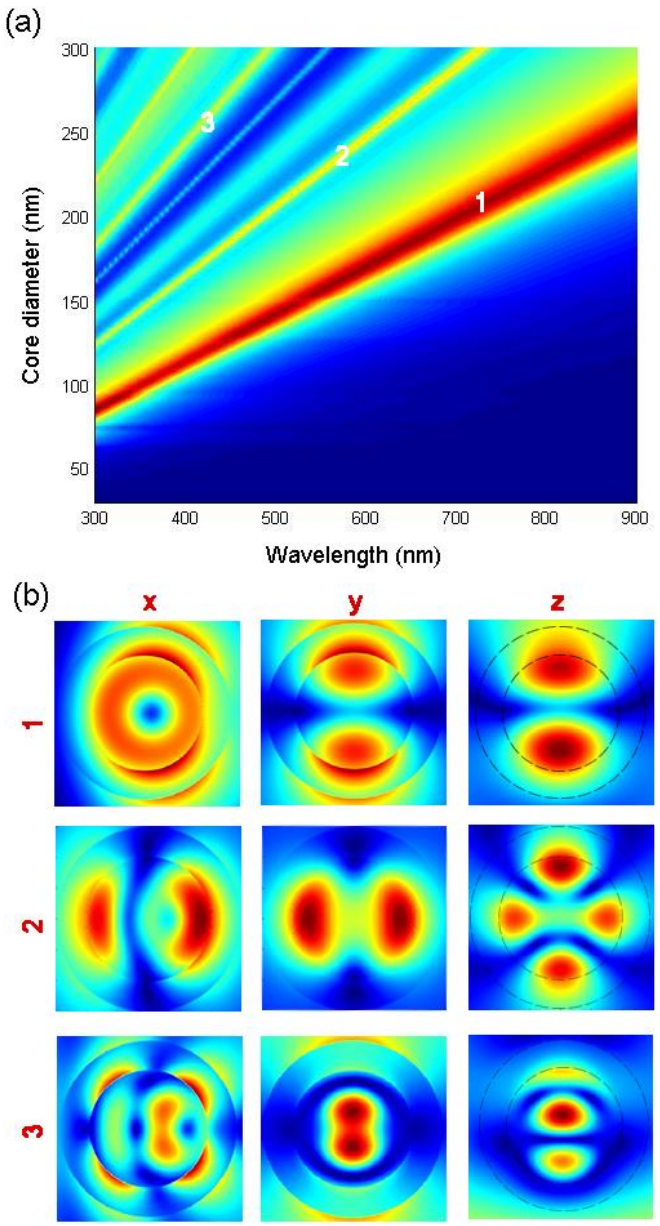

Figure 5.4: FDTD-simulated map for resonant Mie scattering and near field profiles of core-shell nanospheres. (a) Scattering map describing the positions of the first three resonant modes. (b) Near field profiles of the first three resonant modes as observed from x, y and z axes. Fields are localized inside the nanostructure and exhibit a leaky-mode behavior.

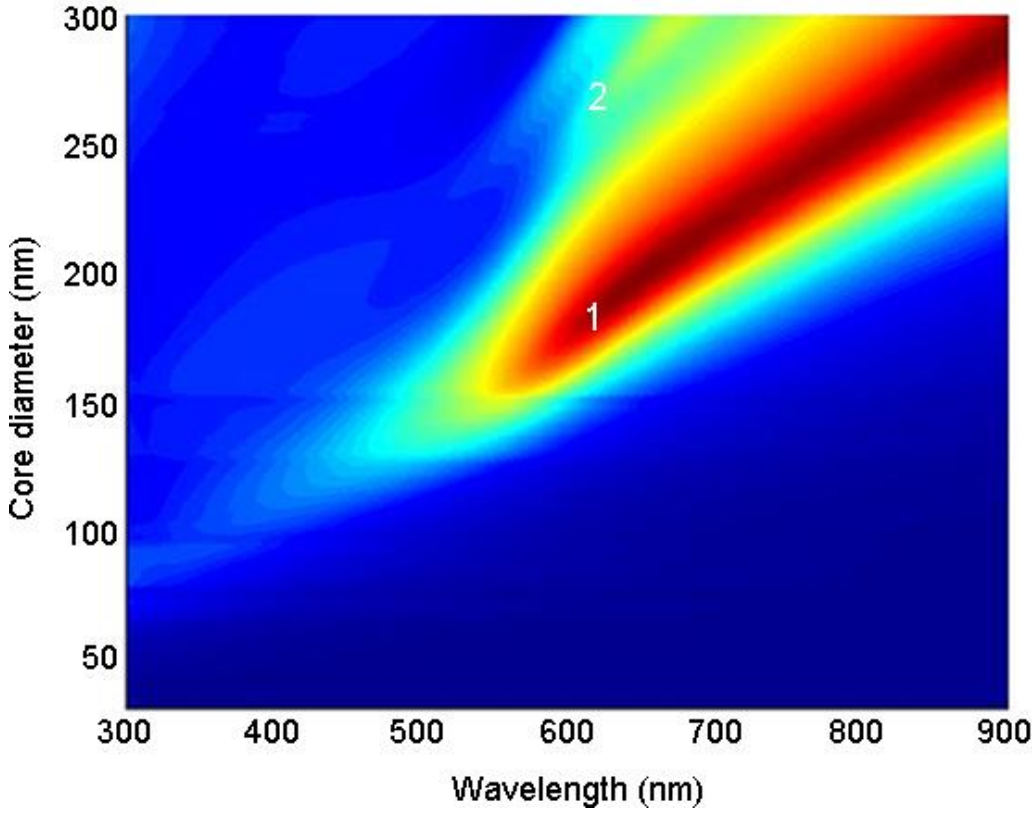

Figure 5.5: Map of resonant Mie scattering calculated using real material parameters. Higher orders were observed to disappear, likely due to the higher optical density of arsenic selenide in the smaller wavelengths of the visible region.

represent the resonant profiles inside the nanostructure and display a leaky-mode resonance behavior (Figure 5.4b), which is associated with the selective scattering of light in a specific wavelength depending on particle size. For theoretical investigation, scattering maps are calculated assuming a constant refractive index and negligible absorption. Near field profiles are observed from all three axes. Here, the axes x, y, and z correspond to magnetic field, propagation vector and electric field, respectively. In order to observe near field profiles, a core diameter of 150 nm was selected for the simulation of Mie scattering.

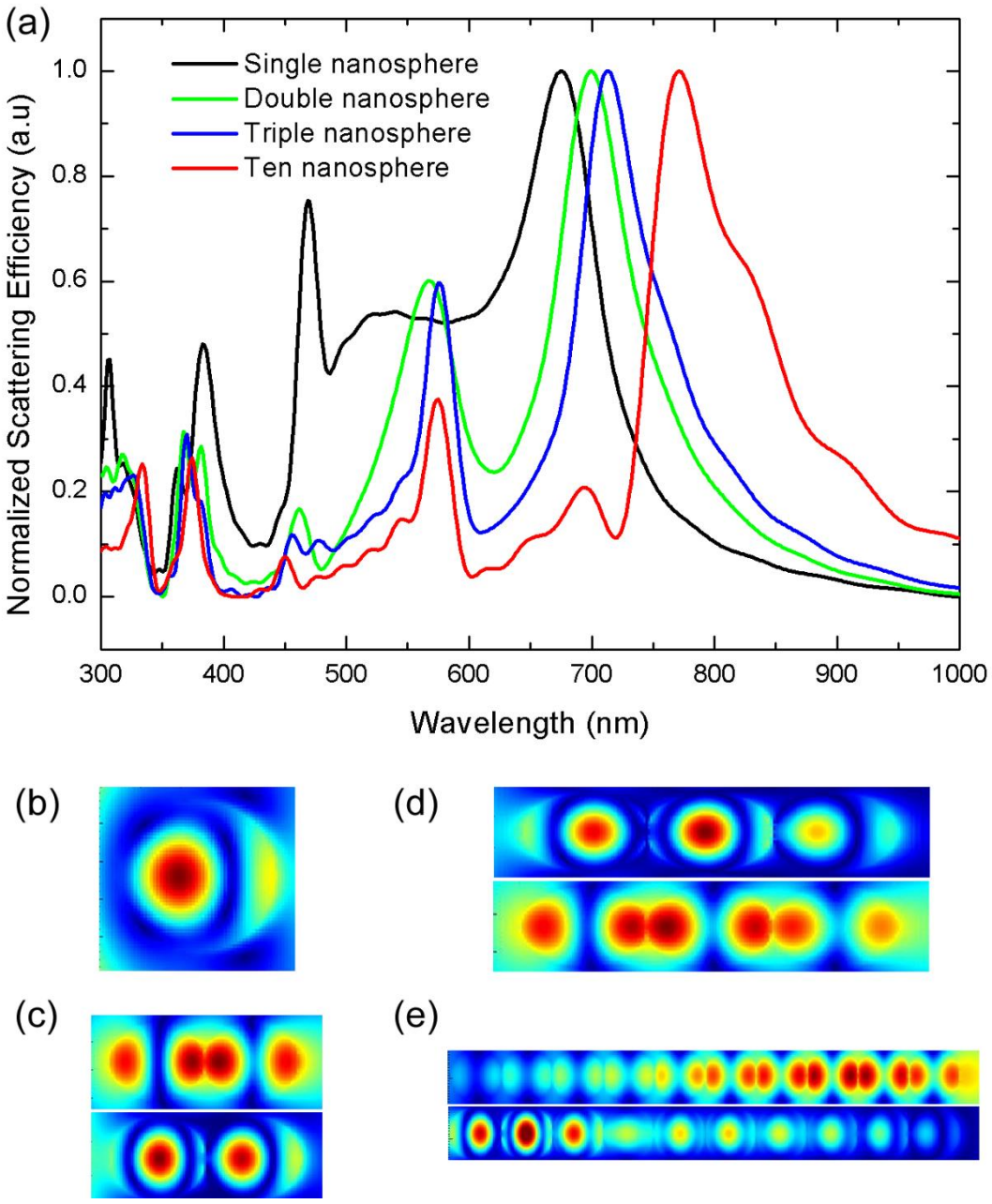

Figure 5.6: (a) Coupled cavity features of a nanosphere array. Waveguides produced by individual spheres exhibit coupled cavity features. (b) Near field profile of scattering modes demonstrate that light can propagate through the spheres by using these modes.

The use of real material parameters results in major decreases in scattering efficiency for smaller wavelengths, due to absorption by the core. From scattering maps, it can be observed that the lower modes broaden in scattering spectra and higher orders tend to disappear entirely, especially for smaller sizes (blue region of Figure 5.5). This map is particularly useful for the design of colored nanostructures.

Coupled-cavity formation from individual spheres is also demonstrated using a linear array of periodically arranged spheres. It is interesting to note that a red-shift in the first resonance mode was observed with increasing numbers of spheres (Figure 5.6a). After a certain chain length, however, the rate of shift declined and eventually stopped. Near field profiles of the first and second scattering modes show that light propagation occurs through the spheres. These profiles imitate the first and second resonant mode profiles existing in a single sphere (Figure 5.6b).

5.2.3 Scattering calculations for Core-shell Schemes

In addition to core-shell nanowires and nanospheres, many other options are available for core-shell schemes suitable for the observation of resonant Mie scattering. I performed simulations for nanosprings, shell-embedded discrete nanorods and core-shell nanospheres, nanochains and nanowires (Figure 5.7). Unique scattering characteristics were displayed by each of these configurations. Here I consider real material parameters for my simulations, and observe higher scattering peaks in the red part of the visible spectrum. Scattering calculations are simulated for a constant diameter of 200 nm in all cases. A 3 μm-long nanostructure (or series of nanostructures, where applicable) was utilized for all simulations. 250 nm rods with inter-structural distances of 200 nm were simulated to represent shell-embedded rods.

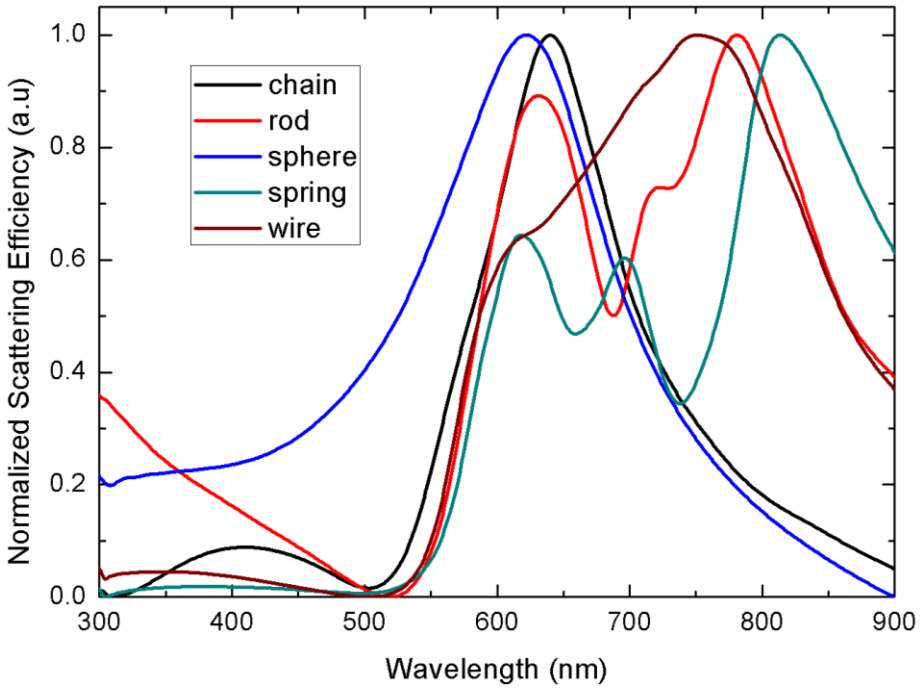

Figure 5.7: FDTD simulation of fabricated nanoschemes. Scattering profiles of each fabricated scheme is simulated for nanostructure diameters of 200 nm. The use of real ellipsometric constants results in the disappearance of higher modes, especially in lower wavelengths where scattering is hindered by absorption by the As_2Se_3 core. Structure lengths are 3 μm for each scheme. 250 nm rods with inter-structural distances of 200 nm were utilized for discrete rod simulations. While all fabricated nanostructures are expected to yield a red-orange color at 200 nm, pronounced differences are present in their scattering characteristics.

It must be stressed that Mie scattering characteristics of nanowires and discrete rods exhibited significant differences, despite their similarity in organization. Nanosprings also displayed interesting scattering properties due to their rotating structure, which led to the production of a non-symmetric structure profile. Nanochains and core-shell nanospheres, which possess same building blocks but different inter-spatial distances, show similar scattering behavior with slight differences in red-shifts and a narrower scattering band in the former.

5.3 Structural Coloration on Glass-Polymer Core-Shell Nanostructures

5.3.1 Measurement Setup

Resonant Mie scattering can be engineered successfully for structural coloring, as the scattering efficiency is adequately high for the observation of coloration even to the unaided observer [33].

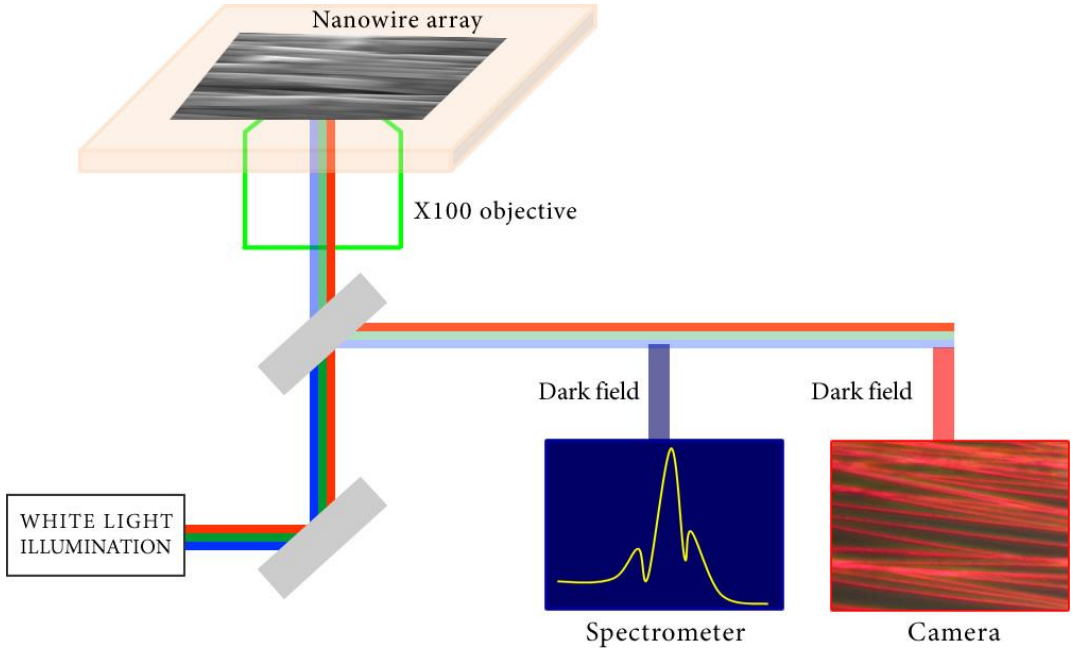

Figure 5.8: Schematics of experimental set-up for scattering measurements from nanowires and nanospheres. The optical image of a nanowire array is shown. Structures with diameters smaller than 200 nm were obtained using the dark field mode of an inverted microscope. The scattering spectrum was taken by a UV-Vis spectrometer coupled to the microscope.

To this end, I use ISR and thermal instability techniques to obtain core-shell nanoschemes displaying large-scale Mie scattering based coloration. Briefly, core-shell nanostructures are dispersed on glass and structures displaying the desired colors are selected for characterization under dark field illumination using an inverted light microscope. Scattered light is collected by a MAYA spectrometer. Optical images of colored nanostructures are taken by a digital camera attached to the microscope. The experimental setup for scattering measurements is shown in Figure 5.8.

5.3.2 Core-Shell Nanowires

Core-shell nanowires produced by iterative size reduction were successfully engineered to display size-dependent structural coloration originating from Resonant Mie Scattering (Figure 5.9a,b). A high-refractive index As_2Se_3 glass was selected as the core material in order to enhance scattering efficiency and make the observation of vivid hues feasible. The size of the core region is one of the main parameters for the determination of scattering characteristics. As the core-shell nanowire diameters decrease, the thickness of the shell region likewise decreases, resulting in very thin shell layers that cannot significantly alter the core-mediated structural coloration displayed by the nanowires. Nanowires in a diameter range of 30-200 nm could span the entire visible spectrum, and primary colors were clearly observed for 175 nm (red), 42 nm (green) and 35 nm (blue) diameter core-shell nanowires following the removal of the PES sheath (Figure 5.10b). Dark field illumination was used in order to increase the resolution of the images. The cross sections of the three core-shell nanowires are shown in the TEM image (Figure 5.10a). The shell layer is barely visible due to smears caused by the ultramicrotome and the low contrast between the PVDF and PES regions.

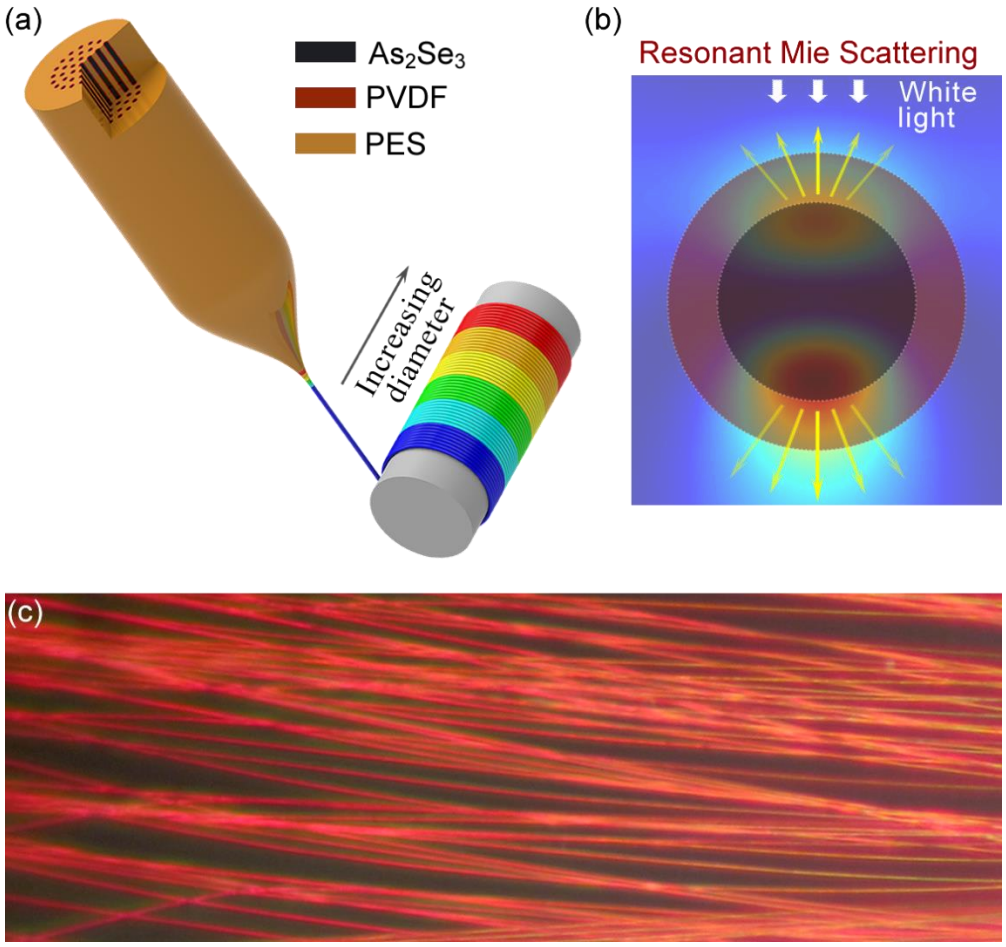

Figure 5.9: (a) A novel thermal size reduction technique is used to obtain indefinitely long, scalable core-shell nanowires. The structure consists of a high-dielectric semiconducting (As_2Se_3) core, a piezoelectric polymer (PVDF) shell and a high-temperature thermoplastic (PES) cladding. The structures show native structural coloration based on their size-dependent properties. (b) Core-shell structures, when scaled down to a diameter range between 30-200 nm, show resonant small particle scattering. Mass-produced, indefinitely long and large-area core-shell nanowire arrays can be colored by (c) Mie scattering .

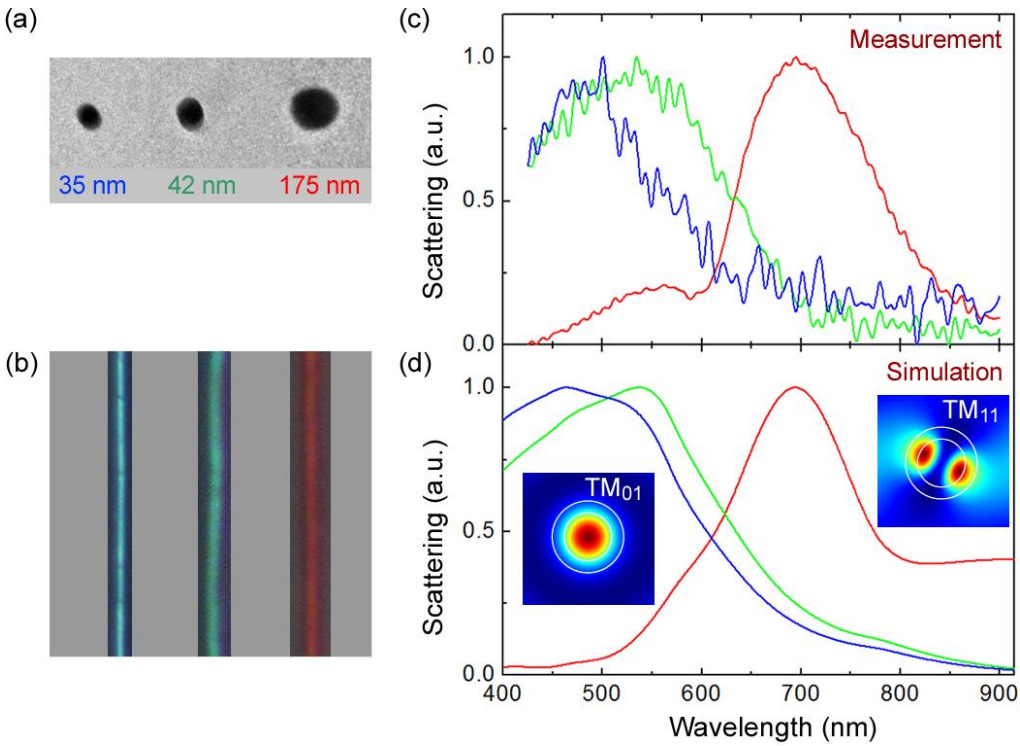

Figure 5.10: (a) TEM images of polymer embedded As_2Se_3/PVDF core-shell nanowires. (b) Size-dependent Mie scattering from 35 nm (blue), 42 nm (green), and 175 nm (red) core-shell nanowires. (c) Spectroscopic dark field scattering measurements from these three core-shell nanowires show size-dependent resonant peaks at 470 (blue), 530 (green), and 700 (red). (d) Numerical FDTD calculations of scattering from these nanowires agree well with the measurements. Inset: Resonant modes are identified using FDTD simulations. In the calculations, I used wavelength-dependent refractive indices and extinction coefficients obtained from spectroscopic ellipsometry measurements.

Spectra measured from three colored nanowire types are shown in Figure 5.10c. Three resonant Mie scattering peaks were observed at 470 nm (blue), 530 nm (green) and 700 nm (red). FDTD simulations reproduce the measurement peaks, confirming the resonant scattering effect within the core-shell nanowires (Figure 5.10d) for TM polarized light. Blue and green peaks are attributed to the TM_{10} resonance mode, while the red peak is attributed to the TM_{11} mode. The scattering efficiency of TE polarization is known to be smaller compared to the TM polarization. In my

experiments, shoulder peaks observed to the left of the red peak are calculated to be the low-efficiency TE_{11} resonant peaks, which do not effectively contribute to coloration. The increasing noise in the scattering intensity in Figure 5c is due to absorption by the As_2Se_3 core.

5.3.3 Core-Shell Nanospheres

As nanospheres are well-characterized in Mie theory and find widespread application in nanoscale optics, I investigated their scattering properties by analytical, simulation and experimental data. I tailored the first mode for selective scattering of light, which is independent of polarization and displays vivid hues with linear dependence on particle size (Figure 5.5).

Colored core-shell nanospheres span the whole visible spectrum within the size range of 100-250 nm, with larger sizes corresponding to higher wavelengths (Figure 5.11a). The thermal basis of the fabrication technique results in a high uniformity and smoothness, which prevents size-dependent shifts in scattering spectra and allows the production nanosphere arrays displaying uniform large-area coloration. Experimental data were collected from large-area nanostructures (Figure 5.11b) and FDTD calculations were performed for nanospheres with average core diameters of 130 nm, 170 nm and 220 nm, corresponding to blue, green and red coloration, respectively. Scattering from core-shell nanospheres can also be expressed by using Lorenz-Mie formalism. To this end, I used analytical equations for expressing resonant scattering from core-shell nanospheres. Here I insert real (n,k) values in order to compare obtained results with FDTD simulations, using nanospheres with core diameters of 140, 170 and 220 nm.

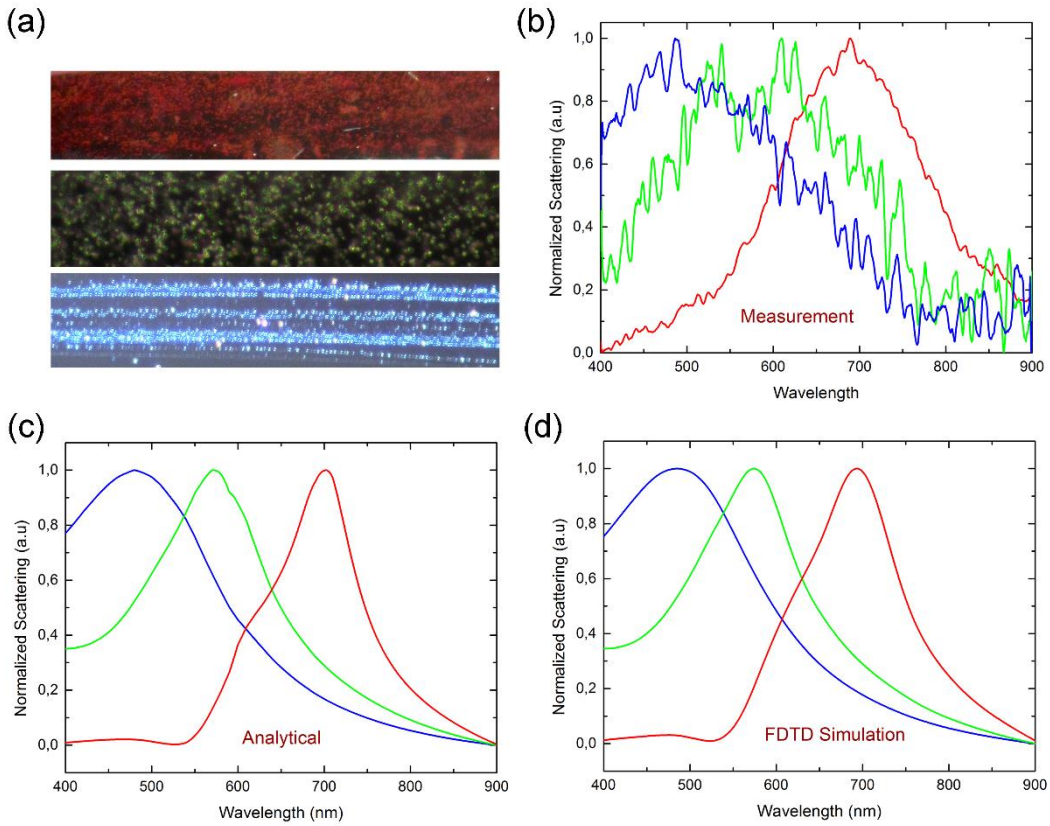

Figure 5.11: Large-area core-shell nanosphere arrays engineered for blue, green and red hues, with average diameters of ~130, 170 and 220 nm, respectively. (d) Scattering from colored nanostructures measured by inverted dark-field microscopy. (e) FDTD simulation technique used for the verification of experimental results. (f) Analytical solutions for light scattering from spherical core-shell nanostructures modeled with Lorenz-Mie theory. Analytical and simulation results overlap, and are consistent with measurement data. Collective scattering from large area spheres with narrow size distributions result in uniform coloration and small shifts in scattering spectra. Ellipsometric material parameters were used in FDTD and analytical calculations.

Observed experimental data are in good agreement with FDTD simulation results, and I likewise find my FDTD calculations and analytical results to be in agreement for the diameters tested (Figure 5.11c,d). In addition, experimental findings are in line with theoretical calculations if we ignore collective scattering from large area sphere arrays.

5.3.4 Large-Area Coloration on Core-Shell Nanoschemes

I show the optical potential of fabricated core-shell dielectric nanostructures by engineering a variety of different nanoschemes for large-area coloration (Figure 5.12a-f). The coloration of core-shell nanostructures primarily depends on the size of the core material, since the PVDF nanoshell and the PES polymer sheath bear low refractive indices and have a negligible effect on hues. The monochromatic coloration of nanostructures produced by described combined ISR-thermal manipulation technique highlights a potential area of application for the fabrication method. Configuring large-area arrays of in-fiber nanospheres, nanosprings, shell-embedded nanorods and nanospheres, and nanochains for coloration is a particularly remarkable ability, and is difficult to replicate using other fabrication techniques. High uniformity and smoothness is paramount for large-area coloration and result in size-dependent color shifts when compromised. Present fabrication method is able to eliminate such errors, suggesting that it is capable of meeting the stringent structural demands inherent to many optical applications. The nanostructures are therefore suitable for large area, in-fiber, flexible surface applications, but it must be noted that physical contact between the nanofeatures inside the shell may induce color shifts via optical coupling. As such, large distances between the in-fiber structures are necessary for adequate coloration.

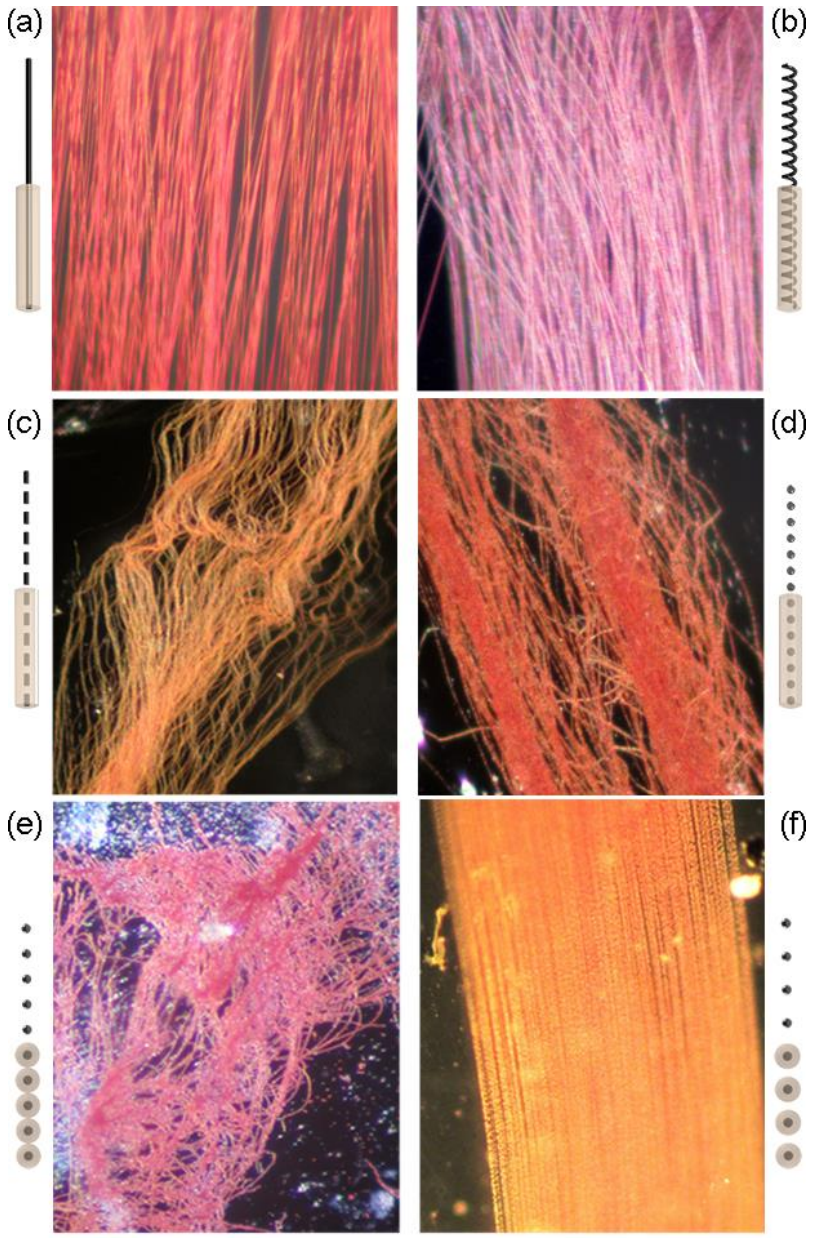

Figure 5.12: Large-area in-polymer coloration of globally oriented nanostructures. Resonant Mie scattering-based coloration is observed on various fabricated nanoschemes. High uniformity and smoothness is paramount for large-area coloration, and result in size dependent color shifts when compromised. Present fabrication method is able to eliminate such structural errors (a-f). Sizes are ~200 nm for all cases.

Chapter 6

NRM Scattering

6.1 Non-Resonant Mie Scattering

Light-matter interactions depend strongly on both intrinsic and extrinsic properties of the interacting material and can result in a wide variety of optical phenomena, most of which are explained by the Mie theory. Examples of optical interactions within the domain of Mie theory include light scattering from particles with high refractive indices and sizes smaller than the wavelength of the incident light, which occurs via the resonant form of Mie scattering and has been discussed in Chapter 5. In addition, Mie theory also encompasses the confinement of light into deep-subwavelength structures via cluster oscillations of free electrons, which is most pronounced in metallic nanostructures, and the observation of resonant absorption effects in high-index semiconductors. All of the above optical mechanisms are associated with a number of unique applications in nanophotonics [102,103,104,105]. However, the interaction of light with low refractive-index nanomaterials, [106,107] such as polymers and some glasses, is not very well-

investigated, and its characterization may reveal many unknown and potentially distinctive optical features.

Throughout the present work, I emphasize the optical applications of polymers that are cheap, flexible and easy to produce in large scales. However, one-dimensional nanoscale polymer structures are not used as frequently as their macro-scale counterparts. Polymers lack many desirable optical and optoelectronic features displayed by metals and semiconductors, and this deficit is especially pronounced in photonics. Despite their disadvantages, however, polymer nanostructures have been utilized for several photonics applications [108,109,110] so far, including in sensors, organic light-emitting diodes (OLEDs), field-effect transistors (FETs) and lasing. Such applications primarily rely on the intrinsic features of polymers, and little work has been performed on how the extrinsic properties of polymer nanostructures alter the optical effects associated with these materials.

In this chapter, I report that effective Mie scattering can occur in a specific region characteristic to polymer materials, and potentially other low-index wavelength-scalable nanostructures. Decreases in the refractive index of a resonant dielectric nanostructure, when complemented with increasing nanostructure diameters, lead to the creation of a region where light is forced to scatter from the core region as opposed to resonating within it. In this special region, the scattering of light is markedly different from high-index and deep-subwavelength scattering phenomena. This behavior can be interpreted as a transition from resonant scattering to the non-resonant region of Mie scattering.

At scales below the wavelength of the incident light, particle sizes may have significant effects on scattering behavior (Figure 6.1a). The interplay between the refractive index and the radial size of the scattered particle results in variable scattering properties. In addition, scattering from deep-subwavelength and high-refractive index materials, such as chalcogenide glass and silicon, may induce leaky mode resonant behavior.

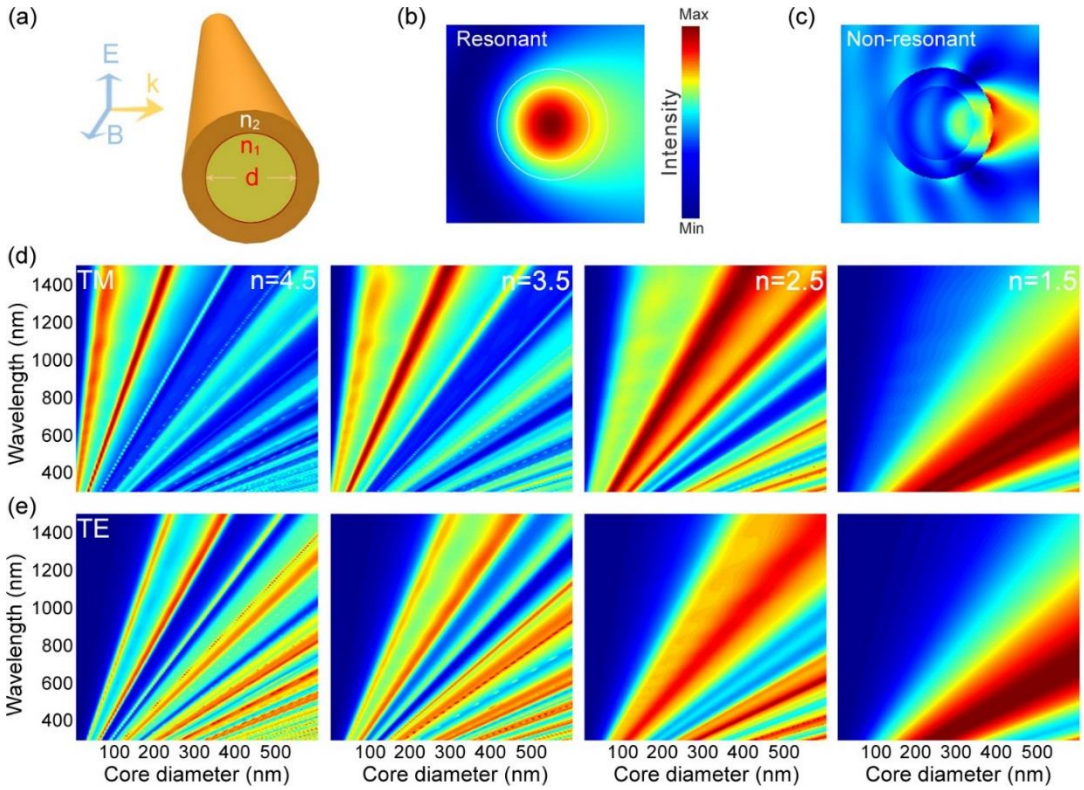

Figure 6.1: Mie scattering from nanostructures. (a) Schematic illustration of light scattering from core-shell nanostructures. Near-field profiles for scattered fields of (b) resonant and (c) non-resonant regimes. In the resonant regime, light confines within nanowire and is then scattered in a leaky mode. However, for low-refractive indices, light cannot be trapped inside nanowires and is instead scattered in the forward direction. (d-e) The transition from resonant to non-resonant Mie scattering regimes can be observed by reducing the refractive index of the nanostructure. While changes between the modes of TE and TM polarizations is observed in higher refractive indices, scattering maps are nearly identical for the low refractive index medium for both polarization types.

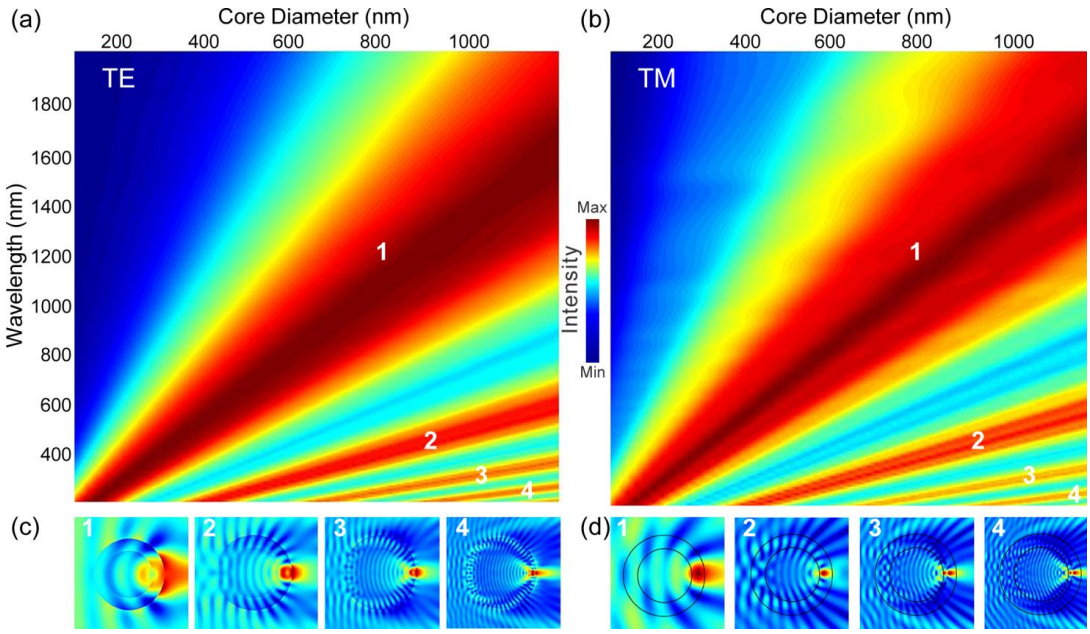

Figure 6.2: NRM scattering maps of core-shell polymer nanowires for (a) TE and (b) TM polarizations. Extending the wavelength and diameter ranges for a fixed *n* of 1.5 in Figure 6.1d,e results in the appearance of lower orders. Electric field profiles of corresponding orders of (c) TE and (d) TM polarizations exhibit strong directional scattering. Field profiles confirm the non-resonant nature of the NRM scattering regime.

In optics, resonance behavior occurs when the incident light is trapped inside the structure, as in whispering gallery modes or resonant Mie scattering (Figure 6.1b). Fabricated nanostructures, however, display non-resonant behavior, which can be inferred from near field profiles of scattered light from a low-index core-shell nanowire geometry (Figure 6.1c).

In non-resonant Mie scattering, light is scattered at specific wavelengths depending on the diameter of 1-D nanostructures. Size-dependence and the broad scattering peaks of this phenemonon are reminiscent of thin-film interference, which relies on multiple reflections or refractions from the boundaries of different media. NRM scattering can be considered to be analogous to this effect. While thin-film

interference is thickness-dependent, its nature is also non-resonant in low-refractive index materials, and resembles NRM scattering in that light interacts with the structure but does not oscillate within in both cases.

The properties of NRM scattering are significantly different than those of resonant Mie scattering. The NRM region is characterized by coupling-free and polarization-independent light scattering in the forward direction, which is very critical for certain applications.

The transition from resonant to non-resonant regimes of Mie scattering can be observed by reducing the refractive index of the nanostructure (Figure 6.1d, e). While splitting is observed between TE and TM polarizations modes in higher refractive indices, scattering maps are nearly identical in low refractive index media for both polarization types. Detailed analysis of NRM scattering can be performed by analyzing the behavior of other orders in this region, as well as their field profiles. Lower orders of TE and TM polarizations appear in extended diameter and wavelength ranges (Figure 6.2a,b). For both polarizations, lensing effect can be observed in the forward-scattered and non-resonant field profiles of lower scattering orders (Figure 6.2c,d). Unlike the first order, subsequent scattering peaks are very narrow.

In Mie scattering, particle sizes are comparable to the wavelength of the incident light. If the diameter to wavelength ratio exceeds 10, geometric optics is generally sufficient to explain the interactions between light and the particle. For example, the fourth scattering order in my calculations appears in the ~200 nm wavelength region for a structure with core diameter of ~1200 nm, which means that the structure is ~6 times larger than the wavelength of light (Figure 6.2a,b). Therefore, higher orders do not fall within the Mie scattering zone. As a matter of fact, light-matter interactions after this point are not classified as scattering. However, many spherical and toroidal microresonators benefit from the higher modes of this system.

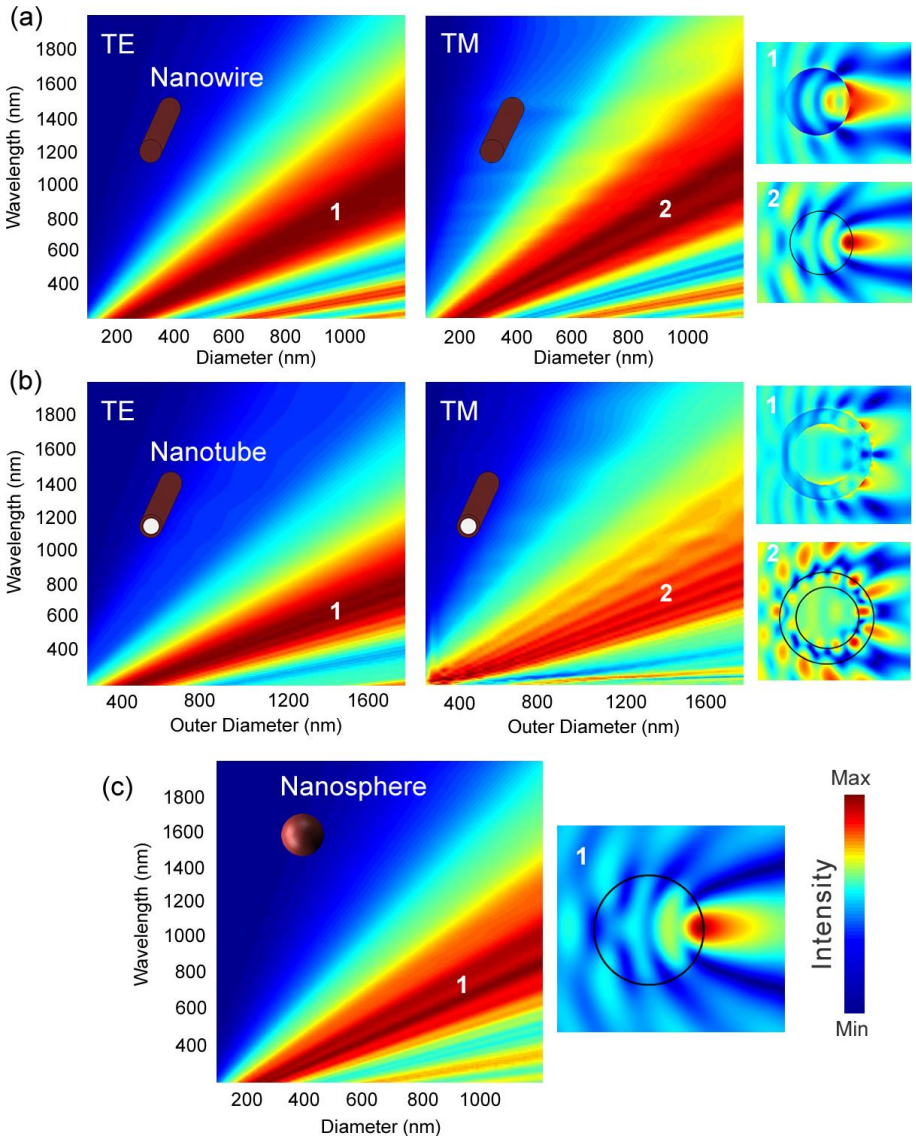

Figure 6.3: NRM scattering in various geometries. (a) NRM scattering in bare nanowires. Electric field profiles of first order of TE and TM polarizations exhibit forward scattering behaviour, as would be expected. (b) Nanotube geometry is another interesting structure for the observation of this scattering regime. Field profiles of NRM scattering from this geometry differ slightly from the nanowire case, although they also exhibit forward scattering behavior. Nanotubes are one of the most favorable geometries in microfluidics, and NRM scattering is therefore promising in this field. Inner/outer diameter ratio of the nanotube is 1:1.5 for all calculations. (c) For sphere geometry, non-resonant field distribution verifies forward-scattering feature as in 1D nanostructure cases.

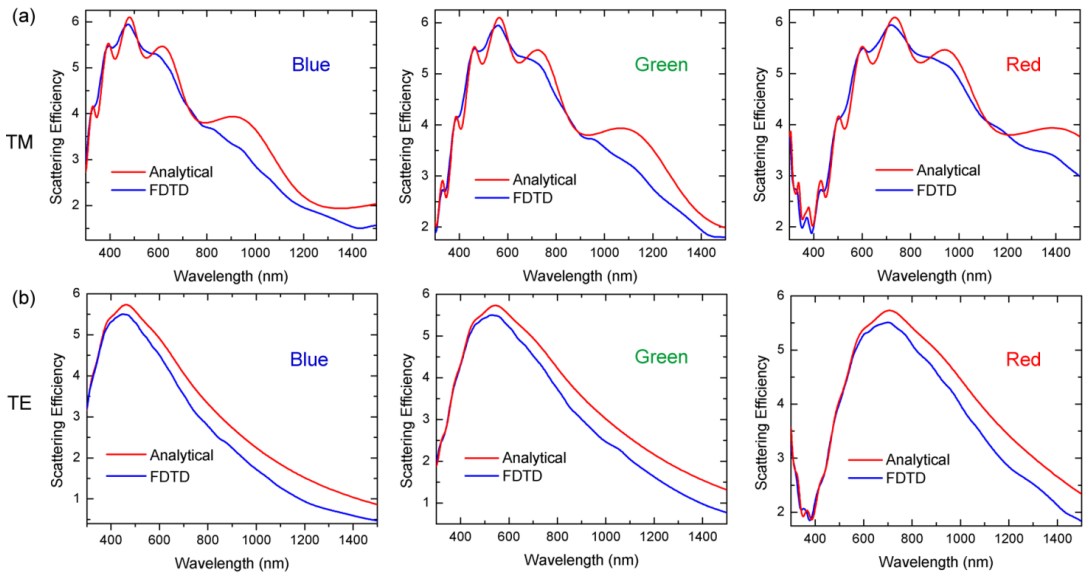

Figure 6.4: Comparison of analytical solutions with FDTD simulations. Analytically solved scattering equations for both (a) TE and (b) TM polarizations were compared with FDTD simulation results. The method used for analytical solutions is based on vector wave harmonic expansion of scattered light. Simulated results are in good agreement with theoretical calculations. Nanowires used for comparison have core diameters of 340, 400, 520 nm for blue, green, and red coloration, respectively.

I used core-shell geometry in above calculations due to its practical simplicity in fabrication stage. Refractive index of the shell layer represents PVDF polymer and does not affect optical properties of both resonant and non-resonant case. In other words, same results hold for bare nanowires (Figure 6.3a). Non-resonant Mie scattering applicable in diverse set of nanostructures. Nanotube is one of the outstanding geometry that fall into this set. Scattering from this geometry results with narrower peak compared with nanowires. Electric field profile of it is non-resonant but diffused somewhat (Figure 6.3b). Scattering from subwavelength nanotube geometry can be used in microfluidics for sensing applications. I also investigated scattering features of low-index and subwavelength spheres. They have similar non-resonant features as well, even scattering is fully independent from polarization (Figure 6.3c).

Scattering of light from 1-D nanostructures can also be expressed analytically. To verify analytical results derived for TE and TM polarizations, I compared these results with my FDTD simulations. Results are plotted for three different core-shell sizes corresponding to red, green and blue coloration. Analytical and FDTD results are found to be in good agreement (Figure 6.4). Analytical equations solved for core-shell nanowires are also applicable for nanotube and bare nanowires, if the refractive indices are set to reflect the schemes in question (e.g. bare nanowires can be simulated by assuming a "shell region" with the refractive index of air).

6.2 Optical Properties of NRM Scattering

This scattering regime has several important optical features. First of all, NRM scattering exhibits coupling-free behavior. Side-by-side nanostructures do not change the peak position of scattered light (Figure 6.5a). Their intensity field profiles remain non-resonant and the lensing behavior is unchanged in the scattered field. Therefore it is suggested that this mechanism is appropriate for large-scale applications. This property is also present in bare nanowires (Figure 6.6c,d). However, in resonant Mie scattering, scattered light is significantly affected by the adjacency of particles, and this is undesirable in many practical cases [111].

Coupled-cavity resonance [112] is an interesting optical phenomenon that is generally observed in resonant systems. In coupled nanowires, the main scattering peak at 650 nm splits into two peaks at 450 nm and 1060 nm (Figure 6.5b). The scattering preserves its non-resonant nature for the low energy peak at 1060 nm (see the field profile in Figure 6.7c). The higher energy peak at 450 nm displays coupling behavior, where the electric field is concentrated between two nanowires (see the field profile in Figure 6.7d).

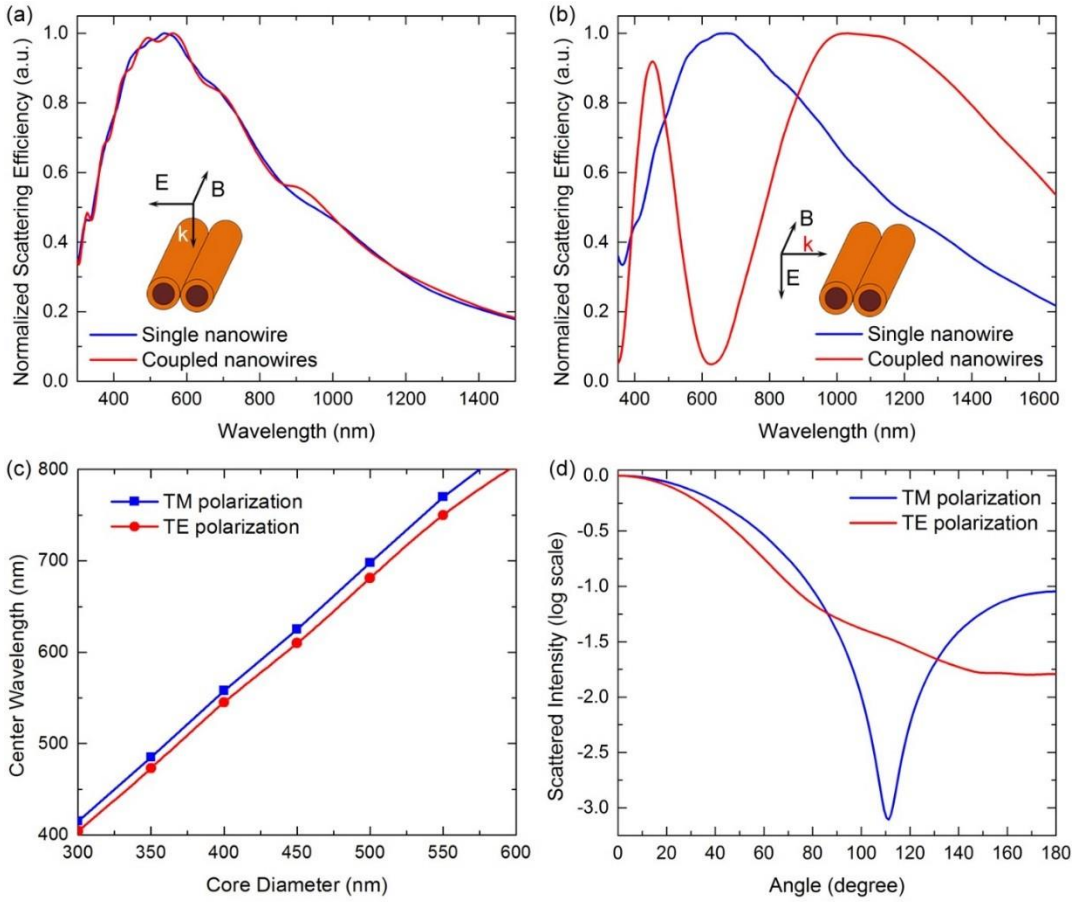

Figure 6.5: Optical properties of NRM scattering. (a) Coupling-free scattering can be obtained for illumination perpendicular to the coupling axis (as shown in the inset). (b) Mode splitting is observed when light is incident on coupled nanowires. (c) Scattering from low refractive index nanostructures displays a polarization independent behavior. (d) Far-field intensity profiles indicate that light mostly scattered along the forward direction. Very high forward to backward scattering ratios are obtained for both polarizations.

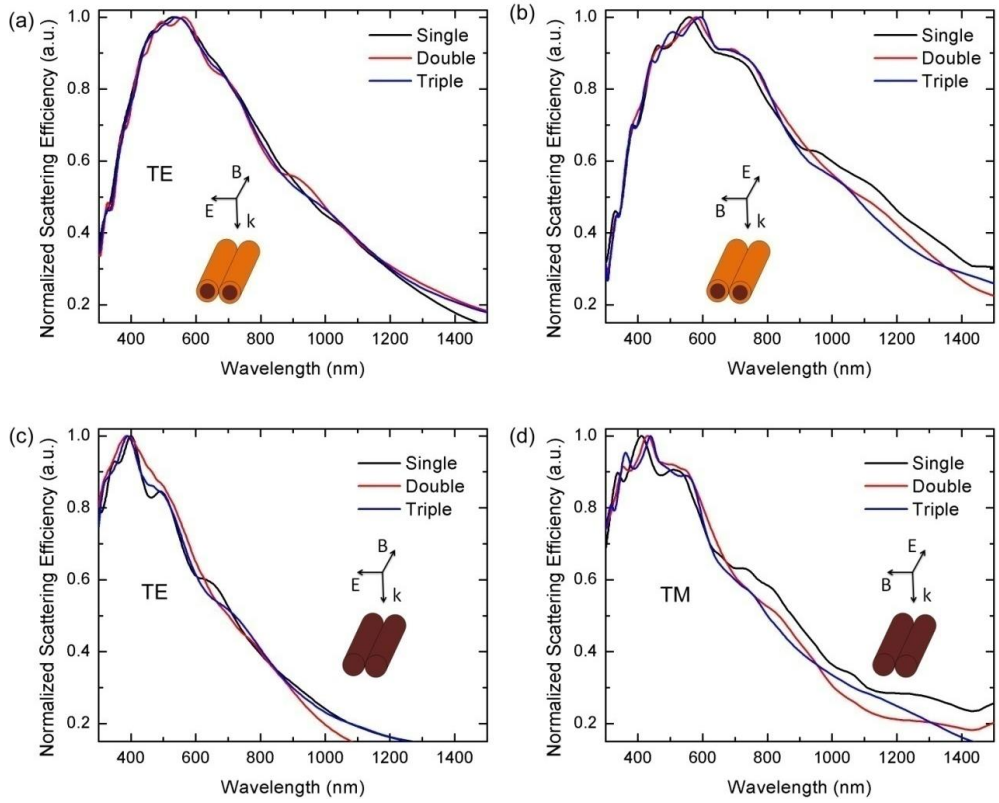

Figure 6.6: Coupling-free scattering. Side-by-side nanowires do not induce optical coupling, which is markedly different from resonant Mie scattering. For both (a) TE and (b) TM polarizations scattering spectrum is unaffected from number of side-by-side core-shell nanowires. Same results hold for bare nanowires (c,d).

Non-resonant light scattering in fabricated nanowires is also found to be polarization-independent (Figure 6.5c), which is critical for various applications such as thin-film photovoltaics. There is a very small shift of 10-20 nm, between the scattering peaks of TE and TM polarizations. However, light scattering becomes a linear function of diameter and this shift disappears for unpolarized scattering, which is obtained by averaging the two polarization peaks. This observation also holds for lower orders of NRM scattering. The extent of resonant scattering, for example, strictly depends on type of polarization (Figure 6.1c,d).

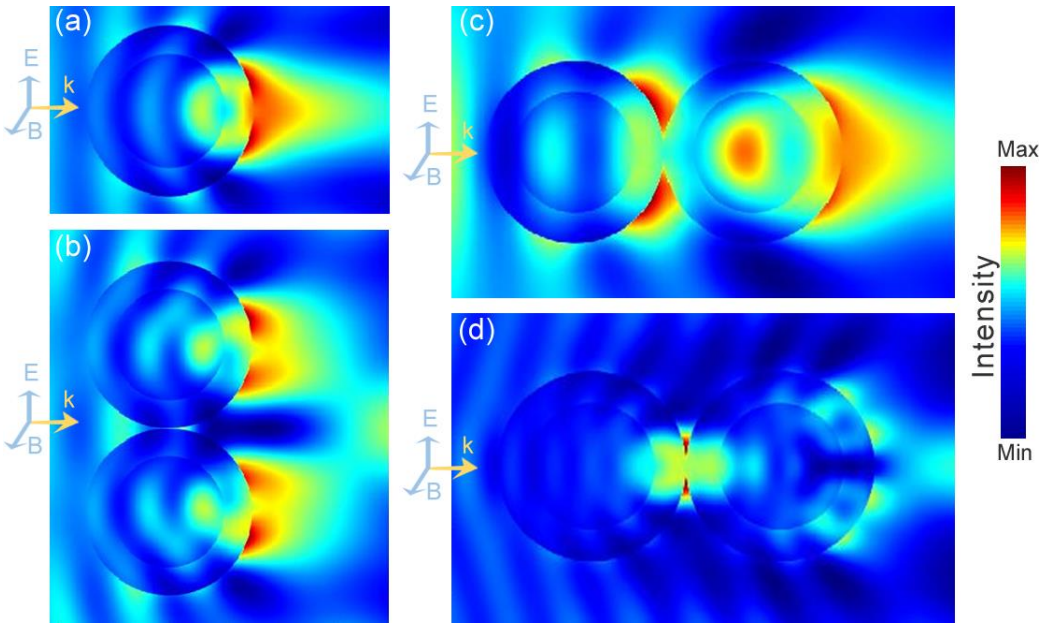

Figure 6.7: Field profiles of coupled nanowires. (a) Near field profile of scattering from a single core-shell nanowire. (b) The field profile corresponds to a 550 nm peak in Figure 6.5a. Electric field distribution within the core-shell structure is almost unaffected from the number of nanowires that are arrayed side-by-side. (c-d) Scattered light exhibits coupled cavity behavior in overlapping nanowires. Profiles in (c) and (d) correspond to 1060 nm and 450 nm peaks in splitting, respectively shown in Figure 6.5b.

Another important property of this new regime is the strong forward scattering observed in both polarizations (Figure 6.5d). Forward to backward scattering intensity ratio exceeds 50, which is markedly different from resonant Mie scattering (for which the ratio in question is around 1). As the scattering of light is mainly in the forward direction, this feature can be utilized in applications where the trapping of light is required. It is interesting that there is almost no scattering in the sidelong direction for both polarizations. This explains why nanowires are coupling-free when arranged side-by-side, but strongly affected when overlapped.

6.3 Coloration on All-Polymer Core-Shell Nanowires

Structural coloration is observed in free-standing nanowires with diameters below 600 nm. To obtain free-standing nanowires, the supporting layer is etched with DCM. Since the shell layer is resistive to DCM, it protects the core region from this etchant, provided that the etching durations are kept sufficiently short. Red, green and blue colors are selected among dispersed core-shell nanostructures for characterization under bright field illumination using an inverted light microscope.

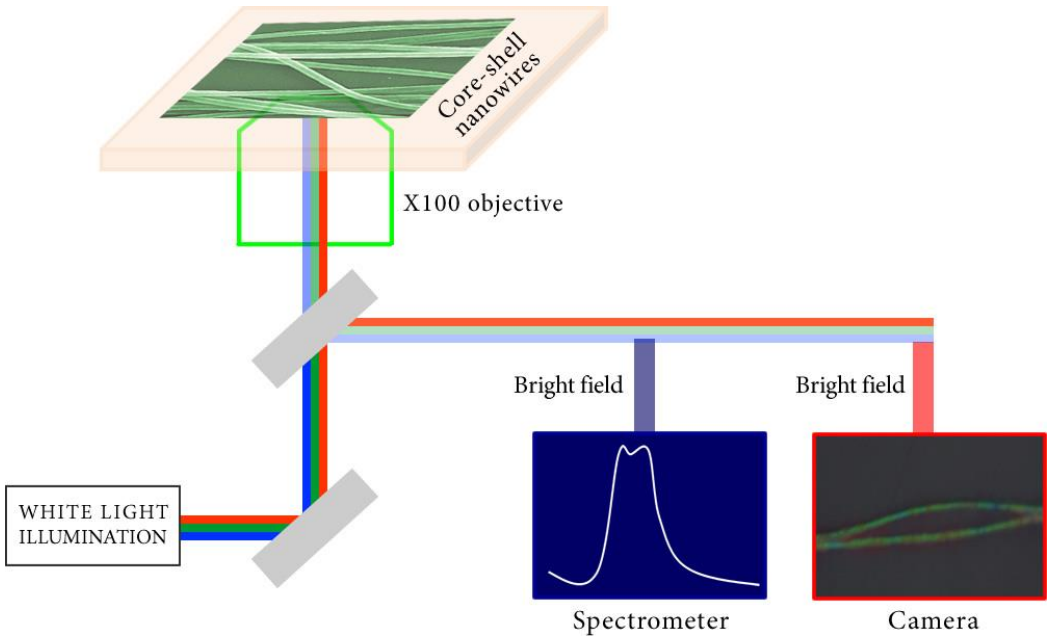

Figure 6.8: Measurement setup for structural coloration. Schematics of experimental set-up used for scattering measurements of polymer nanowires. Optical microscope images of individual colored nanowires are obtained in the bright field mode of an inverted microscope. The scattered light is collected by a UV-Vis-NIR MAYA spectrometer coupled to the microscope.

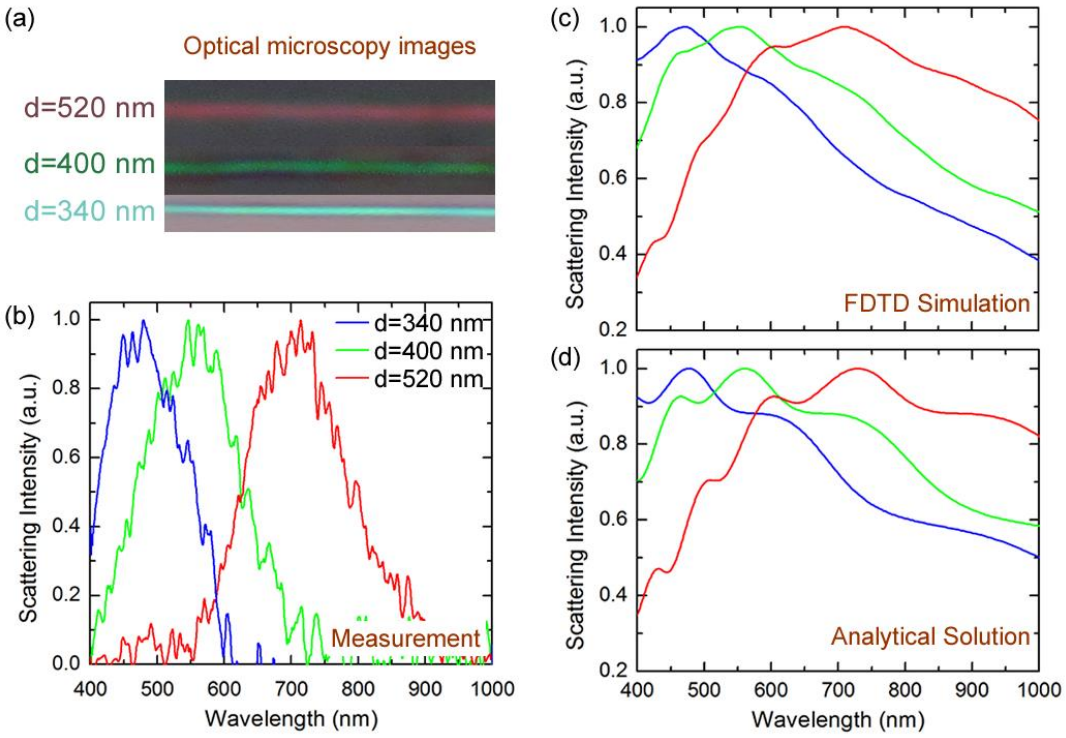

Figure 6.9: Structural coloration of polymeric nanostructures. Light scattering from core-shell nanostructures designed for red, green and blue coloration was investigated experimentally and theoretically. (a) Optical microscope images of colored nanostructures. Red, green and blue hues were observed on nanowires with core diameters of 340, 400, and 520 nm, respectively. (b) Scattering measurements performed by using inverted optical microscope in bright field mode (Detailed measurement setup is given in Figure 6.8). (c) Scattering from low refractive index nanostructures are simulated by using a FDTD technique with ellipsometric constants. (d) An analytical solution based on the vector wave harmonic expansion of scattered light is developed for core-shell geometry. Experimental measurements agree well with the analytical and simulated results.

Scattered light is collected by using a MAYA spectrometer. Optical images of colored nanostructures are taken by a digital camera attached to the microscope. The experimental setup for scattering measurements is detailed in Figure 6.8. FDTD method, a very efficient and powerful simulation technique, is used here for the comparison of simulation results with experimental measurements.

Numerical results of scattering from core-shell nanostructure for TE and TM polarizations are obtained by FDTD simulations, and averaged to yield an unpolarized light approximation. Experimental results are also in accordance with my simulations. Red, green and blue nanostructures investigated under microscope possess core diameters around 340 nm, 400 nm and 520 nm, respectively (Figure 6.9a-d). A variety of novel applications can be devised by utilizing an iterative size reduction technique in the fabrication of polymer nanostructures with broad material options, further enhancing the flexibility of polymer materials in nanoscale material engineering. Two such applications are discussed in Chapter 9.

6.4 Photonic Nano-Blade Lithography (NBL)

Very high orders of NRM scattering can be utilized in the design of a novel type of lithographic technique, which we call photonic nano-blade lithography. Here I propose to use low-refractive index core-shell nanowires in order to obtain 1D nano-grating or nano-holes, taking advantage of the deep-subwavelength focusing characteristics of scattering from core-shell nanowires (Figure 6.10a). To this end, UV lasers could be used to focus scattered light on a photoresist-covered surface, facilitating the localized absorption of the UV light throughout the photoresist. This portion of photoresist would then solidify or dissolve, depending on whether the surface was coated by a negative or positive photoresist.

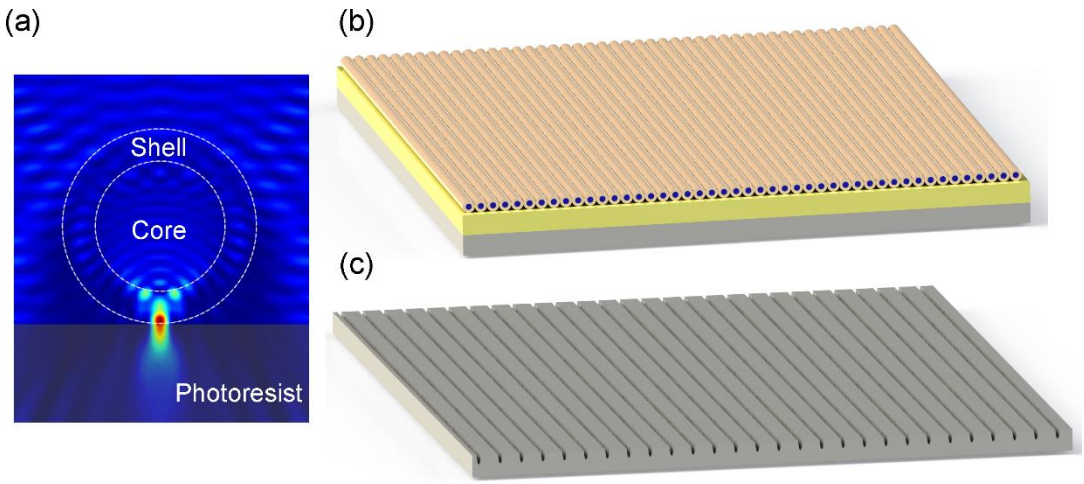

Figure 6.10: Nano-blade lithography uses the focusing feature of NRM scattering in order to expose the photoresist in sub-wavelength sizes. Consequently, 1D grating structures or holes can be fabricated.

The surface pattern can then be utilized to obtain a series of 1D holes (or 1D gratings) as described in Figure 6.10 b,c.

Chapter 7

Nanoshell Interference

7.1 Nanoshell Interference Effect

Interference is a well-characterized optical phenomenon, and involves multiple reflections from two or more material surfaces interacting with each other to create a distinct pattern of enhanced and diminished intensity bands [113]. Thin film interference (TFI) is a very special case under this process [114]. TFI is well-understood in planar geometries, and finds widespread use in antireflection coatings, mirrors and optical filters. Examples of TFI can also be found in the structural colorations of living organisms. However, it is not well understood whether and how light interference occurs in smaller particles, and the investigation of this issue is one of the most interesting topics in nanoscale optics, especially following the development of advanced nano-characterization and fabrication techniques.

I have recently observed thin film interference on core-shell nanostructures, and utilized this phenomenon for the design of colored nanoparticles. In this chapter, I report the investigation and characterization of this phenomenon in core-shell micro/nanospheres and micro/nanowires. Low-refractive index planar materials on a

high refractive index substrate results in the creation of thin film interference. In core-shell structures, the wire or sphere core corresponds to the substrate in conventional thin film interference, while the shell region represents the thin film. Here, a variety of effects may arise due to the material properties of the core and/or shell. Small core sizes can be utilized to take advantage of the Mie scattering phenomenon (Chapter 5) while larger cores can act as scattering objects due to their bulk. However, since thin film interference is mediated exclusively by the shell region, core-light interactions are undesirable for the observation of this phenomenon at the nanoscale. As such, I eliminate possible core-light interactions by choosing a core size between these two extremes.

Here I utilize previously described combined ISR-thermal modification method for the fabrication of functional core-shell micro/nanostructures displaying a nanosized analogue to the thin film interference phenomenon. Nanoshell interference is demonstrated via the structural coloration process. Shell size is found to determine the color of the core-shell structure. By changing shell thickness in the 150-300 nm range, any color in the visible spectrum can be obtained. I propose a variety of novel application areas for colored nanostructures, including potential uses as optical nanosensors, in particle mapping efforts, or for the visual determination of nanoshell sizes.

7.1.1 Core-shell Micro/nanowires

Nanoshell interference determines structure coloration in the visible spectrum when shell thicknesses are in the nanoscale and the core diameter is at or slightly above the sub-micron range. High refractive index chalcogenide glasses enhance interference effects and PVDF, with its relatively low refractive index, causes high Fresnel reflection from the polymer/chalcogenide interface.

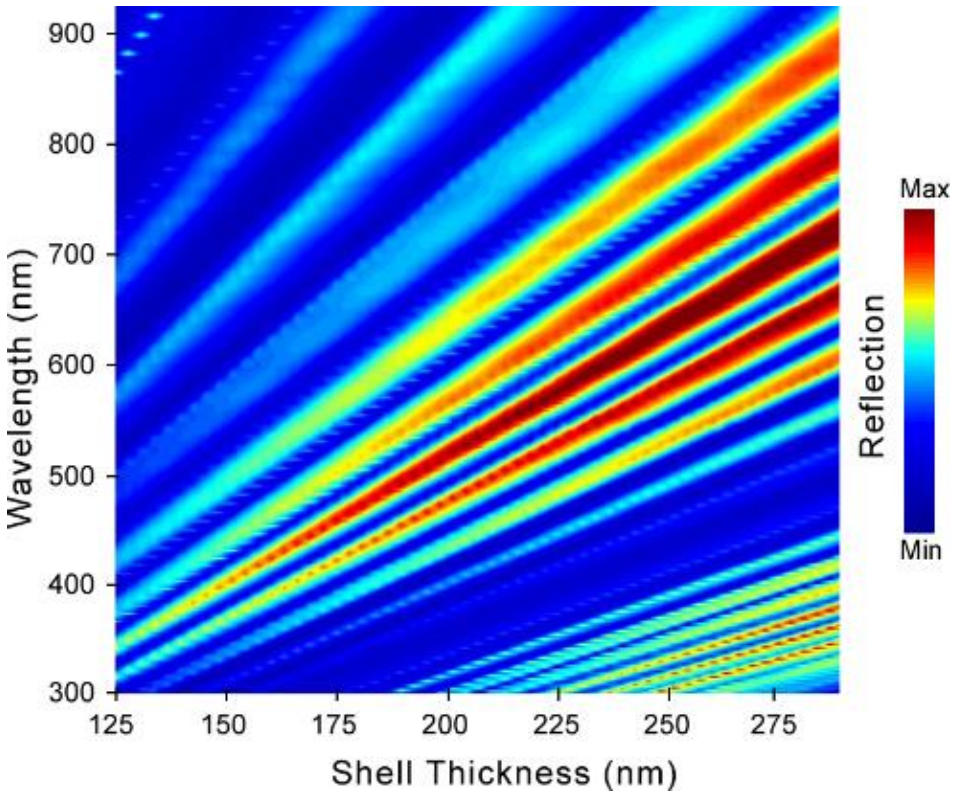

Figure 7.1: Nanoshell interference mechanism is demonstrated in spectroscopic FDTD simulations of size-scalable As_2Se_3/PVDF core-shell nanowires, using TM polarized light. Nanoshell interference is effective for shell size in the 150-300 nm range. The formation of reflection peaks is due to shell layer interference. Secondary high frequency interference in larger nanowires does not compromise coloration.

The nanoshell interference map exhibits broadly similar characteristics to conventional thin film interference maps. Interference orders can be observed in Figure 7.1. TE and TM polarizations possess similar optical behaviors. However, the reflection peaks separate for TE and TM polarizations below a certain diameter limit, typically below the sub-micron range.

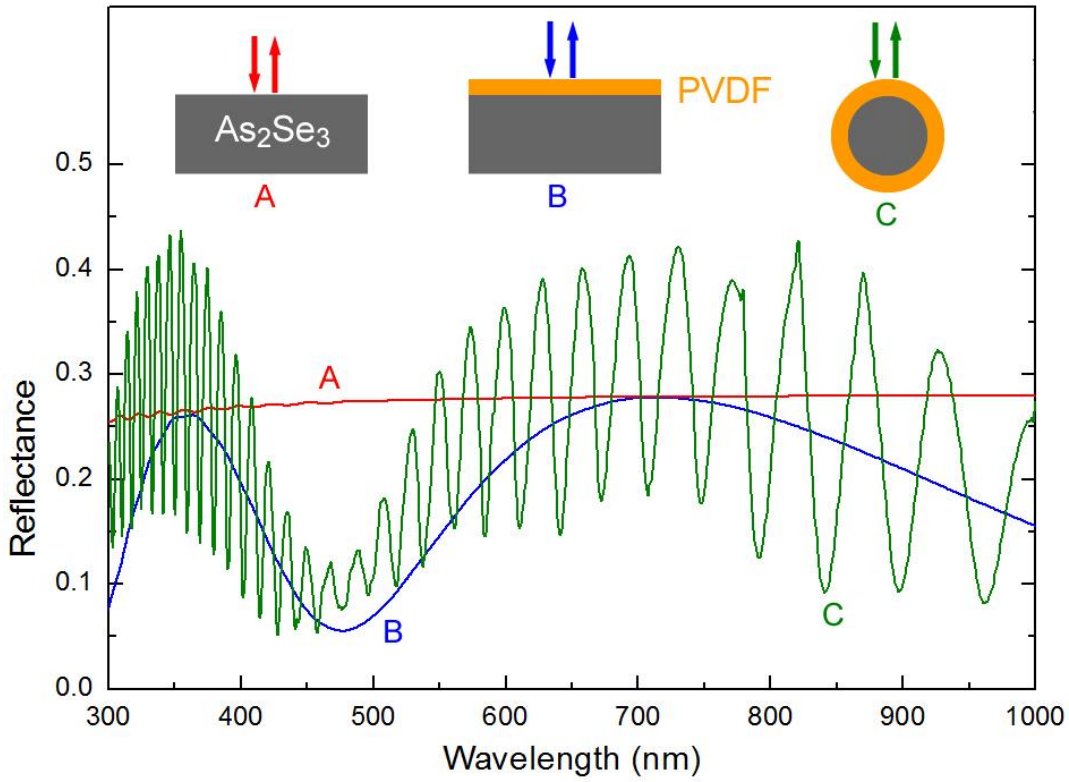

Figure 7.2: Theoretical analysis of structures associated with cylindrical core-shell nanowires. Reflection spectra of three different geometries were determined by FDTD simulations. Reflection from the As_2Se_3 substrate (red) is constant throughout the spectrum, as expected from Fresnel equations. Spectra of thin film interference for PVDF film on As_2Se_3 substrate (blue), and shell on nanowire (green) exhibit similar behaviors and peak in closest spectal points. Shell and core thicknesses are set at 250 nm and 1000 nm, respectively.

In Figure 7.2 I present a comparison between the thin film interferences of bare and coated surfaces and coated wires. Here we can observe that the first two interference orders bear roughly identical peak wavelengths for both planar and 1D geometries. Calculations are performed for a PVDF thickness of 250 nm. Core diameter is assumed to be 1 micron for wires and infinite for the planar geometries. I omit the absorption

of arsenic selenide material for my theoretical investigations, and assume constant refractive indices for both PVDF and arsenic selenide. The position of maximum reflection from core-shell nanowires can be estimated from $m\lambda/n_{shell} = 2t_{shell}$, where m = 1, 2, ..., is order of interference, λ is the free space wavelength of incident light, n_{shell} is the refractive index of shell layer, and t_{shell} is the thickness of the shell layer. For instance, a 270 nm thick PVDF shell results in a maximum reflection at λ = 761 nm, which is very close to experimental values and numerical FDTD predictions (Figure 7.6c,d).

Some features of the above-described nanoshell interference phenomenon differ from those of conventional thin film interference. Due to cylindrical symmetry, light perception in nanoshell interference can be independent from the incident angle. A series of nanowires can therefore be utilized to construct a planar region that displays a thin film interference phenomenon that is fully independent from the incident angle. These nanostructures can be used in flexible surface applications due to their one-dimensional nature and small size scale.

7.1.2 Core-shell Micro/nanospheres

The characteristics of nanoshell interference on a spherical geometry is described in Figure 7.3. Light interference is directly related to the thickness of the coated structure. Different orders of interference are observable in this map. The first constructive order of interference can be engineered to fall within to the visible spectrum of light. By altering shell thickness between 150-300 nm, it is possible to cover the full visible spectrum as in 1D case. I keep the radius of the core constant at 1 micron throughout my numerical calculations. Refractive indices of the core and shell layers are taken to be constant at 3.25 and 1.41, respectively.

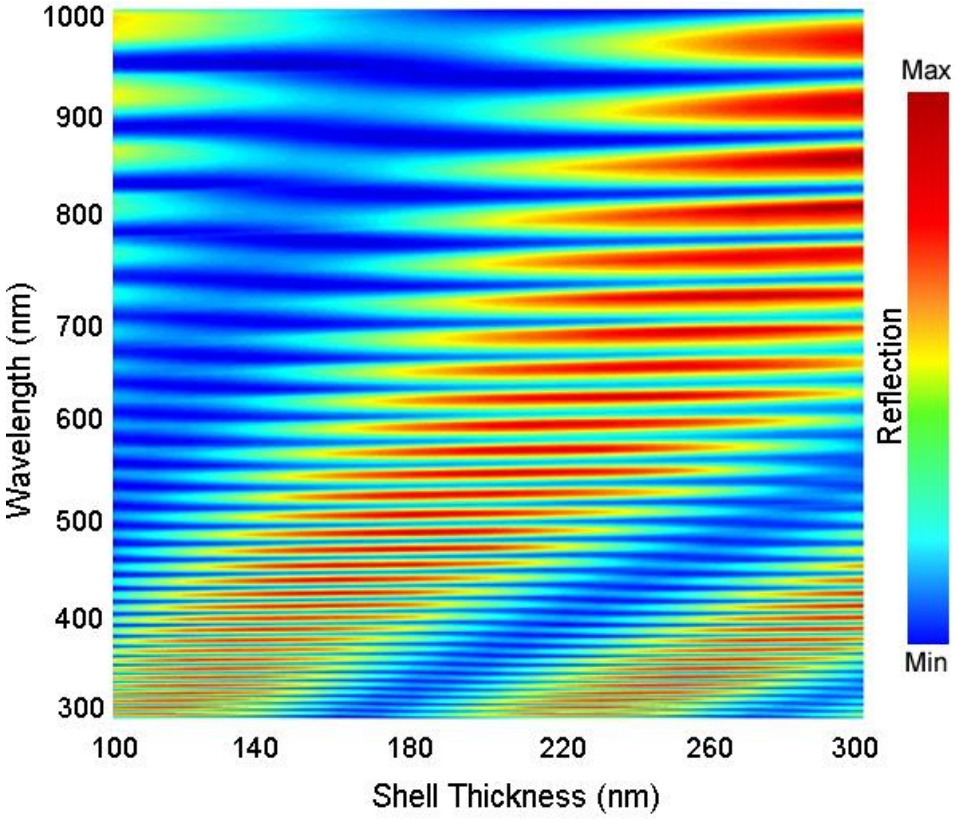

Figure 7.3: Nanoshell interference phenomenon in coated microspheres. Multiple reflections from different material interfaces result with constructive and destructive interferences. First two order of interference appear in the calculated size and wavelength range. Rapid and slow oscillations are originated from core and shell region respectively. During calculations, sphere diameter is taken constant as 1 μm.

Primary modulations observed in the map are caused by thin film interference. Secondary modulations, however are induced by the core of the structure. The frequency of oscillations can be decreased by decreasing the core size. Resonant Mie scattering becomes effective below a certain core size, and results in the disappearance of certain modes.

7.2 Coloration on Core-Shell Microwires and Microspheres

Chalcogenide and polymer core-shell nanowires show novel coloration properties and for the first time facilitate the observation of thin film interference-based coloration from a core-shell micro/nanowire structure. Thin film interference dominates for shell thicknesses in the range of 150-300 nm, and combined ISR-thermal instability technique (Chapters 2, 3) is highly suitable for the synthesis of nanostructures with shells in this thickness range (Figure 7.4a-c). Absorption from the core or shell regions appears to be an undesirable property for structural color formation. PVDF has a refractive index of 1.42 and virtually no absorption in the visible range, rendering it an ideal material for nanoshell coloration. As_2Se_3 has a high refractive index (varying from 3.36 to 3.00) and a non-zero extinction coefficient below 600 nm (Figure 2.5), but this does not prevent the observation of the coloration mechanism described in this chapter.

Optical properties of individual core-shell structures are investigated under an inverted light microscope. The PES sheath is removed by DCM exposure to isolate the individual core-shell nanowires.

Upon bright field illumination, three core-shell nanowires with core diameter around 1 μm (700-1100 nm) and shell thicknesses of 170, 195 and 270 nm show non-iridescent and vivid primary colors occurring via thin film interference from the PVDF shells (Figure 7.6b). The PVDF shell layer and As_2Se_3 core region can be observed from the cross section of the core-shell nanowires (Figure 7.6a). The cross-section is imaged after exposure via ultramicrotomy. I use bright field microscopy and collect reflected light from the nanowires by coupling a spectrometer (Maya 2000 Pro VUV) to the microscope (Figure 7.5).

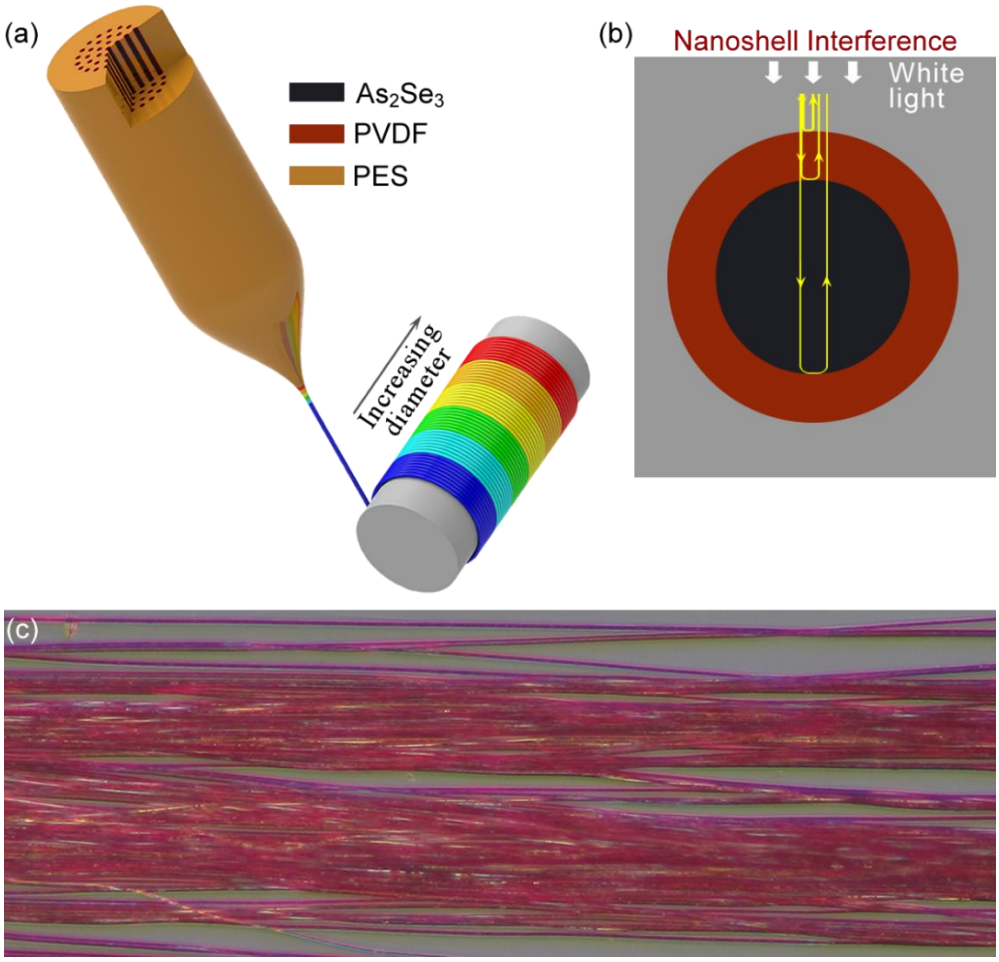

Figure 7.4: (a) A novel thermal size reduction technique is used to obtain indefinitely long, scalable core-shell nanowires. The structure consists of a high-dielectric semiconducting As_2Se_3 core, a piezoelectric polymer (PVDF) shell and a high-temperature thermoplastic (PES) cladding. The structures show native structural coloration based on size-dependent properties. (b) Structural coloration based on non-resonant interference for shell sizes between 150 and 300 nm, where coloration results from multiple reflections from core-shell interfaces.

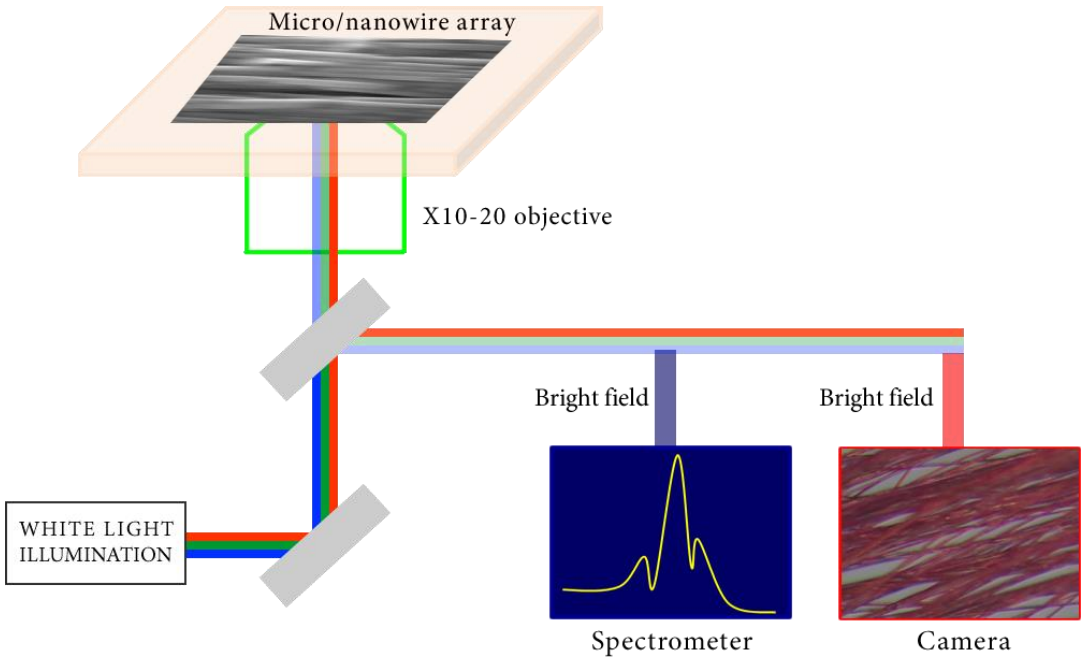

Figure 7.5: Schematics of the experimental set-up for reflection measurements. Optical image and reflection data were obtained using the bright field mode of an optical microscope. The reflection spectrum was taken by a UV-Vis spectrometer coupled to the microscope.

The microscope lamp can only provide efficient illumination in the 425-900 nm range. Therefore, only this region was considered for analysis. Spectra measured from three nanowire types are shown in Figure 7.6c. Three distinct peaks, corresponding to the three core-shell nanowire types, can be observed at 465 nm (blue), 525 nm (green) and 740 nm (red), and the last peak is modulated by secondary interference from the core region. This modulation effect is suppressed for the first and second peaks due to the optical density of the core region. Finite difference time domain (FDTD) simulations are used to study the reflection behavior of core-shell nanowires in both TM and TE polarizations.

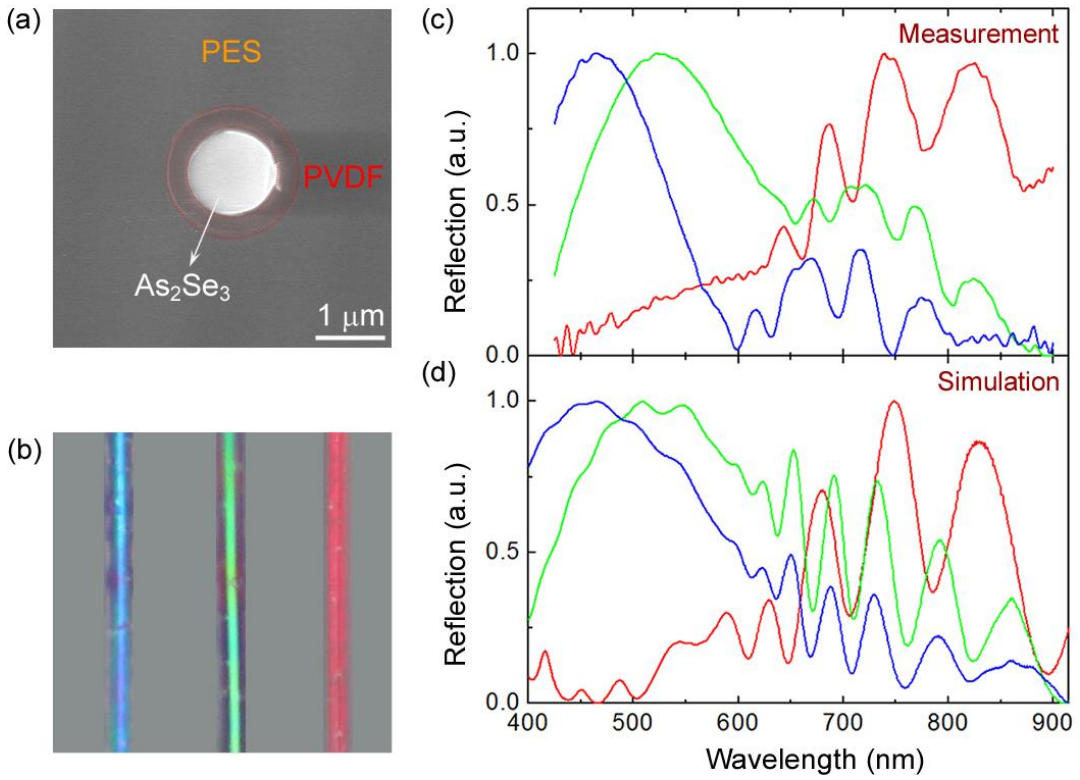

Figure 7.6: (a) SEM image of the polymer embedded As_2Se_3 (core)/PVDF (shell) microwire/nanoshell. (b) Size-dependent coloration from the shell layers of the 170 nm (blue), 195 nm (green) and 270 nm (nanoshells). (c) Spectroscopic bright field reflection measurements from the three core-shell structures show size dependent interference peaks at 470 (blue), 520 (green) and 750 (red). Modulation in the red spectra is due to secondary interference from the core region. (d) FDTD simulations are in agreement with the measurements.

Simulations are carried out using spectroscopic optical constants of As_2Se_3 and PVDF, and measurements were performed via ellipsometry. The reflection behavior is similar for both polarization types. As such, only the TM polarization is shown here (Figure 7.6d).

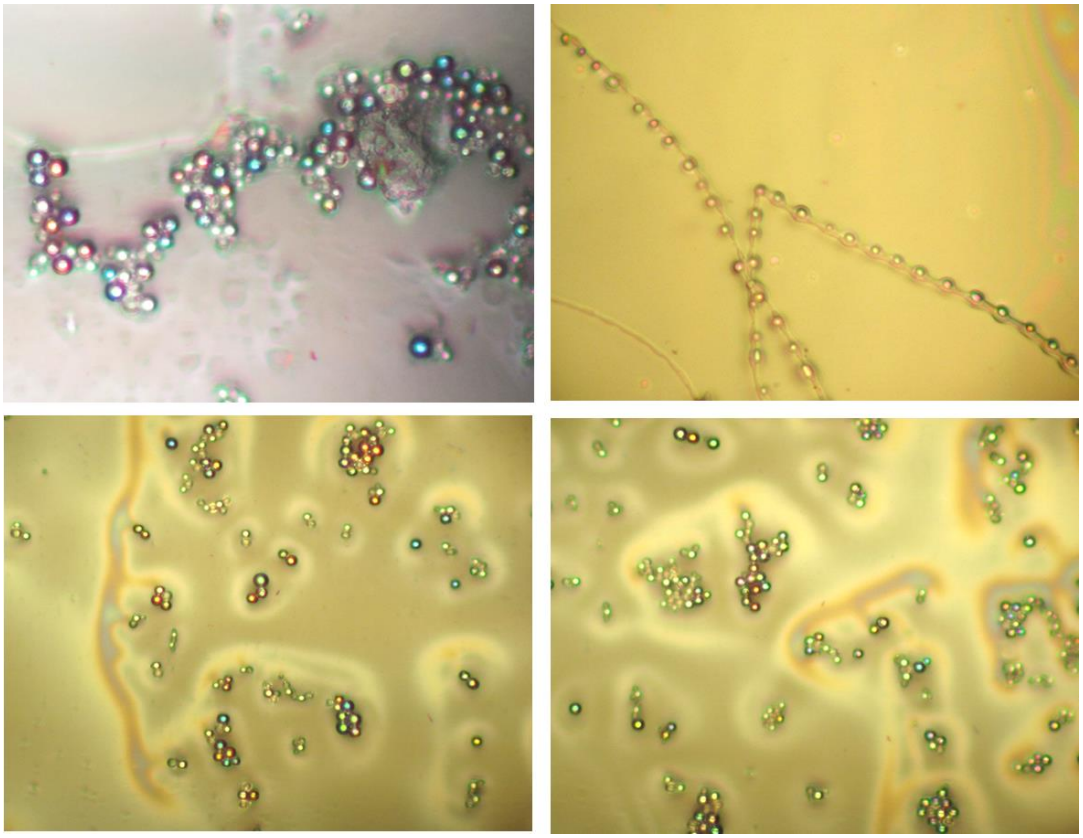

Figure 7.7: Core-shell microspheres colored via the nanoshell interference. Nonuniform shell thicknesses cause reflection of different colors. Vivid hues of any color can be obtained via the altering the thickness of shell region. Microsphere chain observed to colored via the same effect (righ image on the top). Colored spheres possess core diameter of 1-2 μm.

My simulations and measured data are largely in accordance with each other, and display both the primary interference from the shell and secondary interference from the core region. The simulations also confirm the omnidirectionality (non-iridescence) of the interference effect created by cylindrical symmetry.

Nanoshell coloration can also be observed in core-shell microspheres (Figure 7.7) fabricated using core-shell microwires (see Chapter 3 for fabrication details). Coloration is fully independent of polarization and incident light angle, and the shells, which are responsible for creating interference patterns in the visible spectrum, display

nanoscale thicknesses. I conclude the entire visual spectrum can be reflected by colored microspheres, which can be designed to display a specific color by predicting the required shell thickness.

7.3 Emerging Applications of Nanoshell Interference

An interesting application of the nanoshell interference phenomenon is the colorimetric determination of shell thickness using the wavelength of the observed color [115]. As each color corresponds to a particular shell size, the visual properties of a colored structure array can be utilized for the determination of shell thicknesses without resorting to complex characterization techniques.

I select three different colors (orange, green, and blue, indicated as 1,2,3 in the Figure 7.8a) for shell size determination. These colors correspond to wavelength values of ~615 nm, 505 and 475 nm, respectively. Using described nanoshell interference map, I can directly predict corresponding shell sizes of ~155 nm, 175 nm and 220 nm for core-shell structures with blue, green and orange hues, respectively. It should also be noted that the interference map given in Figure 7.8b is calculated using real material parameters.

Nanoshell interference can be also utilized for the determination of the core material by analyzing the amount of light reflected from different core-shell interfaces. It is also apparent that changes in the core refractive index result in alterations in the intensity of reflected light (Figure 7.9).

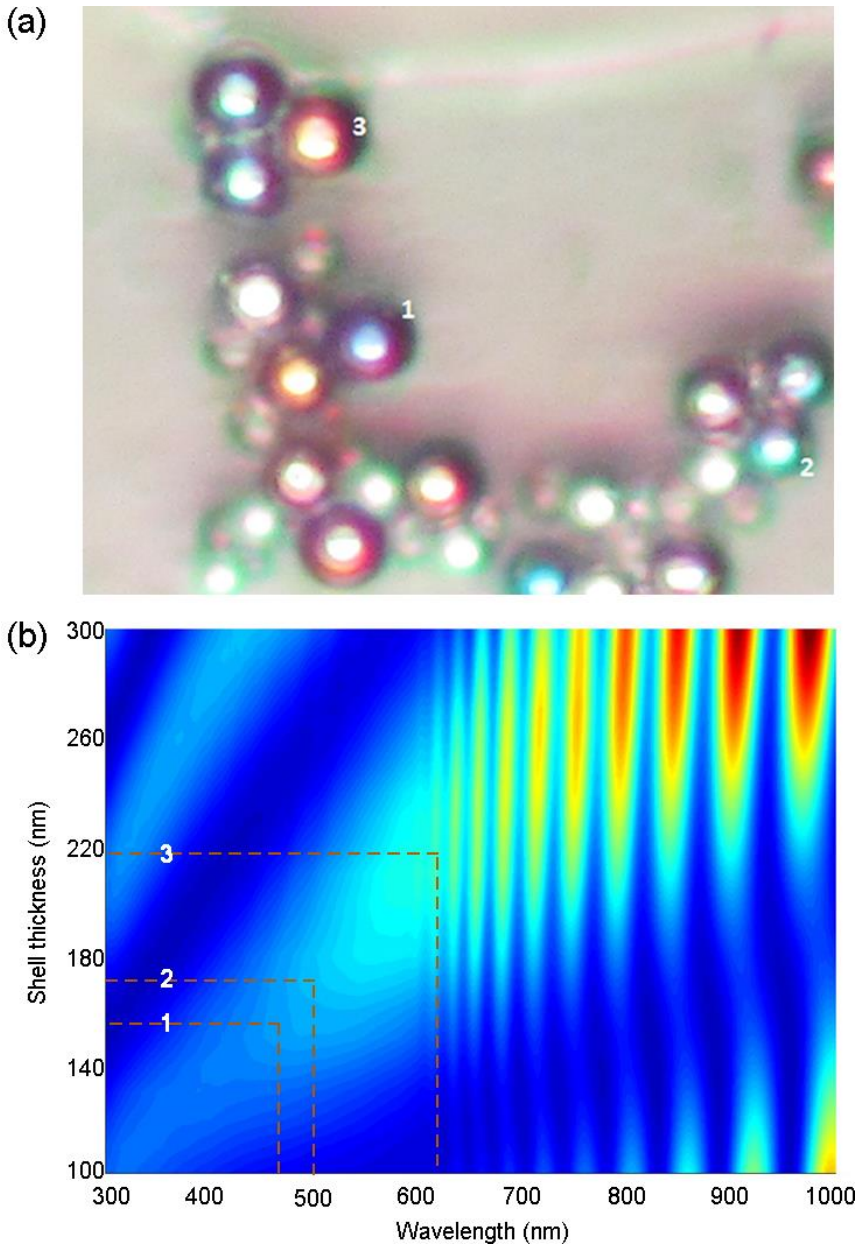

Figure 7.8: Shell size determination, an interesting application of nanoshell interference. As each color corresponds to specific shell thickness we can use this feature in order to determine thicknessess of shell layer without using any complex characterization technique.

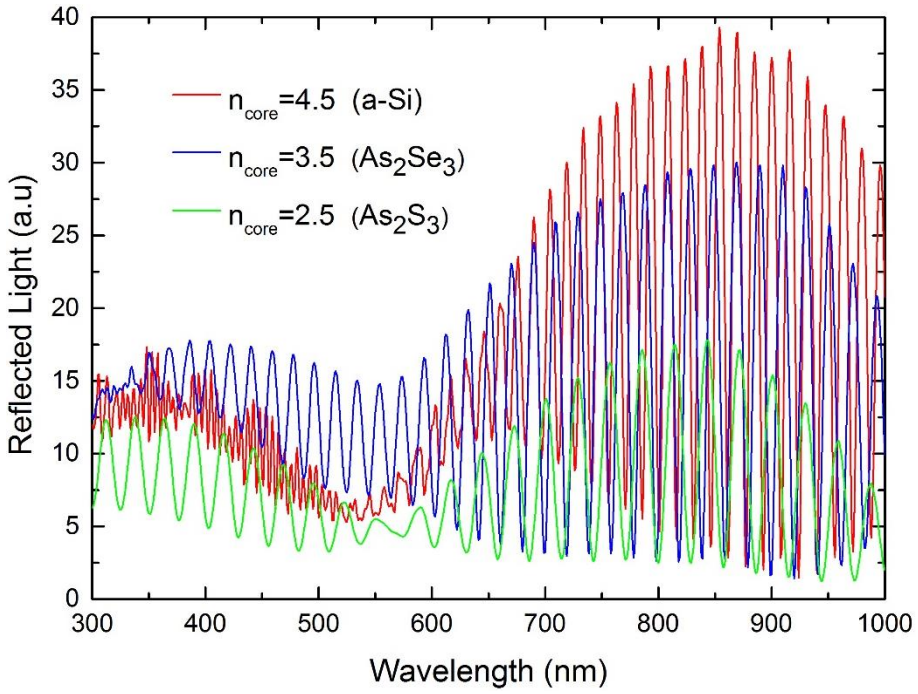

Figure 7.9: Depending on core material light can be reflected from interfaces in distinct amounts which can be used for discriminating core material composition. Three representative refractive indices 4.5, 3.5 and 2.5 which corresponds to a-Si, As_2Se_3 and As_2S_3 glasses can be easily detected according to their brightness..

Simulations have been performed for core materials with refractive indices of 4.5, 3.5 and 2.5, which correspond to the refractive indices of a-Si, As_2Se_3 and As_2S_3 glasses respectively. The resulting reflection patterns are quite distinctive (Figure 7.9), and we therefore conclude that positions and distributions of these nanomaterial mixtures can be inferred directly using a conventional optical microscope, without the requirements of convoluted computational techniques, provided that the observer has a rough idea on the identity of the core material [116].

Chapter 8

In-fiber Photonic Crystal Structures Mimicking Mallard Feather

8.1 Structural Coloring in Nature

Pigments and structural coloration are equally important for the production of colored structures in biological systems [117]. While pigments function by absorbing or reflecting specific wavelengths of light, structural coloration might be based on scattering, diffraction or interference, and many biological systems are equipped with specialized geometries, such as thin film interfaces [118,119], photonic crystals [120, 121] and layered films [122], capable exhibiting such phenomena. Because of the diversity and functionality of photonic crystal structures, their investigation and structural imitation [123,124,125] is very promising for the development of various applications in both nano- and macroscale optics. Photonic crystal structures of different types can be observed in nature, and their functions in living systems are not only limited to coloration. The structural properties of these systems can therefore be imitated using conventional nanoengineering materials for a wide variety of practical applications.

Photonic crystals in living organisms can be distinguished by their irisdescent colors and periodically arranged structures. However, the lattice constant of these photonic crystals are generally comparable to the wavelength of reflecting light (and usually occur as rods and holes with radii of 100-200 nm), which is generally difficult to fabricate using conventional methods. A variety of novel micro- and nanofabrication techniques have been developed to overcome this difficulty and imitate the functional properties of photonic crystals. Here I report the investigation and imitation of unusual photonic crystal structures observed in the barbules of mallard drakes by iterative size reduction.

8.2 Investigation of Mallard Feather

Feathers of mallard drakes (*Anas platyrhynchos* L.) were investigated for their structural properties. Head and neck feathers of *A. platyrhynchos* drakes are observed to display a vivid green coloration, while flight feathers are blue in color (Figure 8.1a). Optical images of head and neck feathers demonstrate that their iridescence is dependent on the incident angle: The green hue observed under x5 magnification (Figure 8.1b) changes into a distinctive blue color under x20 magnification (Figure 8.2c).

8.2.1 Structure of the Mallard Feather

Structural components of bird feathers are generally similar, possibly due to evolutionary constraints imposed by the requirements of flight. However, some feather elements have gained a secondary function (coloration for communication and mating displays) and their structures may be imitated to replicate the vivid structural colors they exhibit. Feather barbules are generally responsible for structural coloration of birds, and I investigate the barbule morphology under scanning electron microscopy in order to determine the structures responsible for coloration. Feathers were embedded in epoxy resin and feather sections were taken by an ultramicrotome prior

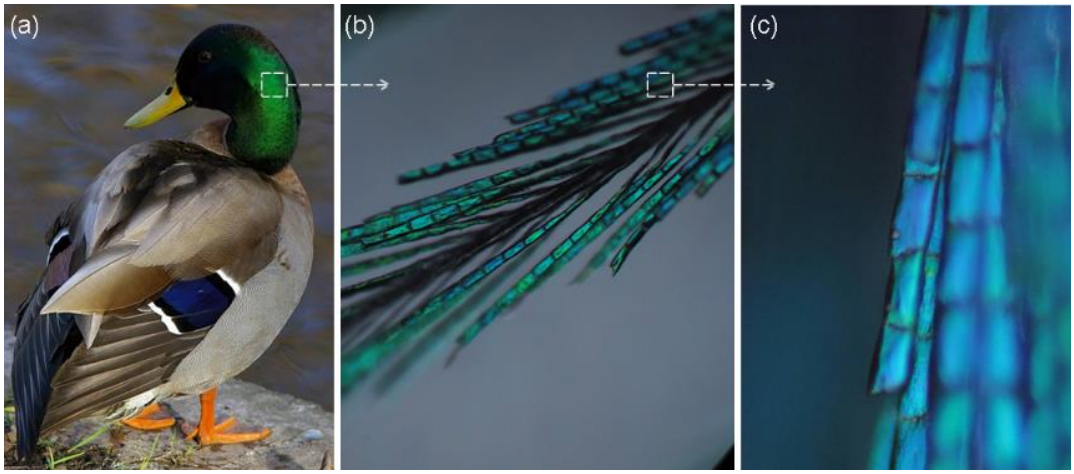

Figure 8.1: Optical microscopy images of mallard neck feathers**.** As magnification, increases the color of the mallard feather changes from green to blue, which suggests that iridescence is responsible for the observed color. Macroscopic coloration is induced by nanoscale features exist in the barbules.

to imaging. Both longitudinal and cross-sectional images are taken from barbule samples. Cross-sectional images are difficult to obtain due to the low refractive index contrast of barbule components, and SEM imaging is performed under both high pressure and low pressure modes to bypass this problem.

Cross-sectional images reveal that the structure possesses a non-circular cross-section, which may serve to maximize the surface areas of the barbule elements responsible for structural coloration. Well-aligned hexagonal arrays of rods are observed to occur on barbule edges. These rods each measure several hundreds of nanometers, and are responsible for the large-scale coloration observed in mallard drakes. It is also notable that the rods are discrete throughout the barbule and do not form a continuous wire structure. This property can be observed in Figure 8.2c.

Coloration is caused by 5-6 layers arranged along the edges of barbules. Mallard feathers, as with those of other birds, are primarily composed of melanin pigments (rods) embedded in a keratin matrix (filling material). These materials display a moderate refractive index contrast, which allows the reflection of a narrow band of wavelengths, though the position of this band is altered depending on viewing angle. Melanin and keratin have refractive indeces of 2 and 1.54, respectively.

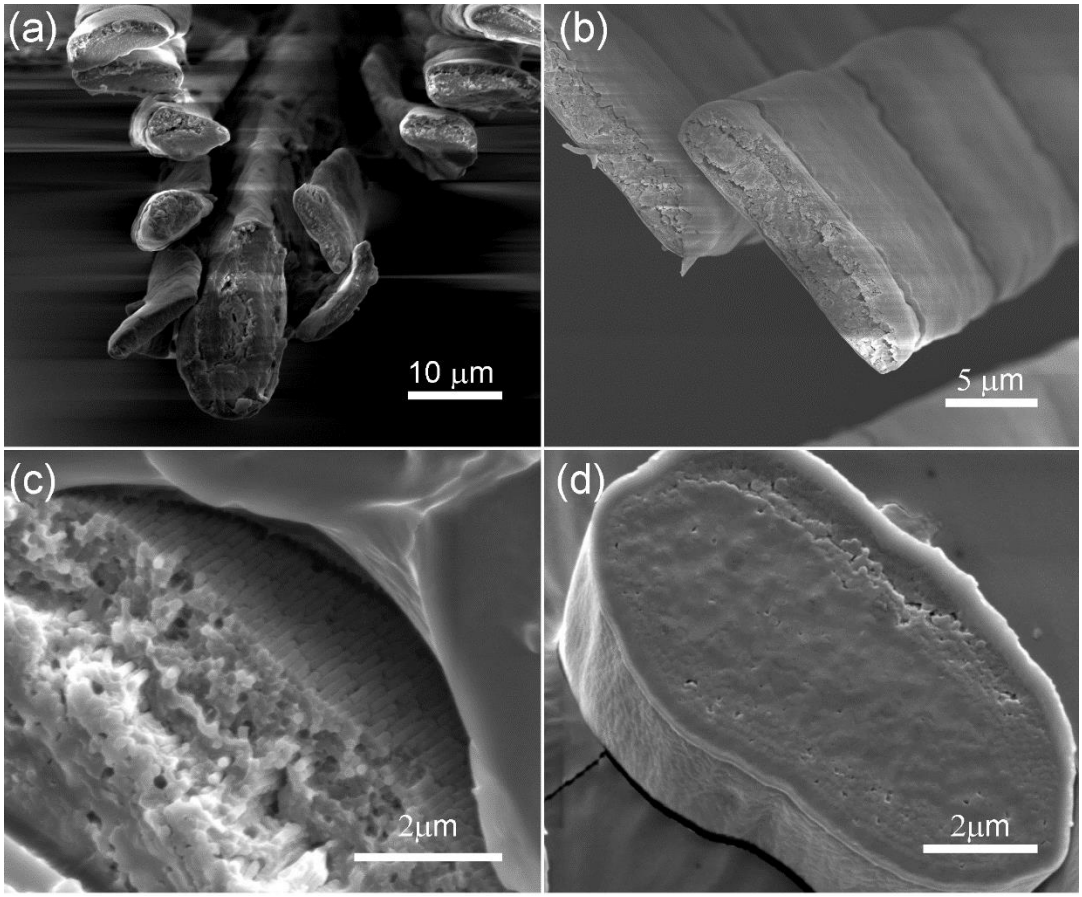

Figure 8.2: Cross-sectional and longitudinal SEM images of mallard feather barbule. Hexagonal arrays of rods are observed to be distributed throughout the outer side of barbule. Melanin rods are discrete within the barbule and their lengths are in submicron range.

Parameters that define photonic crystal structures are measured directly from SEM images of the cross-section. The lattice constant, which corresponds to the spacing between two rods, is around 200 nm. Each individual rod bears a diameter of 170 nm. These values are critical in the design of photonic crystal effect-based coloration (Figure 8.3a).

Inner regions of mallard feathers do not appear to display a regular structure. Melanin rods exist within this area, but are arranged at random. This region is unlikely to exhibit structural coloring, and possibly acts as structural support for the feather (Figure 8.3b).

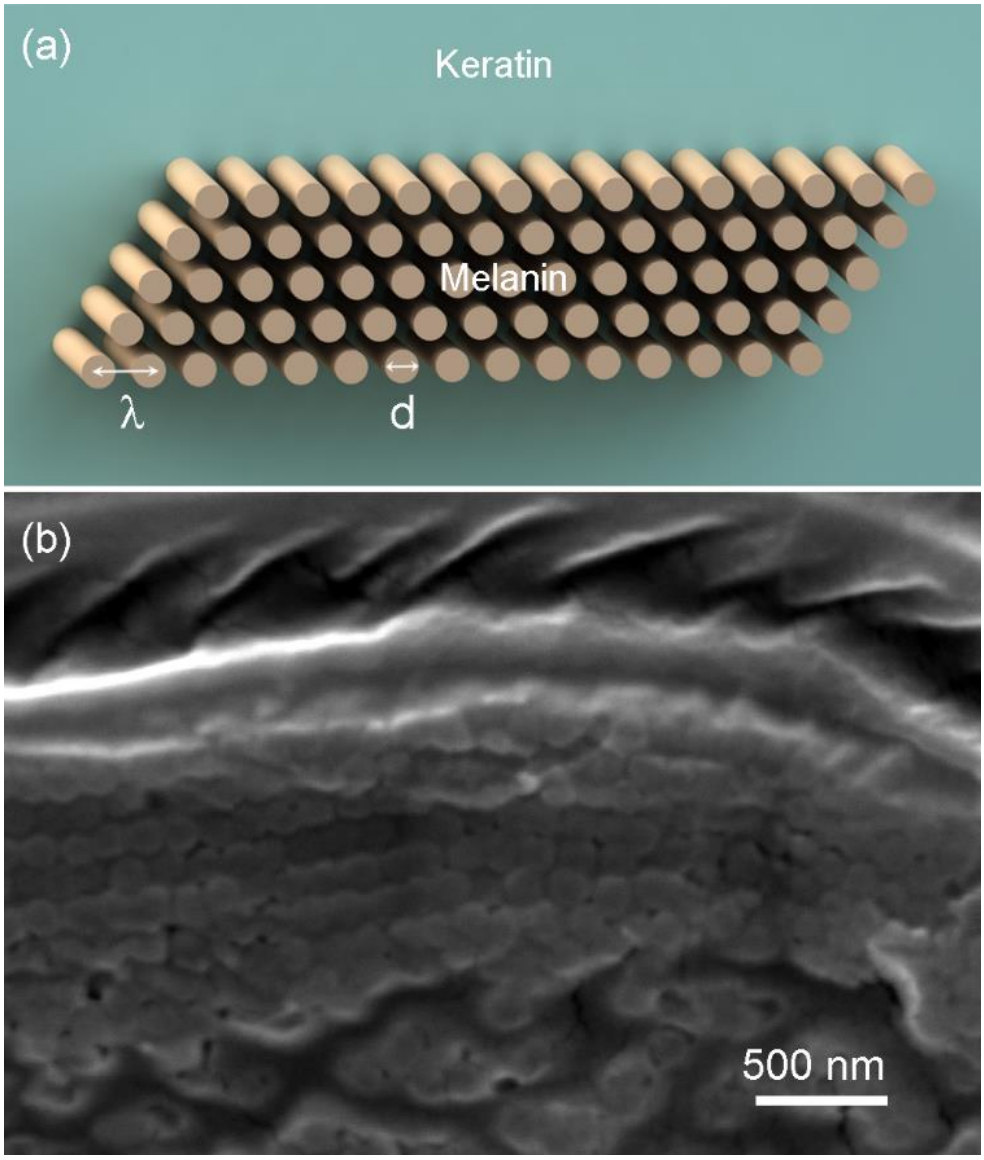

Figure 8.3: (a) Scheme representing the distribution of melanin rods embedded in the keratin matrix. Lattice constant (λ) and diameter (d) are main parameters in the photonic crystals. (b) SEM image of hexagonal arrays of rods in mallard feather. Lattice constant and diameter oberved from SEM images are around 210 nm and 170 nm respectively.

8.2.2 Optical Characterization

Design parameters obtained from SEM images of head feather barbules are used in FDTD simulations to confirm whether the coloration observed is truly mediated by the photonic crystal effect. Simulation results are given in Figure 8.4a,b. For a lattice constant (λ) of 210 nm and a rod diameter (d) of 170 nm, I predict that the simulated structures will reflect green light, as is observed in mallard feathers under light microscopy. Material refractive indices for melanin and keratin are taken as 2 and 1.54, respectively.

I also run a set of simulations in order to explore the band structure of the structural configuration observed in the cross-section of barbule. It is clear that a band-gap occurs in the green region of the visible spectrum, which is responsible for the vivid green hue observed in mallard feathers (Figure 8.1). It is notable that the band-gap present in this region is a partial photonic band-gap. Another interesting point is that the band-structure is predicted to reflect in the UV region.

I measure the reflection spectra of mallard head feathers by using a MAYA spectrometer and compare experimental data with FDTD simulation results. FDTD simulations are performed using material data (refractive index) and array information (rod radius, lattice constant) from SEM images (Figure 8.5). It is apparent that simulation and measurement results are in good agreement for the photonic crystal parameters obtained from neck feather barbules. UV reflection observed from mallard feathers suggests that that the feathers also serve to protect the animal from ultraviolet radiation. The distinctive green coloration may also play a role in communication, and especially in mating and rivalry displays. Experimental measurement and simulations support that green color in these structures is indeed caused by the presence of photonic crystals. Using the structural orientation of barbule elements, it is possible to fabricate novel materials to be utilized as photonic crystal based textiles.

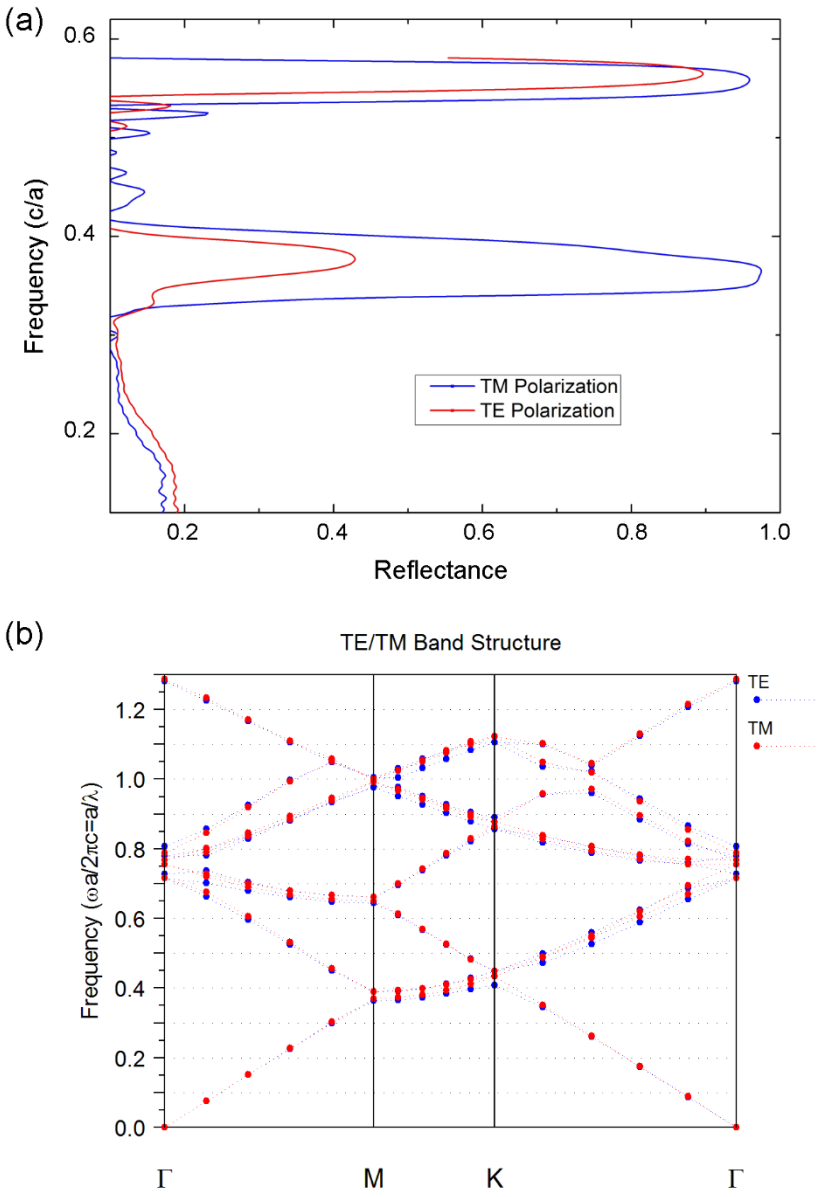

Figure 8.4: (a) Simulation of reflection by neck feather barbules. Lattice and rod diameter values were measured from SEM images. (b) It is clear that a partial band-gap exists in the green portion of the spectrum. This is the cause of the green color observed in mallard feathers.

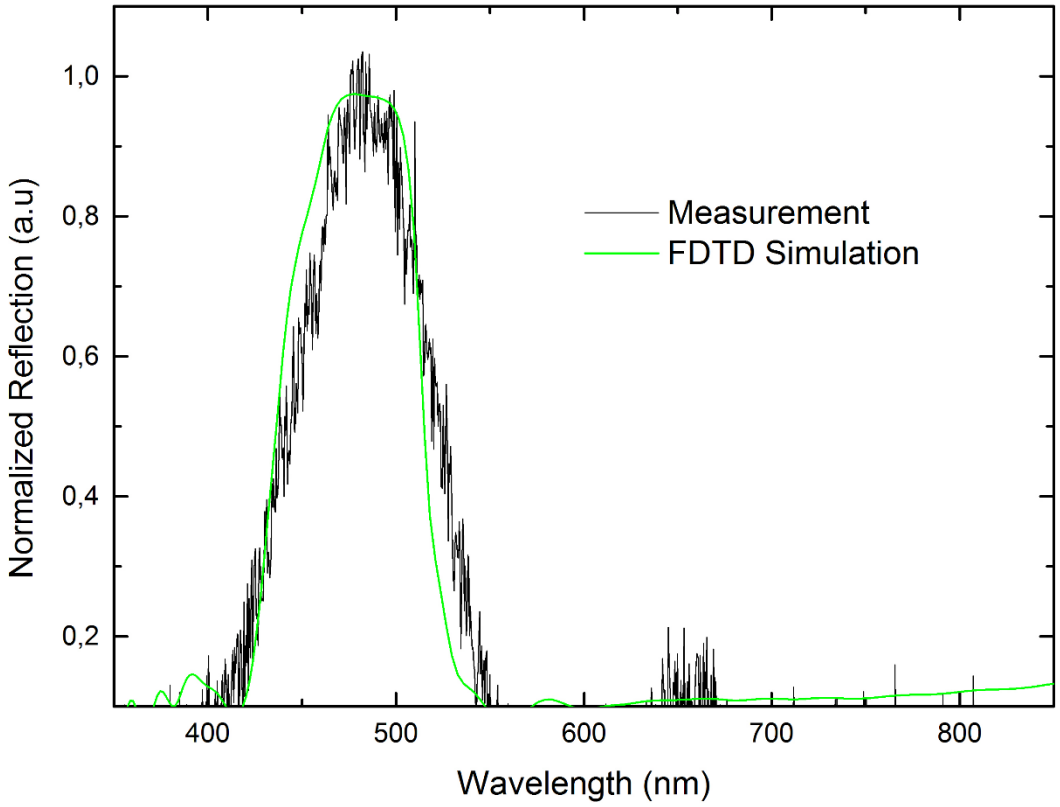

Figure 8.5: Experimental and simulation results of mallard feather. It is apparent that my observations and simulation results are in good agreement. FDTD simulation is performed for material parameters obtained from SEM images of mallard drake feather.

8.3 Mimicking of Mallard Feather Structure

Structural coloration mechanisms of different avian species can be imitated for the design of a vast variety of novel micro- and nanoscale devices. Here I use iterative size reduction (Chapter 2) in order to mimic the structural colors and UV-reflective properties observed in mallard feathers. Data from SEM images is utilized to design the fabrication procedure and determine simulation parameters.

8.3.1 Material Selection

Mallard feathers display a low index contrast between the melanin rods and the keratin matrix, which is responsible for creating the narrow reflection bands displayed by these structures. As such, this property should be reflected in the materials used in the imitation of the structural colors observed in mallard feathers. In addition, the materials utilized should be thermally compatible for the drawing process to be feasible. I run a set of simulations in order to select optically and thermally compatible materials for biomimetic photonic crystal fabrication. Materials shown in Table 8.1 display highly compatible thermal properties and can be utilized for the thermal drawing process described in Chapter 2. However, the use of polymer and glass components results in photonic crystals with broad band-gaps, which makes it difficult to design the resulting structures for monochromatic hues. While As_2Se_3 and As_2S_3 avoid this issue and are suitable for my purposes, here I prefer to utilize all-polymer materials for enacting the mimicking process, as polymer materials are generally flexible and biocompatible.
PC and PVDF are therefore selected as the material components and optically characterized for the optimization of fabrication process. PC possesses a refractive index of 1.6 and exhibits a refractive index contrast of 0.2 with PVDF in the visible region, imitating the melanin/keratin matrix properties to a reasonable degree.

Material Rod/Filling	**Rod (n_1)**	**Filling (n_2)**	**Bandgap (nm)**
PES/PVDF	1.7	1.41	50
PC/PVDF	1.65	1.41	30
As_2S_3/PVDF	2.7	1.41	180
As_2Se_3/As_2S_3	3.25	2.7	20
As_2S_3/ PC	2.7	1.65	150

Table 8.1. Material selection for structural coloration. All-polymer structures are suitable for mimicking process due to low refractive index contrast.

These two polymers are also thermally compatible, which is essential for my fabrication process. It should also be mentioned that the selected configuration is highly similar to the original structure observed in mallard feathers, and displays a rectangular cross-section which may serve to enhance the structural coloring observed from the photonic crystal surface.

8.3.2 Results

Microstructures composed of hexagonal arrays of nanorods with rectangular cross-sections are obtained following three drawing steps, and bear a great resemblance to the structure of mallard feathers. SEM images of step I and step II fibers are given in Chapter 2, and here I only show the SEM images of step III fibers, though the images in question are relatively low-quality due to the very low contrast between the refractive indices of the photonic crystal components (Figure 8.6a). Lattice constants and rod diameters of fabricated photonic crystal structures are 210 nm and ~165 nm, respectively. There is some irregularity in the diameters of PC nanorods, though the lattice constant, which is the major factor in the determination of band positions and gaps, is almost constant. Minor deformations in rod structures effect slight alterations on the coloration process, but do not significantly alter the overall color.

Longitudinal SEM images reveal that the PVDF shell acts as an embedding matrix for PC nanorods. Impurities are observed to remain on the PVDF surface, but are too small to display Mie scattering or thin film interference, and are therefore assumed to play an insignificant role in coloration. While FIB can also be used to cut photonic crystal structures for the acquisition of more smooth surfaces and better contrast, I find that the nanorods are damaged during the FIB cutting process, and therefore only utilize an ultramicrotome for the "polishing" process (Figure 8.6b).

Hexagonal arrays of PVDF-embedded PC rods mimic the photonic crystal structure observed in mallard feathers (Figure 8.7a). Optical microscope images reveal that green and red colors (Figure 8.7b) are reflected from fabricated 2D all-polymer photonic crystal structures.

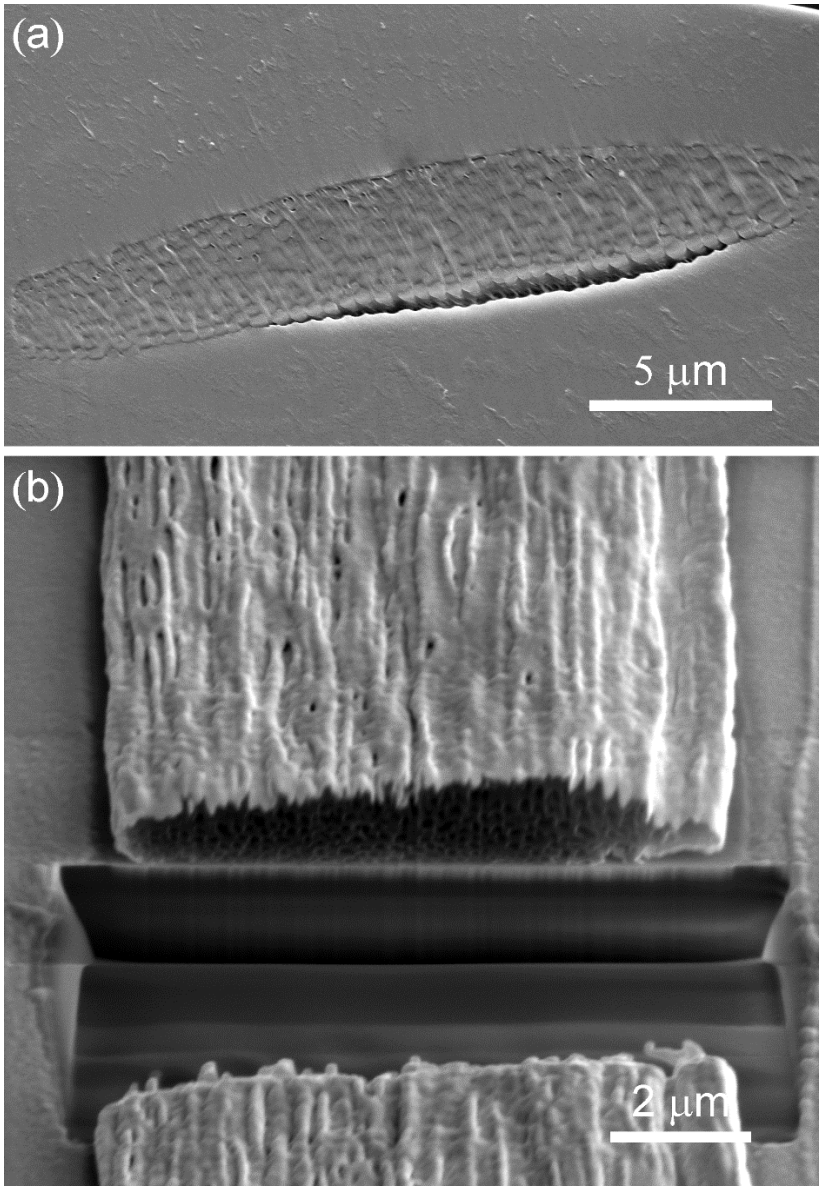

Figure 8.6: SEM images of fabricated nanostructures. As a result of three iterative drawing steps lattice constants of photonic crystals reached into nanoscale. In particular SEM image represent photonic crystal that possess lattice constant of ~200 nm.

Reflection spectra of colored photonic crystal structures are acquired under inverted light microscopy (Figure 8.7c), and experimental measurements are supported by theoretical predictions via FDTD simulations. Calculations were performed based on photonic crystal parameters (i.e. lattice constant and rod diameters) observed in SEM images, and are given in Figure 8.7d.

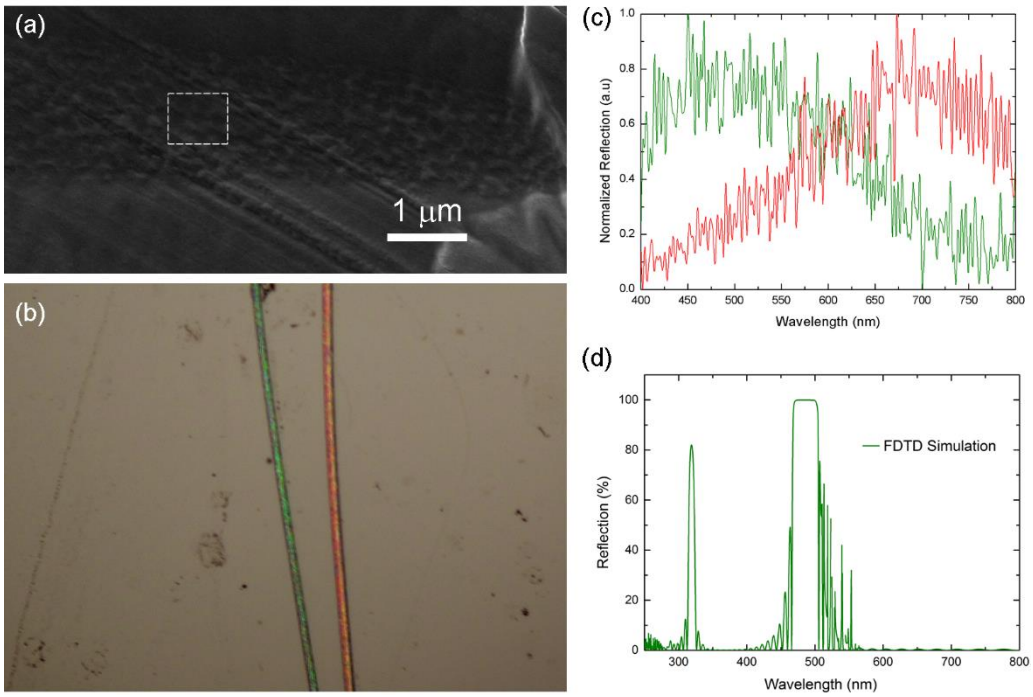

Figure 8.7: Functional biomimicry of mallard neck feathers. (a) SEM images reveal the hexagonal distribution of PC rods inside the PVDF matrix. (b) Distinctive colors observed under light microcopy confirm the presence of photonic crystal effects for lattice constants around 200 nm. (c) Reflection measurementsof colored photonic crystal structures. (d) FDTD simulations performed for a lattice constant of 210 nm and diameter 170 nm.

Fabricated photonic crystal fibers also exhibit iridescent characteristics. I investigate this property of fibers under inverted light microscope. Green color of photonic crystal fiber shift into blue as the angle of incidence light increases (Figure 8.8).

In addition to photonic crystals with rectangular cross-sections, the same effect was observed on cylindrical all-polymer core-shell nanowires. SEM and optical microscope images of photonic crystal structures with circular cross-sections are shown in Figure 8.9a. As with rectangular cross-section fibers, the colors exhibited by these fibers are caused by their composition as 2D photonic crystals. The coloration is not uniform throughout the fiber due to rapidly fluctuating structure dimensions, though this effect is not clearly observable in Figure 8.9b.

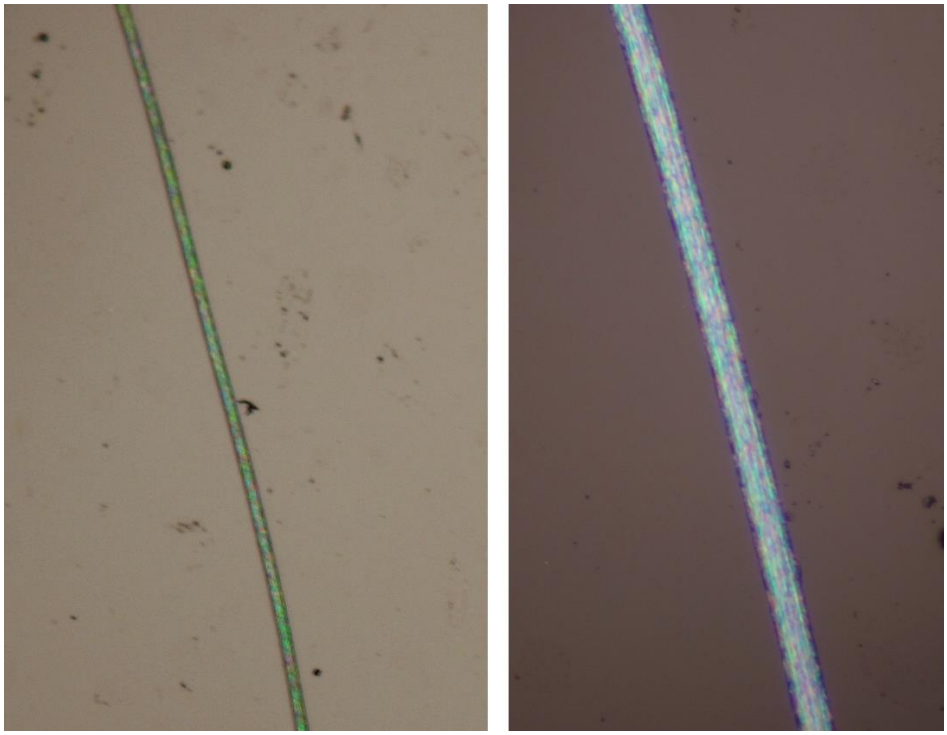

Figure 8.8: Iridescence in mimicked photonic crystal fiber. As I increase magnification of light microscope which corresponds to increasing of angle of incident light, green colors transform into blue color as result of present phenomenon.

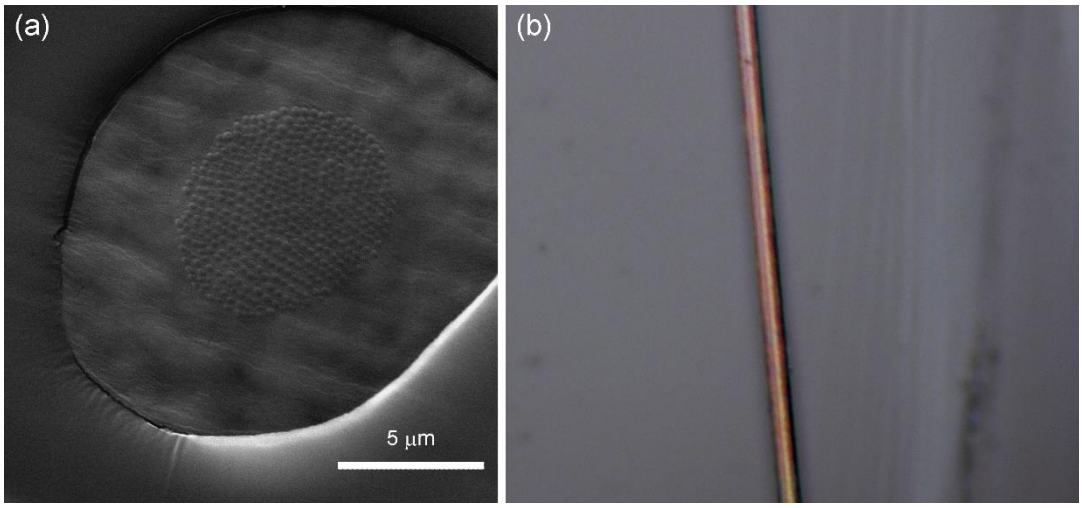

Figure 8.9: (a) Fiber containing several hundreds of PC rods located inside a circular zone. (b) It is demonstrated that the photonic crystal effect can be observed even with a circular structure design.

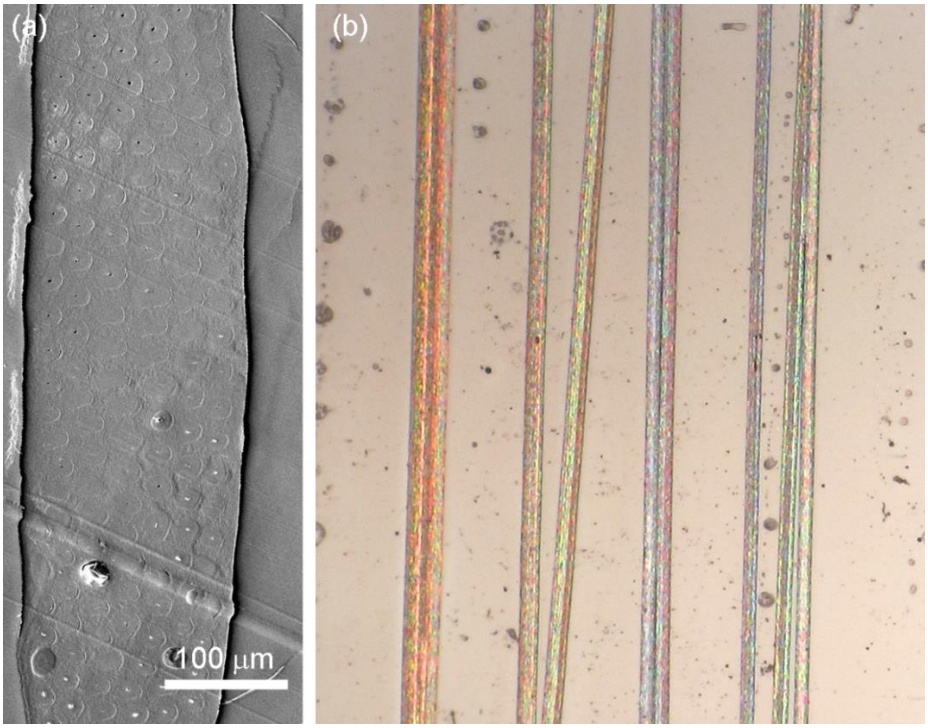

Figure 8.10: (a) Photonic crystals fabricated from microwires produced by nucleated ISR. (b) These structures are also well-suited for photonic crystal-based coloration.

I also produce biomimetic photonic crystals using an alternative preform, where polymer layers are wrapped around a quartz tube "nucleus" that is subsequently removed prior to drawing. The hole created by the nucleus shrinks and eventually closes during the drawing process. Photonic crystals produced using step II microwires are shown in Figure 8.10a. Fabricated photonic crystal structures are composed of highly uniform hexagonal arrays of PC rods embedded in a PVDF matrix. Vivid hues can be obtained for any color using varying lattice constants and rod diameters (Figure 8.10b).

Chapter 9

Solar Cell and Sensor Applications of Core-Shell Nanostructures

9.1 Light trapping with core-shell nanowires

Thin-film solar cells are third generation optoelectronic designs that capitalize on the low material usage and high conversion efficiencies associated with thin films [126]. Electronic and optical properties of the materials used in such applications are both critical in the design of thin-film solar cells. Amorphous silicon is a very popular material for such designs, as it is cheap, can be procured in abundance, and possesses modest electronic and excellent optical features. Fabrication methods are currently quite well-developed for a-Si based solar cells, and efforts to improve the efficiency of this solar cell type have mostly ceased in the past decade [127]. However, undesired scattering or reflection behaviors are frequently observed in these solar cells due to the different optical constants displayed by solar cell layer elements. As such, current efforts on a-Si based thin-film solar cells are directed towards the elimination of this problem by maximizing the amount of light absorbed inside the absorbance layer. Light-trapping techniques are frequently utilized to this end [128,129,130,131,132].

Each light-trapping technique has its own distinctive set of useful optical features. However, many such techniques are difficult to utilize in practical applications, and while light-trapping device schemes based plasmonics, surface texturing and photonic crystals effects have been documented, such designs are unsuitable for mass production and are currently limited to proof of concept models. Therefore, the main challenge associated with light-trapping apparatuses is not the design these structures, but their production in scales and costs demanded by the practical applications of solar cells.

Low-refractive index materials are generally transparent in the visible spectrum, and are therefore desirable for many nanophotonics applications. Such materials are widely used for the enhancement of light absorption in solar cells, and can be applied as nanostructured coatings on optoelectronic devices and antireflective systems. In this study, I use 1D low-refractive index nanostructures in order to accumulate solar radiation, and provide theoretical and experimental demonstrations of absorption enhancement by these structures. One dimensional nanostructures, and especially core-shell nanowires, are scalable up to macroscopic sizes, display a natural lattice arrangement mediated by the shell region, and are capable of broad angle perception, which makes them particularly advantageous for the efficient capture of solar radiation.

In this chapter, I detail the synthesis of core-shell nanowires with different material compositions and fabrication parameters, and investigate how these structures facilitate the trapping of light inside an absorptive layer located beneath an array of nanowires. ISR is capable of producing large-area, indefinitely long, uniform, flexible, self-aligned core-shell nanostructures, which I believe to be ideal for the purpose outlined in this chapter. Another important aspect of the present study is that the core-shell nanostructures utilized are composed exclusively of polymers. PC and PVDF, the polymer components in question, possess low-refractive indices, do not absorb in the visible region, are low-cost and do not generate hazardous waste products. In addition, the PVDF shell region of fabricated core-shell nanowires is strongly hydrophobic, which allows the nanofiber arrays to display self-cleaning properties. I also show that these 1D enhancement effects can be used in any thin-film solar cell, including a-Si, CIGS, CdTe, c-Si and pc-Si-based designs.

I engineer fabricated all-polymer core-shell nanowires to feature two complementary enhancement techniques in the same structure, such that absorption enhancement is caused by both NRM scattering and the textured surface effect. The former manifests as sharp peaks on the right (red) side of the absorption spectrum, which suggests that NRM scattering-based absorption enhancement occurs at specific wavelengths. These wavelengths can be altered by increasing or decreasing the diameter of the core-shell nanowires responsible for the enhancement, and absorption enhancement can be optimized by moving these peaks onto regions where the absorptive layer displays poor absorptive capacity. The core-shell geometry displayed by fabricated nanowires is advantageous because it stimulates more coupling modes than the bare nanowire geometry, and the shell region may allow efficient coupling by acting as a natural separator between core regions. The latter phenomenon, the textured surface effect, is dominant for smaller wavelengths, and occurs when the nanowire diameter is comparable to the wavelength of the incident light. This causes an anti-reflective effect analogous to the anti-reflective properties of lepidopteran eyes.

Absorption enhancement by all-polymer core-shell nanowires are demonstrated using both theoretical calculations utilizing a conventional a-Si thin film solar cell design, and experimental measurements with an As_2Se_3 absorbent layer.

9.1.1 Theoretical Investigation

Thin film solar cells utilized for theoretical investigations are composed of a silver back contact, an AZO layer, an amorphous silicon absorbent and an ITO front contact (Figure 9.1a). Simulations are performed with a monolayer of core-shell nanowires on this solar cell design, and are given in Figure 9.1b. An overall enhancement of ~14% can be achieved for unpolarized light in amorphous silicon cells. This value reaches around 20% when crystalline silicon is used as the absorbent material, and local enhancements are observed to exceed 300% in both cases. Simulations in Figure 9.1b are performed for TE polarization and the optical generation rate was calculated by integrating the product of solar spectrum intensities and the absorption within the silicon layer. Core diameter and shell thickness are set to 400 nm and 100 nm,

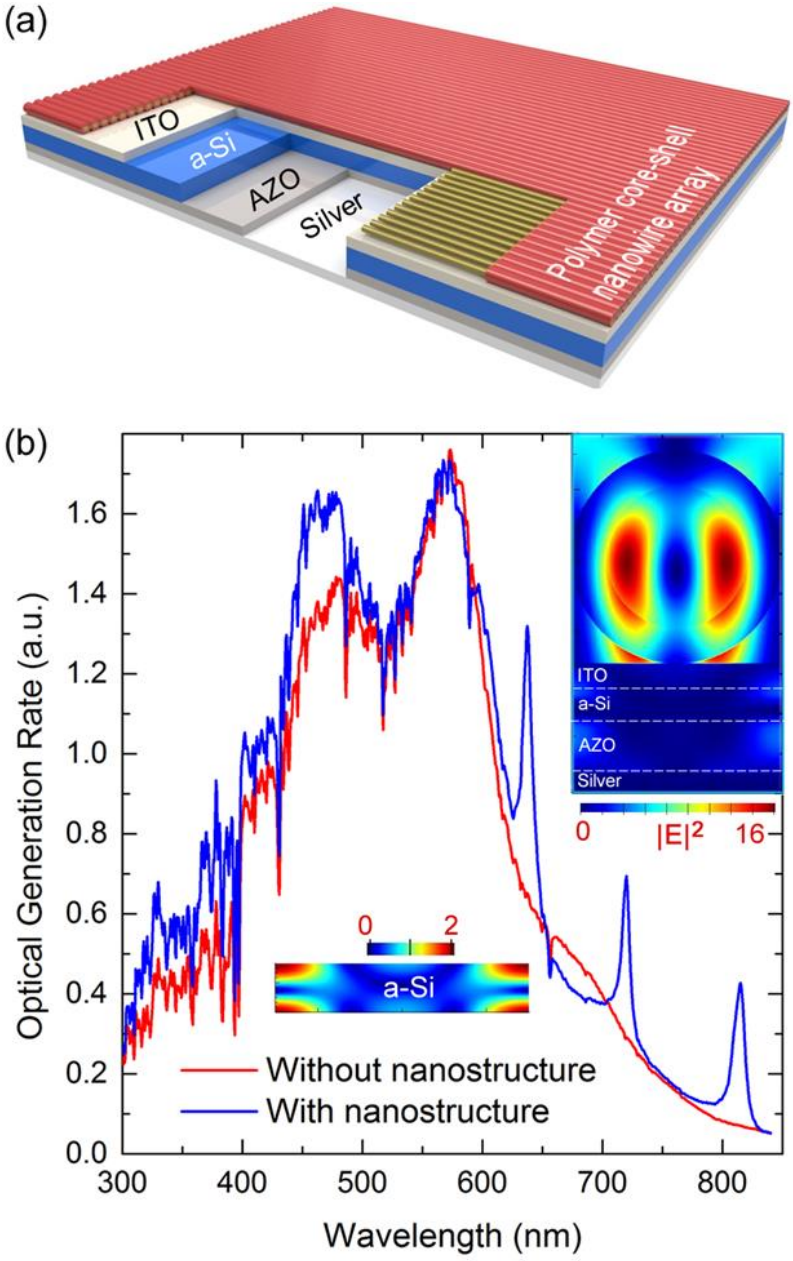

Figure 9.1: Absorption enhancement by all-polymer core-shell nanowires. Core-shell nanowire arrays were simulated on top of a conventional solar cell composed of a silver back contact, an AZO layer, an amorphous silicon absorbent and an ITO front contact. Textured surface and NRM based coupling effects (dominant on the left and right side of plot, respectively) result in enhanced absorption. TE polarization is used for the investigation of absorption enhancement, TM polarization yields similar results.

respectively. Periodic boundary conditions are utilized to simplify calculations. Similar enhancements can be observed for TM polarization.

Photons propagating throughout the nanowire and solar cell layers experience an adiabatic increase of refractive indices, passing successively through air to PVDF shell, PC core, ITO front contact and a-Si layers with refractive indices of 1, 1.41, 1.58, 2 and 4 (and after passing through these regions, light is reflected from the silver back contact to be absorbed further by the a-Si layer). The PVDF shell serves as a separator between nanowires, and is responsible for triggering what I describe as a 1D analogue to the antireflective properties of moth eyes. This effect is dominant on left side of the visible spectrum, and can be optimally utilized for absorption enhancement in regions where the absorbent layer already displays a strong absorption capacity.

Unlike texturing effect, NRM scattering is more effective in spectral regions where the absorbent material displays little to no absorptive capacity. In follows that, in an ideal absorption enhancer, the texture effect should be engineered to occur on the absorptive region, and NRM scattering peaks should fall on the tail of the absorption band, where little to no absorption is present.

Due to the forward scattering behavior characteristic to the NRM scattering regime, these nanostructures can efficiently increase the amount of collected light. The working principle behind this enhancement is a strong coupling between the core-shell nanowire and the thin layer amorphous silicon. It should be noted that the high refractive index silicon layer exhibits resonant characteristics by itself, while the low-refractive index core-shell nanowire does not. When brought in close proximity, however, these two layers exhibit a distinct near field profile within both the a-Si thin film and the core-shell nanowire (Insets in Figure 9.2 b). It is also significant that the nanowire array described in Figure 9.1a displays a scattering-based enhancement profile similar to those on single nanowires, as side coupling effects are suppressed in low-refractive index nanowires (Chapter 6). Enhancement profiles of TE and TM polarizations show slight differences in their scattering peaks, though they induce similar enhancement rates. Materials used in the composition of core-shell nanowires are optically compatible for scattering in the NRM regime.

Core-shell ***Type of absorbent***	**TE (%)**	**TM (%)**	**Average (%)**
PES/PVDF *a-Si*	15.65	14.74	15.2
PC/PVDF *a-Si*	14.75	13.45	14.1
PES/PVDF *Poly-Silicon*	21	17.25	19.125
PC/PVDF *Poly-Silicon*	19.54	17.53	18.53

Table 9.1. Different designs for light trapping. All-polymer core-shell nanowires induce absorption enhancements of ~14% for a-Si and ~20% for c-Si. Enhancement value are almost independent of polarization type.

Simulations are performed for different sizes, configurations (e.g. bare and core-shell nanowires) and compositions in order to understand the effects of size, geometry and material on the enhancement of light absorption.

Enhancement rates are observed to change significantly depending on the composition of the absorbent and coating layers. I performed simulations for core-shell nanowires and absorptive layers composed of a variety of materials, the results of which are given in Table 9.1. Calculations are performed for a fixed core diameter (400 nm) and shell thickness (100 nm). While PES cores are observed to be associated with higher enhancement values than PC cores, it must be noted that my simulations ignore absorption by the core region, and the higher absorption capacity of PES in lower wavelengths may render it an inferior material in practical applications. In addition, while crystalline silicon is observed to exhibit a higher absorption rate than its amorphous counterpart, higher production and processing costs associated with crystalline silicon discourages its use in solar cells, which are generally intended for large-scale production. Amorphous silicon can be procured in abundance and is relatively cost-effective, and therefore lends itself well for large-area fabrication efforts. PVDF is used as the shell layer in all calculations and is ideal for this purpose

due to its low refractive index and lack of absorption in the visible region. Simulated enhancement values take into account the contributions of both NRM scattering and the texture effect. Absorption enhancement values for TE and TM polarizations are generally comparable, despite displaying slight differences. I therefore conclude that the enhancement effect observed in my core-shell nanowires is nearly polarization-independent. As solar radiation is unpolarized and requires effective trapping for both polarization types, this property makes fabricated nanowire arrays effective enhancer agents for the trapping of solar energy.

Similar enhancement behaviors are also observed in other regular 1D and OD geometries. Potential absorption enhancers are required to possess low-refractive indices and sizes in the sub-micron scale in order to exhibit similar trapping effects, and simulations can be performed to determine the efficiency of various nanostructure geometries. I choose and compare bare and core-shell nanowire configurations due to their widespread usage and ease of scalability. Simulation results suggest that the core-shell arrangement is superior to bare nanowires for the enhancement of light absorption. This is due to a more effective coupling of NRM orders into silicon modes, a greater extent of adiabatic optical transition, and a better texturing effect. Intensity differences in three NRM scattering-induced peaks, which occur on the right side of the absorption spectrum in both cases, clearly demonstrate this point.

Peaks denoted “1”, “2” and “3” in Figure 9.2 are identical in position for both bare and shell-coated nanowires. However, the intensities of peaks 1 and 3 are suppressed in bare nanowires compared to the intensity profiles of their core-shell counterparts. Simulations are performed for same material composition, nanostructure size and polarization type (TE), and absorption enhancement rates for bare and core-shell geometries are calculated to be 16.5% and 18.5%, respectively. Enhancement values are calculated by comparing area-under-curve values of solar cell absorption spectra with and without nanostructure presence.

I also explore the effect of nanostructure size in the enhancement of thin film absorption by core-shell nanowires. Significant changes in the position and magnitudes of peaks are observed following the alteration of nanowire diameters.

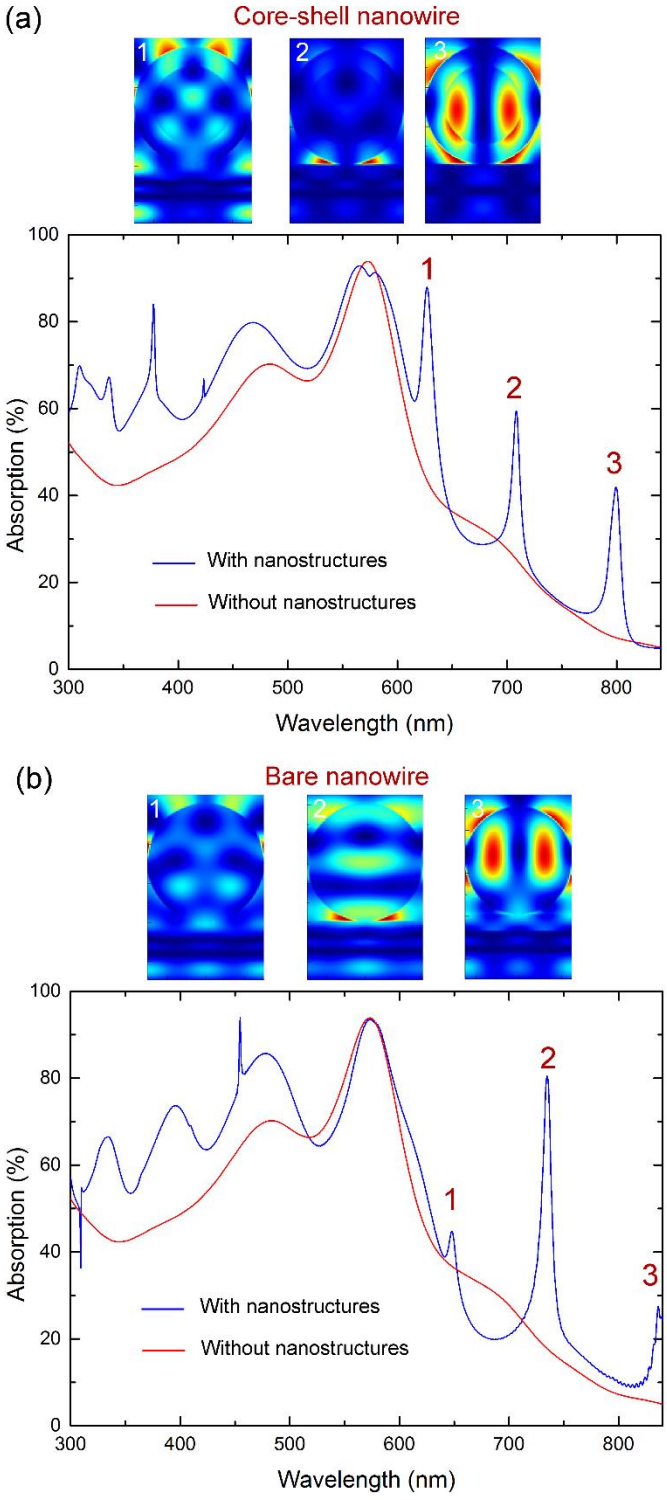

Figure 9.2: Nanostructure geometry has profound implications on the amount of absorption enhancement. Bare and core-shell nanowire geometries exhibit significant differences in enhancement rates. Absorption enhancement values of 16.5 and 18.5% are observed for bare and core-shell nanowires, respectively.

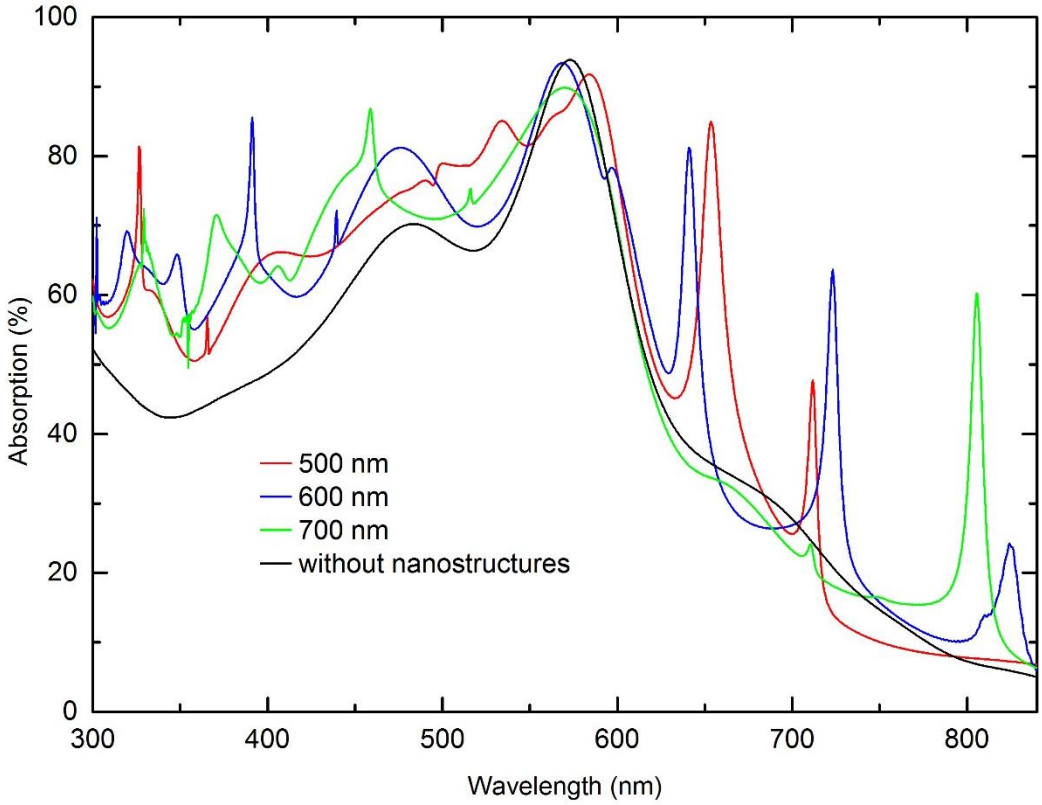

Figure 9.3: Effect of core-shell nanowire sizes on absorption enhancement, investigated using three nanowire diameters. Enhancement values are observed to be around 15%, 17.5 % and 14% for 500, 600 and 700 nm structures, respectively.

I perform simulations for three core-shell sizes of 500 nm, 600 nm and 700 nm, and calculate the optimal nanowire diameter to be around 600 nm (Figure 9.3). Coupling peaks experience blue- and redshifts for smaller and larger sizes, respectively, and a reduced number of scattering-induced coupling peaks are observed for non-optimal core sizes. The core-shell ratio is kept constant throughout the simulations, though the core is principally responsible for the effects observed.

Enhancement values of core-shell nanowires with overall diameters of 500, 600 and 700 nm are observed to be around 15%, 17.5 % and 14%, respectively. Shell sizes also affect the position of NRM scattering-based enhancement peaks. As such, both core sizes and separation distances (which scale with the shell thickness) can be altered to optimize the absorption enhancement process.

9.1.2 Experimental

ISR-mediated fabrication of monolayer-like nanowire arrays is described in Chapter 2. I use step III fibers containing shell embedded nanowires for the observation of the light trapping feature of low-refractive index nanostructures. PVDF and PC are the materials used as shell and core components, respectively. Instead of a solar cell, a bare-bones design containing a silicon substrate, silver back layer and As_2Se_3 absorber was utilized for the experimental demonstration of the absorption enhancement effect. As_2Se_3 glass is chosen for its high absorption capacity, especially in the visible spectrum.

The absorption profile of an As_2Se_3 thin film with a thickness of 80 nm is simulated prior to experimental measurements. In the presence of nanostructure-coated surfaces, two enhancement mechanisms are observed near the red and violet ends of the visible spectrum, caused by the texture effect on smaller wavelengths and NRM scattering-based coupling on higher wavelengths. The effect of NRM scattering in higher wavelengths is observed to be particularly pronounced, as As_2Se_3 does not normally absorb effectively in these wavelengths. An overall enhancement of ~24% was obtained for a core-shell nanowire diameter of 600 nm (Figure 9.4).

Experimental measurements are then performed in order to observe the enhancement of absorption in silver-As_2Se_3-core-shell nanowire system. The system in question is produced by coating a silicon substrate with 100 nm of silver and ~140 nm of As_2Se_3. A ~30 μm thick layer of free-standing planar nanowire arrays is utilized for absorption enhancement. This structure is produced by etching the outer PC layer of ISR-produced step III core-shell nanowires on a glass surface, which results in the production of sheathless nanowires linked by PVDF polymer shells.

This nanowire layer is then placed on the As_2Se_3 surface and utilized as a planar nanowire layer. Fabrication details are provided in Chapter 2, though here it is noted that the acquisiton of self-organized nanowire arrays without the use of dedicated steps for alignment or paralleling is a remarkable feature of described fabrication technique. Core-shell nanowires constituting the nanowire layer had average diameters of 600 nm.

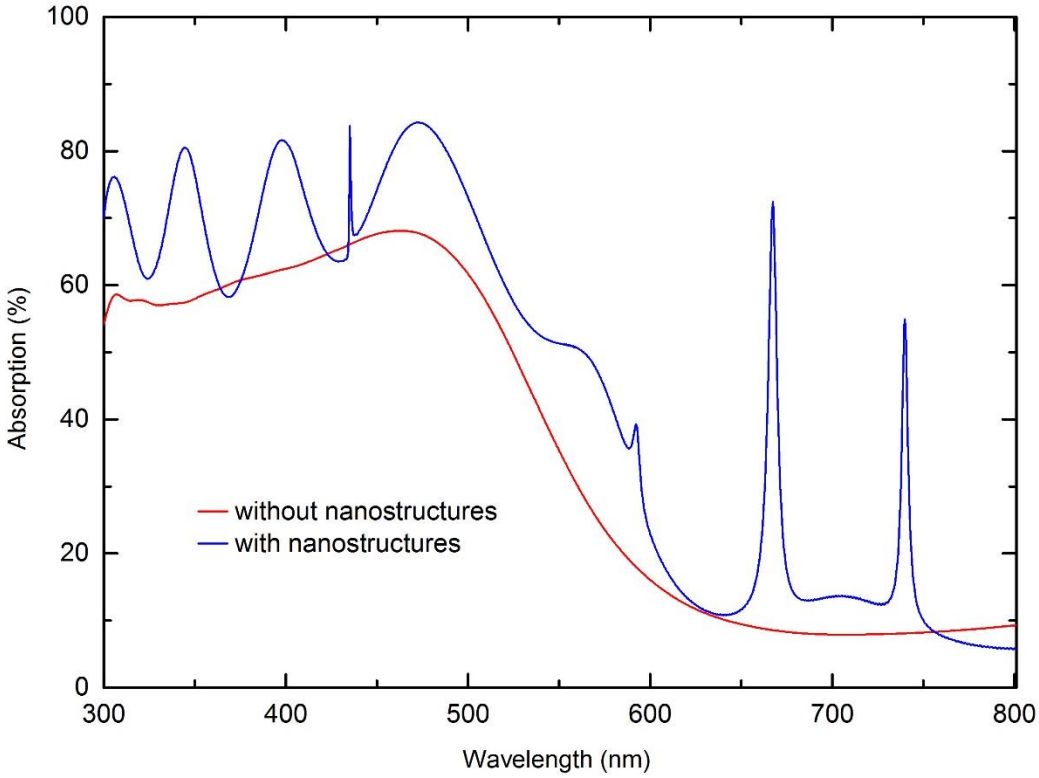

Figure 9.4: Nanostructure-mediated absorption enhancement of As_2Se_3. The enhancement rate is calculated to be ~24%. Both NRM scattering and textured surface effect participate in the absorption enhancement.

Measurements are performed under inverted light microscopy, reflection data of bare silver is used as a background prior to the measurement of uncoated and core-shell nanowire-coated samples. Sample measurements were divided by the reference spectrum prior to analysis and are given in Figure 9.5b. Significant amounts of absorption enhancement are observed in nanowire-supported absorptive surfaces, especially in the blue part of the visible spectrum (which is attributable to the texturing effect). Nanowire-coated surfaces display absorption enhancement values of ~6% compared to uncoated As_2Se_3 thin film layers. However, NRM scattering peaks are not observed in my experiments, possibly because a thicker As_2Se_3 layer (of 140 nm) was utilized for my experimental measurements. Absorption enhancement results are simulated using a thicker As_2Se_3 layer to further characterize this effect.

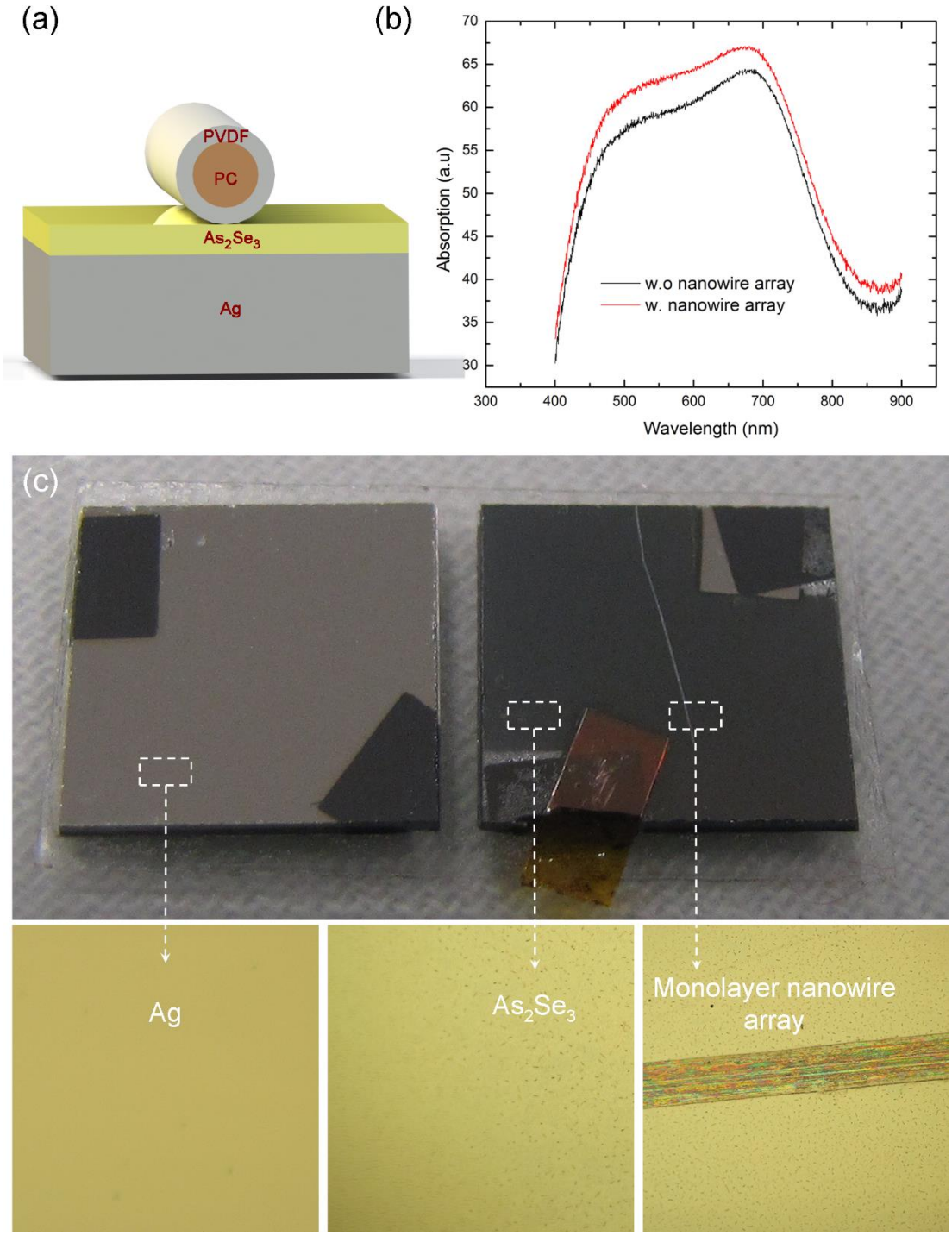

Figure 9.5: (a) Schematic used in the experiment. (b) Absorption measurement for As_2Se_3 thin film with and without core-shell naowires. Observed enhancement is around ~6 %. (c) Optical microscope images of coated silver, thin-film As_2Se_3 and monolayer nanowire layers.

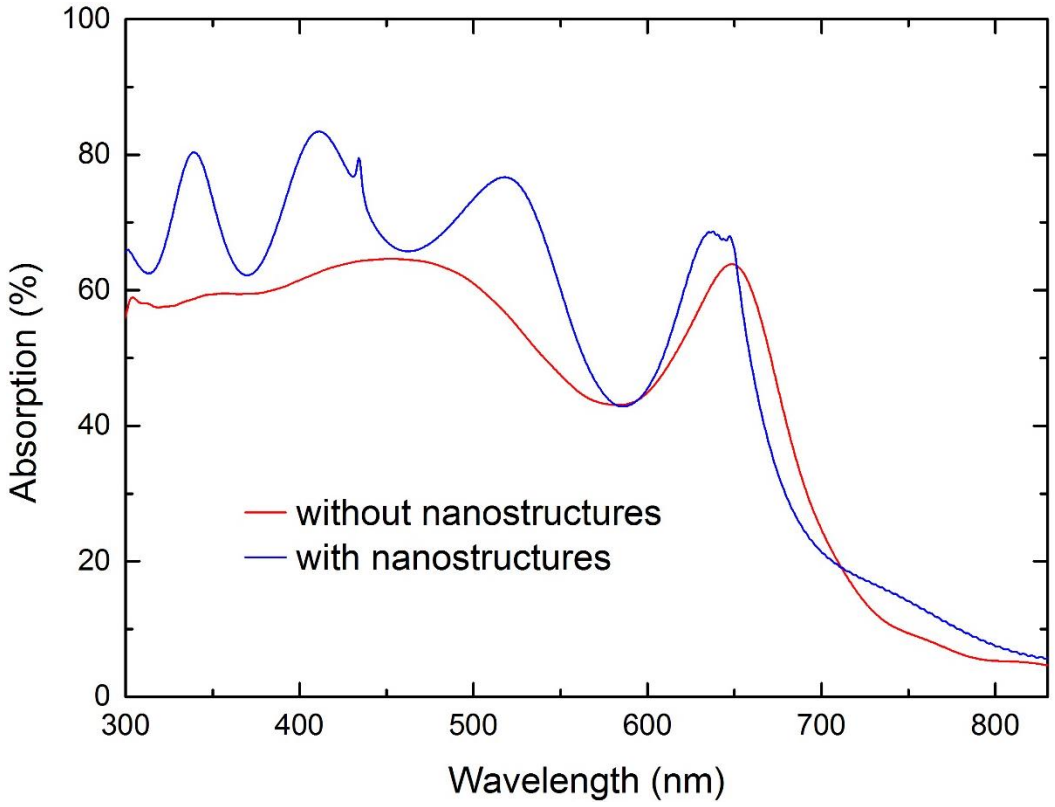

Figure 9.6: As we increase thickness of As_2Se_3 thin film its aborption profile red-shifts. All-polymer core-shell nanowires with diameters of 600 nm induce absorption enhancement of ~13.5 %. Obviously, textured effect is responsible in this enhancement and NRM scattering cannot contribute into this due to thicker absorbent layer.

The overall absorption profile of As_2Se_3 is different for bulk and thin films, and a broad absorption peak(s) dominates in the smaller wavelengths for a 80 nm thickness of As_2Se_3. This absorption peak displays a redshift when the film size is increased.

This observation is verified by simulating the absorption enhancement behavior of a 140 nm-thick As_2Se_3 layer. The absorption peaks of this thicker film appears in higher wavelengths of the visible spectrum, and the simulation results are in good agreement with my experimental measurements. As such, I conclude that thin As_2Se_3 layers are necessary for NRM scattering, and fabricated all-polymer core-shell nanowires cannot induce NRM scattering-based absorption enhancements on a 140 nm-thick layer of As_2Se_3, though textured effects still appear to be effective at this

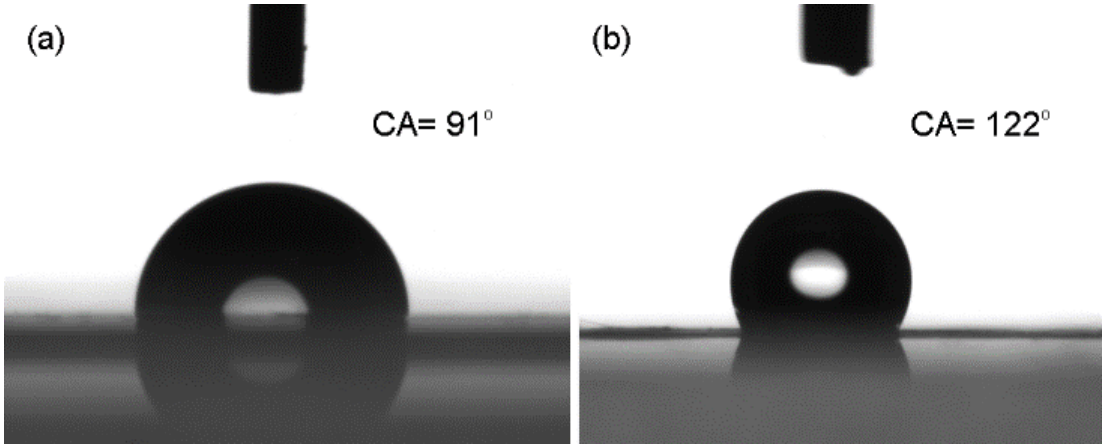

Figure 9.7: Contact angle measurement of (a) PVDF film and (b) nanowire array. PVDF polymer is hydrophobic by itself due to containing fluoride. However, core-shell nanowires add two degree of roughness which are originated due to; submicron roughness of core-shell nanowires and nano-roughness of PVDF shell.

thickness (Figure 9.6). The underlying reason behind NRM scattering-mediated absorption enhancement is the coupling effect between a-Si modes and NRM scattering orders. While this coupling is also expected to occur in thicker films, the NRM scattering bands probably occur outside the visible region (e.g. in higher wavelengths, such as NIR, which As_2Se_3 cannot absorb). The nanotexturing effect, however, is independent of absorbent film thickness, and can be observed even in thicker layers of As_2Se_3. An overall enhancement value of ~13.5% is calculated for the thicker layer of As_2Se_3 case. While my experimental results are lower than this predicted enhancement value, it must be noted that the non-uniform coating of the absorbent layer or the silver metal might have induced a detrimental effect on the enhancement process. Also, UV region does not contribute on measured enhancement data.

High surface hydrophobicities can allow many devices to exhibit self-cleaning properties. As solar cells are expected to withstand inclement weather for extended periods of time, self-cleaning is a very desirable property for surface materials used in these devices. I investigate the hydrophobic potential of fabricated core-shell nanowires, and observe contact angles of 90° and 122.1° for PVDF polymer films and

all-polymer core-shell nanowire arrays, respectively. PVDF is a fluoride-containing polymer, and fluorinated residues are well-known to promote hydrophobicity (Figure 9.7a). However, fabricated nanowire arrays are more hydrophobic than PVDF polymer films, suggesting that material composition is not the only factor determining the hydrophobicity of these nanostructures. It is suggested that the additional hydrophobic behavior is caused by the two-layered order of roughness inherent to fabricated all-polymer core-shell nanowires, where the sub-micron roughness of core-shell nanowire and the nano-roughness of PVDF shell both contribute to the hydrophobicity of described nanomaterial surfaces (Figure 9.7b).

9.2 Sensor Applications

9.2.1 NRM Scattering based Sensor

Optical nanosensors are another area that can benefit immensely from materials displaying NRM scattering-based effects. Dielectric materials find widespread use in resonator-based sensor systems as microspheres, photonic crystals, microcapillaries and diffraction gratings [133]. A tradeoff between detection limit and sensitivity is generally observed in these systems. Both parameters can be significant in specific applications. For example, detection limit is a crucial for molecular level sensing, while sensitivity can become important in color sensors [134].

Sensitivity values of NRM scattering results are highly promising for refractive index-based sensor applications. Present NRM scattering-based method increases the sensitivity of all low-index nanostructure-based measurement efforts, though at the expense of a low detection limit. In resonant Mie scattering, changes in the refractive index of the surrounding medium generally do not induce significant spectral shifts. However, when optical index of the ambient medium is increased from 1 to 1.4 with increments of 0.05, the broad peak of NRM-scattered light blueshifts and narrows in a refractive index-dependent manner for core-shell nanostructures (Figure 9.8a). Sensitivity values over 2000 RIU/nm are observed for core radii higher

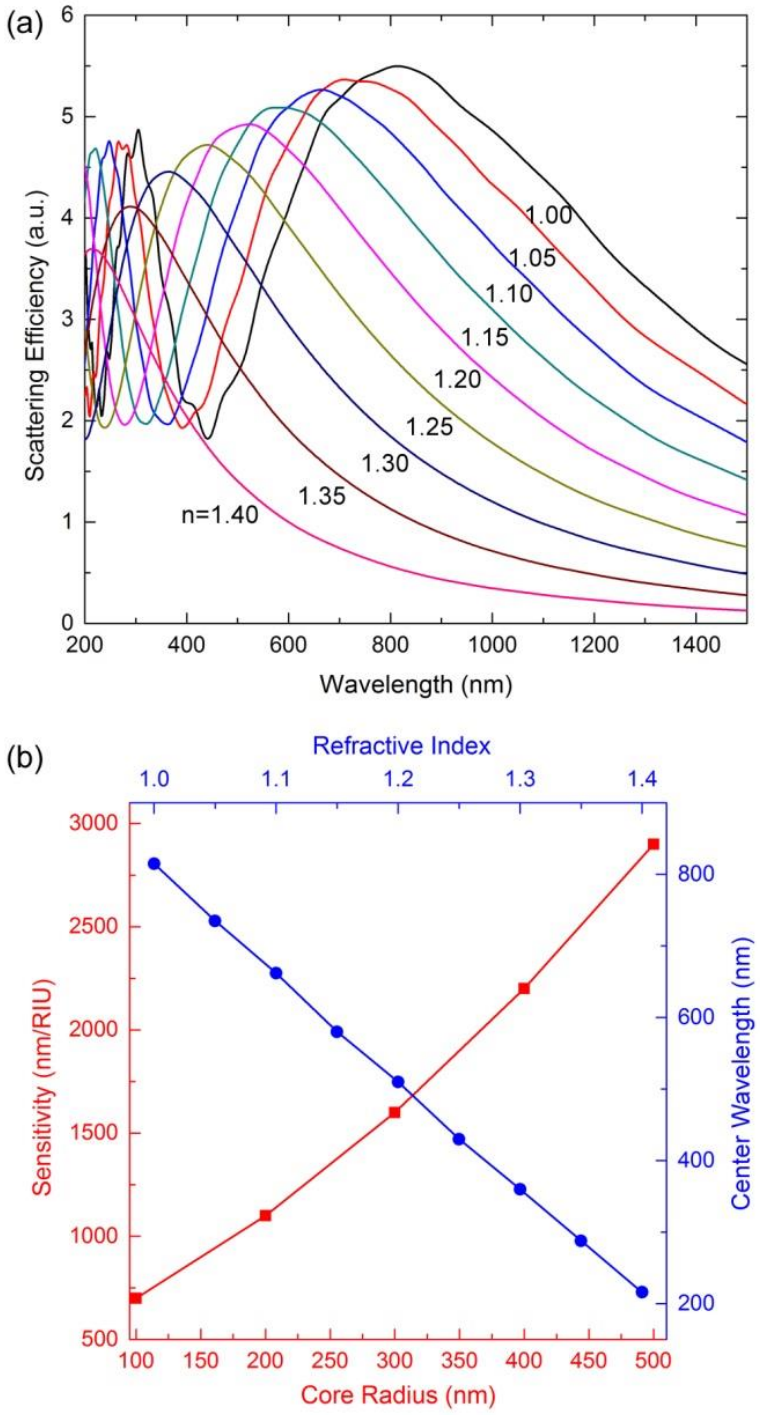

Figure 9.8: Sensitivity parameters of NRM scattering. (a) Rapid shifts in scattering spectra can be observed by changing the refractive index of the medium surrounding core-shell structures with core radii of 300 nm, and correspond to high sensitivity values. (b) Size-dependent sensitivity values (left and bottom axes) plotted with medium-dependent shifts of the center wavelength (right and top axes).

than 400 nm. For these sizes, NRM scattering peaks appear in the near infrared region, though embedding the nanostructures in any common solvent will be adequate to pull the NRM peaks into the visible region (Figure 9.8b). To the best of my knowledge, NRM scattering-based detection method reaches record values in sensitivity among any sensor scheme, and is superior to cutting-edge plasmonics sensors in the visible spectrum [135].

9.2.2 Nanoshell Interference based Sensor

Thin film interference-based sensors are well-known for their sensitivity [136]. I explore the sensitivity of the nanoshell interference effect on nanoshell-covered microspheres by simulating the changes in the intensity spectra of these particles in different media. It is apparent that the intensity of reflection decreases as the refractive index of surrounding medium is increased (Figure 9.9). This effect can be utilized in the design of refractive index-based sensors.

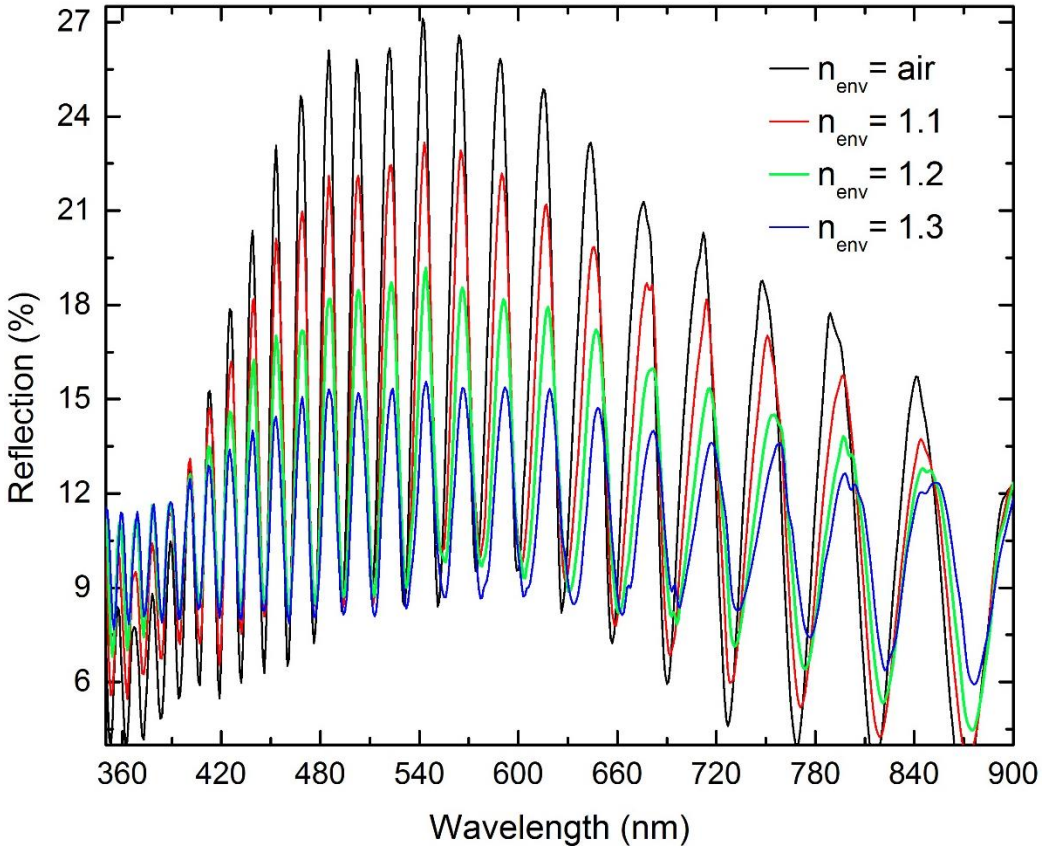

Figure 9.9: Changes in nanoshell interference-based reflection values depend on the refractive index of the surrounding medium, which may be utilized in optical sensors. Reflection intensity determines the performance of sensitivity.

Chapter 10

Supercontinuum Generation in Nanowire Arrays

10.1 Introduction

Chalcogenide nanowires exhibit many of the common features associated with nano-scale materials, such as low power consumption, high speed and high density packing, which have made them very attractive for various applications in non-volatile phase change memory construction. In addition, because these glasses generally have exceptionally high nonlinear optical constants, they are highly suitable for nonlinear photonics applications such as optical switching and supercontinuum generation. The development of fabrication methods for the production of complex chalcogenide nanowire structures is necessary to improve their performance, and may result in the discovery of novel functionalities in this class of nanomaterials. Here I report the first successful fabrication of ordered long arrays of chalcogenide nanowires, and theoretically demonstrate that the synthesized nanowires can be utilized for the generation of extreme supercontinua. The principal advantage of the structures produced in their high power throughput and broad spectrum generation. Supercontinuum

generation [137,138,139] is mainly utilized in photodynamic therapies, optical tomography, telecommunication, spectroscopy, optical frequency metrology and for military applications.

10.2 Nonlinear Fiber Optics

The response of a given material to light depends on many parameters. Light is linearly polarized when it interacts with conventional dielectric materials, which can be expressed as following;

$$P = \varepsilon_0(\chi^{(1)} \cdot E + \chi^{(2)} : EE + \chi^{(3)} \vdots EEE + \cdots)$$

The second or higher terms are negligible for linear material response, and the equation is reduced to the first term. Material response will depend on higher terms when significant fluctuations occur on the intensity of the electric field, or when material properties are altered . Nonlinear optics should be utilized in such cases [140].

The higher order terms become significant for nonlinear material responses, and each term must be characterized separately in such occassions. The electric field is a crucial parameter for the observation of nonlinear phenomena. As such, stronger electric fields may render higher terms more significant. However it should be noted that very high intensities are inapplicable and undesirable in many cases because of power dissipation and the destruction of the interacting material.

Short pulse durations are frequently used to increase the power output, and mode-locking can be utilized to provide pulse durations in the femtosecond scale. Peak power and average power outputs scale with pulse duration and widths. While average powers

are generally in the mW level, peak powers can reach several MWs with the use of very short pulses. Such power levels are required in many high-power applications.

Material properties can also be manipulated to alter the nonlinear material response. It is, for example, possible to select materials with higher $\chi^{(2)}$ and $\chi^{(3)}$ terms, which are related to the nonlinear material indices of the material in question.The term $\chi^{(2)}$ is responsible many interesting nonlinear effects, including sum and difference frequency generation and optical parametric oscillation, while the third-order term, $\chi^{(3)}$, may facilitate the observations of optical Kerr effect, self-phase modulation, cross-phase modulation, third harmonic generation, four wave mixing, two photon absorption, stimulated Raman scattering and stimulated Brillouin scattering. It should be noted that inversion symmetry occurs in many glasses, which renders $\chi^{(2)}$ negligible. However, this term is significant for certain other materials, and several methods can be utilized to artificially break the inversion symmetry.

One of the most important applications of nonlinear material–light interactions is in the generation of supercontinua, which is generally observed to occur in waveguides. This phenomenon is associated with the spectral broadening of light, mainly by the self-phase modulation effect.

As_2Se_3 possesses one of the highest nonlinear refractive index coefficients among any material, andits main transparency window extends from ~700 nm to ~16 μm. These two features render this glass an ideal choice for observing supercontinuum generation in the telecommunication band or IR regions.

Several studies have been conducted on the observation of spectral broadening in As_2Se_3 waveguides [141], and this material was observed to substantially decrease the threshold point of broadening. However, current methods are inadequate for generating sufficient light intensities to warrant the use of As_2Se_3 waveguides in practical applications. Therefore a pre-amplifier is generally used in order to increase the power of the supercontinuum light, which increases system costs and power consumption.
Here I detail the observation of the supercontinuum effect on an As_2Se_3 glass nanowire array, and demonstrate that proposed novel scheme is highly advantageous for the generation of high power outputs, with higher powers being associated with greater nanowire numbers within the array.

10.3 Pulse Propagation Inside the Fiber

The pulse propagation inside a fiber is governed by the nonlinear Schrödinger equation.

$$\frac{\partial A}{\partial z} + \frac{\alpha}{2}A + i\frac{\beta_2}{2}\frac{\partial^2 A}{\partial t^2} = i\gamma|A|^2 A$$

The first term corresponds to propagation in the spatial domain. The second and third terms represent losses and dispersion. The last term stands for nonlinearity.

$\beta_2 = (\frac{d^2\beta}{d\omega^2})$, is the group velocity dispersion parameter;

$\gamma = \frac{n_2\omega_0}{CA_{eff}}$, is the nonlinear parameter;

α, is the absorption coefficient of the material;

Nonlinear and dispersion lengths (which represent the distances at which nonlinearity and dispersion start to appear) can also be derived from this equation, and are expressed as;

Dispersion length: $L_D = \frac{T_0^2}{|\beta_2|}$

Nonlinear Length: $L_{NL} = \frac{1}{\gamma P_0}$

Dependance of the refractive index on optical intensity can be defined as;

$$n(\omega, I) = n_0(\omega) + n_2 I(t)$$

Frequency dependency is responsible for dispersion and pulse broadening, while intensity dependency leads to a nonlinear phase shift and, consequently, spectral broadening. This phase shift can be expressed as;

$$\Phi_{NL}(t) = \frac{2\pi}{\lambda} n_2 I(t) L$$

Therefore, the pulse experiences pulse shifts as it propagates, which results in spectral changes. If phase matching is satisfied, many effects (SPM, XPM, HHG, FWM) can be observed to occur simultaneously in the output of the fiber. Nonlinearity is therefore significantly affected by material parameters (n_2), propagation lengths and the intensity of light.

10.4 Dispersion Engineering

The high material dispersion of As_2Se_3 leads to only a moderate spectral broadening in visible or near IR regions. However it is possible to find a region where dispersion does not occur by taking into account the waveguide dispersion. At this "zero point", the pulse can propagate through the fiber without experiencing distortion. The total dispersion can be defined as;

Total Chromatic Dispersion = Material Dispersion + Waveguide Dispersion

Each factor should be considered individually. To this end, I calculate and provide the wavelength dependent dispersion data of As_2Se_3 glass (Figure 10.1). Dispersion characteristics of As_2Se_3 is obtained by fitting the refractive index data of As_2Se_3 into the Sellmeier equation. Dispersion in As_2Se_3 glass is found to be higher in the standard telecommunication wavelength (1.55 μm).

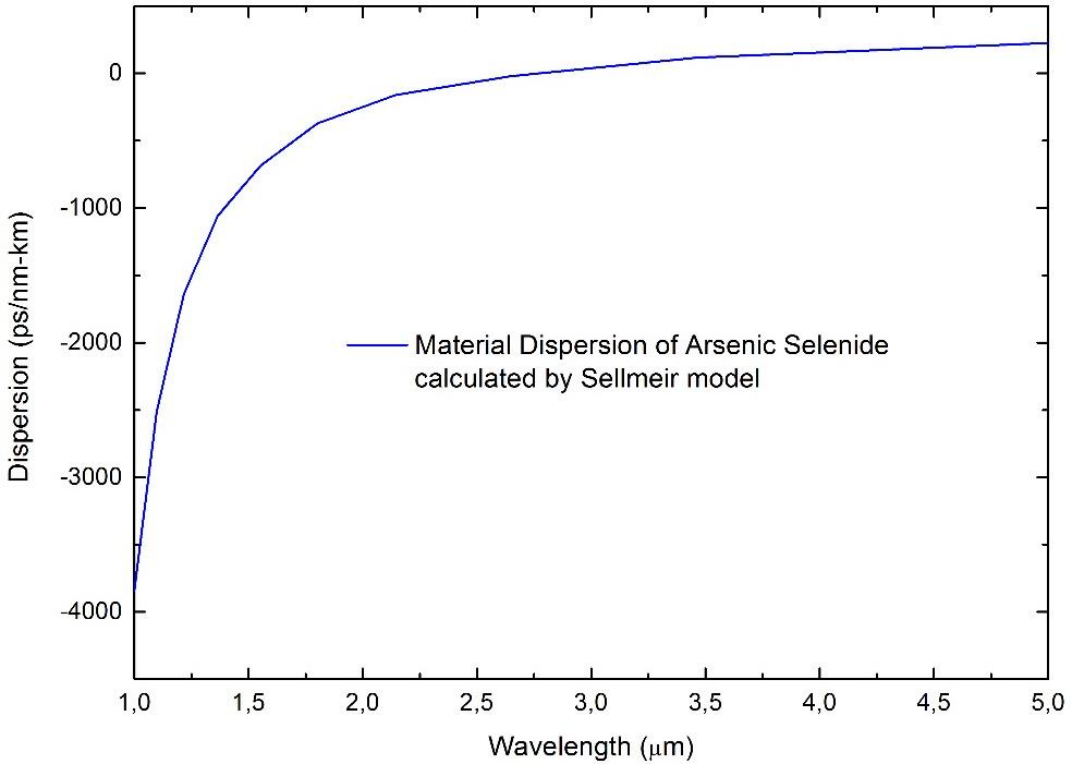

Figure 10.1: Material dispersion is derived from material parameters of As_2Se_3 glass (*n,k*) by implementing Sellmeir model. Dispersion in the 1.55 μm wavelength is very high and can distort femtosecond pulse in short propagation distances.

D is -805.4 ps/nm/km for bulk As_2Se_3 material. While material dispersion is an intrinsic feature of the material in question and cannot be altered via any external modification, waveguide dispersion can be altered by changing the diameter of the fiber waveguide. I calculated waveguide dispersion of As_2Se_3 in fibers with varying diameters, using MODE Solutions to simulate the dispersion results for a wavelength of 1.55 μm (Figure 10.2). Material dispersion results were then utilized to find the zero dispersion diameter of As_2Se_3 fibers. The zero dispersion point was calculated to be ~1 μm for a wavelength of 1.55 μm.

Zero dispersion points have also been calculated for other wavelengths. Figure 10.3 demonstrates that nanowires can be utilized effectively for a wide range of wavelengths without experiencing pulse distortion. Smaller wavelengths appear to require smaller nanowire diameters.

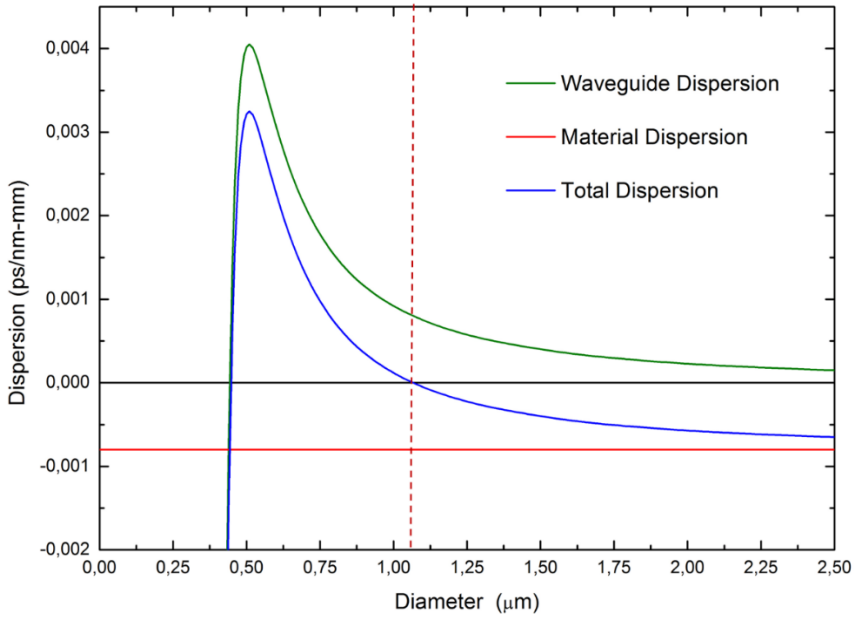

Figure 10.2: Dispersion engineering with waveguide dispersion and material dispersion. Zero dispersion point for 1.55 μm wavelength calculated to be at ~1 μm core diameter.

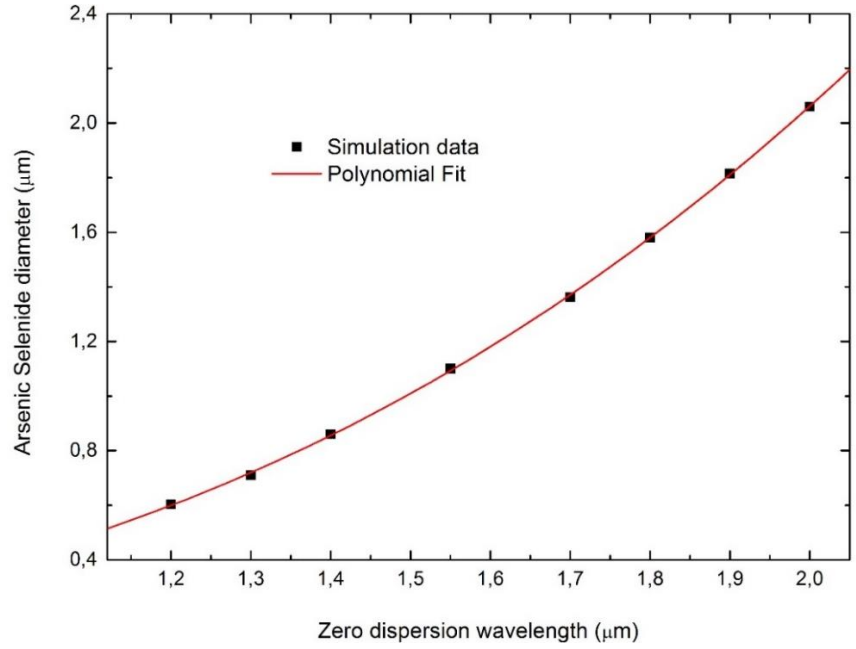

Figure 10.3: Zero dispersion points for different operating wavelengths. Material dispersion alters as the wavelength changes. Therefore waveguide size required to be set accordingly in order to compensate material dispersion with waveguide dispersion.

10.5 Supercontinuum Generation in Nanowire Array

In order to examine the nonlinear features of the nanowire array, I perform a set of FDTD simulations using a zero dispersion diameter corresponding to a wavelength of 1.55 μm. I defined pulse width as 250 fs. Operation wavelength was set at 1.55 μm. In order to decrease simulation times, I used a smaller length of nanowires (2 μm). However, I compensated for this change by using a higher power intensity input of 2.65 kW/μm^2. The nonlinear index of the nanowires was set at $n_2=1.6\text{x}10^{-17}$ m^2/W. I ran simulations for both single nanowires and a nanowire array containing 20 equally spaced nanowires. During simulation, I inserted both the nonlinear refractive index coefficient and the material (*n*,*k*) data in order to account for both nonlinearity and dispersion.

Simulation results obtained for both cases are given in Figure 10.4. It is curious that the nanowire array induced the spectral broadening ($\Delta\lambda\approx400$ nm) of the incident femtosecond light, while single nanowires ($\Delta\lambda\approx100$ nm) did not display such an effect significantly under identical light intensity and propagation lengths. Here I also demonstrate that the power output scales with the number of nanowires in the array. It is suggested that, for a sufficiently high number of nanowires, fabricated in-fiber nanostructures can directly be used as a supercontinuum source without requiring the amplification of the power input.

Another nonlinear effect is high harmonic generation (HHG) (Figure 10.4). Third and fifth harmonics modes, which correspond respectively to wavelengths of ~500 and 300 nm, are generated as a result of nonlinear light-matter interactions. The nanowire array is again superior to the single nanowire under identical illumination conditions.

In conclusion, the novel in-fiber nanowire arrays described in the present chapter are remarkably easy to produce and handle, allow the generation of high power, wavelength-scalable supercontinua, and bear vast implications in nonlinear nanowire photonics.

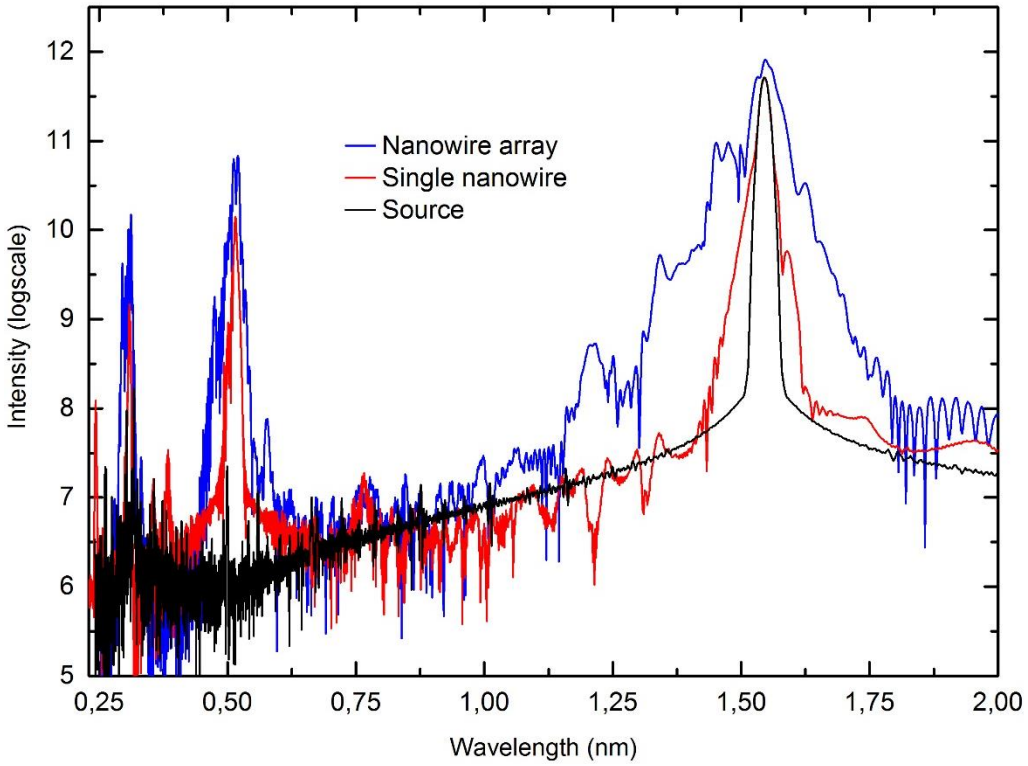

Figure 10.4: Supercontinuum generation from nanowire array. Nanowire array induce efficent supercontinuum generation and supply higher power output in compare to single nanowire under same illumination conditions. Pulse width of source defined as 250 fs. Supercontinuum generation phenomenon is associated with self-phase modulation effect. Third and higher harmonics generation appear in the left portion of spectrum.

Chapter 11

Conclusions

The present work describes the fabrication of novel core-shell nanostructures by using two novel fabrication techniques in conjunction, and demonstrates that the nanostructures fabricated by this combination method are highly suitable for a wide range of both emerging and well-established photonics applications. Proposed fabrication scheme encompasses two straightforward methods that can be utilized for the production of a tremendous diversity of nanostructures.

First, I describe a novel fabrication technique, Iterative Size Reduction (ISR), for the production of indefinitely long glass-polymer core-shell nanowires by the heat-mediated elongation of a macroscopic preform. Using this method, core-shell nanowires with diameters as low as 10 nm even below can be produced within three drawing steps. ISR-produced in-fiber nanowires are highly uniform in radial and axial scales, and a broad size range of micro- and nanostructures can be fabricated by altering the reduction factor during any of the drawing steps involved. Materials utilized in described fabrication technique are chalcogenide glasses and high temperature engineering polymers, which bear similar glass transition characteristics and allow the drawing process to occur at relatively low temperatures. However, this technique can be extended to any combination of materials, provided that each

component displays a similar set of thermoplastic properties. Using described novel fabrication method, I also report the first successful production of all-polymer core-shell nanowires, and demonstrate these nanostructures to be sufficiently uniform and smooth to be utilized in many optical applications. In addition to 1D nanostructures, ISR may potentially be utilized in the fabrication of other photonic structures. This functionality is demonstrated by synthesizing all-polymer photonic crystal structures with rectangular cross sections in three iterative fabrication steps, and by producing a monolayer of 1D nanostructures capable of aligning without the use of conventional post-synthesis treatments. These nanostructures are highly promising in a variety of applications, especially as antireflective coatings on optoelectronic devices.

Then I modify described nanofabrication method with an additional step to facilitate the production of a vast array of complex core-shell nanostructures. This additional step relies on Rayleigh-Plateu instabilities to mediate the fragmentation of an ISR-produced nanowire into a series of novel core-shell nanostructures. These structures exist in a transitory temperature region immediately preceding the conversion of core-shell nanowires into core-shell nanospheres. Large-area, size-controlled nanosprings, nanorods, nanospheres, nanochains can be produced prior to the complete fragmentation of the nanowire array. By combining ISR with this novel thermal modification process, I describe a low-cost, high-throughput process by which globally aligned, arbitrarily long arrays of hierarchical nanostructures can be produced within a robust polymer sheath, circumventing handling issues associated with previous nanostructure platforms and allowing simple macroscopic manipulation of the composite fiber. The capacity to produce single and multimaterial nanostructures in flexible fibers has widespread and profound implications in a large host of fields, as the method in question is applicable for different start configurations and can be tailored for the intrinsic optical, electrical, mechanical and/or thermal properties of the material components.

I observe and report that a variety of rare and potentially important optical phenomena take place on core-shell nanostructures produced by decsribed novel combination of fabrication methods. These phenomena, and their potential applications, are listed as follows.

I describe light scattering from high-refractive index deep-subwavelength particles using fabricated glass-polymer core-shell nanowires and nanospheres. Theoretical calculations are performed under Mie theory to describe the scattering behavior of both nanostructure types, and both nanowires and nanospheres are designed for large-scale structural coloration. I also demonstrate that fiber-embedded one dimensional nanostructures can also be designed, singly or collectively, as iridescent or solid color centers for array- or photonic crystal-based coloration. In addition to potential applications in textile and decoration industries, these nanostructures can be used as functional modules in solar cell concentrators, stimuli responsive polymers and biological imaging applications. Two-dimensional lattices of fabricated nanowires may potentially exhibit a negative index of refraction at the optical domain, and one-dimensional coupled nanowire arrays can be used to generate slow-light. In-fiber obtained nanostructures may also facilitate the development of in-fiber nanodevices with significant advantages over on-chip devices.

I explore an obscure light scattering phenomenon which I observe in fabricated all-polymer core-shell nanowires, and infer to potentially extend to any low-index, wavelength-scalable material. This effect results in the creation of a non-resonant Mie regime, which displays significant differences compared resonant Mie scattering and is characterized by a number of promising optical features. In clear contrast to characteristic Mie scattering, I observe strictly forward-scattered and coupling-free optical fields in the vicinity of the nanostructures for both polarizations of the incident light. Scattering characteristics of this regime are thoroughly investigated and proposed for diverse applications, including structural coloring and nano-photolithography. Directional, polarization-independent and coupling-free Mie scattering from cylindrical and spherical low refractive index nanostructures has highly promising optical properties that may prove critical in a number of nanotechnology applications.

I confirm the presence of the thin film interference phenomenon on small size scales, which I henceforth call “nanoshell interference”, by characterizing the interaction of visible light with glass-polymer core-shell spheres with diameters around 1-2 μm. I detail the creation of thickness-dependent vivid hues via nanoshell-induced interference, and demonstrate that the effect in question displays significant

advantages compared to conventional thin film interference. Nanoshell interference may potentially facilitate the design of novel photonic devices and characterization methods, and I propose that this phenomenon can be utilized in size determination and mapping applications for the investigation of core-shell nanostructure behavior, which may be difficult to characterize by conventional means.

I investigate the unusual photonic crystal structures responsible for structural coloration in mallard neck feathers, and identify the responsible elements as melanin rods embedded a keratin matrix. Selective advantages of the coloration and UV reflection observed in mallard feathers are discussed. Barbules responsible for coloration display a high aspect ratio and a rectangular cross section, and are mimicked for the first time using all-polymer core-shell nanowires fabricated by ISR. Fabricated mallard-mimetic photonic crystals are biocompatible and flexible, and can be produced in arbitrary lengths. In addition to coloration, these photonic crystal structures are promising for sensor applications.

I investigate two distinctive light-trapping effects on all-polymer core-shell nanowires and provide evidence that absorption enhancements observed as a result of these light-trapping phenomena are applicable to third generation optoelectronic devices such as thin film solar cells. The trapping of light in core-shell nanowires is based on two simple but powerful optical effects: NRM scattering, which strongly scatters light in the forward direction, and texturing effect, which minimizes light reflection and is a 1D analogue of the anti-reflective properties observed in moth eyes. All-polymer core-shell nanowires are chosen due to their ease of fabrication and exceptional optical properties. Proposed novel nano-platform is easily scalable across a wide size range and permits the efficient coupling of light into the modes of a thin-film absorbent layer, especially compared to bare nanowires. Overall enhancement values observed as a result of these two effects can be as high as ~14% for a-Si and ~20% for c-Si. Local enhancements can exceed 300%. I also demonstrate that fabricated all-polymer core-shell nanowires display increased hydrophobicity, possibly due to their possession of two different scales of roughness (submicron-scale roughness on nanowires and nanoscale roughness on the shell region), which renders them suitable for the production of self-cleaning solar cells.

I perform NRM scattering and nanoshell interference simulations to show that fabricated glass-polymer and all-polymer nanowires are highly suitable for a variety of sensing applications. Record sensitivity parameters are observed for NRM scattering from all-polymer nanowires, and the sensory potential of nanoshell interference is demonstrated by recording changes in reflection spectra in response to environmental cues. These features can be utilized to great effect for refractive index-based sensor applications.

Finally, I take advantage of the high nonlinear refractive index of As_2Se_3 glass to generate supercontinua in core-shell nanostructures. To this end, I minimize potential pulse distortions experienced during light propagation by calculating the region at which the dispersions caused by waveguide and material effects negate each other. I then show that nanowires with diameters equal to this zero disperison point can be utilized as effective supercontinuum generators. I demonstrate that the use of a nanowire array is more effective than a single nanowire for the generation of supercontinua. Remarkable power outputs are observed following light propagation through the entire length of the fiber array, and the output is found to be proportional to the number of equally spaced nanowires present in the nanowire array. In addition, identical light intensities are observed to induce the generation of broader spectra in arrays, compared to single nanowires. It is suggested that these properties render described fibers feasible for direct utilization in many applications without the use of a power amplifier.

I conclude that described fabrication techniques and the nanostructures I produced can meet the rigorous demands of many cutting-edge optical applications, and provide a remarkable combination of advantages compared to many top-down and bottom-up approaches. Fabricated novel core-shell nanostructures may spur the development of practical applications based on a wide variety of nanoscale phenomena, and facilitate the observation of many yet-unknown optical features. In addition, the novel photonics applications demonstrated in this work may perhaps assist in the solution of many global challenges regarding energy, health, security and the environment.

Bibliography

[1] N. I. Zheludev, "What diffraction limit?," *Nature Mater.*, vol. 7, p. 420, 2008.

[2] D.K. Gramotnev and S.I. Bozhevolnyi, "Plasmonics beyond the diffraction limit," *Nature Photon.*, vol. 4, p. 83, 2010.

[3] H. C. Hulst, "Light scattering: by small particles," *Courier Dover Publications*, 1957.

[4] L. Hu, and G. Chen, "Analysis of optical absorption in silicon nanowire arrays for photovoltaic applications," *Nano Lett.*, vol. 7, p. 3249, 2007.

[5] Y. Akahane, T. Asano, B. S. Song and S. Noda, "High-Q photonic nanocavity in a two-dimensional photonic crystal," *Nature*, vol. 425, p. 944, 2003.

[6] K. Seo, M. Wober, P. Steinvurzel, E. Schonbrun, Y. Dan, T. Ellenbogen and K. B. Crozier, "Multicolored vertical silicon nanowires," *Nano Lett.*, vol. 11, p. 1851, 2011.

[7] R. Sapienza, P. D. Garcia, J. Bertolotti, M. D. Martin, A. Blanco, L. Vina, C. Lopez and D. S. Wiersma, "Observation of resonant behavior in the energy velocity of diffused light," *Phys. Rev. Lett.*, vol. 99, p. 233902, 2007.

[8] L. Cao, P. Fan, E. S. Barnard, A. M. Brown and M. L. Brongersma, "Tuning the color of silicon nanostructures," *Nano Lett.*, vol. 10, p. 2649, 2010.

[9] Y. H. Fu, A. I. Kuznetsov, A. E. Miroshnichenko, Y. F. Yu and B. Luk'yanchuk, "Directional visible light scattering by silicon nanoparticles," *Nature Commun.*, vol. 4, p. 1527, 2013.

[10] J. Zi, X. Yu, Y. Li, X. Hu, C. Xu, X. Wang, X. Liu and R. Fu, "Coloration strategies in peacock feathers," *Proc. Natl. Acad. Sci.*, vol. 100, p. 12576, 2003.

[11] S. J. Wilson and M. C. Hutley, “The optical properties of moth eye antireflection surfaces,” *J. Mod. Opt.*, vol. 29, p. 993, 1982.

[12] H. Deniz, T. Khudiyev, F. Buyukserin and M. Bayindir, “Room temperature large-area nanoimprinting for broadband biomimetic antireflection surfaces,” *Appl. Phys. Lett.,* vol. 99, p. 183107, 2011.

[13] M. Sayer and K. Sreenivas, "Ceramic thin films: fabrication and applications," *Science*, vol. 247, p. 1056, 1990.

[14] P. J. Sazio, A. Amezcua-Correa, C. E. Finlayson, J. R. Hayes, T. J. Scheidemantel, N. F. Baril, B. R. Jackson, D. J. Won, F. Zhang, E. R. Margine, V. Gopalan, V. H. Cresp and J. V. Badding, “Microstructured optical fibers as high-pressure microfluidic reactors,” *Science*, vol. 311, p. 1583, 2006.

[15] A. P. Suryavanshi, J. Hu and M. F. Yu, “Meniscus-controlled continuous fabrication of arrays and rolls of extremely long micro- and nano-fibers,” *Adv. Mater.,* vol. 20, p. 793, 2008.

[16] J. C. Hulteen and R. P. Van Duyne, “Nanosphere lithography: A materials general fabrication process for periodic particle array surfaces,” *J. Vac. Sci. Technol., A,* vol. 13, p. 1553, 1995.

[17] B. Tian, P. Xie, T. J. Kempa, D. C. Bell and C. M. Lieber, “Single-crystalline kinked semiconductor nanowire superstructures,” *Nature Nanotech.*, vol. 4, p. 824, 2009.

[18] P. Caroff, K. A. Dick, J. Johansson, M. E. Messing, Deppert, K. and L. Samuelson, “Controlled polytypic and twin-plane superlattices in III–V nanowires,” *Nature Nanotech.,* vol. 4, p. 50, 2009.

[19] H. Wang, C. S. Levin and N. J. Halas, “Nanosphere arrays with controlled sub-10-nm gaps as surface-enhanced Raman spectroscopy substrates,” *JACS*, vol. 127, p. 14992, 2005.

[20] P. Yang, "Nanotechnology: Wires on water," *Nature*, vol. *425*, p. 243, 2003.

[21] P. A. Smith, C. D. Nordquist, T. N. Jackson, T. S. Mayer, B. R. Martin, J. Mbindyo and T. E. Mallouk, "Electric-field assisted assembly and alignment of metallic nanowires," *Appl. Phys. Lett.*, vol. 77, p. 1399, 2000.

[22] B. D. Gates, Q. Xu, M. Stewart, D. Ryan, C. G. Willson and G. M. Whitesides, "New approaches to nanofabrication: molding, printing, and other techniques," *Chem. Rev.-Columbus*, vol. 105, p. 1171, 2005.

[23] Y. Chen and A. Pepin, "Nanofabrication: Conventional and nonconventional methods," *Electrophoresis*, vol. 22, p. 187, 2001.

[24] D. Tsivion, M. Schvartzman, R. Popovitz-Biro, P. von Huth and E. Joselevich, "Guided growth of millimeter-long horizontal nanowires with controlled orientations," *Science*, vol. 333, p. 1003, 2011.

[25] Z. Sun, E. Zussman, A. L. Yarin, J. H. Wendorff and A. Greiner, "Compound core-shell polymer nanofibers by co-electrospinning," *Adv. Mater.* vol. 15, p. 1929, 2003.

[26] S. Dougherty and J. Liang, "Core–shell polymer nanorods by a two-step template wetting process," *Nanotechnology*, vol. 20, p. 1, 2009.

[27] W. Lu and C. M. Lieber, "Nanoelectronics from the bottom up," *Nature Mater.*, vol. 6, p. 841, 2007.

[28] C. Thelander, P. Agarwal, S. Brongersma, J. Eymery, L. F. Feiner, A. Forchel, M. Scheffler, W. Riess, B. J. Ohlsson, U. Gösele and L. Samuelson "Nanowire-based one-dimensional electronics," *Mater. Today*, vol. 9, p. 28, 2006.

[29] C. M. Lieber and Z. H. Wang, "Functional nanowires," *MRS Bull.*, vol. 32, p. 99, 2007.

[30] I. Brodie and J. J. Muray, “The physics of micro/nano-fabrication,” *Springer*, 1992.

[31] M. Yaman, T. Khudiyev, E. Ozgur, M. Kanik, O. Aktas, E. O. Ozgur, H. Deniz, E. Korkut and M. Bayindir, “Arrays of indefinitely long uniform nanowires and nanotubes,” *Nature Mater.*, vol. 10, p. 494, 2011.

[32] T.Khudiyev, M. Yaman and M. Bayindir, “Tailoring self-organized nanostructured morphologies in kilometer-long polymer fibre,” (submitted).

[33] T. Khudiyev, E. Ozgur, M. Yaman and M. Bayindir, “Structural Coloring in Large Scale Core–Shell Nanowires,” *Nano Lett.*, vol. 11, p. 4661, 2011.

[34] T. Khudiyev and M. Bayindir, “Emergent optical properties of cylindirical core-shell polymer nanostructures,” (submitted).

[35] T. Khudiyev, T. Dogan and M. Bayindir, “Nanobiomimicry of iridescent structures in the *Anas platyrhynchos* drakes” (in preparation).

[36] T. Khudiyev, Y. Cetin and M. Bayindir, “Engineering all-polymer core-shell nanowires as a light-trapping nano-platform” (in preparation).

[37] T. Khudiyev and M. Bayindir, “Supercontinuum generation from nanowire array” (in preparation).

[38] I. W. Donald, “Production, properties and applications of microwire and related products,” *J. Mater. Sci.*, vol. 22, p. 2661, 1987.

[39] Y. Yu, V. E. Ferry, A. P. Alivisatos and L. Cao, “Dielectric Core–Shell Optical Antennas for Strong Solar Absorption Enhancement,” *Nano Lett.*, vol. 12, p. 3674, 2012.

[40] H. Fang, W. Wu, J. Song and Z. L. Wang, “Controlled growth of aligned polymer nanowires,” *J. Phys. Chem. C*, vol. 113, p. 16571, 2009.

[41] M. Goto, A. Kasahara and M. Tosa, "Synthesis of polymer nanowires by pulsed laser irradiation," *Appl. Phys. Express,* vol. 2, p. 5503, 2009.

[42] H. D. Tran, D. Li and R. B. Kaner, "One-dimensional conducting polymer, nanostructures: Bulk synthesis and applications," *Adv. Mater.,* vol. 21, p. 1487, 2009.

[43] D. H. Reneker and I. Chun, "Nanometre diameter fibers of polymer, produced by electrospinning," *Nanotechnology,* vol. **7**, p. 216, 1996.

[44] X. Zhang, J. Zhang, W. Song and Z. Liu, "Controllable synthesis of conducting polypyrrole nanostructures," *J. Phys. Chem. B,* vol. 110, p. 1158, 2006.

[45] A. Noy, A. E. Miller, J. E. Klare, B. L. Weeks, B. W. Woods and J. J. DeYoreo, "Fabrication of luminescent nanostructures and polymer nanowires using dip-pen nanolithography," *Nano Lett.,* vol. 2, p. 109, 2002.

[46] T. Thurn-Albrecht, J. Schotter, G. A. Kastle, N. Emley, T. Shibauchi, L. Krusin-Elbaum, K. Guarini, C. T. Black, M. T. Tuominen and T. P. Russell, "Ultrahigh-density nanowire arrays grown in self-assembled diblock copolymer templates," *Science,* vol. 290, p. 2126, 2000.

[47] S. Shabahang, J. J. Kaufman, D. S. Deng and A. F. Abouraddy, "Observation of the Plateau-Rayleigh capillary instability in multi-material optical fibers," *Appl. Phys. Lett.,* vol. 99, p. 161909, 2011.

[48] T. Khudiyev and M. Bayindir, "Iterative Size Reduction Technique for Optical Nanostructures," *Frontiers in Optics. Optical Society of America,* 2012.

[49] J. J. Kaufman, G. Tao, S. Shabahang, E. H. Banaei, D. S. Deng, X. Liang, S. G. Johnson, Y. Fink and A. F. Abouraddy, "Structured spheres generated by an in-fiber fluid instability," *Nature,* vol. 487, p. 463, 2012.

[50] H. Hou, L. Wang, F. Gao, G. Wei, J. Zheng, X. Cheng, B. Tang and W. Yang, "Mass production of SiC/SiOx nanochain heterojunctions with high purities," *CrystEngComm,* vol. 15, p. 2986, 2013.

[51] H. Yoo, J. I. Lee, H. Kim, J. P. Lee, J. Cho and S. Park, "Helical Silicon/Silicon Oxide Core–Shell Anodes Grown onto the Surface of Bulk Silicon," *Nano Lett.*, vol. 11, p. 4324, 2011.

[52] H. W. Liang, S. Liu and S. H. Yu, "Controlled Synthesis of One-Dimensional Inorganic Nanostructures Using Pre-Existing One-Dimensional Nanostructures as Templates," *Adv. Mater.*, vol. 22, p. 3925, 2010.

[53] K. Ramasamya and A. Guptab, "Routes to self-assembly of nanorods," *J. Mater. Res.*,vol. 15, p. 16, 2013.

[54] G. Caputoa and N. Pinna "Nanoparticle self-assembly using π–π interactions," *J. Mater. Chem. A*, vol. 1, p. 2370, 2013.

[55] S. Das, P. Ranjan, P. S. Maiti, G. Singh, G. Leitus and R. Klajn, "Dual-Responsive Nanoparticles and their Self-Assembly," *Adv. Mater.*, vol. 25, p. 422, 2013.

[56] M. Grzelczak, J. Vermant, E. M. Furst and L. M. Liz-Marzán, "Directed self-assembly of nanoparticles," *ACS Nano*, vol. 4, p. 3591, 2010.

[57] S. Chen, H. Hou, P. Hu, J. H. Wendorff, A. Greiner and S. Agarwal, "Polymeric nanosprings by bicomponent electrospinning," *Macromol. Mater. Eng.*, vol. 294, p. 265, 2009.

[58] M. C. Rechtsman, J. M. Zeuner, Y. Plotnik, Y. Lumer, D. Podolsky, F. Dreisow, S. Nolte, M. Segev and A. Szameit, "Photonic Floquet topological insulators," *Nature*, vol. 496, p. 196, 2013.

[59] J. K. Gansel, M. Thiel, M. S. Rill, M. Decker, K. Bade, V. Saile, G. Freymann,

S. Linden and M. Wegener, "Gold helix photonic metamaterial as broadband circular polarizer" *Science*, vol. 325, p. 1513, 2009.

[60] T. Cantrell, G. Corti, M. Beaux, T. Prakash, D. N. McIlroy, T. F. Turba and M. G. Norton, "Next Generation Nanospring-enhanced Catalytic Converters," *Clean Technology, Hydrogen & Transportation*, p. 267, 2010.

[61] V. V. R. Sai, D. Gangadean, I. Niraula, J. M. Jabal, G. Corti, D. N. McIlroy, D. E. Aston, J. R. Branen and P. J. Hrdlicka, "Silica nanosprings coated with noble metal nanoparticles: highly active SERS substrates," *J. Phys. Chem. C*, vol. 115, p. 453, 2010.

[62] V. Dobrokhotov, L. Oakes, D. Sowell, A. Larin, J. Hall, A. Kengne, P. Bakharev, G. Corti, T. Cantrell, T. Prakash, J. Williams and D. N. McIlroy, "Toward the nanospring-based artificial olfactory system for trace-detection of flammable and explosive vapors," *Sensor Actuat B-Chem*, vol. 168, p. 138, 2012.

[63] X. L. Wu, Q. Liu, Y. G. Guo and W. G. Song, "Superior storage performance of carbon nanosprings as anode materials for lithium-ion batteries," *Electrochem. Commun.*, vol. 11, p. 1468, 2009.

[64] J. Liu, Y. L. Lu, M. Tian, F. Li, J. Shen, Y. Gao and L. Zhang, "The Interesting Influence of Nanosprings on the Viscoelasticity of Elastomeric Polymer Materials: Simulation and Experiment," *Adv. Mater.*, vol. 23, p. 1156, 2013.

[65] V. Varshney, A. K. Roy, D. S. Dudis, J. Lee and B. L. Farmer, "A novel nano-configuration for thermoelectrics: helicity induced thermal conductivity reduction in nanowires," *Nanoscale*, vol. 4, p. 5009, 2012.

[66] G. Chen, J. Wu, Q. Lu, H. R. Gutierrez, Q. Xiong, M. E. Pellen, J. S. Petko, D. H. Werner and P. C. Eklund, "Optical antenna effect in semiconducting nanowires," *Nano Lett.*, vol. 8, p. 1341, 2008.

[67] H. Park, K. J. Byeon, K. Y. Yang, J. Y. Cho and H. Lee, "The fabrication of a patterned ZnO nanorod array for high brightness LEDs," *Nanotechnology*, vol. 21, p. 355304, 2010.

[68] J. X. Wang, X. W. Sun, Y. Yang, H. Huang, Y. C. Lee, O. K. Tan and L. Vayssieres, "Hydrothermally grown oriented ZnO nanorod arrays for gas sensing applications," *Nanotechnology*, vol. 17, p. 4995, 2006.

[69] W. U. Huynh, J. J. Dittmer and A. P. Alivisatos, “Hybrid nanorod-polymer solar cells,” *Science*, vol. 295, p. 2425, 2002.

[70] G. Pellegrini, G. Mattei and P. Mazzoldi, “Nanoantenna arrays for large-area emission enhancement” *J. Phys. Chem. C*, vol. 115, p. 24662, 2011.

[71] X. Wang, H. Li, X. Yu, X. Shi and J. Liu, “High-performance solution-processed plasmonic Ni nanochain-Al_2O_3 selective solar thermal absorbers,” *Appl. Phys. Lett.*, vol. 101, p. 203109, 2012.

[72] Z. Gu, F. Liu, X. Li and Z. W. Pan, “Luminescent GeO2–Zn2GeO4 hybrid one dimensional nanostructures,” *CrystEngComm*, vol. 15, p. 2904, 2013.

[73] M. A. Rafiq, K. Masubuchi, Z. A. Durrani, A. Colli, H. Mizuta, W. I. Milne and S. Oda, “Conduction bottleneck in silicon nanochain single electron transistors operating at room temperature,” *Jpn. J. Appl. Phys.*, vol. 51, p. 5202, 2012.

[74] Y. Zhao, Z. Xie, H. Gu, L. Jin, X. Zhao, B. Wang and Z. Gu, “Multifunctional photonic crystal barcodes from microfluidics,” *NPG Asia Mater.*, vol 4, e25, 2012.

[75] A. I. Kuznetsov, A. B. Evlyukhin, M. R. Gonçalves, C. Reinhardt, A. Koroleva, M. L. Arnedillo, R. Kiyan, O. Marti and B. N. Chichkov, “Laser fabrication of large-scale nanoparticle arrays for sensing applications,” *ACS Nano*, vol. 5, p. 4843, 2011.

[76] K. S. Kunz and R. J. Luebbers, “The finite difference time domain methods for electromagnetics*,” CRC press*, 1993.

[77] Y. Chung and N. Dagli, “An assessment of finite difference beam propagation method,” *IEEE J Quant. Electron.*, vol 26, p. 1335, 1990.

[78] P. J. Flatau and B. T. Draine, “Discrete-dipole approximation for scattering calculations,” *J. Opt. Soc. Am. A*, vol. 11, p. 1491, 1994.

[79] G. Gouesbet and J. A. Lock, “Rigorous justification of the localized approximation to the beam-shape coefficients in generalized Lorenz-Mie theory. II. Off-axis beams,” *J. Opt. Soc. Am. A*, vol. 11, p. 2516, 1994.

[80] Solutions, F. D. T. D. Version 8.5.0., *Lumerical Solutions. Inc., Vancouver, BC, Canada*., 2013.

[81] C. F. Bohren, and D. R. Huffman, “Absorption and scattering of light by small particles,” (John Wiley & Sons Inc.: New York, 1998).

[82] Solutions, MODE Version 5.0., *Lumerical Solutions. Inc., Vancouver, BC, Canada*., http://www. lumerical. com.

[83] G. Placzek, “The Rayleigh and Raman Scattering,” *Lawrence Radiation Laboratory*, vol. 526, 1959.

[84] A. T. Young, “Rayleigh scattering,” *Appl. Opt*, vol. 20, p. 533, 1981.

[85] A. Ashkin and J. M. Dziedzic, “Observation of optical resonances of dielectric spheres by light scattering,” *Appl. Opt.*, vol. 20, p. 1803, 1981.

[86] P. Bassan, H. J. Byrne, F. Bonnier, J. Lee, P. Dumas and P. Gardner, “Resonant Mie scattering in infrared spectroscopy of biological materials–understanding the ‘dispersion artefact’,” *Analyst*, vol. 134, p. 1586, 2009.

[87] P. K. Jain, K. S. Lee, I. H. El-Sayed and M. A. El-Sayed, “Calculated absorption and scattering properties of gold nanoparticles of different size, shape, and composition: applications in biological imaging and biomedicine” *J. Phys. Chem. B*, vol. 110, p. 7238, 2006.

[88] I. S. Saidi, S. L. Jacques and F. K. Tittel, “Mie and Rayleigh modeling of visible-light scattering in neonatal skin,” *Appl. Opt.*, vol. 34, p. 7410, 1995.

[89] Y. Yu and L. Cao, “Coupled leaky mode theory for light absorption in 2D, 1D, and 0D semiconductor nanostructures,” *Opt. Express*, vol. 20, p. 13847, 2012.

[90] P. Latimer, “Light scattering by ellipsoids,” *J. Colloid Interface Sci.*, vol. 53, p. 102, 1975.

[91] C. F. Bohren, “Light scattering by an optically active sphere,” *Chem. Phys. Lett.*, vol. 29, p. 458, 1974.

[92] K. F. Ren, G. Gréhan and G. Gouesbet, “Scattering of a Gaussian beam by an infinite cylinder in the framework of generalized Lorenz–Mie theory: formulation and numerical results,” *J. Opt. Soc. Am. A*, vol. 14, p. 3014, 1997.

[93] J. R. Wait, “Scattering of a plane wave from a circular dielectric cylinder at oblique incidence,” *Can. J. Phys*, vol. 33, p. 189, 1955.

[94] R. T. Wang and H. C. Van de Hulst, “Application of the exact solution for scattering by an infinite cylinder to the estimation of scattering by a finite cylinder,” *Appl. Opt.*, vol. 34, p. 2811, 1995.

[95] W. C. Mundy, J. A. Roux and A. M. Smith, “Mie scattering by spheres in an absorbing medium,” *J. Opt. Soc. Am. A*, vol. 64, p. 1593, 1974.

[96] J. R. Hodkinson and I. Greenleaves, “Computations of light-scattering and extinction by spheres according to diffraction and geometrical optics, and some comparisons with the Mie theory,” *J. Opt. Soc. Am. A*, vol. 53, p. 577, 1963.

[97] Y. L. Xu, “Electromagnetic scattering by an aggregate of spheres,” *Appl. Opt.*, vol. 34, p. 4573, 1995.

[98] F. Vollmer and S. Arnold, “Whispering-gallery-mode biosensing: label-free detection down to single molecules,” *Nature Methods*, vol. 5, p. 591, 2008.

[99] L. Collot, V. Lefevre-Seguin, M. Brune, J. M. Raimond and S. Haroche, “Very high-Q whispering-gallery mode resonances observed on fused silica microspheres,” *Europhys. Lett.*, vol. 23, p. 327, 1993.

[100] P. J. D. R. G. Chylek, J. D. Pendleton and R. G. Pinnick, "Internal and near-surface scattered field of a spherical particle at resonant conditions," *Appl. Opt.*, vol. 24, p. 3940, 1985.

[101] M. I. Mishchenko, L. D. Travis and A. A. Lacis, "Scattering, Absorption, and Emmision of Light by Small Particles," *Cambridge university press*, 2002.

[102] L. Cao, J. S. Park, P. Fan, B. Clemens and M. L. Brongersma, "Resonant Germanium Nanoantenna Photodetectors," *Nano Lett.*, vol. 10, p. 1229, 2010.

[103] L Cao, P. Fan, A. P. Vasudev, J. S. White, Z. Yu, W. Cai, J. A. Schuller, S. Fan and M. L. Brongersma, "Semiconductor nanowire optical antenna solar absorbers," *Nano Lett.*, vol. 10, p. 439, 2010.

[104] T. J. Kempa, J. F. Cahoon, S. K. Kim, R.W. Day, D.C. Bell, H. G. Park and C.M. Lieber, "Coaxial multishell nanowires with high-quality electronic interfaces and tunable optical cavities for ultrathin photovoltaics," *Proc. Natl. Acad. Sci.*, vol. 109, p. 1409, 2012.

[105] S. Kim, J. Jin, Y. J. Kim, In. Y. Park, Y. Kim and S. W. Kim, "High-harmonic generation by resonant plasmon field enhancement," *Nature*, vol. 453, p. 757, 2008.

[106] M. Retsch, M. Schmelzeisen, H. J. Butt and E. L. Thomas, "Visible Mie scattering in nonabsorbing hollow sphere powders," *Nano Lett.*, vol. 11, p. 1389, 2011.

[107] J. H. Lee, H. W. Ro, R. Huang, P. Lemaillet, T. A. Germer, C. L. Soles and C. M. Stafford, "Anisotropic, Hierarchical Surface Patterns via Surface Wrinkling of Nanopatterned Polymer Films," *Nano Lett.*, vol. 12, p. 5995, 2012.

[108] A. Noy, A. E. Miller, J. E. Klare, B. L. Weeks, B. W. Woods and J. J. DeYoreo, "Fabrication of luminescent nanostructures and polymer nanowires using dip-pen nanolithography," *Nano Lett.*, vol. 2, p. 109, 2002.

[109] A. M. Kumar, S. Jung and T. Ji, "Protein biosensors based on polymer nanowires, carbon nanotubes and zinc oxide nanorods," *Sensors*, vol. 11, p. 5087, 2011.

[110] K. H. Cheng, Y. Zhong, B. Y. Xie, Y. Q. Dong, Y. Hong, J. Z. Sun, B. Z. Tang and K. S. Wong, "Fabrication of and ultraviolet lasing in TPE/PMMA polymer nanowires," *J. Phys. Chem. C*, vol. 112, p. 17507, 2008.

[111] L. Cao, P. Fan and M. L. Brongersma, "Optical coupling of deep-subwavelength semiconductor nanowires," *Nano Lett.*, vol. 11, p. 1463, 2011.

[112] M. Bayindir, B. Temelkuran and E. Ozbay, "Tight-binding description of the coupled defect modes in three-dimensional photonic crystals," *Phys. Rev. Lett.*, vol 84, p. 2140, 2000.

[113] S. Pancharatnam, "Generalized theory of interference, and its applications," *In Proceedings of the Indian Academy of Sciences-Section A*, vol. 44, p. 247, Springer India,1956, November.

[114] J. F. Seely and W. R. Hunter, "Thin film interference optics for imaging the O II 834-Å airglow," *Appl. Opt.*, vol. 30, p. 2788, 1991.

[115] G. Brönstrup, C. Leiterer, N. Jahr, C. Gutsche, A. Lysov, I. Regolin, W. Prost, F. J. Tegude, W. Fritzsche and S. Christiansen, "A precise optical determination of nanoscale diameters of semiconductor nanowires," *Nanotechnology*, vol. 22, p. 385201, 2011.

[116] O. Mudanyali, E. McLeod, W. Luo, A. Greenbaum, A. F. Coskun, Y. Hennequin, C. P. Allier and A. Ozcan, "Wide-field optical detection of nanoparticles using on-chip microscopy and self-assembled nanolenses," *Nature Photon.*, vol. 7, p. 240, 2013.

[117] M. Srinivasarao, "Nano-optics in the biological world: beetles, butterflies, birds, and moths" *Chem. Rev.*, vol. 99, p. 1935, 1999.

[118] D. W., Lee and R. Graham, "Leaf optical properties of rainforest sun and extreme shade plants," *Am. J. Bot.*, p. 1100, 1986.

[119] J. Huxley, "The coloration of Papilio zalmoxis and P. antimachus, and the discovery of Tyndall blue in butterflies," *Proceedings of the Royal Society of London. Series B. Biological Sciences*, vol. 193, p. 441, 1976.

[120] P. J. Herring, "Reflective systems in aquatic animals," *Comparative Biochemistry and Physiology Part A: Physiology*, vol. 109, p. 513, 1994.

[121] H. Yin, L. Shi, J. Sha, Y. Li, Y. Qin, B. Dong, S. Meyer, X. Liu and J. Zi, "Iridescence in the neck feathers of domestic pigeons," *Phys. Rev. E*, vol. 74, p. 051916, 2006.

[122] K. S. Gould and D. W. Lee, "Physical and ultrastructural basis of blue leaf iridescence in four Malaysian understorey plants," *Am. J. Bot.*, vol. 83, p. 45, 1996.

[123] J. H. Kim, J. H. Moon, S. Y. Lee and J. Park, "Biologically inspired humidity sensor based on three-dimensional photonic crystals" *Appl. Phys. Lett.*, vol. 97, p. 103701, 2010.

[124] T. S. Kustandi, H. Y. Low, J. H. Teng, I. Rodriguez, and R.Yin, "Mimicking Domino-Like Photonic Nanostructures on Butterfly Wings," *Small*, vol. 5, p. 574, 2009.

[125] M. Kolle, P. M. Salgard-Cunha, M. R. Scherer, F. Huang, P. Vukusic, S. Mahajan, J. J. Baumberg and U. Steiner, "Mimicking the colourful wing scale structure of the Papilio blumei butterfly," *Nature Nanotech.*, vol. 5, p. 511, 2010.

[126] A. G. Aberle, "Thin-film solar cells," *Thin Solid Films*, vol. 517, p. 4706, 2009.

[127] J. Poortmans and Arkhipov, V. (Eds.). "Thin film solar cells: fabrication, characterization and applications," *John Wiley & Sons.*, vol. 5, 2006.

[128] J. Müller, B. Rech, J. Springer and M. Vanecek, "TCO and light trapping in silicon thin film solar cells," *Sol. Energy*, vol. 77, p. 917, 2004.

[129] F. J. Haug, T. Söderström, D. Dominé and C. Ballif, "Light trapping effects in thin film silicon solar cells," In *MRS Spring Meeting, San Francisco, USA.*, 2009, January.

[130] R. Dewan and D. Knipp, "Light trapping in thin-film silicon solar cells with integrated diffraction grating," *J. Appl. Phys.*, vol. 106, p. 074901, 2009.

[131] V. E. Ferry, J. N. Munday and H. A. Atwater, "Design considerations for plasmonic photovoltaics," *Adv. Mater.*, vol. 22, p. 4794, 2010.

[132] V. E. Ferry, A. Polman and H. A. Atwater, "Modeling light trapping in nanostructured solar cells," *ACS Nano*, vol. 5, p. 10055, 2011.

[133] G. Brambilla, F. Xu, P. Horak, Y. Jung, F. Koizumi, N. P. Sessions, E. Koukharenko, X. Feng, G. S. Murugan, J. S. Wilkinson and D. J. Richardson, "Optical fiber nanowires and microwires: fabrication and applications," *Advances in Optics and Photonics*, vol. 1, p. 107, 2009.

[134] M. Khorasaninejad, N. Abedzadeh, J. Walia, S. Patchett and S. S. Saini, "Color matrix refractive index sensors using coupled vertical silicon nanowire arrays," *Nano Lett.*, vol. 12, p. 4228, 2012.

[135] J. Homola, S. Yee and G. Gauglitz, "Surface plasmon resonance sensors: review," *Sens. Actuator B*, vol. 54, p. 3, 1999.

[136] B. H. Lee, Y. H. Kim, K. S. Park, J. B. Eom, M. J. Kim, B. S. Rho and H. Y. Choi, "Interferometric fiber optic sensors," *Sensors*, vol. 12, p. 2467, 2012.

[137] T. A. Birks, W. J. Wadsworth and P. S. J. Russell, "Supercontinuum generation in tapered fibers," *Opt. Lett.*, vol. 25, p. 1415, 2000.

[138] J. M. Dudley, G. Genty and S. Coen, "Supercontinuum generation in photonic crystal fiber," *Rev. Mod. Phys.*, vol. 78, p. 1135, 2006.

[139] P. B. Corkum, C. Rolland and T. Srinivasan-Rao, “Supercontinuum generation in gases,” *Phys. Rev. Lett.*, vol. 57, p. 2268, 1986.

[140] G. P. Agrawal, “Nonlinear fiber optics,” *Springer Berlin Heidelberg*, 2000.

[141] D. I. Yeom, E. C. Mägi, M. R. Lamont, M. A. Roelens, L. Fu and B. J. Eggleton, “Low-threshold supercontinuum generation in highly nonlinear chalcogenide nanowires,” *Opt. Lett.*, vol. 33, p. 660, 2008.

Appendix

Matlab script for scattering calculations.

TM polarization

```
clear all;
clc;
m1=1.58;
m2=1.41;
a=260;
b=a*1.5;
dx=0.000033579*a;
z=0.004188*a:dx:0.020944*a;
w=0.004188*b:dx*1.5:0.020944*b;
bn=zeros(length(w),1);
q=zeros(length(w),1);

for t=1:length(z)
  clc;
    t
     x=0.004188*a+(t-1)*dx;
     y=0.004188*b+(t-1)*dx*1.5;

    J=m2*besselj(0,x*m2)-
(m2^3/m1^2)*besselj(0,x*m1)*(besselj(-1,x*m2)-
besselj(1,x*m2))/(besselj(-1,x*m1)-besselj(1,x*m1));
    Y=(m2^3/m1^2)*besselj(0,x*m1)*(bessely(-1,x*m2)-
bessely(1,x*m2))/(besselj(-1,x*m1)-besselj(1,x*m1))-
m2*bessely(0,x*m2);
    C=m2*besselj(0,y*m2)+m2*(J/Y)*(bessely(0,y*m2));
    D=(m2^3)*(besselj(-1,y*m2)-
besselj(1,y*m2))+(m2^3)*(J/Y)*(bessely(-1,y*m2)-
bessely(1,y*m2));
   bn(1)=(abs((C*(besselj(-1,y)-besselj(1,y))-
besselj(0,y)*D)/(C*(besselh(-1,y)-besselh(1,y))-
besselh(0,y)*D))).^2;
for u=2:51

    J=m2*besselj(u-1,x*m2)-(m2^3/m1^2)*besselj(u-
1,x*m1)*(besselj(u-2,x*m2)-besselj(u,x*m2))/(besselj(u-
2,x*m1)-besselj(u,x*m1));
```

```
    Y=(m2^3/m1^2)*besselj(u-1,x*m1)*(bessely(u-2,x*m2)-
bessely(u,x*m2))/(besselj(u-2,x*m1)-besselj(u,x*m1))-
m2*bessely(u-1,x*m2);
    C=m2*besselj(u-1,y*m2)+m2*(J/Y)*(bessely(u-1,y*m2));
    D=(m2^3)*(besselj(u-2,y*m2)-
besselj(u,y*m2))+(m2^3)*(J/Y)*(bessely(u-2,y*m2)-
bessely(u,y*m2));
    bn(u)=bn(u-1)+2*(abs((C*(besselj(u-2,y)-besselj(u,y))-
besselj(u-1,y)*D)/(C*(besselh(u-2,y)-besselh(u,y))-besselh(u-
1,y)*D))).^2;
end;
bn(t)=bn(u);
q(t)=2*bn(t)./x;
end;

figure
plot(z,q);
length(w)
length(bn)
```

TE polarization

```
clear all;
clc;
m1=1.58;
m2=1.41;
a=260;
b=a*1.5;
dx=0.000033579*a;
z=0.004188*a:dx:0.020944*a;
w=0.004188*b:dx*1.5:0.020944*b;
an=zeros(length(w),1);
q=zeros(length(w),1);

for t=1:length(z)
  clc;
    t
     x=0.004188*a+(t-1)*dx;
     y=0.004188*b+(t-1)*dx*1.5;

    J=m1*m2*besselj(0,x*m1)*(besselj(-1,x*m2)-
besselj(1,x*m2))-m2*m1*besselj(0,x*m2)*(besselj(-1,x*m1)-
besselj(1,x*m1));
    Y=m2*m1*bessely(0,x*m2)*(besselj(-1,x*m1)-
besselj(1,x*m1))-m1*m2*besselj(0,x*m1)*(bessely(-1,x*m2)-
bessely(1,x*m2));
    D=(m2^2)*(Y/J)*besselj(0,y*m2)+(m2^2)*(bessely(0,y*m2));
    C=(m2^2)*(Y/J)*(besselj(-1,y*m2)-
besselj(1,y*m2))+(m2^2)*(bessely(-1,y*m2)-bessely(1,y*m2));
```

```
   an(1)=(abs((D*(besselj(-1,y)-besselj(1,y))-
besselj(0,y)*C)/(D*(besselh(-1,y)-besselh(1,y))-
besselh(0,y)*C))).^2;
for u=2:51

    J=m1*m2*besselj(u-1,x*m1)*(besselj(u-2,x*m2)-
besselj(u,x*m2))-m2*m1*besselj(u-1,x*m2)*(besselj(u-2,x*m1)-
besselj(u,x*m1));
    Y=m2*m1*bessely(u-1,x*m2)*(besselj(u-2,x*m1)-
besselj(u,x*m1))-m1*m2*besselj(u-1,x*m1)*(bessely(u-2,x*m2)-
bessely(u,x*m2));
    D=(m2^2)*(Y/J)*besselj(u-1,y*m2)+(m2^2)*(bessely(u-
1,y*m2));
    C=(m2^2)*(Y/J)*(besselj(u-2,y*m2)-
besselj(u,y*m2))+(m2^2)*(bessely(u-2,y*m2)-bessely(u,y*m2));
   an(u)=an(u-1)+2*(abs((D*(besselj(u-2,y)-besselj(u,y))-
besselj(u-1,y)*C)/(D*(besselh(u-2,y)-besselh(u,y))-besselh(u-
1,y)*C))).^2;

end;
an(t)=an(u);
q(t)=2*an(t)./x;
end;

 figure
plot(z,q);
length(w)
%length(bn)
```